Braunschweiger Schriften zur Mechanik Nr. 62-2007

A computational model for seismically induced liquefaction

von

Vera Struckmeier

Institut für Angewandte Mechanik

Technische Universität Braunschweig

Herausgegeben vom Mechanik-Zentrum der
Technischen Universität Braunschweig

Schriftleiter: Prof. Dr. rer. nat. H. Antes
Institut für Angewandte Mechanik
Postfach 3329
38023 Braunschweig

Von der Fakultät Architektur, Bauingenieurwesen und Umweltwissenschaften
der Technischen Universität Carolo-Wilhelmina zu Braunschweig
zur Erlangung des Grades eines Doktor-Ingenieur (Dr.-Ing.)
genehmigte Dissertation

Eingereicht am 30. März 2007
Mündliche Prüfung am 7. Mai 2007

Berichterstatter

Prof. Dr. rer. nat. H. Antes
Prof. Dr. Ing. T. Crespellani
Eur. Ing. Prof. A.H.C. Chan

BSM 62-2007
ISBN 9783-920395-61-6

A computational model for seismically induced liquefaction

Dissertation

submitted to and approved by the

Faculty of Architecture, Civil Engineering and Environmental Sciences
University of Braunschweig - Institute of Technology

and the

Faculty of Engineering
University of Florence

in candidacy for the degree of a
Doktor-Ingenieur (Dr.-Ing.) /
Dottore di Ricerca in Risk Management on the Built Environment$^{\star)}$

by

Vera Struckmeier
from Hamburg, Germany

Submitted on	30 March 2007
Oral examination on	7 May 2007
Professoral advisors	Prof. Dr. rer. nat. H. Antes
	Prof. Dr. Ing. T. Crespellani
	Eur. Ing. Prof. A.H.C. Chan

2007

$\star$)Either the German or the Italian form of the title may be used

The dissertation is published in an electronic form by
the Braunschweig university library at the address

http://www.biblio.tu-bs.de/ediss/data/

Acknowledgments

First of all, I wish to express my deep gratitude to my supervisor Prof. Heinz Antes for the support and the encouragement provided during the period of my research work. I would like also to thank him for the opportunity he gave me to work together with the Computational Engineering group of the department of Civil Engineering, University of Birmingham.

I sincerely wish to express my deep appreciation to Prof. Andrew H.C. Chan from the University of Birmingham together with Prof. Martin Schanz from the University of Graz for their useful suggestions, comments and revisions of this thesis.

I would like to thank Prof. Teresa Crespellani for her interest in my research and her valuable advice on writing the thesis.

To all my colleagues in the Institute of Applied Mechanics at the Technical University Braunschweig I would like to express my thanks for their support.

The work is financially supported by the Deutsche Forschungsgemeinschaft within the international graduate research program »Risk Management of Natural and Civilisation Hazards on Buildings and Infrastructure«. I thank Prof. Udo Peil and Prof. Claudio Borri for conceiving and coordinating this international doctoral course.

To all my friends, my family and especially to Stephan Capellaro I would like to thank for their patience with me during the final stages of writing this work.

I wish to dedicate this thesis to my parents
Lisa and Heinrich Struckmeier.

Contents

Introduction

Significant damage to embankments, dams, building foundations, and infrastructure can be produced by liquefaction induced by an earthquake. The greatest impact could be seen at destroyed infrastructure, especially the failure of bridges, roads, and container ports. The destructive earthquake at Kobe on January 17th, 1995 caused an economic loss of about US $100 bn [133]. The cost of reinstatement of the sixth largest container port in the world due to ground liquefaction were estimated at US $12.8 bn. At the artificial Port Island (Kobe), subsidence of up to 3 m and shifts in the artificial coastline of more than 5 m were found [133]. In principal, earthquake

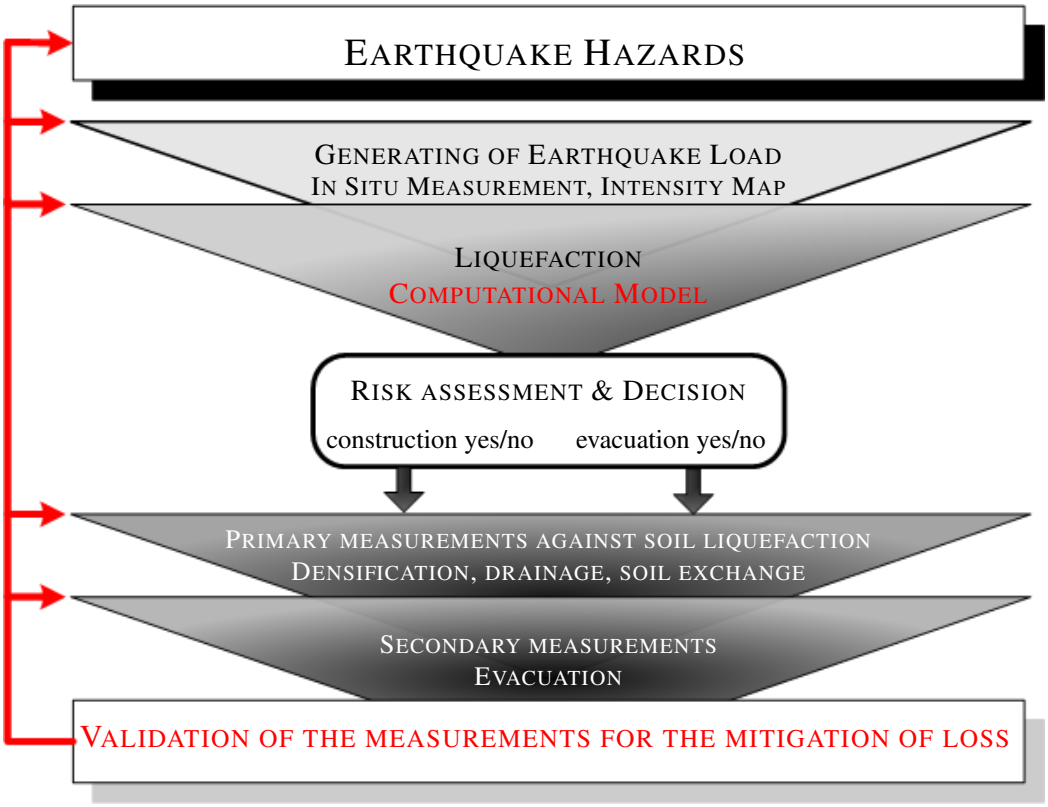

Figure 1: Risk assessement & Risk mitigation process

risk is the combination of two basic components, hazard and vulnerability [123], where an important seismic hazard is ground failure due to liquefaction [40]. In contrast to other natural hazards, earthquakes are to all intents and purposes impossible to predict [133]. Taking earthquake hazard as a given invariant, the main focus is to develop measures to reduce the potential loss due to earthquake induced liquefaction (see figure 1). Vulnerability of the exposed objects, e.g., embankments, dams, buildings, and foundations can be reduced by different structural and geotechnical engineering methods. These methods are mappings of hazardous zones, in situ measurements [41, 42] or computer simulation. Risk assessment in terms of vulnerability reduction implies evaluation of these methods. Therefore, a simulation model for the problem of

ground liquefaction is established in this thesis (see, figure 2). Liquefaction occurs in saturated soils due to earthquake excitation. Sediment types most susceptible to liquefaction are clay-free deposits of loose sand and silts in areas with high ground water level. If liquefaction happens, the cohesionless saturated undrained soil under earthquake motion could lose some or all of its strength. This is caused by an increase of interstitial pore pressure and, therefore, a decrease in the normal stress, thus, a decrease in the strength of the skeleton. This phenomenon, termed *soil liquefaction*, happens when in some instances the shear strength can drop down to zero. Then, the soil behaves almost like a viscous fluid. This phenomenon cannot be described by the behavior of a single phase material. A theory which takes into account the pore pressure as further degree of freedom in addition to the displacements of the solid skeleton is Biot's theory [20, 19] of fluid saturated porous media. The basic features of the numerical model for the simulation of ground liquefaction are the description by the behavior of a two phase material, e.g., Biot's theory of porous media, the enhancement of the constitutive model with respect to nonlinear soil behavior in the form of a non-associative bounding surface model »Pastor-Zienkiewicz mark III Model« and the application of the earthquake motion. These specifications have to be considered. This is done by decomposing the considered infinite-domain into a FEM sub-domain for the near field where non-linear material behavior occurs, and the BEM sub-domain for the far field to enable energy dissipation through radiation. Therefore, for treating wave propagation problems in non-linear poroelastic media, a coupling of the Finite Element Model with the Boundary Element Model within a single computational model seems to be a natural approach.

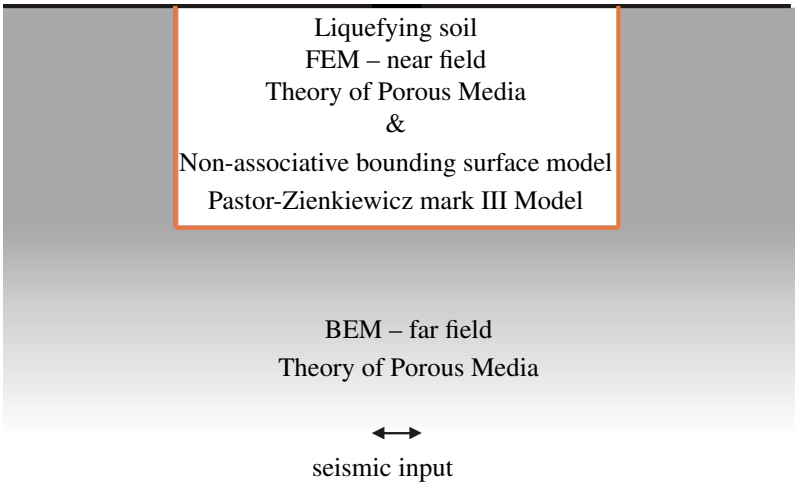

Figure 2: Basic features of the numerical model for simulation of ground liquefaction

Iterative coupling of FEM and BEM

In order to simulate ground liquefaction, it is advantageous to utilise the strengths of two different popular and powerful analysing tools, the Finite Element Method (FEM) and the Boundary Element Method (BEM). Combining both methods in the same computer program, therefore, would be the most efficient way to deal with problems that contain features which requires both BE and FE capabilities. In many unbounded field problems for instance, boundary elements

may provide appropriate conditions to represent the infinite domain while finite elements can solve complex material properties in finite domain. Boundary elements are also of interest in regions of singularities which arise under concentrated loads or in fracture mechanics, but finite elements may be adequate for layered continuum, anisotropic and non-linear materials. For problems like ground liquefaction where only a subdomain of the infinite region is exhibit to non-linear behavior, it is attractive to subdivide the model into a near-field (using FEM) and a far-field (using BEM).

Existing coupling methods can be roughly classified into three groups: Finite Element Method hosted, Boundary Element Method hosted, and those not belonging to one of these groups, the direct coupling method and the iterative domain decomposition method. The first type essentially treats the boundary element subdomain as a large finite element (super-element). Here, coupling is enforced by using the variational formulation, forcing the BE matrices to become symmetric by using an energy minimization scheme and presenting the BE matrices as stiffness matrices.

Zienkiewicz et al. [189] combined variational principles and integral equations to symmetrize the BE stiffness matrix for elastostatics problems and Beer and Meek [9] for elastoplasticity. Many publications followed that dealt with the same theme (see, for example, Shaw and Falby [153] and Margulies [110]). Based on least square error minimization, Brebbia [29] symmetrized the BE stiffness matrix by averaging the off-diagonal terms to improve computational convenience and efficiency. In this approach, the finite element region is treated as an equivalent boundary element.

Conversely, the BEM based approach treats the FE subdomain as an equivalent BE subregion by converting the stiffness equations of the FE subdomain to BEM-like equations (Zienkiewicz et al. [189], Kelly et al. [93]). These equations are then coupled with those of the BE subdomain while satisfying continuity and equilibrium along the interface. This method of coupling involves no matrix inversion as in the FEM hosted procedures, but unfortunately it destroys the positive characteristics of symmetry and bandedness that originally exist in the FEM.

Li et al. [102] devised an interesting approach, the bi-condensation method which involves the elimination of all the internal and external degrees of freedom in the FE stiffness matrix that do not relate to the interface of the BE-FE mesh. An overview of direct methods is given by Beskos [10, 12, 13]. Beskos and coworkers [90] were among the first who coupled the FEM with the BEM in time domain. Later, Antes and von Estorff [3, 4, 5, 166, 163] developed a general coupled FE-BE for soil-structure interaction in time domain. Also, Antes and coworkers [164, 2] presented a coupling methodology for fluid-structure analysis.

In the conventional methods of coupling the BE and FE solution matrices either the BE matrices have to be presented as stiffness matrices for the equation system of the FEM or the FE forces have to be transformed into tractions and linked with the tractions of the BE matrices for the equation system of the BEM. However, the direct coupling method may destroy the desirable features originally existing in the FEM matrices, namely, symmetry, sparsity, bandedness, and positiv definiteness, allowing, thus, the implementation of efficient solution algorithms.

Gerstle et al. [81] presented a solution method which is iterative in nature. The sub-domains are analyzed independently by applying trial displacements to degrees of freedom on the interface. The conjugate gradient domain decomposition solver is used to predict a new set of

trial interfacial displacements for the next iteration. The method of Gerstle is only applicable to symmetric BEM formulation. Perera [122] presented a parallel method based on the interface equilibrium of Steklov-Poincaré. Kamiya [88] employed the renewal methods known as Schwarz Neumann-Neumann and Schwarz Dirichlet-Neumann methods. It should be noted, however, that the above methods presented in [122, 88] are not applicable for problems where Neumann boundary conditions are specified on the entire external boundary of the FEM subdomain. When only Neumann boundary conditions can be imposed, it leads to singularity of matrices and non-unique solution. An example of such a problem is a local non-linarity (FEM) in an infinite domain (BEM). Kamiya and Iwase [87] introduced an iterative analysis using conjugate gradient and condensation. This method has the same limitations as mentioned above, it's limited of being applicable to only symmetric BEM formulation. Lin [103], Feng and Owen [76] presented an algorithm similar to the Schwarz Dirichlet-Neumann method. The algorithm is based on assigning an arbitrary displacement vector to the interface of the BEM sub-domain. Then, the energy equivalent nodal forces of the obtained interface tractions are treated as boundary condition for the FEM subdomain to solve for the interfacial displacements. The procedure is iterated until convergence is achieved. For cases where the Neumann boundary conditions are specified on the entire external boundary of the BEM sub-domain, one may use the method presented in reference [103, 76]. Elleithy and Al-Gahtani [68] presented an overlapping domain decomposition method for coupling the FEM and BEM. The domain of the original problem is subdivided into a FEM sub-domain, a BEM sub-domain, and a common region, which is modeled by both methods. The method overcomes situations where the Neumann boundary conditions are specified on the entire external boundary of the FEM subdomain. The overlapping, however, may create serious complication in the Schwarz method, even when the global problem is that of a simple geometry.

More general as the standard domain decomposition methods are the interface relaxation methods [104, 135]. In the interface relaxation methods, a corrective term at each time step is employed. The interface boundary conditions are iteratively updated until convergence is achieved. A relaxation parameter is used within the iteration procedure to enable or to accelerate convergence. The interface relaxation method has the same advantages as the domain decomposition method and, moreover, allows to handle unrelated partial differential equation problems within different subdomains.

Elleithy [72, 73, 74] and Tanaka presented two interface relaxation algorithms for coupling FEM and BEM, the algorithm in [72] was enhanced for elasto-plasticity [75, 157, 165] problems. Elleithy [69, 70, 67] investigated the convergence of the Dirichlet Neumann domain decomposition coupling method. This method is enhanced in this thesis for coupling of poroelastic/poroplastic FEM with BEM subdomains.

Biot's Poroelasticity A historical review on the subject of multiphase continuum mechanics identifies two poroelastic theories which have been developed and are used nowadays, namely Biot's theory and the Theory of Porous Media, discussed in detail in the work of de Boer [55, 56, 53].

Darcy [50] studied the flow through rigid porous media and the relationship between flow of the pore fluid and the gradient of the hydrostatic pressure. Later, Darcy's law was applied to consolidation problems by Terzaghi [160]. Based on the work of von Terzaghi, a theoretical

description of porous materials saturated by a viscous fluid was presented by Biot [16, 15]. This was the starting point of Biot's theory of poroelasticity. In the following years, Biot extended his theory to anisotropic cases [17] and also to poroviscoelasticity [18]. The dynamic extension of Biot's theory was published in 1956 in two papers, one covering the low frequency range [20] and the other one covering the high frequency range [21]. One of the significant findings in these papers was the identification of three different wave types for a 3-d continuum, namely two compressional waves and one shear wave. The additional compressional wave is also known as the slow wave and has been experimentally confirmed [124]. In Biot's original approach, a fully saturated material was assumed. The extension to a nearly saturated (partially saturated) poroelastic solid was presented by Vardoulakis and Beskos [162].

Based on the work of Fillunger [77], a different approach, the Theory of Porous Media has been developed. This theory is based on the axioms of continuum theories of mixtures [161, 24] extended by the concept of volume fractions by Bowen [25, 26] and by the research group of Ehlers [54, 63, 65, 64, 57]. Thus, the Theory of Porous Media proceeds from the assumption of immiscible and superimposed continua with internal interactions. Remarks on the equivalence of both theories are found in the work of Bowen [26], Ehlers and Kubik [66] and Schanz and Diebels [149]. In all these publications, linear versions of both theories are compared and, finally, the equivalence can only be shown if Biot's apparent mass density is set to zero. Here, Biot's theory is used but the results can be simply transferred to the Theory of Porous media because in the following the apparent mass density will be neglected and the equivalence of the mathematical operator ensures to have the same fundamental solutions, however, with different material constants. In the following, a two-phase material consisting of an elastic solid skeleton and an interstitial fluid is assumed. Furthermore, the assumption of full saturation is made, e.g., the whole pore space is filled with the fluid. The balance laws and the constitutive equations contains in the most general case the variables of solid and fluid displacements and pore pressure. In most cases, these variables are modified introducing the seepage velocity, describing the fluid movement relative to the solid frame, instead of the absolute fluid displacements. The governing equations are then usually formulated using one of two different sets of unknowns: either the pore pressure is eliminated and the solid displacements and seepage velocity remain, denoted as u_i^s-u_i^f-formulation in the following, or the seepage velocity is eliminated, and the solid displacements and pore pressure are selected as unknowns. Bonnet [22] has shown that the latter choice is sufficient to describe a poroelastic continuum. This reduction of unknowns, denoted as u_i^s-p-formulation, is only possible in a transformed domain, e.g., in the Laplace domain. Zienkiewicz [187] introduced a simplified poroelastic model to make a u_i^s-p-formulation in time domain possible.

Discretization of the near-field – FEM A powerful computational tool for the analysis of non-linear behavior in the near-field is the Finite Element Method. A finite element formulation for consolidation problem based on Biot's theory was first suggested by Sandhu and Wilson [142] and enhanced by Ghaboussi and Wilson [82, 83] for saturated porous elastic solids. For solving wave propagation problems for non-linear applications, further development took place by Zienkiewicz et al. [187, 176], Prevost [126, 127], Zienkiewicz and Shiomi [183], Lewis and Schrefler [101], Simon [156, 155], Zienkiewicz and Chan [177]. The later introduced a simplified poroelastic FEM [177] where the governing differential equation can be solved directly

in the time domain. This simplification neglects only the inertia effect of the fluid but not those of the solid skeleton. The area of validity of this approach has been studied by Zienkiewicz et al. [187] showing that problems with low frequency acceleration can be treated well by this approach, e.g., applications in earthquake engineering like liquefaction are possible. For the simulation of liquefaction, i.e., pore pressure generation under cyclic loading, modern constitutive laws are required: There is the class of multi-surface-kinematic-hardening models which were first proposed by Mroz [111, 112, 113]. Zienkiewicz et al. [119] developed a generalized plasticity model, the Pastor-Zienkiewicz Mark III model. It belongs to the class of bounding surface models which was originally proposed by Krieg [97] and Dafalias and Popov [48]. The more generell »Bounding Surface theory« was introduced later by Dafalias and Hermann [47]. Other models which can reproduce cyclic loading are belonging to hypoplasticity [96] or to incrementally nonlinear models [51].

If ground liquefaction induced by a seismic load is treated numerically, energy dissipation through the soil medium has to be taken into account. These physical observations are mathematically formulated in the Sommerfeld radiation condition [158]. In the FEM, special methods have to be applied to fulfill this condition, i.e., to ensure that no energy is reflected from the artificial boundary back into the domain, namely: First, viscous boundary conditions were used. These consists of dashpots which absorb the wave energy of plane waves (see, Zienkiewicz and Newton [181] and Lysmer and Kuhlmeyer [107]). Second, the use of radiation boundary conditons was suggested by Zienkiewicz and others [173]. Third, to use the so-called infinite elements [14]. Fourth, FE cloning or the method of the consistent inifinitesimal finite element cell method originally proposed by Dasgupta [52], nowadays better known under the term scaled boundary finite element method (SFBFEM) [172, 170]. Alternative methods and further development for the application to viscoelastic material are discussed by Wolf, Kim and others [94, 140, 141, 139, 171, 115]. Another well-known numerical method for the simulation of unbounded sub-regions is the Boundary Element Method (BEM), where the Sommerfeld radiation condition is implicitly fulfilled. In 1977-78 Brebbia and Domínguez [28, 27] demonstrated that the BEM, like the FEM, can be considered as special case of the general weighted residuals formulation of the governing differential equation. Contrary to the FEM, fundamental solution are used as weighting functions instead of the variation of ansatz functions.

Discretization of the far-field – BEM The BEM regarded as an integral equation method was first applied to potential theory by Fredholm [78] and it was enhanced for elastostatics by Kupradze [98]. The term BEM first appears in 1977 in the works of Banerjee and Butterfield [8] and Brebbia and Domínguez [28]. For a historical overview of boundary integral methods the reader is referred to the work of Beskos [11], also an introduction to BEM is given in Brebbia et al. [30].

Cruse and Rizzo [45, 43] published the first boundary integral formulation for elastodynamics in Laplace domain, with an inverse transformation into time domain. A direct solution in time domain was developed by Mansur [109, 108], Antes [1], and Karabalis and Beskos [89, 91], respectively. An overview of BEM in elastodynamics may be found in [10, 12].

A BE formulation for poroelastic media was first obtained in frequency domain by Cheng and others and Domínguez [39, 58]. A solution in time domain for poroelastic media was developed by Wiebe and Antes [167] under the condition of vanishing damping between the solid skeleton

and the fluid. Later, Chen and Dargush [37] proposed an analytical inverse transformation of the fundamental solutions in Laplace domain. Schanz and Antes [146, 144] proposed a time-dependent BE formulation for poroelastic media where the fundamental solution in Laplace domain is transformed by the convolution quadrature method [105, 106] to the time domain.

For coupling the BEM with the FEM, the same physical conditions are required. The FEM uses a simplified poroelastic model. This simplification neglects only the inertia effects of the fluid but not those of the solid skeleton. In the following, this approach will be called *simple poro* model. In contrast to the FEM, for the Boundary Element Method (BEM) no fundamental solution and, therefore, no BE formulation has been published for the simple poro model. This is due to the availability of the above mentioned time domain formulation of the general poroelastic model [145]. However, for treating also wave propagation problems in a non-linear poroelastic model, e.g., to take liquefaction into account, a coupled BE-FE procedure seems to be the best choice. But, for such coupled formulation, a BE formulation for the simple poro model must be available. Therefore, in chapter 3, a fundamental solution for simple poro is developed and implemented in the BEM program.

Scope of this Work

The numerical procedure which is required to simulate ground liquefaction is characterized by three special features, the chosen continuum mechanical model in the form of porous media, the enhancement of the constitutive model with respect to nonlinear soil behavior, and the application of the earthquake motion. These special features can be taken into account when the numerical model is divided into a FEM sub-domain for the near field, where non-linear material behavior occurs, and the BEM sub-domain for the far field, to avoid wave reflection.
Therefore, in this PhD thesis, a iterative coupling scheme for porous media was developed and verified and further applied to a coupled FEM/BEM halfspace which is liquefying in the FEM area. The proposed algorithm is based on the sequential Dirichlet-Neumann method with double relaxation. An interface relaxation algorithm for iterative coupling of the FEM and BEM domain was developed by Lin and also by Feng and Owen [76] for application in linear elastostatics. The enhancement of the Dirichlet-Neumann algorithm, which is suggested in this thesis, can be applied to the coupling of linear and non-linear poroelastic problems, like liquefaction. Furthermore, with the developed algorithm, the FEM program SWANDYNE, developed by the Computational Engineering group of the department of Civil Engineering, University of Birmingham could be coupled with the BEM code of the Institute of Applied Mechanics, in which a linear BE formulation for simplified poroelasticity has been developed and implemented.
These formulation was developed because the FEM program uses the simplified theory of poroelasticity. For coupling both numerical schemes, the same basic assumptions on the physical conditions are required.
In chapter 1, the Biot's constitutive equations are recalled and the assumptions for neglecting of the seepage velocity are given. The governing equations for the theory of poroelasticity for the FEM are discussed in chapter 2 and for the BEM in chapter 3. The derivation of the fundamental solution for the simple poro case by using Hörmander's method is given in section 3.1, and a visualization of the fundamental solution is presented. To validate the BEM program, test examples are solved in section 3.3. The investigated examples for 2-d and 3-d are chosen in a

way that they can be compared with a 1-d analytical solution for a poroelastic column.
In chapter 4, the constitutive model »Pastor-Zienkiewicz mark III (1986) Model», which is implemented in the FEM program Swandyne, is explained. Therefore, in the first section 4.1 of this chapter, an introduction to the classical theory of plasticity is given. Because the basic features of the used bounding surface model are founded on the basic theory of Critical State Models, these are described in detail in section 4.2. The above mentioned PZ mark III model, which belongs to this group of bounding surface models, is discussed in the last section 4.3.
The feasibility and validity of the proposed coupling algorithm, which is derived in chapter 5, is verified by solving different examples. The coupling of different examples for linear-elastic, poroelastic and poroplastic material behaviour is investigated and validated by comparison of the coupled FEM-BEM solution with those obtained using the FEM and the BEM separately (see section 5.1, 5.3). Further, the coupling algorithm is tested with respect to influence of spatial discretization and time step size (see section 5.2). The influence of the variation of different material parameters is investigated in the example of a 2-d halfspace in section 5.3. Some of the considered examples in this section reach the limit state of liquefaction where either sinusoidal loads or for seismic input are tested.
The main focus of this work is to treat wave propagation problems in a non-linear poroelastic model, e.g., to take liquefaction into account, through an iterative coupled FEM/BEM domain. Therefore, a linear description of the geometry in terms of small displacements and small deformation gradients is assumed. Furthermore, for the FEM non- linear constitutive equations and for the BEM area linear constitutive equations are considered.
Throughout this work, the Einstein summation convention is applied over repeated indices in a monomial, i.e., $a_{ij}b_{jk} = \sum_{j=1}^{dim} a_{ij}b_{jk}$.
Latin indices receive the values 1,2 in two dimensions (2-d), respectively, the values 1,2,3 in three dimensions (3-d), $dim = 2$ or 3 according to context, i.e., for a 2-d resp. 3-d problem.
Commas $()_{,i}$ denote spatial derivatives and dots $\dot{()}$ indicate the time derivative. As usual, the Kronecker delta is denoted by δ_{ij}. A list of applied symbols can be found on page 125.

1 Biot's Theory of Poroelasticity

Following Biot's approach to model the behavior of porous media, an elastic deformable skeleton with a statistical distribution of interconnected pores is considered [17]. This porosity is denoted by

$$\phi = \frac{V^{\mathrm{f}}}{V}\,, \tag{1.1}$$

where V^{f} is the volume of the interconnected pores contained in a sample of bulk volume V. Contrary to these pores, the sealed pores will be considered as part of the solid. Full saturation is assumed leading to $V = V^{\mathrm{f}} + V^{\mathrm{s}}$ with the volume of the solid V^{s}, i.e., a two-phase material is considered.

1.1 Constitutive Assumptions

One possible representation of poroelastic constitutive equations is to divide the total stress into its effective stress component (solid) and the stresses which are part of the fluid. In the poroelastic constitutive equations the total stress $\sigma_{ij} = \sigma^{\mathrm{s}}_{ij} + \sigma^{\mathrm{f}}\delta_{ij}$ and the pore pressure $p = -(1/\alpha)\,\sigma^{\mathrm{f}}$ are the independent variables [16]. The effective stress is defined as $\sigma^{\mathrm{s}}_{ij} = \sigma_{ij} + \alpha\delta_{ij}p$, where the stresses (effective stress σ^{s}_{ij} and total stress σ_{ij}) are tensile positive while the pore pressure p is positive in compression. Constitutive relationships will, however, still be written in the general form using an incremental definition

$$d\sigma^{\mathrm{s}}_{ij} = D_{ijkl}(d\varepsilon_{kl} - d\varepsilon^{0}_{kl}) \tag{1.2}$$

where D_{ijkl} is the tangential matrix dependent on the state variables and history and $d\varepsilon^{0}_{kl}$ corresponds to the increment of thermal or similar autogeneous strain and of the grain compression $\delta_{ij}\dot{p}/3K_{\mathrm{s}}$. The latter is generally neglected in soil problems.

With Biot's effective stress coefficient α which is usually taken for soils as $\alpha \approx 1$ and the solid displacement u_i the equation for linear elastic material reads

$$\sigma_{ij} = Gu_{i,j} + \left(K - \frac{2}{3}G\right)u_{k,k}\delta_{ij} - \alpha\delta_{ij}p \tag{1.3}$$

with the shear modulus and the compression modulus of the solid frame G and K, respectively. In this equation, a linear strain displacement relation is used, i.e., small deformation gradients are assumed. Additional to the total stress σ_{ij}, as a second constitutive equation, the variation of the fluid volume per unit reference volume ζ is introduced

$$\zeta = \alpha u_{k,k} + \frac{\phi^2}{R}p \tag{1.4}$$

with material constant R. This variation of fluid ζ is defined by the mass balance over a reference volume, i.e., by the continuity equation

$$\frac{\partial \zeta}{\partial t} + q_{i,i} = a \tag{1.5}$$

with the specific flux $q_i = \phi w_i$, the seepage velocity w_i, and a source term $a(t)$.

Further, the balance of momentum for the bulk material must be fulfilled. This dynamic equilibrium is given by

$$\sigma_{ij,j} + F_i = \rho \frac{\partial^2 u_i}{\partial t^2} + \phi \rho_f \frac{\partial w_i}{\partial t} \,, \tag{1.6}$$

with the bulk body force per unit volume F_i and the bulk density $\rho = \rho_s (1-\phi) + \phi \rho_f$ (ρ_s and ρ_f denotes the solid and fluid density, respectively). Next, the fluid transport in the interstitial space expressed by the specific flux $q_i = \phi w_i$ is modeled with a generalized Darcy's law

$$\phi w_i = q_i = -\kappa \left(p_{,i} + \rho_f \frac{\partial^2 u_i}{\partial t^2} + \frac{\rho_a + \phi \rho_f}{\phi} \frac{\partial w_i}{\partial t} - f_i^f \right) \,, \tag{1.7}$$

where κ denotes the permeability. Permeability has the dimensions of $[\text{length}^3 \cdot \text{time}]/[\text{mass}]$ which is different from the usual soil mechanics convention, k which has the dimension of velocity, i.e., $[\text{length}]/[\text{time}]$. Their values are related by $\kappa = k/(\rho_f g)$ where ρ_f and g are the fluid density and gravitational acceleration, respectively, at which the permeability is measured. In equation (1.7), an additional density, the apparent mass density ρ_a is introduced by Biot [20] to describe the interaction between fluid and skeleton. The apparent mass density is defined as $\rho_a = C\phi\rho_f$ where C is a factor depending on the geometry of the pores and the frequency of excitation. At low frequency, Bonnet and Auriault [23] measured C = 0.66 for a sphere assembly of glass bead. For a higher frequency range, a certain functional dependence of C on frequency has been proprosed based on conceptual porosity structures, e.g., in [21] and [23].

The five equations (1.3-1.7) represent Biot's linear theory of a poroelastic continuum. To eliminate in these five equations the seepage velocity w_i, Darcy's law has to be rearranged to find an expression for the seepage velocity. Obviously, due to the different time derivatives of w_i, this is not possible in time domain. However, if the inertia effects of the relative velocity of the fluid can be neglected, i.e., $\partial w_i/\partial t$ can be set to zero in (1.6 and 1.7), the elimination of the seepage velocity is possible. This results in the simplified dynamic equilibrium

$$\sigma_{ij,j} + F_i = \rho \frac{\partial^2 u_i}{\partial t^2} \,, \tag{1.8}$$

and the simplified dynamic version of Darcy's law

$$\phi w_i = q_i = -\kappa \left(p_{,i} + \rho_f \frac{\partial^2 u_i}{\partial t^2} - f_i^f \right) \,. \tag{1.9}$$

Now, Darcy's law (1.9) can be used to replace the seepage velocity in the above equations (1.3-1.5). Rearranging them yields the governing set of differential equations for the unknowns solid

displacement u_i and pore pressure p

$$G u_{i,jj} + \left(K + \frac{1}{3} G \right) u_{j,ij} - \alpha p_{,i} - \rho \frac{\partial^2 u_i}{\partial t^2} = -F_i \tag{1.10a}$$

$$\kappa p_{,ii} - \frac{\phi^2}{R} \frac{\partial p}{\partial t} - \alpha \frac{\partial u_{i,i}}{\partial t} + \kappa \rho_{\mathrm{f}} \frac{\partial^2 u_{i,i}}{\partial t^2} = f_i^{\mathrm{f}} - a \, . \tag{1.10b}$$

To complete the set of equations, the relation between strains and displacements has to be specified. Aiming at the equations of motion to model wave propagation phenomena, it is sufficient to formulate a linear kinematic equation. Hence, in the following, the relation of the solid/fluid strain to the solid/fluid displacement is chosen linear, respectively

$$\varepsilon_{ij}^{\mathrm{s}} = \frac{1}{2} \left(u_{i,j}^{\mathrm{s}} + u_{j,i}^{\mathrm{s}} \right) \qquad \varepsilon_{kk}^{\mathrm{f}} = u_{k,k}^{\mathrm{f}} \tag{1.11}$$

assuming small deformation gradients.

This simplification and, subsequent, the possibility to represent the governing equations with this reduced set of unknowns has been published by [187]. There, the authors discussed with the help of an analytical 1-d example the limitations of this simplification. Summarizing their results, in soil mechanics or geomechanical applications with mostly low frequency acceleration the complete Biot theory does not differ from the simplified form.

In the next section, the partial differential equations are multiplied by appropriate weighting functions (Method of weighted residuals) resulting in the weak form of the governing partial differential equations. Further, the domain is divided into subdomains (elements) and discretized by appropriate shape function (Galerkin Method) for the Finite Element formulation.

2 Finite Element Solution of the Biot Equation

2.1 Boundary Condition

- The Boundary Condition for the solid phase are prescribed displacement

$$u_i(\mathbf{x},t) = \bar{u}_i(\mathbf{x},t) \text{ on } \partial\Omega_{\mathrm{u}} \tag{2.1a}$$

- or prescribed total traction with n_j defining the outward normal of the surface:

$$\sigma_{ji}(\mathbf{x},t)\, n_j = \bar{t}_i(\mathbf{x},t) \text{ on } \partial\Omega_{\mathrm{t}} \tag{2.1b}$$

- The boundary condition for the fluid phase are prescribed outflow

$$n_i q_i(\mathbf{x},t) = \bar{q}(\mathbf{x},t) \text{ on } \partial\Omega_{\mathrm{q}} \tag{2.1c}$$

- or prescribed pressure:

$$p(\mathbf{x},t) = \bar{p}(\mathbf{x},t) \text{ on } \partial\Omega_{\mathrm{p}} \tag{2.1d}$$

- In the u-p formulation the boundary equation (2.1c) will be set as a natural boundary condition:

$$\bar{q} = -n_i \kappa \left(p_{,i} + \rho_{\mathrm{f}} \ddot{u}_i^{\mathrm{f}} - f_i^{\mathrm{f}} \right) \tag{2.1e}$$

2.2 u-p Discretization of the Biot equation

The interaction of full saturated media was discussed in the previous chapter 1, the solution of these equations can be done in a discrete form by the finite element method. With appropriate weighting functions, the equation system can be rewritten in an integral form, with the dynamic equilibrium of the soil-fluid mixture (1.6) and with the boundary condition (2.1b) the governing equation is

$$\int_{\Omega} u_i^{\star} \left[\sigma_{ji,j} + F_i - \rho \frac{\partial^2 u_i}{\partial t^2} \right] \mathrm{d}\Omega + \int_{\Gamma_{\mathrm{t}}} u_i^{\star} \left[\bar{t}_i - \sigma_{ji} n_j \right] \mathrm{d}\Gamma = 0 \,, \tag{2.2a}$$

where $u_i^{\star}$ are weighting functions which fulfill the boundary condition (2.1a) of prescribed displacement. With the dynamic equilibrium for the fluid (1.5, 1.9) and with the natural boundary

condition (2.1e) the second governing equation is obtained

$$\int_\Omega p^\star \left[-\kappa\left(p_{,ii}+\rho_\mathrm{f}\frac{\partial^2 u_{i,i}}{\partial t^2}-f^\mathrm{f}_{i,i}\right)\right]\mathrm{d}\Omega+\int_\Omega p^\star\left[\frac{\phi^2}{R}\frac{\partial p}{\partial t}+\alpha\frac{\partial u_{i,i}}{\partial t}\right]\mathrm{d}\Omega+ \int_{\Gamma_\mathrm{q}} p^\star\left[\bar{q}_i-\kappa n_i\left(p_{,i}+\rho_\mathrm{f}\ddot{u}^\mathrm{f}_i-f^\mathrm{f}_i\right)\right]\mathrm{d}\Gamma=0\,, \tag{2.2b}$$

where $p^\star$ is a set of arbitrary weighting functions which satisfies the boundary condition (2.1d) of prescribed pressure. If the fluid body force in the domain integral is constant, it's derivative will be zero and the fluid body force is only applied through the natural boundary condition (2.1e). Equation (2.2) can be rewritten

$$\int_\Omega u^\star_{i,j}\sigma_{ji}\,\mathrm{d}\Omega+\int_\Omega u^\star_i\rho\frac{\partial^2 u_i}{\partial t^2}\,\mathrm{d}\Omega=\int_\Omega u^\star_i F_i\,\mathrm{d}\Omega+\int_{\Gamma_\mathrm{t}} u^\star_i\bar{t}_i\,\mathrm{d}\Gamma\,, \tag{2.3a}$$

$$\int_\Omega p^\star_{,i}\kappa\left(p_{,i}+\rho_\mathrm{f}\frac{\partial^2 u_i}{\partial t^2}\right)\mathrm{d}\Omega+\int_\Omega p^\star\left(\frac{\phi^2}{R}\frac{\partial p}{\partial t}+\alpha\frac{\partial u_{i,i}}{\partial t}\right)\mathrm{d}\Omega = \int_\Omega p^\star_{,i}\kappa f^\mathrm{f}_i\mathrm{d}\Omega-\int_{\Gamma_\mathrm{q}} p^\star\bar{q}_i\,\mathrm{d}\Gamma\,, \tag{2.3b}$$

by using Green's identity for the first term on the left hand side. Equation (2.3) represents the weak form of Biot's governing equations.

2.2.1 Discretization in space

Spatial discretizaton of equation (2.3) leads to

$$\sum_{e=1}^{E}\left[\int_{\Omega_e} u^e_{i,j}\sigma_{ji}\,\mathrm{d}\Omega+\int_{\Omega_e} u^e_i\left(\rho\frac{\partial^2 u_i}{\partial t^2}-F_i\right)\mathrm{d}\Omega-\int_{\Gamma_{\mathrm{t}e}} u^e_i\bar{t}_i\,\mathrm{d}\Gamma\right]=0\,, \tag{2.4a}$$

$$\sum_{e=1}^{E}\left[\int_{\Omega_e} p^e_{,i}\kappa\left(p_{,i}+\rho_\mathrm{f}\frac{\partial^2 u_i}{\partial t^2}-f^\mathrm{f}_i\right)\mathrm{d}\Omega+\int_{\Omega_e} p^e\left(\frac{\phi^2}{R}\frac{\partial p}{\partial t}+\alpha\frac{\partial u_{i,i}}{\partial t}\right)\mathrm{d}\Omega+\int_{\Gamma_{\mathrm{q}e}} p^e\bar{q}_i\,\mathrm{d}\Gamma\right]=0\,, \tag{2.4b}$$

where $u_i=N^\mathrm{u}_K\bar{u}_{Ki}$ and $p=N^\mathrm{p}_L\bar{p}_L$ are a set of weighting functions which are non-zero locally. Application of shape functions and utilizing Biot's effective stress coefficient α at equation (2.4)

leads to the following set of equations for the solid

$$\sum_{e=1}^{E}\left[\int_{\Omega_e}\left(N^{\mathrm{u}}_{K,j}\right)^{\mathrm{T}}\sigma^{\mathrm{s}}_{ji}\,\mathrm{d}\Omega-\int_{\Omega_e}\left(N^{\mathrm{u}}_{K,i}\right)^{\mathrm{T}}\alpha N^{\mathrm{p}}_{L}\,\mathrm{d}\Omega\bar{p}_L+\int_{\Omega_e}\left(N^{\mathrm{u}}_{K}\right)^{\mathrm{T}}\rho N^{\mathrm{u}}_{K}\,\mathrm{d}\Omega\ddot{u}_{Ki}\right]$$
$$-\sum_{e=1}^{E}\left[\int_{\Omega_e}\left(N^{\mathrm{u}}_{K}\right)^{\mathrm{T}}F_i\,\mathrm{d}\Omega+\int_{\Gamma_{t\,e}}\left(N^{\mathrm{u}}_{K}\right)^{\mathrm{T}}\bar{t}_i\,\mathrm{d}\Gamma\right]=0\,, \tag{2.5a}$$

in matrix notation

$$\int_{\Omega}\mathbf{B}^{\mathrm{T}}\sigma^{\mathrm{s}}\,\mathrm{d}\Omega-\mathbf{Q}\bar{\mathbf{p}}+\mathbf{M}\ddot{\mathbf{u}}=\mathbf{f}^{(\mathbf{t})}$$

and for the fluid, respectively

$$\sum_{e=1}^{E}\left[\int_{\Omega_e}\left(N^{\mathrm{p}}_{L,i}\right)^{\mathrm{T}}\kappa N^{\mathrm{p}}_{L,i}\mathrm{d}\Omega\bar{p}_L+\int_{\Omega_e}\left(N^{\mathrm{p}}_{L,i}\right)^{\mathrm{T}}\kappa\rho_{\mathrm{f}}N^{\mathrm{u}}_{K}\mathrm{d}\Omega\ddot{u}_{Ki}+\int_{\Omega_e}\left(N^{\mathrm{p}}_{L}\right)^{\mathrm{T}}\alpha N^{\mathrm{u}}_{K,i}\,\mathrm{d}\Omega\dot{u}_{Ki}\right]$$
$$+\sum_{e=1}^{E}\left[\int_{\Omega_e}\left(N^{\mathrm{p}}_{L}\right)^{\mathrm{T}}\frac{\phi^2}{R}N^{\mathrm{p}}_{L}\,\mathrm{d}\Omega\dot{\bar{p}}_L\right]-\sum_{e=1}^{E}\left[\int_{\Omega_e}\left(N^{\mathrm{p}}_{L,i}\right)^{\mathrm{T}}\kappa f^{\mathrm{f}}_{i}\mathrm{d}\Omega-\int_{\Gamma_{\mathrm{q}\,e}}\left(N^{\mathrm{p}}_{L}\right)^{\mathrm{T}}\bar{q}_i\,\mathrm{d}\Gamma\right]=0\,, \tag{2.5b}$$

in matrix notation

$$\mathbf{H}\bar{\mathbf{p}}+\mathbf{G}\ddot{\mathbf{u}}+\mathbf{Q}^{\mathrm{T}}\dot{\mathbf{u}}+\mathbf{S}\dot{\bar{\mathbf{p}}}=\mathbf{f}^{(\mathbf{q})}$$

where

$\mathbf{B}=\mathbf{S}\mathbf{N}^{\mathrm{u}}$ displacement-strain transformation matrix for plane strain and axisymmetric condition in 2-d (see Zienkiewicz [184]

$\sigma^{\mathrm{s}}=\mathbf{D}\mathbf{B}\bar{\mathbf{u}}$ defines the effective stress for the linear form of the constitutive law

$\mathbf{Q}=\int_{\Omega}\mathbf{B}^{\mathrm{T}}\alpha\mathbf{m}\mathbf{N}^{\mathrm{p}}\,\mathrm{d}\Omega$ is the coupling matrix, where

$(\mathbf{m})^{\mathrm{T}}=[1,1,1,0]$ is a vector equivalent to the Kronecker δ_{ij}, for plane strain,

$\mathbf{H}=\int_{\Omega}\left(\nabla\mathbf{N}^{\mathrm{P}}\right)^{\mathrm{T}}\kappa\nabla\mathbf{N}^{\mathrm{P}}\,\mathrm{d}\Omega$ is the permeability matrix,

$\mathbf{S}=\int_{\Omega}\left(\mathbf{N}^{\mathrm{p}}\right)^{\mathrm{T}}\frac{\phi^2}{R}\mathbf{N}^{\mathrm{p}}\,\mathrm{d}\Omega$ is the compressibility matrix,

$\mathbf{G}=\int_{\Omega}\left(\nabla\mathbf{N}^{\mathrm{p}}\right)^{\mathrm{T}}\kappa\rho_{\mathrm{f}}\mathbf{N}^{\mathrm{u}}\,\mathrm{d}\Omega$ is the dynamic seepage forcing matrix.

The effect of **G** has been discussed in detail by Leung [100]: in the low frequency range as in the case of earthquake motion, the dynamic seepage acceleration can be omitted. Its retention is computationally undesirable as it will leave the overall matrix unsymmetric. In the program Swandyne, the **G** matrix is neglected on the left hand side of the equation system if a symmetric version of the global matrix is used. Numerical studies to the effect of the dynamic seepage acceleration can be found in Chan [34]. The right-hand terms in equation (2.5) are defined by

$$\mathbf{f}^{\mathrm{T}} = \int_{\Omega} (\mathbf{N}^{\mathrm{u}})^{\mathrm{T}} (\phi \rho_{\mathrm{f}} + (1-\phi)\rho_{\mathrm{s}})\, \mathbf{b}\, \mathrm{d}\Omega - \int_{\Gamma_t} (\mathbf{N}^{\mathrm{u}})^{\mathrm{T}} \bar{\mathbf{t}}\, \mathrm{d}\Gamma \tag{2.6}$$

$$\mathbf{f}^{\mathrm{q}} = \int_{\Omega} (\nabla \mathbf{N}^{\mathrm{p}})^{\mathrm{T}} \kappa \rho_{\mathrm{f}} \mathbf{b}\, \mathrm{d}\Omega - \int_{\Gamma_{\mathrm{q}}} (\mathbf{N}^{\mathrm{p}})^{\mathrm{T}} \bar{\mathbf{q}}\, \mathrm{d}\Gamma \tag{2.7}$$

The governing equations (2.5) contains implicitly the two unknown parmeters u and p . For the isotropic linear elastic case the first term of the constitutive relations (2.5a) represents the internal force term which can be written as

$$\mathbf{P}(\bar{\mathbf{u}}) = \int_{\Omega} \mathbf{B}^{\mathrm{T}} \sigma^{\mathrm{s}}\, \mathrm{d}\Omega = \int_{\Omega} \mathbf{B}^{\mathrm{T}} \mathbf{D}_{\mathrm{elastic}} \mathbf{B}\, \mathrm{d}\Omega \bar{\mathbf{u}} = \mathbf{K}_{\mathrm{elastic}} \bar{\mathbf{u}} \tag{2.8}$$

where $\mathbf{K}_{\mathrm{elastic}} = \int_{\Omega} \mathbf{B}^{\mathrm{T}} \mathbf{D}_{\mathrm{elastic}} \mathbf{B}\, \mathrm{d}\Omega$ is the linear elastic stiffness matrix, which is symmetric [184]. However, in problems where the solid-phase behaviour is non-linear, only the tangential stiffness matrix $\mathbf{K}_{\mathrm{T}}$ can be defined. The consistent tangential stiffness matrix can be obtained by performing full differentiation on the internal force term $\mathbf{P}(\bar{\mathbf{u}})$ [154].

$$\mathbf{K}_{\mathrm{T}} = \frac{\partial \mathbf{P}(\bar{\mathbf{u}})}{\partial \bar{\mathbf{u}}} = \int_{\Omega} \mathbf{B}^{\mathrm{T}} \mathbf{D}_{\mathrm{T}} \mathbf{B}\, \mathrm{d}\Omega \tag{2.9}$$

$$\frac{\partial \mathbf{P}(\bar{\mathbf{u}})}{\partial t} = \frac{\partial \mathbf{P}(\bar{\mathbf{u}})}{\partial \bar{\mathbf{u}}} \frac{\partial \bar{\mathbf{u}}}{\partial t} \tag{2.10}$$

Integration of the above matrices usually requires numerical techniques. A standard method is the Gaussian quadrature [184], where the integrands are evaluated at specific points of the element, then weighted and summed. The procedure is carried out in terms of a set of local coordinates. Since the discretization in space has been carried out, equation (2.5) represent a set of ordinary differential equations in time. For convenience, the equations are written in the following form with the assumption of linear elastic behavior of the solid skeleton:

$$\begin{bmatrix} \mathbf{M} & \mathbf{0} \\ \mathbf{G} & \mathbf{0} \end{bmatrix} \begin{bmatrix} \ddot{\bar{\mathbf{u}}} \\ \ddot{\bar{\mathbf{p}}} \end{bmatrix} + \begin{bmatrix} \mathbf{0} & \mathbf{0} \\ \mathbf{Q}^{\mathrm{T}} & \mathbf{S} \end{bmatrix} \begin{bmatrix} \dot{\bar{\mathbf{u}}} \\ \dot{\bar{\mathbf{p}}} \end{bmatrix} + \begin{bmatrix} \mathbf{K} & -\mathbf{Q} \\ \mathbf{0} & \mathbf{H} \end{bmatrix} \begin{bmatrix} \bar{\mathbf{u}} \\ \bar{\mathbf{p}} \end{bmatrix} = \begin{bmatrix} \mathbf{f}^{\mathrm{t}} \\ \mathbf{f}^{\mathrm{q}} \end{bmatrix} \tag{2.11a}$$

For *drained behaviour*, the equation set can be written in the following form (by dropping the time derivatives)

$$\begin{bmatrix} \mathbf{K} & -\mathbf{Q} \\ \mathbf{0} & \mathbf{H} \end{bmatrix} \begin{bmatrix} \bar{\mathbf{u}} \\ \bar{\mathbf{p}} \end{bmatrix} = \begin{bmatrix} \mathbf{f}^{\mathrm{t}} \\ \mathbf{f}^{\mathrm{q}} \end{bmatrix} \tag{2.11b}$$

in which $\bar{\mathbf{p}}$ can be separately determined by solving the second equation.

For *undrained behaviour*, the second equation is integrated, the permeability (and compressibility) matrices are set to zero, i.e. $\mathbf{H} = \mathbf{0}$, $\mathbf{f}^{\mathrm{q}} = \mathbf{0}$ and (usually-because of undrained condition) $\mathbf{S} = \mathbf{0}$ resulting in a zero diagonal term in the jacobian matrix.

$$\begin{bmatrix} \mathbf{M} & \mathbf{0} \\ \mathbf{0} & \mathbf{0} \end{bmatrix} \begin{bmatrix} \ddot{\bar{\mathbf{u}}} \\ \mathbf{0} \end{bmatrix} + \begin{bmatrix} \mathbf{K} & -\mathbf{Q} \\ \mathbf{Q}^{\mathrm{T}} & \mathbf{0} \end{bmatrix} \begin{bmatrix} \bar{\mathbf{u}} \\ \bar{\mathbf{p}} \end{bmatrix} = \begin{bmatrix} \mathbf{f}^{\mathrm{t}} \\ \mathbf{0} \end{bmatrix} \tag{2.12a}$$

In the steady state case, the matrix results in absence of the fluid compressiblity in

$$\begin{bmatrix} \mathbf{K} & -\mathbf{Q} \\ \mathbf{Q}^{\mathrm{T}} & \mathbf{0} \end{bmatrix} \begin{bmatrix} \bar{\mathbf{u}} \\ \bar{\mathbf{p}} \end{bmatrix} = \begin{bmatrix} \mathbf{f}^{\mathrm{t}} \\ \mathbf{0} \end{bmatrix} \tag{2.12b}$$

which only has a unique solution when the number of $\bar{\mathbf{u}}$ variables in $\mathbf{N}^{\mathrm{u}}$ is greater as the number of $\bar{\mathbf{p}}$ variables in $\mathbf{N}^{\mathrm{p}}$. This is one of the requirements of the patch test of Zienkiewicz et al. [175, 182, 184, 185] and of the Babuska-Brezzi condition [6, 7, 31]. Time differentiation and successive integration is a possible way of introducing computationally non-linear behaviour, this is the reason why K_{T} appears in equation (2.9). However, care must be exercised in the choice of the initial conditons because the set of possible solution trajectories is modified through time differentiation. The integration in time will be dealt in section 2.2.3, but the next section considers the choice of possible element types.

2.2.2 Choice of Elements

Isoparametric elements [184] are used in the FEM program Swandyne [177], where the coordinates within an element are interpolated using the same shape functions as for the variables. In equation (2.5) different shape functions ($\mathbf{u} = \mathbf{N}^{\mathrm{u}}\bar{\mathbf{u}}$, $\mathbf{p} = \mathbf{N}^{\mathrm{p}}\bar{\mathbf{p}}$) have been used for representing fluid pressure and displacements. The order of the shape function for fluid pressure is one order lower than the order of the shape function for the displacement, when the undrained limit state is approached. If the undrained limit state is never approached, the choice of elements is wide. However, due to the presence of first order spatial derivatives in the differential operators, it is necessary to use C_0 continous shape functions [184]. Most of the element types available in SWANDYNE fulfill the convergence criteria for the undrained limit [174], only bi-linear u and p quadrilateral does not fulfill it, but they are still usefull, when the permeability is sufficiently large [186]. The 2D elements used in Swandyne are presented in figure 2.1

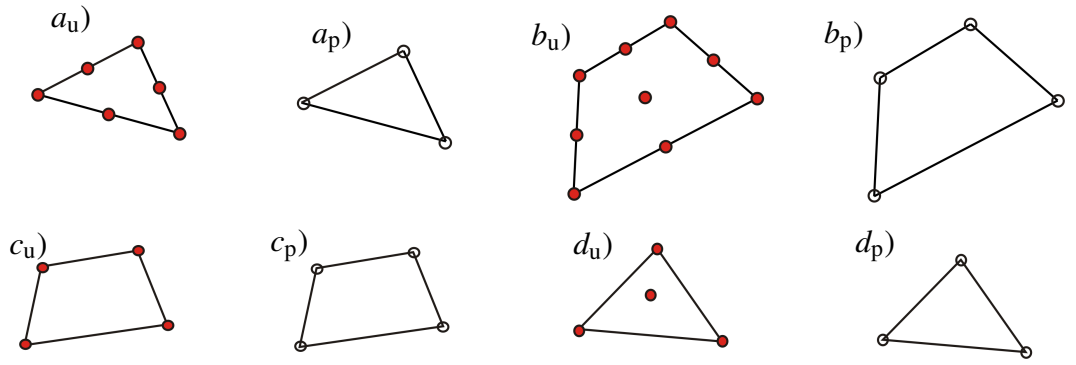

Figure 2.1: Elements for poroelastic analysis in SWANDYNE, displacement (u) and pressure (p) formulation. (a_u) quadratic, (a_p) linear, (b_u) biquadratic, (b_p) bilinear, (c_u) linear, (c_p) linear, (d_u) linear (with cubic bubble), (d_p) bilinear

2.2.3 Discretization in time/Integration in time

To complete the numerical solution procedure, it is necessary to integrate the ordinary differential equation (2.9), (2.11a) in time. Two similar, but distinct methods of time discretisation evolved separately. The first is known as the SSpj-Single Step pth order scheme for jth order differential equation $(p > j)$. This was developed by Zienkiewicz *et al.* [192, 191]. The SSpj scheme is used in SWANDYNE-I. Here, in SWANDYNE-II, an extension of the original Newmark method [114] the Generalized Newmark method (GNpj) proposed by Katona and Zienkiewicz [92] was used. For the GNpj method initial conditions $\bar{\mathbf{u}}_\mathbf{n}$, $\dot{\bar{\mathbf{u}}}_\mathbf{n}$ and $\dot{\bar{\mathbf{p}}}_\mathbf{n}$ are required at time step t_n where $\ddot{\bar{\mathbf{u}}}_{\mathbf{n+1}}$ and $\dot{\bar{\mathbf{p}}}_{\mathbf{n+1}}$ remain as unknowns. The equation set (2.9, 2.11a) can now be rewritten in the following form

$$\mathbf{P}(\bar{\mathbf{u}}_{\mathbf{n+1}}) = \int_\Omega \mathbf{B}^{\mathrm{T}} \boldsymbol{\sigma}^{\mathrm{s}}_{\mathbf{n+1}} \,\mathrm{d}\Omega = \int_\Omega \mathbf{B}^{\mathrm{T}}_{n+1} \Delta\boldsymbol{\sigma}^{\mathrm{s}}_{\mathbf{n}} \,\mathrm{d}\Omega + \mathbf{P}(\bar{\mathbf{u}}_\mathbf{n}) \tag{2.13}$$

$$\mathbf{K}_{\mathrm{T}} = \frac{\partial \mathbf{P}(\bar{\mathbf{u}})}{\partial \bar{\mathbf{u}}} = \int_\Omega \mathbf{B}^{\mathrm{T}} \mathbf{D}_{\mathrm{T}} \mathbf{B} \,\mathrm{d}\Omega$$

and

$$\begin{bmatrix} \mathbf{M} & \mathbf{0} \\ \mathbf{0} & \mathbf{0} \end{bmatrix} \begin{bmatrix} \ddot{\bar{\mathbf{u}}}_{\mathbf{n+1}} \\ \ddot{\bar{\mathbf{p}}}_{\mathbf{n+1}} \end{bmatrix} + \begin{bmatrix} \mathbf{0} & \mathbf{0} \\ \mathbf{Q}^{\mathrm{T}} & \mathbf{S} \end{bmatrix} \begin{bmatrix} \dot{\bar{\mathbf{u}}}_{\mathbf{n+1}} \\ \dot{\bar{\mathbf{p}}}_{\mathbf{n+1}} \end{bmatrix} + \begin{bmatrix} \mathbf{K}_{\mathrm{T}} & -\mathbf{Q} \\ \mathbf{0} & \mathbf{H} \end{bmatrix} \begin{bmatrix} \bar{\mathbf{u}}_{\mathbf{n+1}} \\ \bar{\mathbf{p}}_{\mathbf{n+1}} \end{bmatrix} = \begin{bmatrix} \mathbf{f}^{\mathrm{t}}_{n+1} \\ \mathbf{f}^{\mathrm{q}}_{n+1} \end{bmatrix} \tag{2.14}$$

by discretization in time.

The Generalised Newmark method [92] can be considered as a generalization of Newmark's two parameter time integration scheme. There, Newmark's scheme is interpreted as a Taylor series expansion. Considering as starting equation a second-order (dynamic) equation of the type

$$\mathbf{M}\ddot{\mathbf{x}} + \mathbf{C}\dot{\mathbf{x}} + \mathbf{K}\mathbf{x} = \mathbf{f}, \tag{2.15}$$

the equation (2.15) is rewritten for two discrete times t_n, t_{n+1} as

$$\mathbf{M}\ddot{\mathbf{x}}_\mathbf{n} + \mathbf{C}\dot{\mathbf{x}}_\mathbf{n} + \mathbf{K}\mathbf{x}_\mathbf{n} = \mathbf{f}_\mathbf{n} \tag{2.16}$$

$$\mathbf{M}\ddot{\mathbf{x}}_{\mathbf{n+1}} + \mathbf{C}\dot{\mathbf{x}}_{\mathbf{n+1}} + \mathbf{K}\mathbf{x}_{\mathbf{n+1}} = \mathbf{f}_{\mathbf{n+1}} \tag{2.17}$$

The values x_n, $\dot{x}_n$ are know from the initial conditions, and with equation (2.16) the value of the acceleration $\ddot{x}_n$ can be found. If there are initial conditions, this solution for the value of the acceleration $\ddot{x}_n$ is necessary. In the following, the Generalized Newmark method is applied for the mixed formulation. In SWANDYNE, the displacement term is discretized using a second order algorithm GN22 because equation (2.15) is a second-order differential equation and therefore the minimum order of the scheme required is two.

(i)

$$\begin{aligned}
\mathbf{u}_{n+\Delta\ddot{\bar{u}}_n} &= \tilde{\mathbf{x}}_{\mathbf{n+1}} = \mathbf{x}_\mathbf{n} + \dot{\mathbf{x}}_\mathbf{n}\Delta t + \ddot{\mathbf{x}}_\mathbf{n}\frac{\Delta t^2}{2} \\
\dot{\mathbf{u}}_{n+\Delta\ddot{\bar{u}}_n} &= \dot{\tilde{\mathbf{x}}}_{\mathbf{n+1}} = \dot{\mathbf{x}}_\mathbf{n} + \ddot{\mathbf{x}}_\mathbf{n}\Delta t \\
\ddot{\mathbf{u}}_{n+\Delta\ddot{\bar{u}}_n} &= \ddot{\tilde{\mathbf{x}}}_{\mathbf{n+1}} = \ddot{\mathbf{x}}_\mathbf{n}
\end{aligned}$$

(ii)

$$\begin{aligned}
\Delta\ddot{\mathbf{u}}_\mathbf{n} = &\left(\mathbf{M} + \frac{\Delta t^2}{2}\beta_2\mathbf{K}_\mathrm{T}\right)^{-1}\left(\bar{\mathbf{F}}^\mathbf{t} - \mathbf{M}\ddot{\tilde{\mathbf{x}}}^\mathrm{u} + \mathbf{Q}\dot{\tilde{\mathbf{x}}}^\mathrm{p} - \mathbf{K}\tilde{\mathbf{x}}^\mathrm{u}\right) \\
&+ \left(-\Delta t\theta\mathbf{Q}\right)^{-1}\left(\bar{\mathbf{F}}^\mathbf{q} - \mathbf{Q}^\mathrm{T}\dot{\tilde{\mathbf{x}}}^\mathrm{u} - \mathbf{S}\ddot{\tilde{\mathbf{x}}}^\mathrm{p} - \mathbf{H}\dot{\tilde{\mathbf{x}}}^\mathrm{p}\right)
\end{aligned}$$

(iii)

$$\begin{aligned}
\mathbf{u}_{\mathbf{n+1}} = \mathbf{x}_{\mathbf{n+1}} &= \tilde{\mathbf{x}}_{\mathbf{n+1}} + \beta_2\Delta\ddot{\tilde{\mathbf{u}}}_\mathbf{n}\frac{\Delta t^2}{2} \\
\dot{\mathbf{u}}_{\mathbf{n+1}} = \dot{\mathbf{x}}_{\mathbf{n+1}} &= \dot{\tilde{\mathbf{x}}}_{\mathbf{n+1}} + \beta_1\Delta\ddot{\tilde{\mathbf{u}}}_\mathbf{n}\Delta t \\
\ddot{\mathbf{u}}_{\mathbf{n+1}} = \ddot{\mathbf{x}}_{\mathbf{n+1}} &= \ddot{\tilde{\mathbf{x}}}_{\mathbf{n+1}} + \Delta\ddot{\tilde{\mathbf{u}}}_\mathbf{n}
\end{aligned} \tag{2.18}$$

and for the pressure a first order discretization is used GN11

(i)

$$\begin{aligned}
\mathbf{p}_{n+\Delta\dot{\bar{p}}_n} &= \dot{\tilde{\mathbf{x}}}_{\mathbf{n+1}} = \dot{\mathbf{x}}_\mathbf{n} + \ddot{\mathbf{x}}_\mathbf{n}\Delta t \\
\dot{\mathbf{p}}_{n+\Delta\dot{\bar{p}}_n} &= \ddot{\tilde{\mathbf{x}}}_{\mathbf{n+1}} = \ddot{\mathbf{x}}_\mathbf{n}
\end{aligned}$$

(ii)

$$\begin{aligned}
\Delta\dot{\mathbf{p}}_\mathbf{n} = &\left(\Delta t\beta_1\mathbf{Q}^\mathrm{T}\right)^{-1}\left(\bar{\mathbf{F}}^\mathbf{t} - \mathbf{M}\ddot{\tilde{\mathbf{x}}}^\mathrm{u} + \mathbf{Q}\dot{\tilde{\mathbf{x}}}^\mathrm{p} - \mathbf{K}\tilde{\mathbf{x}}^\mathrm{u}\right) \\
&+ \left(\Theta\Delta t\mathbf{H} + \mathbf{S}\right)^{-1}\left(\bar{\mathbf{F}}^\mathbf{q} - \mathbf{Q}^\mathrm{T}\dot{\tilde{\mathbf{x}}}^\mathrm{u} - \mathbf{S}\ddot{\tilde{\mathbf{x}}}^\mathrm{p} - \mathbf{H}\dot{\tilde{\mathbf{x}}}^\mathrm{p}\right)
\end{aligned}$$

(iii)

$$\begin{aligned}\mathbf{p_{n+1}} &= \dot{\mathbf{x}}_{\mathbf{n+1}} = \dot{\tilde{\mathbf{x}}}_{\mathbf{n+1}} + \Delta\dot{\tilde{\mathbf{p}}}_{\mathbf{n}}\Theta\Delta t \\ \dot{\mathbf{p}}_{\mathbf{n+1}} &= \ddot{\mathbf{x}}_{\mathbf{n+1}} = \ddot{\tilde{\mathbf{x}}}_{\mathbf{n+1}} + \Delta\dot{\tilde{\mathbf{p}}}_{\mathbf{n}}\end{aligned} \tag{2.19}$$

The parameters β_1, β_2, Θ, may be chosen in the range from 0-1, but for unconditional stability of the recurrence scheme it is required [190, 34] to use

$$\beta_2 \geq \beta_1 \geq \frac{1}{2} \quad \text{and} \quad \Theta \geq \frac{1}{2}.$$

The optimal choice of these values is a matter of computational convenience; the discussion about these topic may be found in the literature. Insertion of the relation (2.18, 2.19) in equation (2.14) yields to a general nonlinear equation set in which only $\Delta\ddot{\tilde{\mathbf{u}}}_{\mathbf{n}}$ and $\Delta\dot{\tilde{\mathbf{p}}}_{\mathbf{n}}$ remain as unknowns. These equations can be rewritten as

$$\psi^{(1)}_{n+1} = \mathbf{M}_{(n+1)}\Delta\ddot{\tilde{\mathbf{u}}}_{\mathbf{n}} + \mathbf{P}\left(\bar{u}_{n+1}\right) - \mathbf{Q}_{n+1}\Theta\Delta t\Delta\dot{\tilde{\mathbf{p}}}_{\mathbf{n}} - F^{(1)}_{n+1} = \mathbf{0} \tag{2.20}$$

$$\psi^{(2)}_{n+1} = \mathbf{Q}^{\mathrm{T}}_{n+1}\beta_1\Delta t\Delta\ddot{\bar{u}}_n + \mathbf{H}_{n+1}\Theta\Delta t\Delta\dot{\tilde{\mathbf{p}}}_{\mathbf{n}} + \mathbf{S}_{n+1}\Delta\dot{\tilde{\mathbf{p}}}_{\mathbf{n}} - F^{(2)}_{n+1} = \mathbf{0} \tag{2.21}$$

where $F^{(1)}_{n+1}$ and $F^{(2)}_{n+1}$ can be evaluated explicitly from the information at time t_n, the internal force term $\mathbf{P}\left(\bar{\mathbf{u}}_{\mathbf{n+1}}\right)$ is defined in equation (2.13), and $\Delta\sigma^{\mathrm{s}}_n$ is evaluated by integrating the constitutive relationship $\delta\sigma^{\mathrm{s}} = \mathbf{D}_{\mathrm{T}}\left(\mathbf{B}\delta\bar{\mathbf{u}} - \delta\varepsilon^{\mathbf{0}}_{\ell}\right)$, whereas $\bar{\mathbf{u}}_{n+1}$ and $\bar{\mathbf{p}}_{n+1}$ at time step t_{n+1} are defined in equation (2.18, 2.19). The non-linear equation set (2.20, 2.21, 2.13) has to be solved by a convergent, iterative process, e.g., some kind of Newton Raphson procedure is used typically written as

$$\mathbf{J}\begin{Bmatrix}\Delta\ddot{\tilde{\mathbf{u}}}_{\mathbf{n}} \\ \Delta\dot{\tilde{\mathbf{p}}}_{\mathbf{n}}\end{Bmatrix}^{\ell+1} = -\begin{Bmatrix}\psi^{(1)}_{n+1} \\ \psi^{(2)}_{n+1}\end{Bmatrix}^{\ell} \tag{2.22}$$

where ℓ is the iteration number. The jacobian matrix can be written as

$$\begin{bmatrix}\frac{\partial\psi^{(1)}_{n+1}}{\partial\left(\Delta\ddot{\tilde{\mathbf{u}}}_{\mathbf{n}}\right)} & \frac{\partial\psi^{(1)}_{n+1}}{\partial\left(\Delta\dot{\tilde{\mathbf{p}}}_{\mathbf{n}}\right)} \\ \frac{\partial\psi^{(2)}_{n+1}}{\partial\left(\Delta\ddot{\tilde{\mathbf{u}}}_{\mathbf{n}}\right)} & \frac{\partial\psi^{(2)}_{n+1}}{\partial\left(\Delta\dot{\tilde{\mathbf{p}}}_{\mathbf{n}}\right)}\end{bmatrix} = \begin{bmatrix}\left(\mathbf{M}_{n+1} + \frac{\Delta t^2}{2}\beta_2\mathbf{K}_{\mathbf{T}\,n+1}\right) & \left(-\Delta t\theta\mathbf{Q}_{n+1}\right) \\ \left(\Delta t\beta_1\mathbf{Q}^{\mathrm{T}}{}_{n+1}\right) & \left(\Theta\Delta t\mathbf{H}_{n+1} + \mathbf{S}_{n+1}\right)\end{bmatrix} \tag{2.23}$$

and can be made symmetric by a simple scalar multiplication of the second row (providing K_{T} is itself symmetric) [186]. In the linear case, a single »iteration« solves the problem exactly.

3 BEM Formulation

In Finite Element formulations for poroelastic continua, a representation of Biot's theory using the unknowns solid displacement and pore pressure is preferred. Such a formulation is possible either for quasi-static problems or for dynamic problems if the inertia effects of the fluid are neglected. Contrary to theses formulations, a Boundary Element Method (BEM) for the general case of Biot's theory in time domain has been published. If the advantages of both methods are required, it is common practice to couple both methods. However, for such a coupled FE/BE procedure, a BEM for the simplified dynamic Biot theory as used in FEM must be developed. Therefore, here, the fundamental solutions as well as a BE time stepping procedure is presented for the simplified dynamic theory where the inertia effects of the fluid are neglected.

3.1 Fundamental Solutions

In this section, fundamental solutions for the simplified Biot's equations are derived. These solutions will be later used in a Convolution Quadrature based BE formulation. Therefore, it is sufficient and to the authors knowledge the only possible way to deduce the fundamental solutions in Laplace domain. To do so, first, the set of governing equations (1.10) is transformed to Laplace domain, denoted by $\mathscr{L}\{f(t)\} = \hat{f}(s)$ with the complex Laplace variable s. Further, vanishing initial conditions are assumed. This leads in operator notation to

$$\mathbf{B}\begin{bmatrix}\hat{u}_i^s\\ \hat{p}\end{bmatrix} = -\begin{bmatrix}\hat{F}_i\\ \hat{a}\end{bmatrix} \qquad \mathbf{B} = \begin{bmatrix}\left(G\nabla^2 - s^2\rho\right)\delta_{ij} + \left(K + \frac{1}{3}G\right)\partial_i\partial_j & -\alpha\partial_i\\ -s\left(\alpha - s\kappa\rho_f\right)\partial_i & \kappa\partial_{ii} - \dfrac{\phi^2 s}{R}\end{bmatrix} \tag{3.1}$$

with the not self-adjoint operator $\mathbf{B}$. Fundamental solutions for the above given systems of differential equations are known in closed form only in Fourier domain or Laplace domain. For Biot's theory in its complete form, fundamental solutions in Laplace domain are available [150]. Also, in time domain such solutions have been developed, however, not in closed form [35, 36]. As the simple poro formulation results from a simplification of Biot's theory, there is a hope to find fundamental solutions by introducing these simplifications in the known fundamental solutions of Biot's complete theory. Unfortunately, the mathematical operator in (3.1) is too different, so that new fundamental solutions have to be calculated. But, the operator type is still an elliptical operator so the same method as for Biot's theory to find the fundamental solutions, the method of Hörmander [86], can be used. Here, the procedure of deriving the fundamental solution is presented step by step.

In equation (3.1) the partial derivative $()_{,i}$ is denoted by ∂_i and $\nabla^2 = \partial_{ii}$ is the Laplacian operator. Note that all the operators in $\mathbf{B}$ in equation (3.1) are elliptic and not self-adjoint.

$$\mathbf{B}^* = \begin{bmatrix} A\delta_{ij} + B\partial_{ij} & E\partial_j \\ C\partial_i & D \end{bmatrix} \qquad \begin{aligned} A &= G\nabla^2 - s^2\rho \\ B &= K + \tfrac{1}{3}G \\ C &= \alpha \\ D &= \kappa\nabla^2 - \frac{\phi^2 s}{R} \\ E &= s(\alpha - s\kappa\rho_f) \ . \end{aligned} \tag{3.2}$$

A fundamental solution is mathematically spoken a solution of the equation

$$\mathbf{BG} + \mathbf{I}\delta(\mathbf{x}-\mathbf{y}) = \mathbf{0} \tag{3.3}$$

where the matrix of fundamental solutions is denoted by $\mathbf{G}$, the identity matrix by $\mathbf{I}$, and the Dirac distribution by $\delta(\mathbf{x}-\mathbf{y})$. Physically interpreted, the solution at point $\mathbf{x}$ due to a single force at point $\mathbf{y}$ is looked for.

The idea of the method of Hörmander [86] is to reduce the operator given in (3.1) to well known operators. An overview of this method is found in the original work by Hörmander [86] and more exemplary in [145] and [132]. Following this idea, the definition of the inverse matrix operator

$$\mathbf{B}^{-1} = \frac{\mathbf{B}^{\mathrm{co}}}{\det(\mathbf{B})} \tag{3.4}$$

with the matrix of cofactors $\mathbf{B}^{\mathrm{co}}$ is used. The ansatz

$$\mathbf{G} = \mathbf{B}^{\mathrm{co}}\varphi \tag{3.5}$$

for the matrix of fundamental solutions with an unknown scalar function φ inserted in the operator equation $\mathbf{BG} + \mathbf{I}\delta(\mathbf{x}-\mathbf{y}) = \mathbf{0}$ yields to a more convenient representation of equations (3.1)

$$\begin{aligned} \mathbf{B}\mathbf{B}^{\mathrm{co}}\varphi + \mathbf{I}\delta(\mathbf{x}-\mathbf{y}) = \det(\mathbf{B})\,\mathbf{I}\varphi + \mathbf{I}\delta(\mathbf{x}-\mathbf{y}) = \mathbf{0} \\ \rightsquigarrow \quad \det(\mathbf{B})\,\varphi + \delta(\mathbf{x}-\mathbf{y}) = 0 \ . \end{aligned} \tag{3.6}$$

With this reformulation, the search for a fundamental solution is reduced to solve the simpler scalar equation (3.6).

From the mathematical theory of Green's formula it is known that the fundamental solutions should satisfy the adjoint operator [159]. Opposite to elasticity, the governing operator in poroelasticity is not self-adjoint. Therefore, here the solution for the adjoint operator $\mathbf{B}^\star$ is required.

Following formula (3.6), first, the determinant of the operator $\mathbf{B}^\star$ is calculated. This yields to the results

$$\text{2-d:} \quad \det\mathbf{B}^\star = \kappa G\left(K + \frac{4}{3}G\right)\left(\nabla^2 - \lambda_3^2\right)\left(\nabla^2 - \lambda_1^2\right)\left(\nabla^2 - \lambda_2^2\right) \tag{3.7}$$

$$\text{3-d:} \quad \det\mathbf{B}^\star = \kappa G^2\left(K + \frac{4}{3}G\right)\left(\nabla^2 - \lambda_3^2\right)^2\left(\nabla^2 - \lambda_1^2\right)\left(\nabla^2 - \lambda_2^2\right) \tag{3.8}$$

with the roots $\lambda_i,\ i=1,2,3$

$$\begin{aligned}\lambda_{1,2}^2 =& \frac{1}{2}\left[\frac{\phi^2 s}{\kappa R}+\frac{\alpha s(\alpha - s\rho_f\kappa)}{\left(K+\frac{4}{3}G\right)\kappa}+\frac{s^2\rho}{K+\frac{4}{3}G}\right.\\ &\left.\pm\sqrt{\left(\frac{\phi^2 s}{\kappa R}+\frac{\alpha s(\alpha - s\rho_f\kappa)}{\left(K+\frac{4}{3}G\right)\kappa}+\frac{s^2\rho}{\left(K+\frac{4}{3}G\right)}\right)^2-4\frac{s^2\rho\phi^2 s}{R\left(K+\frac{4}{3}G\right)\kappa}}\right]\\ \lambda_3^2 =& \frac{\rho s^2}{G}\,.\end{aligned} \tag{3.9}$$

Expressing the determinant using this roots, the scalar equation corresponding to (3.9) is given by

$$\left(\nabla^2-\lambda_3^2\right)\left(\nabla^2-\lambda_1^2\right)\left(\nabla^2-\lambda_2^2\right)\psi+\delta(\mathbf{x}-\mathbf{y})=0 \tag{3.10}$$

using an appropriate abbreviation ψ for every operator, i.e.,

$$\begin{aligned}&\text{2-d:}\quad \psi = G\kappa\left(K+\frac{4}{3}G\right)\varphi\\ &\text{3-d:}\quad \psi = G^2\kappa\left(K+\frac{4}{3}G\right)\varphi\,.\end{aligned} \tag{3.11}$$

The solution of the modified higher order Helmholtz equation (3.10) is

$$\text{2-d:}\quad \psi=\frac{1}{2\pi}\left[\frac{K_0(\lambda_1 r)}{(\lambda_1^2-\lambda_2^2)(\lambda_1^2-\lambda_3^2)}+\frac{K_0(\lambda_2 r)}{(\lambda_2^2-\lambda_3^2)(\lambda_2^2-\lambda_1^2)}+\frac{K_0(\lambda_3 r)}{(\lambda_3^2-\lambda_1^2)(\lambda_3^2-\lambda_2^2)}\right] \tag{3.12}$$

$$\text{3-d:}\quad \psi=\frac{1}{4\pi r}\left[\frac{e^{-\lambda_1 r}}{\left(\lambda_1^2-\lambda_2^2\right)\left(\lambda_1^2-\lambda_3^2\right)}+\frac{e^{-\lambda_2 r}}{\left(\lambda_2^2-\lambda_1^2\right)\left(\lambda_2^2-\lambda_3^2\right)}+\frac{e^{-\lambda_3 r}}{\left(\lambda_3^2-\lambda_2^2\right)\left(\lambda_3^2-\lambda_1^2\right)}\right] \tag{3.13}$$

with the zero order modified Bessel function of second kind $K_0(z)$. Further, the distance between the two points $\mathbf{x}$ and $\mathbf{y}$ is denoted by $r=|\mathbf{x}-\mathbf{y}|$.

Having in mind that the Laplace transformation of the function describes a traveling wave front with constant speed c which is $e^{-rs/c}=\mathscr{L}\{H(t-r/c)\}$ (in 3-d), it is obvious that the above solution (3.13) represents three waves. However, as the roots λ_i are functions of s, here, the wave speeds are time dependent representing the attenuation in a poroelastic continuum. This is in accordance with the well known three wave types of a poroelastic continuum [20]. The roots λ_1,λ_2, and λ_3 correspond to the wave velocities of the slow and fast compressional wave and to the shear wave, respectively. Comparing the fundamental solutions of Biot's complete theory, the same solution is found but different λ_i are calculated. This is essentially the only but important difference. The same is true in 2-d where the damped wave fronts are represented in Laplace domain by the modified Bessel functions $K_0(z)$.

The next steps are to insert the solution ψ back in the definition $\mathbf{G}=\mathbf{B}^{\mathrm{co}}\varphi$ taking into account the proper relation (3.11) between φ and ψ. After calculating the respective matrix of cofactors

$\mathbf{B}^{\mathrm{co}}$, the fundamental solutions are found as

$$\mathbf{G} = \begin{bmatrix} \hat{U}_{ij}^{\mathrm{s}} & \hat{U}_{i}^{\mathrm{f}} \\ \hat{P}_{j}^{\mathrm{s}} & \hat{P}^{\mathrm{f}} \end{bmatrix} = \frac{1}{G\kappa\left(K+\frac{4}{3}G\right)} \begin{bmatrix} \left(F\nabla^2 + AD\right)\delta_{ij} - F\partial_{ij} & -A\alpha\partial_i \\ -AE\partial_i & A\left(B\nabla^2 + A\right) \end{bmatrix} \psi \tag{3.14}$$

with the abbreviations $A = G\nabla^2 - s^2\rho$, $B = \left(K+\frac{1}{3}G\right)$, $D = \kappa\nabla^2 - \phi^2 s/R$, $E = s\left(\alpha - \rho_{\mathrm{f}}\kappa\right)$, $F = BD - C^2 s$. The difference of the 2-d solution and the 3-d solution lies only in different functions ψ from (3.12) or (3.13), respectively. The explicit expressions for the fundamental solutions can be found in the appendix A.

To visualize the differences between the simple poro and Biot's complete theory, the fundamental solution U_{00}^{s} in 2-d and in 3-d is considered in figure 3.1 using the material data of a soil (see table 3.1). The results are plotted for $r = 1\,\mathrm{m}$. In figure 3.1, not the frequency dependent solution is plotted but the time response caused by a unit step loading $H(t)$. This result is obtained using the Convolution Quadrature Method (see, [105, 106, 145]) to solve the convolution integral between the time domain fundamental solution U_{00}^{s} and the load.

The first deviation from zero ($t \approx 0.0002\,\mathrm{s}$) represents the fast compressional wave and the larger effect ($t \approx 0.0012\,\mathrm{s}$) is caused by the shear wave. In both, 2-d and 3-d, no significant differences are visible except at the jump of the shear wave in which the arrival time is slightly later for the simple poro than for the complete theory. Also, the oscillations around this jump are more pronounced, however, this may be rather caused by the numerics than by the different theories.

3.2 Boundary Element Formulation

The boundary integral equation for dynamic poroelasticity in Laplace domain can be obtained using either the corresponding reciprocal work theorem [39] or the weighted residuals formulation [58]. Here, the approach with weighted residuals will be presented. After two partial integrations with respect to the spatial variable, the boundary integral equation is achieved. As this procedure is extensively described in [144, 145], here, only the differences are given.

The poroelastodynamic integral equation can be derived directly by equating the inner product of the fundamental solutions $\mathbf{G}$ (3.14) and the set of governing equations (1.11) to a null vector, i.e.,

$$\int_{\Omega} \mathbf{G}^{\mathrm{T}}\mathbf{B} \begin{bmatrix} \hat{u}_i^{\mathrm{s}} \\ \hat{p} \end{bmatrix} \mathrm{d}\,\Omega = \mathbf{0}\,, \tag{3.15}$$

where the integration is performed over a domain Ω with boundary Γ and vanishing body forces F_i and sources a are assumed. By this inner product, essentially, the error in satisfying the governing differential equations (1.11) is forced to be orthogonal to $\mathbf{G}$. According to the theory of Green's formula and using partial integration, the operator $\mathbf{B}$ is transformed from acting on the vector of unknowns $[\hat{u}_i^{\mathrm{s}}\ \hat{p}]^{\mathrm{T}}$ to the matrix of fundamental solutions $\mathbf{G}$.

These steps are easier understood looking at equation (3.15) written in index notation. This

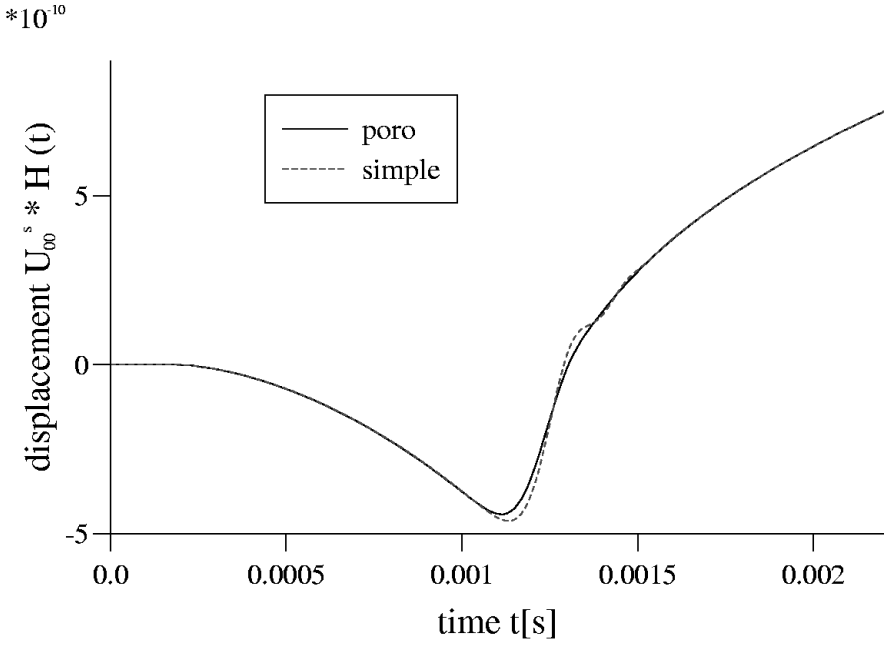

(a) 2-d

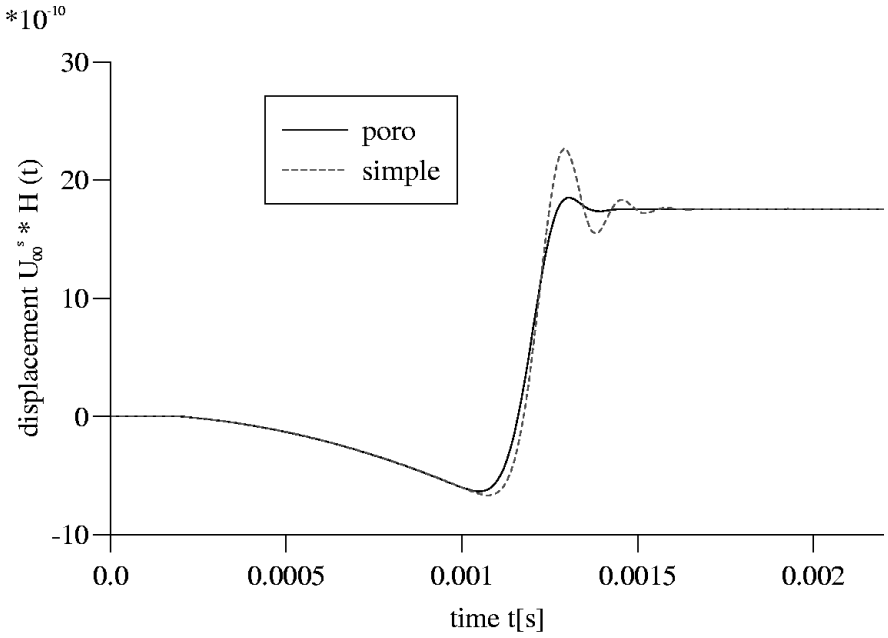

(b) 3-d

Figure 3.1: Fundamental solution U_{00}^{s} convoluted with $H(t)$ versus time

results in three (two) integral equations for the solid ($j = 1,2,3$ in 3-d and $j = 1,2$ in 2-d)

$$\int_\Omega \Bigg[G\hat{u}^{\mathrm{s}}_{i,kk}\hat{U}^{\mathrm{s}}_{ij} + \left(K + \frac{1}{3}G\right)\hat{u}^{\mathrm{s}}_{k,ik}\hat{U}^{\mathrm{s}}_{ij} - \alpha\hat{p}_{,i}\hat{U}^{\mathrm{s}}_{ij} - s^2\rho\hat{u}^{\mathrm{s}}_i\hat{U}^{\mathrm{s}}_{ij} + \kappa\hat{p}_{,kk}\hat{P}^{\mathrm{s}}_j - \frac{\phi^2 s}{R}\hat{p}\hat{P}^{\mathrm{s}}_j - s\left(\alpha - s\rho_{\mathrm{f}}\kappa\right)\hat{u}^{\mathrm{s}}_{k,k}\hat{P}^{\mathrm{s}}_j \Bigg] \mathrm{d}\Omega = 0 \tag{3.16}$$

and one integral equation for the fluid

$$\int_\Omega \Bigg[G\hat{u}^{\mathrm{s}}_{i,kk}\hat{U}^{\mathrm{f}}_i + \left(K + \frac{1}{3}G\right)\hat{u}^{\mathrm{s}}_{k,ik}\hat{U}^{\mathrm{f}}_i - \alpha\hat{p}_{,i}\hat{U}^{\mathrm{f}}_i - s^2\rho\hat{u}^{\mathrm{s}}_i\hat{U}^{\mathrm{f}}_i + \kappa\hat{p}_{,kk}\hat{P}^{\mathrm{f}} - \frac{\phi^2 s}{R}\hat{p}\hat{P}^{\mathrm{f}} - s\left(\alpha - s\rho_{\mathrm{f}}\kappa\right)\hat{u}^{\mathrm{s}}_{k,k}\hat{P}^{\mathrm{f}} \Bigg] \mathrm{d}\Omega = 0\,. \tag{3.17}$$

In the above integral equations, either one or two differentiations have to be transformed by either one or two partial integrations. Two exemplary parts of integral equations (3.16) and (3.17) for the compressible case are presented in detail to show the principal procedure. All other partial integrations for the other parts in integral equations (3.16) and (3.17) can be performed analogously.

First, an integral with one differentiation in the kernel leads to (n_k is the outward normal vector)

$$\int_\Omega s\left(\alpha - s\rho_{\mathrm{f}}\kappa\right)\hat{u}^{\mathrm{s}}_{k,k}\hat{P}^{\mathrm{f}}\,\mathrm{d}\Omega = \int_\Gamma s\left(\alpha - s\rho_{\mathrm{f}}\kappa\right)\hat{u}^{\mathrm{s}}_k n_k\hat{P}^{\mathrm{f}}\,\mathrm{d}\Gamma - \int_\Omega s\left(\alpha - s\rho_{\mathrm{f}}\kappa\right)\hat{u}^{\mathrm{s}}_k\hat{P}^{\mathrm{f}}_{,k}\,\mathrm{d}\Omega \tag{3.18}$$

while an integral with two differentiations is transformed to

$$\begin{aligned}\int_\Omega G\hat{u}^{\mathrm{s}}_{i,kk}\hat{U}^{\mathrm{s}}_{ij}\,\mathrm{d}\Omega &= \int_\Gamma G\hat{u}^{\mathrm{s}}_{i,k}n_k\hat{U}^{\mathrm{s}}_{ij}\,\mathrm{d}\Gamma - \int_\Omega G\hat{u}^{\mathrm{s}}_{i,k}\hat{U}^{\mathrm{s}}_{ij,k}\,\mathrm{d}\Omega \\ &= \int_\Gamma G\hat{u}^{\mathrm{s}}_{i,k}n_k\hat{U}^{\mathrm{s}}_{ij}\,\mathrm{d}\Gamma - \int_\Gamma G\hat{u}^{\mathrm{s}}_i\hat{U}^{\mathrm{s}}_{ij,k}n_k\,\mathrm{d}\Gamma + \int_\Omega G\hat{u}^{\mathrm{s}}_i\hat{U}^{\mathrm{s}}_{ij,kk}\,\mathrm{d}\Omega\,.\end{aligned} \tag{3.19}$$

In both integrations by parts, the divergence theorem is used. Obviously, one integration by parts changes the sign of the resulting domain integral while it remains unchanged in the case of two integrations by parts, i.e., the operator $\mathbf{B}$ is transformed into its adjoint operator $\mathbf{B}^*$.

These steps yields the following system of integral equations given in matrix notation as

$$\int_\Gamma \begin{bmatrix}\hat{U}^{\mathrm{s}}_{ij} & -\hat{P}^{\mathrm{s}}_j \\ \hat{U}^{\mathrm{f}}_i & -\hat{P}^{\mathrm{f}}\end{bmatrix}\begin{bmatrix}\hat{t}_i \\ \hat{q}\end{bmatrix}\mathrm{d}\Gamma - \int_\Gamma \begin{bmatrix}\hat{T}^{\mathrm{s}}_{ij} & \hat{Q}^{\mathrm{s}}_j \\ \hat{T}^{\mathrm{f}}_i & \hat{Q}^{\mathrm{f}}\end{bmatrix}\begin{bmatrix}\hat{u}^{\mathrm{s}}_i \\ \hat{p}\end{bmatrix}\mathrm{d}\Gamma = \begin{bmatrix}\hat{u}^{\mathrm{s}}_j \\ \hat{p}\end{bmatrix}\,. \tag{3.20}$$

To solve the domain integral in equation (3.20) for $\mathbf{y} \in \Omega$,, the definition of fundamental solutions (3.3) and the filter property of the Dirac distribution (B.9) is used. Additionally, the traction vector $\hat{t}_i = \hat{\sigma}_{ij}n_j$ and the normal flux $\hat{q} = -\kappa\left(\hat{p}_{,i} + \rho_{\mathrm{f}}s^2\hat{u}^{\mathrm{s}}_i\right)n_i$ is introduced, and the

abbreviations

$$\hat{T}^{\mathrm{s}}_{ij} = \left[\left(\left(K - \frac{2}{3} G \right) \hat{U}^{\mathrm{s}}_{kj,k} + \alpha s \hat{P}^{\mathrm{s}}_{j} \right) n_i + G \left(\hat{U}^{\mathrm{s}}_{ij,\ell} + \hat{U}^{\mathrm{s}}_{\ell j,i} \right) \right] n_\ell \tag{3.21a}$$

$$\hat{Q}^{\mathrm{s}}_{j} = \kappa \hat{P}^{\mathrm{s}}_{j,i} n_i \tag{3.21b}$$

$$\hat{T}^{\mathrm{f}}_{i} = \left[\left(\left(K - \frac{2}{3} G \right) \hat{U}^{\mathrm{f}}_{k,k} + \alpha s \hat{P}^{\mathrm{f}} \right) n_i + G \left(\hat{U}^{\mathrm{f}}_{i,\ell} + \hat{U}^{\mathrm{f}}_{\ell,i} \right) \right] n_\ell \tag{3.21c}$$

$$\hat{Q}^{\mathrm{f}} = \kappa \hat{P}^{\mathrm{f}}_{,i} n_i \tag{3.21d}$$

are used, where (3.21a) and (3.21b) can be interpreted as being the adjoint term to the traction vector $\hat{t}_i$ and the flux $\hat{q}$, respectively. In the definition of the flux $\hat{q}$, the simplified version of Darcy's law (1.9) is used. However, in its corresponding fundamental solution $\hat{Q}^{\mathrm{f}}$ and in the adjoint term $\hat{Q}^{\mathrm{s}}_{j}$ only a quasi-static version of Darcy's law is found. This is due to the neglect of the inertia effects in the fluid.

When moving $\mathbf{y}$ to the boundary Γ to determine the unknown boundary data, it is necessary to know the behavior of the fundamental solutions when $r = |\mathbf{y} - \mathbf{x}|$ tends to zero, i.e., when an integration point $\mathbf{x}$ approaches a collocation point $\mathbf{y}$. Six of the eight fundamental solutions, four in $\mathbf{G}$ and four calculated by equations (3.21), are singular. The order of their singularity can be determined by series representations with respect to the variable r. This variable is found in these solutions either in the exponential function in the 3-d solutions or in the Bessel functions in case of 2-d. Otherwise, only powers of r appear. So, it is sufficient to insert in the fundamental solutions (A.1a, A.3a) - (A.1d, A.3d) and (A.2a, A.4a) - (A.2d, A.4d) the following series expansions

$$e^{-\lambda_k s r} = \sum_{\ell=0}^{\infty} \frac{\left(-\lambda_k s r\right)^{\ell}}{\ell!} = 1 - \lambda_k s r + \lambda_k^2 s^2 r^2 + \mathscr{O}\left(r^3\right) \tag{3.22}$$

for the exponential function, and for the Bessel functions:

$$K_0\left(\lambda_k s r\right) = -\left(\ln\left(\lambda_k s r\right) - \ln 2 + \gamma\right) + \mathscr{O}\left(r^2\right) \tag{3.23a}$$

$$K_1\left(\lambda_k s r\right) = \frac{1}{\lambda_k s r} + \frac{\lambda_k s r}{2}\left(\ln\left(\lambda_k s r\right) - \ln 2 + \gamma - \frac{1}{2}\right) + \mathscr{O}\left(r^3\right) \tag{3.23b}$$

$$\gamma = \lim_{n\to\infty}\left(\sum_{\nu=1}^{n} \frac{1}{\nu} - \ln n\right) = 0.577216 \text{ (Euler-constant)}$$

Inserting these series in the fundamental solutions and a subsequent ordering with respect to the

power of r yields to the singular behavior. This leads for 3-d to

$$\hat{P}_i^{\mathrm{s}},\ \hat{U}_i^{\mathrm{f}} = \mathscr{O}\left(r^0\right) \tag{3.24a}$$

$$\hat{U}_{ij}^{\mathrm{s}} = \underbrace{\frac{1+\nu}{8\pi E\left(1-\nu\right)}\left\{r_{,i}r_{,j}+\delta_{ij}\left(3-4\nu\right)\right\}\frac{1}{r}}_{\text{elastostatic fundamental solution}} + \mathscr{O}\left(r^0\right) \tag{3.24b}$$

$$\hat{P}^{\mathrm{f}} = \frac{1}{4\pi\kappa}\frac{1}{r} + \mathscr{O}\left(r^0\right) \tag{3.24c}$$

$$\hat{Q}_j^{\mathrm{s}} = \frac{1+\nu}{8\pi E\left(1-\nu\right)}\alpha\left(1-2\nu\right)\left(r_{,n}r_{,j}-n_j\right)\frac{1}{r} + \mathscr{O}\left(r^0\right) \tag{3.24d}$$

$$\hat{T}_i^{\mathrm{f}} = \frac{1}{8\pi\kappa}\left\{s\left(\alpha-s\rho_{\mathrm{f}}\kappa\right)\frac{1-2\nu}{1-\nu}r_{,i}r_{,n}+n_i s\frac{\alpha+s\rho_{\mathrm{f}}\kappa\left(1-2\nu\right)}{1-\nu}\right\}\frac{1}{r} + \mathscr{O}\left(r^0\right) \tag{3.24e}$$

$$\hat{T}_{ij}^{\mathrm{s}} = \underbrace{\frac{-1}{8\pi\left(1-\nu\right)}\left\{\left[\left(1-2\nu\right)\delta_{ij}+3r_{,i}r_{,j}\right]r_{,n}-\left(1-2\nu\right)\left(r_{,j}n_i-r_{,i}n_j\right)\right\}\frac{1}{r^2}}_{\text{elastostatic fundamental solution}} + \mathscr{O}\left(r^0\right) \tag{3.24f}$$

$$\hat{Q}^{\mathrm{f}} = \underbrace{-\frac{r_{,n}}{4\pi r^2}}_{\text{acoustic fundamental solution}} + \mathscr{O}\left(r^0\right)\ . \tag{3.24g}$$

and for 2-d to

$$\hat{P}_i^{\mathrm{s}},\ \hat{U}_i^{\mathrm{f}} = \mathscr{O}\left(r^0\right) \tag{3.25a}$$

$$\hat{U}_{ij}^{\mathrm{s}} = \underbrace{-\frac{1+\nu}{4\pi E\left(1-\nu\right)}\left\{\left(3-4\nu\right)ln\left(r\right)\delta_{ij}-r_{,i}r_{,j}\right\}}_{\text{elastostatic fundamental solution}} + \mathscr{O}\left(r^0\right) \tag{3.25b}$$

$$\hat{P}^{\mathrm{f}} = -\frac{1}{2\pi\kappa}\ln\left(r\right) + \mathscr{O}\left(r^0\right) \tag{3.25c}$$

$$\hat{Q}_j^{\mathrm{s}} = \frac{n_j\left(1+\nu\right)}{4\pi}\frac{\alpha\left(1-2\nu\right)}{E\left(1-\nu\right)}ln\left(r\right) + \mathscr{O}\left(r^0\right) \tag{3.25d}$$

$$\hat{T}_i^{\mathrm{f}} = -\frac{n_i s}{4\pi\kappa\left(1-\nu\right)}\left\{s\rho_{\mathrm{f}}\kappa+\alpha\left(1-2\nu\right)\right\}\ln\left(r\right) + \mathscr{O}\left(r^0\right) \tag{3.25e}$$

$$\hat{T}_{ij}^{\mathrm{s}} = \underbrace{\frac{-2r_{,n}r_{,i}r_{,j}+\left(1-2\nu\right)\left(r_{,n}\delta_{ij}+n_j r_{,i}-n_i r_{,j}\right)}{4\pi\left(1-\nu\right)r}}_{\text{elastostatic fundamental solution}} + \mathscr{O}\left(r^0\right) \tag{3.25f}$$

$$\hat{Q}^{\mathrm{f}} = \underbrace{-\frac{r_{,n}}{2\pi r}}_{\text{acoustic fundamental solution}} + \mathscr{O}\left(r^0\right)\ . \tag{3.25g}$$

In equations (3.24, 3.25), it is shown that the fundamental solutions (3.24a, 3.25a) are either regular, weakly singular (3.24b, 3.25b) – (3.24e, 3.25e) or strongly singular (3.24f, 3.25f) and (3.24g, 3.25g). The strongly singular parts in the kernel functions (3.24f, 3.25f) and (3.24g, 3.25g) are known from elastostatics and acoustics, respectively.

Therefore, shifting in (3.21) point $\mathbf{y}$ to the boundary Γ results in the boundary integral equation

$$\int_\Gamma \begin{bmatrix} \hat{U}_{ij}^{\mathrm{s}} & -\hat{P}_j^{\mathrm{s}} \\ \hat{U}_i^{\mathrm{f}} & -\hat{P}^{\mathrm{f}} \end{bmatrix} \begin{bmatrix} \hat{t}_i \\ \hat{q} \end{bmatrix} \mathrm{d}\Gamma = \cancel{\int}_\Gamma \begin{bmatrix} \hat{T}_{ij}^{\mathrm{s}} & \hat{Q}_j^{\mathrm{s}} \\ \hat{T}_i^{\mathrm{f}} & \hat{Q}^{\mathrm{f}} \end{bmatrix} \begin{bmatrix} \hat{u}_i^{\mathrm{s}} \\ \hat{p} \end{bmatrix} \mathrm{d}\Gamma + \begin{bmatrix} c_{ij} & 0 \\ 0 & c \end{bmatrix} \begin{bmatrix} \hat{u}_i^{\mathrm{s}} \\ \hat{p} \end{bmatrix} \tag{3.26}$$

with the integral free terms c_{ij} and c known from elastostatics and acoustics, respectively, and with the Cauchy principal value integral $\cancel{\int}$. A transformation to time domain gives, finally, the time dependent integral equation for simplified poroelasticity

$$\begin{aligned} &\int_0^t \int_\Gamma \begin{bmatrix} U_{ij}^{\mathrm{s}}(t-\tau,\mathbf{y},\mathbf{x}) & -P_j^{\mathrm{s}}(t-\tau,\mathbf{y},\mathbf{x}) \\ U_i^{\mathrm{f}}(t-\tau,\mathbf{y},\mathbf{x}) & -P^{\mathrm{f}}(t-\tau,\mathbf{y},\mathbf{x}) \end{bmatrix} \begin{bmatrix} t_i(\tau,\mathbf{x}) \\ q(\tau,\mathbf{x}) \end{bmatrix} \mathrm{d}\Gamma\,\mathrm{d}\tau = \\ &\qquad \int_0^t \cancel{\int}_\Gamma \begin{bmatrix} T_{ij}^{\mathrm{s}}(t-\tau,\mathbf{y},\mathbf{x}) & Q_j^{\mathrm{s}}(t-\tau,\mathbf{y},\mathbf{x}) \\ T_i^{\mathrm{f}}(t-\tau,\mathbf{y},\mathbf{x}) & Q^{\mathrm{f}}(t-\tau,\mathbf{y},\mathbf{x}) \end{bmatrix} \begin{bmatrix} u_i(\tau,\mathbf{x}) \\ p(\tau,\mathbf{x}) \end{bmatrix} \mathrm{d}\Gamma\,\mathrm{d}\tau + \begin{bmatrix} c_{ij}(\mathbf{y}) & 0 \\ 0 & c(\mathbf{y}) \end{bmatrix} \begin{bmatrix} u_i(t,\mathbf{y}) \\ p(t,\mathbf{y}) \end{bmatrix} . \end{aligned} \tag{3.27}$$

A boundary element formulation is achieved following the usual procedure. First, the boundary surface Γ is discretized by E iso-parametric elements Γ_e where F polynomial shape functions $N_e^f(\mathbf{x})$ are defined. Hence, the following ansatz functions are used with the time dependent nodal values $u_i^{ef}(t)$, $t_i^{ef}(t)$, $p^{ef}(t)$ and $q^{ef}(t)$

$$\begin{aligned} u_i(\mathbf{x},t) &= \sum_{e=1}^{E}\sum_{f=1}^{F} N_e^f(\mathbf{x})\, u_i^{ef}(t) \quad & t_i(\mathbf{x},t) &= \sum_{e=1}^{E}\sum_{f=1}^{F} N_e^f(\mathbf{x})\, t_i^{ef}(t) \\ p(\mathbf{x},t) &= \sum_{e=1}^{E}\sum_{f=1}^{F} N_e^f(\mathbf{x})\, p^{ef}(t) \quad & q(\mathbf{x},t) &= \sum_{e=1}^{E}\sum_{f=1}^{F} N_e^f(\mathbf{x})\, q^{ef}(t) \ . \end{aligned} \tag{3.28}$$

In equations (3.28), the shape functions of all four variables are denoted by the same function $N_e^f(\mathbf{x})$ indicating the same approximation level of all variables. This is not mandatory but usual (for mixed shape functions see [129]). Inserting these ansatz functions (3.28) in the time dependent integral equation (3.27) yields

$$\begin{aligned} &\begin{bmatrix} c_{ij}(\mathbf{y}) & 0 \\ 0 & c(\mathbf{y}) \end{bmatrix} \begin{bmatrix} u_i^{\mathrm{s}}(\mathbf{y},t) \\ p(\mathbf{y},t) \end{bmatrix} = \\ &\qquad \sum_{e=1}^{E}\sum_{f=1}^{F} \Bigg\{ \int_0^t \int_\Gamma \begin{bmatrix} U_{ij}^{\mathrm{s}}(t-\tau,\mathbf{y},\mathbf{x}) & -P_j^{\mathrm{s}}(t-\tau,\mathbf{y},\mathbf{x}) \\ U_i^{\mathrm{f}}(t-\tau,\mathbf{y},\mathbf{x}) & -P^{\mathrm{f}}(t-\tau,\mathbf{y},\mathbf{x}) \end{bmatrix} N_e^f(\mathbf{x}) \begin{bmatrix} t_i^{ef}(\tau) \\ q^{ef}(\tau) \end{bmatrix} \mathrm{d}\Gamma\,\mathrm{d}\tau \\ &\qquad - \int_0^t \cancel{\int}_\Gamma \begin{bmatrix} T_{ij}^{\mathrm{s}}(t-\tau,\mathbf{y},\mathbf{x}) & Q_j^{\mathrm{s}}(t-\tau,\mathbf{y},\mathbf{x}) \\ T_i^{\mathrm{f}}(t-\tau,\mathbf{y},\mathbf{x}) & Q^{\mathrm{f}}(t-\tau,\mathbf{y},\mathbf{x}) \end{bmatrix} N_e^f(\mathbf{x}) \begin{bmatrix} u_i^{ef}(\tau) \\ p^{ef}(\tau) \end{bmatrix} \mathrm{d}\Gamma\,\mathrm{d}\tau \Bigg\} . \end{aligned} \tag{3.29}$$

Next, a time discretization has to be introduced. Since no time dependent fundamental solutions are known, the 'Convolution Quadrature Method' developed by Lubich [105, 106] is an effective choice compared to inverting the Laplace domain fundamental solutions at every col-

location point in every time step using a series expansion [37, 145]. A brief explanation of the convolution quadrature method can be found in appendix B.3.

Hence, after dividing the time period t in N intervals of equal duration Δt, i.e., $t = N\Delta t$, the convolution integrals between the fundamental solutions and the nodal values are approximated by the convolution quadrature method, i.e., the quadrature formula

$$y(t) = \int_0^t f(t-\tau)\, g(\tau)\, \mathrm{d}\tau \quad \rightarrow \quad y(n\Delta t) = \sum_{k=0}^{n} \omega_{n-k}(\Delta t)\, g(k\Delta t), \tag{3.30}$$

is applied to the integral equation (3.29). The weights ω_{n-k} are determined by the Laplace transformed function $\hat{f}$ and a linear multistep method, $n = 0, 1, \ldots, N$. This results in the following boundary element time stepping formulation for $n = 0, 1, \ldots, N$

$$\begin{aligned}
&\begin{bmatrix} c_{ij}(\mathbf{y}) & 0 \\ 0 & c(\mathbf{y}) \end{bmatrix} \begin{bmatrix} u_i(\mathbf{y}, n\Delta t) \\ p(\mathbf{y}, n\Delta t) \end{bmatrix} = \\
&\qquad \sum_{e=1}^{E} \sum_{f=1}^{F} \sum_{k=0}^{n} \left\{ \begin{bmatrix} \omega_{n-k}^{ef}\left(\hat{U}_{ij}^{\mathrm{s}}, \mathbf{y}, \Delta t\right) & -\omega_{n-k}^{ef}\left(\hat{P}_{j}^{\mathrm{s}}, \mathbf{y}, \Delta t\right) \\ \omega_{n-k}^{ef}\left(\hat{U}_{i}^{\mathrm{f}}, \mathbf{y}, \Delta t\right) & -\omega_{n-k}^{ef}\left(\hat{P}^{\mathrm{f}}, \mathbf{y}, \Delta t\right) \end{bmatrix} \begin{bmatrix} t_i^{ef}(k\Delta t) \\ q^{ef}(k\Delta t) \end{bmatrix} \right. \\
&\qquad \left. - \begin{bmatrix} \omega_{n-k}^{ef}\left(\hat{T}_{ij}^{\mathrm{s}}, \mathbf{y}, \Delta t\right) & \omega_{n-k}^{ef}\left(\hat{Q}_{j}^{\mathrm{s}}, \mathbf{y}, \Delta t\right) \\ \omega_{n-k}^{ef}\left(\hat{T}_{i}^{\mathrm{f}}, \mathbf{y}, \Delta t\right) & \omega_{n-k}^{ef}\left(\hat{Q}^{\mathrm{f}}, \mathbf{y}, \Delta t\right) \end{bmatrix} \begin{bmatrix} u_i^{ef}(k\Delta t) \\ p^{ef}(k\Delta t) \end{bmatrix} \right\}
\end{aligned} \tag{3.31}$$

with the weights, e.g.,

$$\omega_{n-k}^{ef}\left(\hat{U}_{ij}^{\mathrm{s}}, \mathbf{y}, \Delta t\right) = \frac{\mathscr{R}^{-(n-k)}}{L} \sum_{\ell=0}^{L-1} \int_{\Gamma} \hat{U}_{ij}^{\mathrm{s}}\left(\frac{\gamma\left(e^{i\ell\frac{2\pi}{L}}\mathscr{R}\right)}{\Delta t}, \mathbf{y}, \mathbf{x}\right) N_e^f(\mathbf{x})\, \mathrm{d}\Gamma \; e^{-i(n-k)\ell\frac{2\pi}{L}}. \tag{3.32}$$

Note, the calculation of the integration weights is only based on the Laplace transformed fundamental solutions which are available. Therefore, with the time stepping procedure (3.31) a boundary element formulation for simplified poroelastodynamics is given without time dependent fundamental solutions.

To obtain a system of algebraic equations from equation (3.31), collocation is used at every node of the shape functions $N_e^f(\mathbf{x})$. According to $t - \tau = (n-k)\Delta t$, the integration weights ω_{n-k}^{ef} only depend on the difference $n-k$. This property is analogous to elastodynamic time domain BE formulations (see, e.g., [59]) and can be used to establish a recursion formula [144, 145] ($m = n-k$)

$$\omega_0(\mathbf{C})\, \mathbf{d}^n = \omega_0(\mathbf{D})\, \bar{\mathbf{d}}^n + \sum_{m=1}^{n} \left(\omega_m(\mathbf{U})\, \mathbf{t}^{n-m} - \omega_m(\mathbf{T})\, \mathbf{u}^{n-m}\right) \quad n = 1, 2, \ldots, N \tag{3.33}$$

with the time dependent integration weights ω_m containing the Laplace transformed fundamental solutions $\mathbf{U}$ and $\mathbf{T}$, respectively (see, equation (3.32)). Similarly, $\omega_0(\mathbf{C})$ and $\omega_0(\mathbf{D})$ are the corresponding integration weights of the first time step related to the unknown and known boundary data $\mathbf{d}^n$ and $\bar{\mathbf{d}}^n$, respectively, in time step n . Finally, a direct equation solver is applied.

3.3 Validation by Comparison to a 1-d Analytical Solution

In order to validate the proposed boundary element approach, two problems are investigated: first, the results achieved by the simplified BEM are compared to an analytical solution of a 1-d column, and, second, the simplified method is compared with Biot's complete theory at the example of a half space under a vertical load in 2-d and 3-d to study the effects of the simplification on wave propagation phenomenon. In the following tests, the used material data are those of a rock [39] (Berea sandstone) in case of the column and for the half space example those of a coarse water saturated soil [95]. The data for both materials are collected in table 3.1. In contrast to the constitutive equation (1.3) in table 3.1, the Young's modulus E and Poisson's

Table 3.1: Material data of Berea sandstone (rock) and water saturated soil

	$E\left[\frac{\mathrm{N}}{\mathrm{m}^2}\right]$	ν	$\rho\left[\frac{\mathrm{kg}}{\mathrm{m}^3}\right]$	$\rho_f\left[\frac{\mathrm{kg}}{\mathrm{m}^3}\right]$	ϕ	$R\left[\frac{\mathrm{N}}{\mathrm{m}^2}\right]$	α	$\kappa\left[\frac{\mathrm{m}^4}{\mathrm{Ns}}\right]$
rock	$1.44 \cdot 10^{10}$	0.0	2458	1000	0.19	$4.7 \cdot 10^{8}$	0.86	$1.9 \cdot 10^{-10}$
soil	$2.544 \cdot 10^{8}$	0.298	1884	1000	0.48	$1.2 \cdot 10^{9}$	0.98	$3.55 \cdot 10^{-9}$

ratio ν are used and not the shear modulus G and the compression modulus K because Poisson's ratio of Berea sandstone has been changed to $\nu = 0$ to represent better the 1-d behavior of the column in the following example.

3.3.1 Poroelastic Column

A one dimensional (1-d) column of length 3 m as sketched in figure 3.2 is considered. It is assumed that the side walls and the bottom are rigid, frictionless, and impermeable. Hence, the displacements normal to the surface are blocked and the column is otherwise free to slide only parallel to the wall. At the top, the total stress vector $t_y = -1\,\mathrm{N/m^2}\,H(t)$ and the pore pressure $p = 0\,\mathrm{N/m^2}$ is a given, i.e., a normal pressure force starts acting with $t > 0$ and the fluid particles are assumed to be on a free fluid surface. Due to these restrictions, the 3-d continuum is reduced to a 1-d column with the only degree of freedom in y direction. This makes it possible to deduce a semi-analytical solution for comparison with the proposed BE formulation. The derivation follows exactly the same procedure as the corresponding solution for Biot's complete theory [148]. Therefore, it is sketched only briefly.

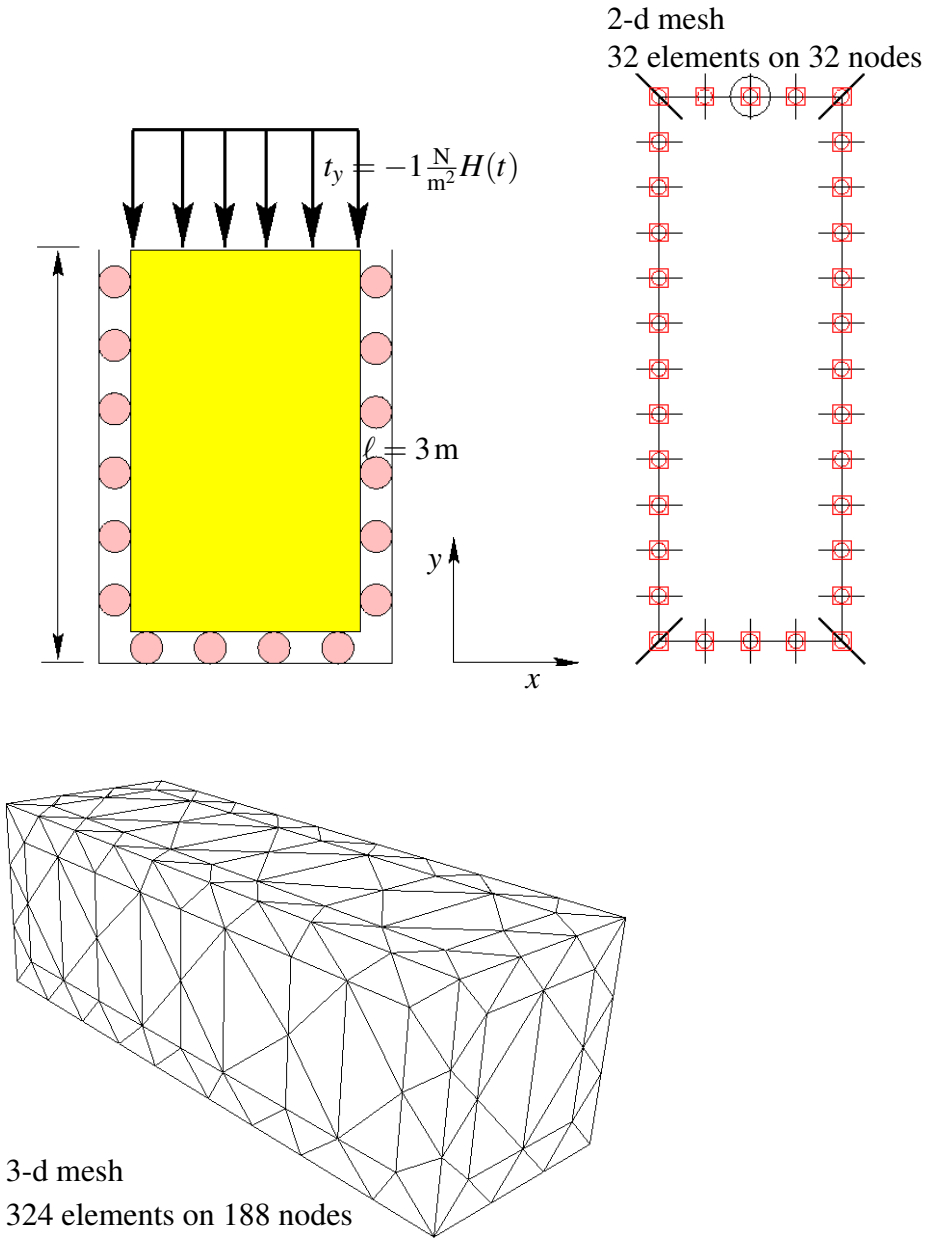

Figure 3.2: Geometry, boundary conditions, and discretizations of the column

Analytical solution For the above given problem, the governing set of differential equations (3.1) is reduced to two scalar coupled ordinary differential equations

$$E\hat{u}^{\mathrm{s}}_{y,yy} - \alpha\hat{p}_{,y} - s^2\rho\hat{u}^{\mathrm{s}}_{y} = 0 \tag{3.34}$$

$$\kappa\hat{p}_{,yy} - \frac{\phi^2 s}{R}\hat{p} - (\alpha - s\rho_{\mathrm{f}}\kappa)\, s\hat{u}^{\mathrm{s}}_{y,y} = 0\,, \tag{3.35}$$

with the modulus $E = K + 4/3G$ and vanishing body forces F_i and sources a. The boundary conditions in Laplace domain are

$$\hat{u}^{\mathrm{s}}_{y}(y=0) = 0, \quad \hat{q}_{y}(y=0) \;\; = 0, \quad \hat{\sigma}_{y}(y=\ell) = -1, \quad \hat{p}(y=\ell) \;\; = 0\,, \tag{3.36}$$

where an impulse function for the temporal behavior $f(t) = \delta(t)$ is assumed together with vanishing initial conditions. Due to the neglected body forces, this is a system of homogeneous ordinary differential equations with inhomogeneous boundary conditions. Such a system can be solved by the following exponential ansatz

$$\hat{u}^{\mathrm{s}}_{y}(y) = Ue^{\lambda s y} \qquad \hat{p}(y) = Pe^{\lambda s y}\,. \tag{3.37}$$

Inserting the ansatz functions (3.37) in equations (3.34) and (3.35) results in an Eigenvalue problem for λ

$$\begin{bmatrix} E\lambda^2 - \rho & -\alpha\dfrac{\lambda}{s} \\ -s(\alpha - s\rho_{\mathrm{f}}\kappa)\,\lambda & \lambda^2\kappa s - \dfrac{\phi^2}{R} \end{bmatrix} \begin{bmatrix} U \\ P \end{bmatrix} = \mathbf{0}\,, \tag{3.38}$$

with the characteristic equation

$$\underbrace{E\kappa s}_{A}\lambda^4 - \underbrace{\left(E\frac{\phi^2}{R} + \phi\kappa s + \alpha(\alpha - s\rho_{\mathrm{f}}\kappa)\right)}_{B}\lambda^2 + \underbrace{\frac{\phi^2\rho}{R}}_{C} \stackrel{!}{=} 0\,. \tag{3.39}$$

The characteristic equation (3.39) has the four complex roots

$$\lambda_1 = -\lambda_3 = \sqrt{\frac{B + \sqrt{B^2 - 4AC}}{2A}}, \quad \lambda_2 = -\lambda_4 = \sqrt{\frac{B - \sqrt{B^2 - 4AC}}{2A}}\,. \tag{3.40}$$

As in the derivation of the fundamental solutions in section 3.1, here lies the difference to Biot's complete theory. The roots in (3.39) are different to the complete case representing the different wave speeds.

These roots lead to the solution of the homogeneous problem

$$\hat{u}^{\mathrm{s}}_{y}(y) = \sum_{i=1}^{4} U_i e^{\lambda_i s y} \qquad \hat{p}(y) = \sum_{i=1}^{4} P_i e^{\lambda_i s y}\,. \tag{3.41}$$

The eight unknown constants U_i and P_i, $i = 1, \ldots, 4$, cannot be determined by the four boundary

conditions (3.36) alone. Also, none of the complex roots can be excluded due to physical reasons. But the Eigenvector of the system (3.38) gives the relation

$$P_i = \underbrace{\frac{E\lambda_i^2 - \rho}{\alpha\lambda_i}}_{d_i} \cdot sU_i \,. \tag{3.42}$$

Finally, when the solution (3.41) with the property (3.42) is inserted into the one-dimensional form of the constitutive equation (1.3)

$$\hat{\sigma}_y(s,y) = E\hat{u}^{\mathrm{s}}_{y,y} - \alpha\hat{p} = E\sum_{i=1}^{4}\lambda_i s U_i e^{\lambda_i s y} - \alpha\hat{p}(s,y) \tag{3.43}$$

and the one-dimensional form of Darcy's law (1.9)

$$\hat{q}_y(s,y) = -\kappa\left(\hat{p}_{,y} + s^2\rho_{\mathrm{f}}\hat{u}^{\mathrm{s}}_y\right) = -\frac{\kappa E s^2}{\alpha}\sum_{i=1}^{4}\lambda_i^2 U_i e^{\lambda_i s y} + \kappa s^2\left(\frac{\rho - \alpha\rho_{\mathrm{f}}}{\alpha}\right)\hat{u}^{\mathrm{s}}_y(s,y) \tag{3.44}$$

the remaining four constants U_i can be fit to the four boundary conditions. This leads to four equations with four unknowns. Also here, with the simplified Darcy's law (3.44), the difference to the complete solution is obvious.

Finally, the solutions for the displacement and the pore pressure are achieved by inserting these coefficients in the ansatz functions (3.41)

$$\hat{u}^{\mathrm{s}}_y = \frac{S_0}{E(d_1\lambda_2 - d_2\lambda_1)}\left[\frac{d_2\left(e^{-\lambda_1 s(\ell-y)} - e^{-\lambda_1 s(\ell+y)}\right)}{s\left(1+e^{-2\lambda_1 s\ell}\right)} - \frac{d_1\left(e^{-\lambda_2 s(\ell-y)} - e^{-\lambda_2 s(\ell+y)}\right)}{s\left(1+e^{-2\lambda_2 s\ell}\right)}\right] \tag{3.45}$$

$$\hat{p} = \frac{S_0 d_1 d_2}{E(d_1\lambda_2 - d_2\lambda_1)}\left[\frac{\left(e^{-\lambda_1 s(\ell-y)} + e^{-\lambda_1 s(\ell+y)}\right)}{1+e^{-2\lambda_1 s\ell}} - \frac{\left(e^{-\lambda_2 s(\ell-y)} + e^{-\lambda_2 s(\ell+y)}\right)}{1+e^{-2\lambda_2 s\ell}}\right] . \tag{3.46}$$

The corresponding stress and flux is calculated with the constitutive equation (3.43) and Darcy's law (3.44), respectively. The time dependent response has to be evaluated with the Convolution Quadrature Method, therefore, the solution is above called semi-analytical.

Comparison with the proposed BE formulation To validate the proposed BE formulation, the above given 1-d analytical solution is compared to a 2-d and a 3-d BE calculation. The used meshes are depicted in figure 3.2. In the following, the displacement solutions are given at the midpoint of the loaded surface, i.e., in 1-d it is $y = \ell = 3\,\mathrm{m}$, and the pressure solutions are given at the midpoint of the support, i.e., in 1-d at $y = 0\,\mathrm{m}$. The comparison is performed in the frequency domain as well as in time domain.

In figure 3.3, the absolute value of the displacement $|\hat{u}^{\mathrm{s}}_y(\omega, y = 3\,\mathrm{m})|$ at the top of the column is plotted versus frequency ω. The analytical results for Biot's theory are named 'poro 1-d' and they are compared to the simplified theory named 'simple 1-d', 'simple 2-d', and 'simple

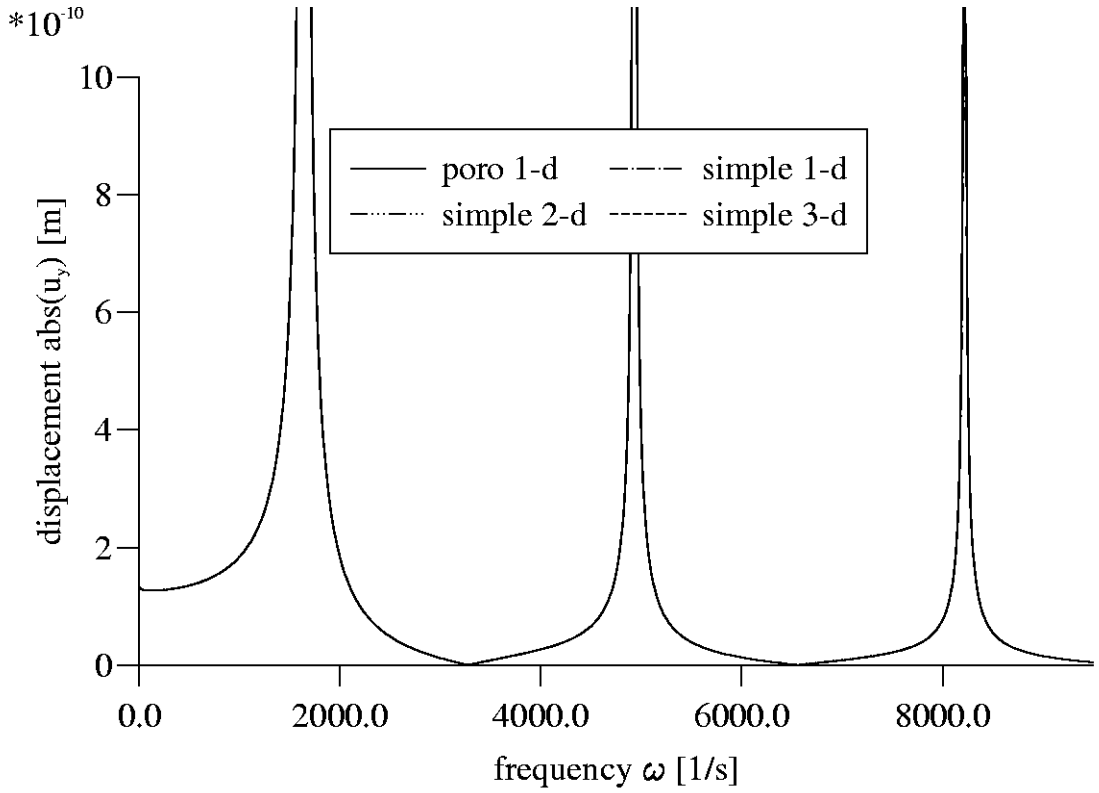

Figure 3.3: Displacement in y-direction at the top of the column versus frequency: Comparison of analytical results with 2-d and 3-d BEM

3-d' for analytical calculation and the 2-d and 3-d BEM results, respectively. The used material data are those of a rock (Berea sandstone, see table 3.1). In figure 3.3, clearly the first three resonance peaks are identified which don't differ for both theories. Further, the proposed BE formulation agrees very well with the analytical solution. Not shown are results of the BE formulation based on Biot's complete theory because they can not be distinguished from the simple poro formulation.

Next, the time dependent behavior is discussed. In figure 3.4, the time history of the displacement $u_y(t, y = 3\,\mathrm{m})$ at the top of the column caused by a step stress loading $t_y(t, y = l) = -1\frac{\mathrm{N}}{\mathrm{m}^2} H(t)$ is depicted. The used time step size is $\Delta t = 0.0001\,\mathrm{s}$. The same comparison as shown in frequency domain is performed. As expected from the frequency domain results, the solutions for Biot's complete theory and the simplified theory coincide perfectly. Also, the 2-d and 3-d BE solution agree very well with the 1-d solution. The minor differences can be minimized by adjusting the time step size closer to an optimal value. As known from the BE formulation for Biot's theory, there exists a lower critical time step size. However, because this lower limit is the same for both poroelastic theories it is not studied here. For the study on this critical time step size, the reader is referred to [145]. Additionally to the displacement results, the pore pressure solution is presented in figure 3.5. Also, in the pressure solution no significant differences between the two poroelastic models are visible. Further, the 2-d and 3-d BE solution approximate the semi-analytical result well where the overshooting at the jumps are caused obviously by the convolution quadrature. However, the non-smooth behavior of the

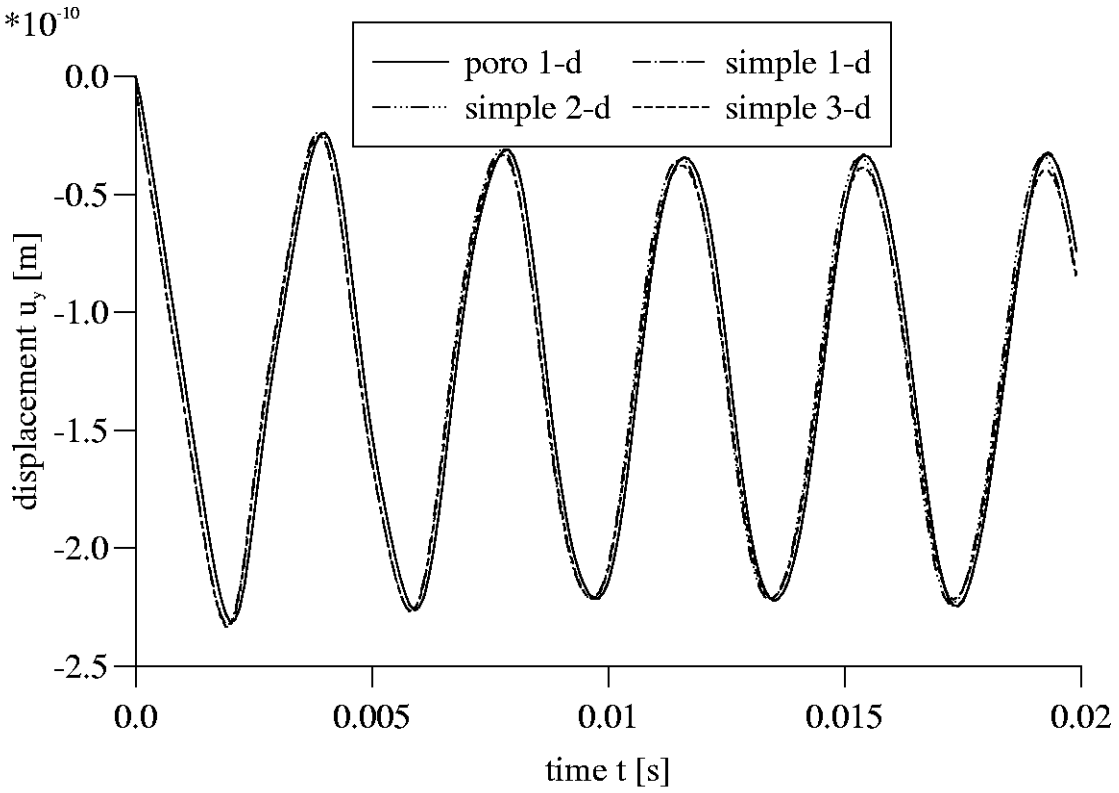

Figure 3.4: Displacement in y-direction at the top of the column versus time: Comparison of analytical results with 2-d and 3-d BEM

pressure is calculated well by the BEM where the 3-d formulation has more problems as the 2-d formulation. This is caused by the difficulties in representing the corner and edges singularities of the 3-d model which does not exist in the 1-d model. These problems are inherent in any BE formulation based on point collocation and conforming elements.

3.3.2 Wave propagation in a Poroelastic Half Space

To demonstrate that the results of the u-p formulation with neglect of the derivative of the seepage velocity are similar to the results of Biot's complete theory, the displacement response and the pore pressure distribution of a poroelastic half space in 2-d and 3-d are compared, respectively. The material data in both test examples are those of a soil (see table 3.1).

2-d model of a poroelastic half space

First, the half space is modeled in 2-d with a strip of 51 m length, where 51 linear elements are used (see figure 3.6). The simulated half-space is loaded by a vertical total stress vector $t_y = -1000\,\mathrm{N/m^2}\,(H(t) - H(\Delta t))$ on an intervall of 1 m and the remaining surface is traction free. The load simulates an impulse by keeping the load over one time step. The free surface is assumed to be permeable, i.e., the pore pressure is zero all over the surface.

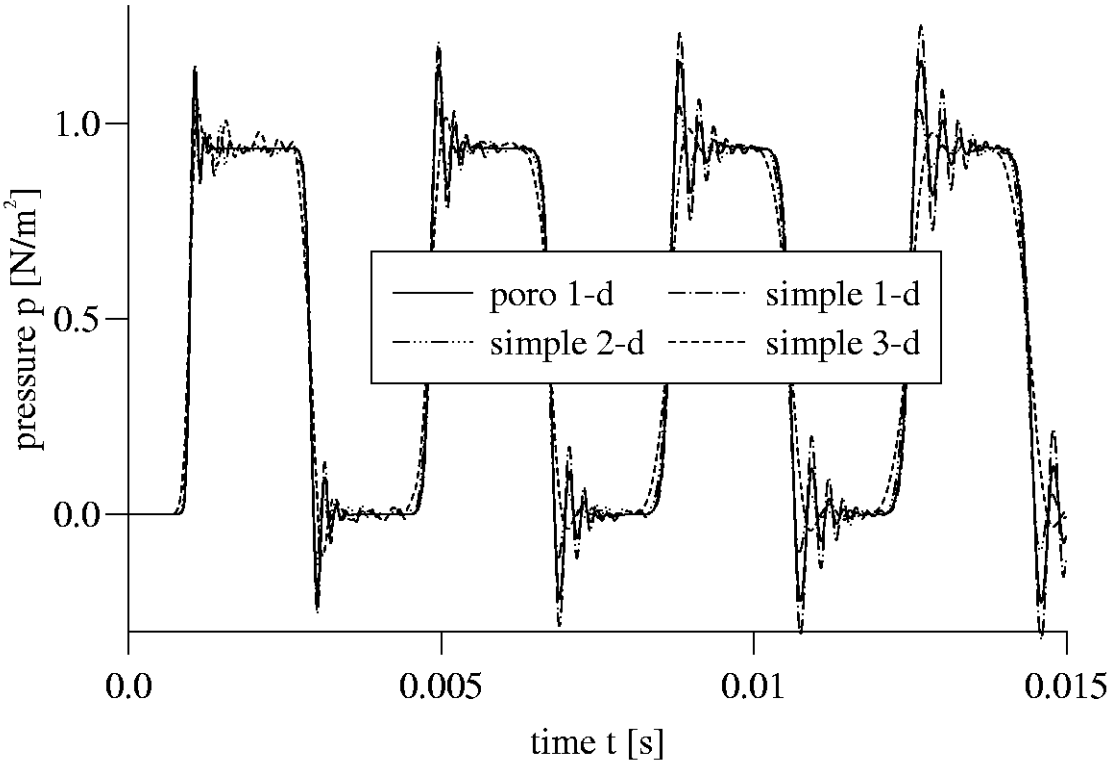

Figure 3.5: Pressure at the bottom of the column versus time: Comparison of analytical results with 2-d and 3-d BEM

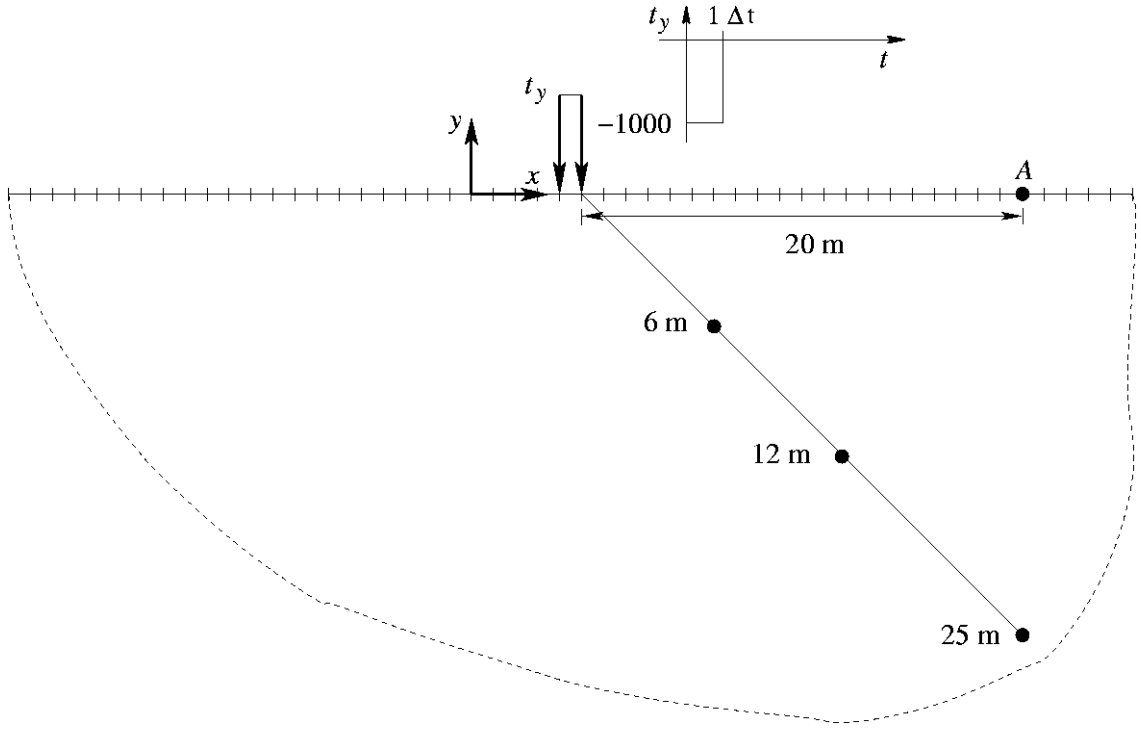

Figure 3.6: Poroelastic half space in 2-d: mesh and loading

First, the time history of the displacement at point A is presented. In figure 3.7, the calculated horizontal and vertical displacement at point A are plotted versus time for both formulations. As before, the u-p formulation with neglect of the derivative of the seepage velocity are denoted *simplified poro* and the original Biot u-p formulation is denoted *poro*. Clearly, the arrival of the fast compressional wave at $t \approx 0.01\,\mathrm{s}$ and of the Rayleigh wave at $t \approx 0.09\,\mathrm{s}$ can be observed. As expected, the slow compressional wave is not visible due to the dispersion effects and the shear wave is covered by the Rayleigh wave. In both coordinate directions no differences are visible between both formulations. The differences in the displacement amplitudes are approximately of the order $\mathscr{O}\left(10^{-3}\right)$. Additionally, the pore pressure distribution under the surface is observed by variation of the depth from -6 to $-20\,\mathrm{m}$. The various locations are depicted in figure 3.6. The time histories of the pore pressure are presented in figure 3.8 for both formulations. As before in the displacement results, no significant differences between the simplified formulation and Biot's equations are found. In all three depths the arrival of the fast compressional wave is observed as a more or less wide peak. After some oscillations of the numerical solution, the pore pressure decreases to zero as expected result for an impulse load.

3-d model of a poroelastic half space

For the 3-d model of the half space, a strip of $33\,\mathrm{m} \times 6\,\mathrm{m}$ has been discretized with 396 triangular linear elements on 238 nodes (see figure 3.9). Different to the 2-d simulation, the half space is loaded by a vertical total stress vector $t_z = -1000\,\mathrm{N/m^2}\,H(t)$ on an area of $1\,\mathrm{m}^2$ which is kept constant over the whole observation period. The remaining surface is traction free and assumed to be permeable, i.e., the pore pressure is zero all over the surface. In figure 3.10, the calculated horizontal and vertical displacement are plotted versus time at point A. Different to the 2-d example, in 3-d some differences between the simplified theory and Biot's theory are visible. However, these differences are very small and in the range which can also be affected by numerics, i.e., also a change in the time step size can result in differences of the same order. So, in principle it can be concluded that also in the 3-d calculation both formulations give the same result.

The pore pressure distribution in different depths comparable to the study in 2-d is presented in figure 3.11. There, the pore pressure is depicted versus time in a depth of $6\,\mathrm{m}, 12\,\mathrm{m}$, and $20\,\mathrm{m}$. Due to the larger distance from the excitation point the fast compressional wave needs different times to reach the chosen points. Also different to the 2-d calculation, the pore pressure does not vanish after the passage of the wave because the load is kept over the total observation period. Further, the pore pressure reduces with increasing depth as expected. Finally, this comparison shows that the simplified theory can be used for the chosen material, a soil and a rock, and the presented excitations. There is no significant difference to Biot's complete theory. This confirms the results presented in [187].

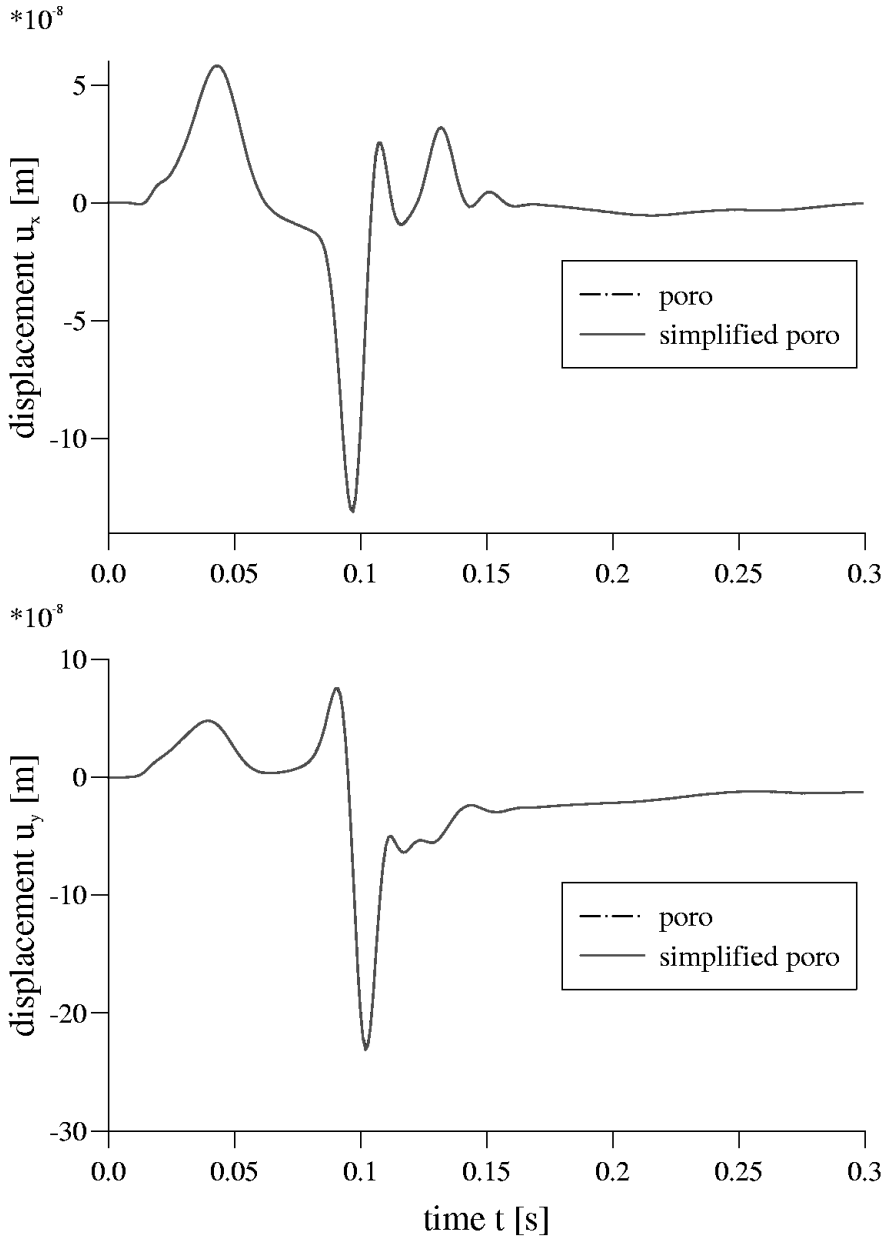

Figure 3.7: Horizontal and vertical displacement at point A i.e., **(a)** horizontal , **(b)** vertical

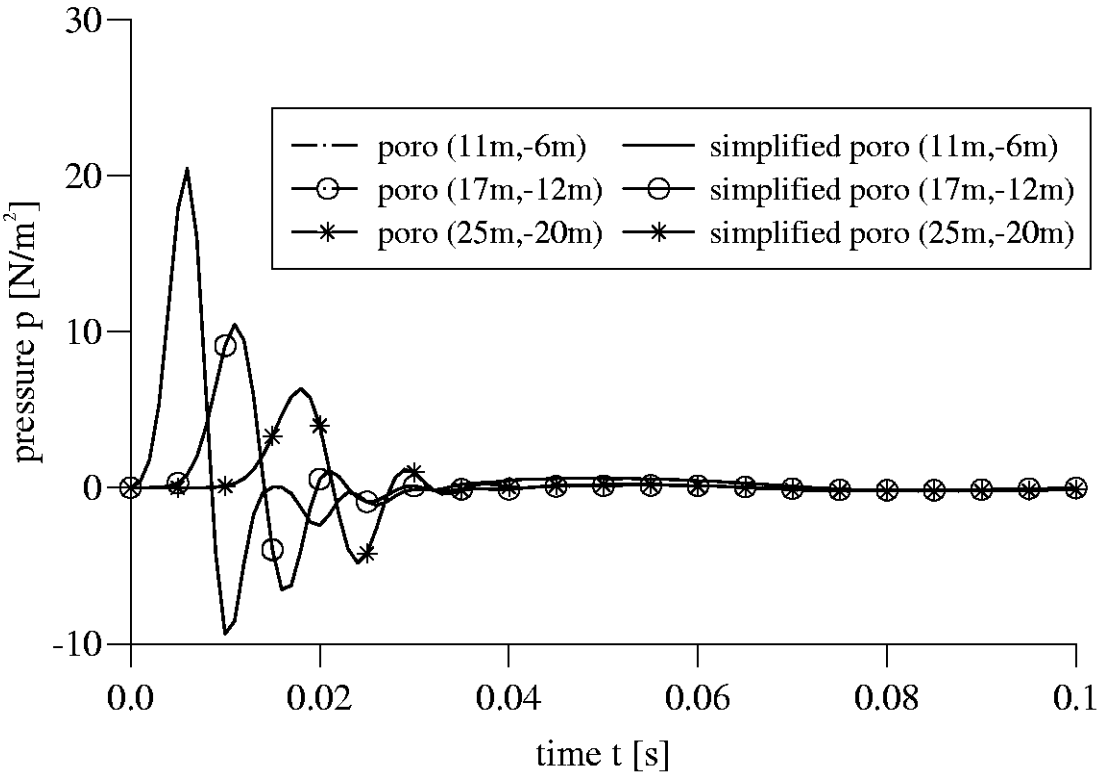

Figure 3.8: Pore pressure distribution below the surface at different points

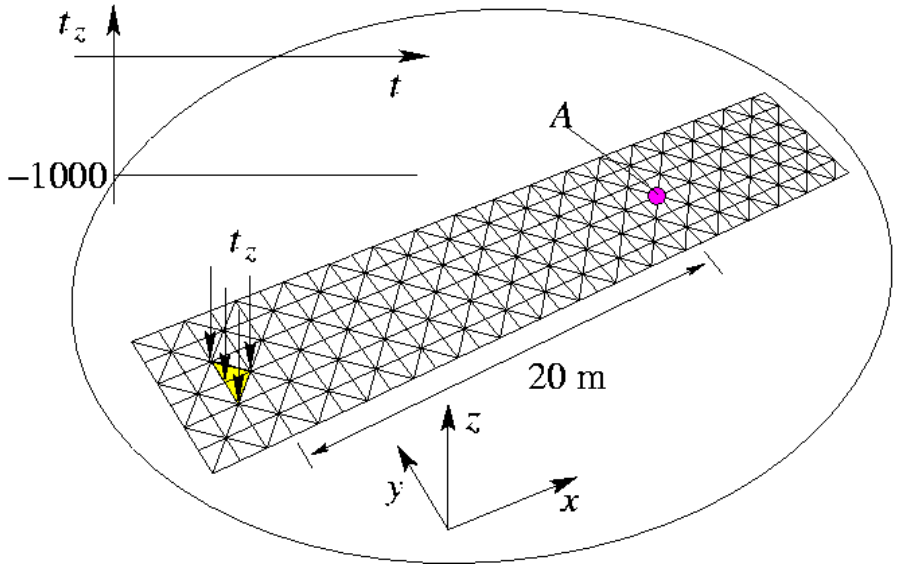

Figure 3.9: Poroelastic half space in 3-d: mesh and loading

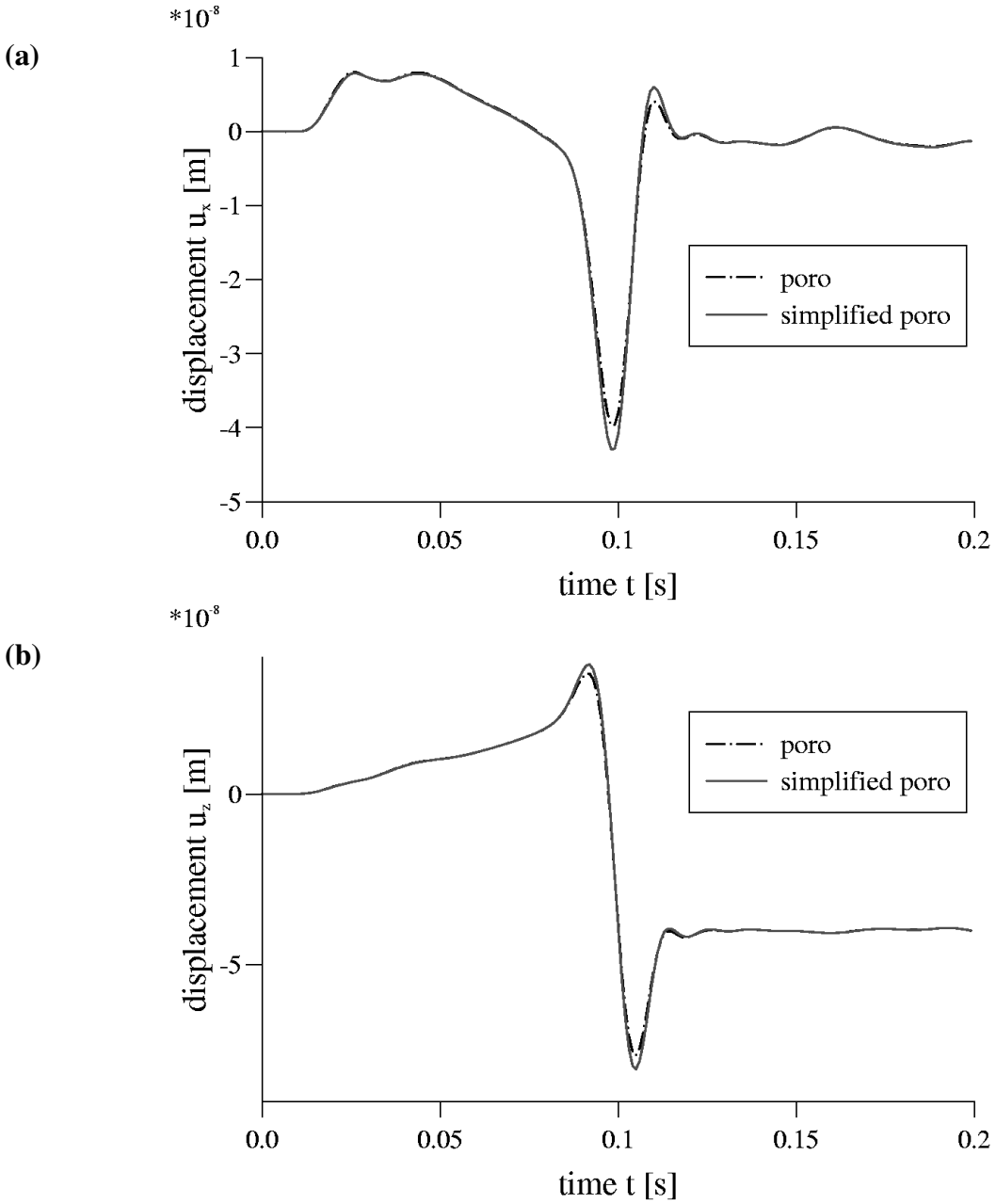

Figure 3.10: Horizontal and vertical displacement at point A i.e., **(a)** horizontal , **(b)** vertical

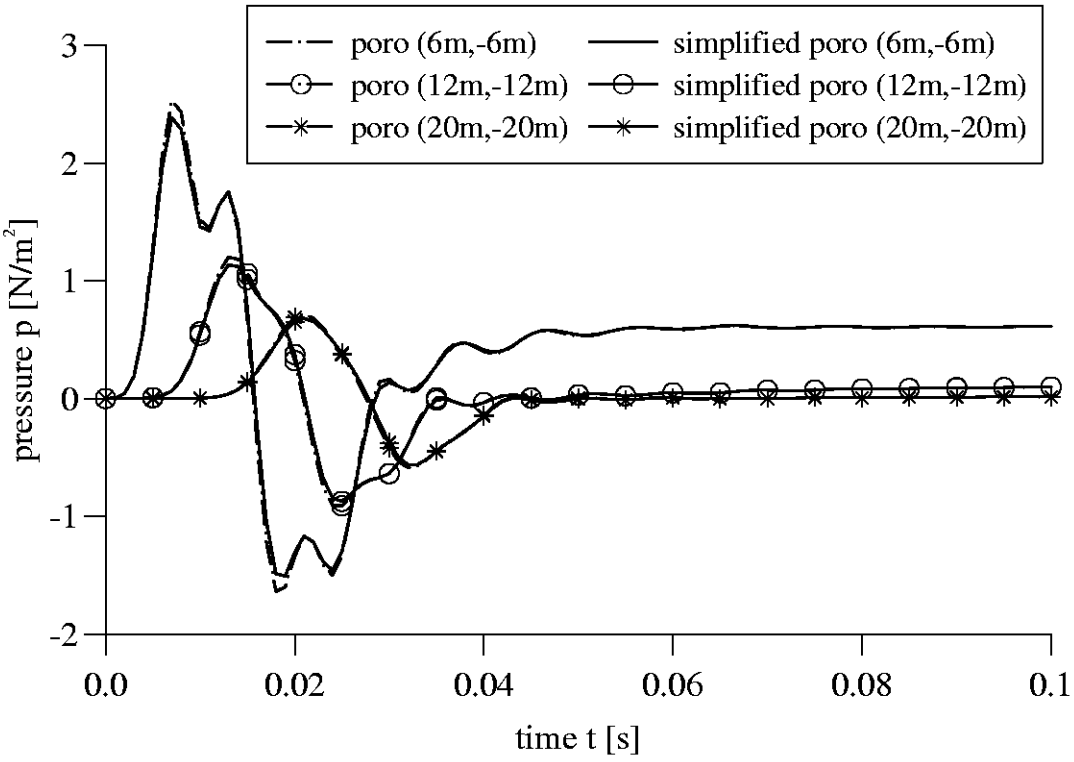

Figure 3.11: Pore pressure distribution below point A

4 Constitutive Relations in Soil Mechanics

The behavior of geotechnical materials may be represented by constitutive models which capture the main features of the mechanical behavior of solids under given conditions of temperature, velocity of load application, level of strain, nature of stress conditions, etc. One factor for the selection of a particular constitutive model is the response of the material depending on time. However, most of the geomaterials under normal engineering conditions present a mechanical behavior which depends on the level of stress, effective stress, pore pressure, past history, direction of load increment, and material structure than on time. To capture these main features, the theory of classical plasticity provide a consistent framework. In fact, the major part of the time dependent behavior observed is generally connected with the pore water flow (see, chapter 1). Biot introduced the concept of effective stresses where the relation between effective stress, total stress, and pore pressure is given by $\sigma'_{ij} = \sigma^{s}_{ij} = \sigma_{ij} + \alpha\delta_{ij}p$. Plasticity-based constitutive models for soils are based upon the effective stresses in the solid skeleton which are denoted by a dash.

First, elastoplastic constitutive soil models based on the theory of classical plasticity were developed by Drucker and Prager. Drucker and Prager proposed in 1952 an elastic perfectly plastic constitutive model with an associated flow rule. However, this model is not able to describe plastic deformations which are found inside the classical yield surface cone. Later, in 1957, Drucker, Gibson and Henkel introduced an elastoplastic model including two fundamental ingredients, a closed yield surface which consisted of a cone and a circular cap, and a hardening law dependent on density, paving the way to modern plasticity.

At the same time, the Critical State Model (CSM) was developed by Roscoe, Schofield and Burland [138, 137, 151] which describes the soil under triaxial conditions, i.e., volumetric hardening, but also a curved surface in the (e, p', q) space, where the residual state lies, was introduced. This line was referred to as the Critial State Line (CSL). The projection of the curved surface in the (e, p', q) space on the (p', q) space gives the CSL. The CSM is able to reproduce the behavior of soil under monotonic loading. Later on, the class of Bounding Surface Models were developed, to describe the material behavior of overconsolidated soil, or phenomena occuring during cyclic loading, such as pore pressure generation in fast processes or densification. The Bounding Surface Model takes into account two forms of hardening:

- density hardening (volumetric stress-strain) as in the critical state theory and
- deviatoric hardening (shear stress-strain) as in the classical plasticity theory.

The main disadvantages of early developed Bounding Surface Models was their inability to reproduce plastic deformations during unloading. In the Pastor-Zienkiewicz Mark III model [119] based on generalized plasticity theory [118], which behaves for loading like a Bounding Surface Model (Dafalias, Hermann) [47], plastic behavior is possible within the loading surface, whereas for unloading plastic material behavior is also assumed. The P-Z Mark III model is a phenomenological model, and is implemented in the Finite Element Code SWANDYNE, which

will be coupled here by an iterative coupling scheme with the BEM Code. This chapter is subdivided into three sections: first, a general description of classical theory of plasticity, further, a description of the critical state model and later, a description of the Bounding Surface Model which is an advanced model.

4.1 Classical Theory of Plasticity

Historically, first elastic-plastic material models were developed to represent the failure mechanism of metal plasticity. The failure mechanism of metal depends on shear deformation at constant volume. For metal, plastic behavior in tension and compression are almost identical. When we suppose metal under unixaxiale tensile load, material behavior under the yield point is linear-elastic (Hooke's law), beyond the yield point it is non-linear. There, the deformation consists of elastic and plastic strains. In the non-linear part, hardening or softening behavior of material can be observed.

Theoretically it has to be distinguished between isotropic and kinematic hardening, which will be explained in the following subsection. For metals, the theory of isotropic hardening can be used because, there, plastic behavior is in tension and compression almost identical. If in the non-linear part no hardening or softening behavior occurs, the material behaves ideal-plastic. Most of the characteristic behaviors of elastic-plastic materials can be seen in uniaxial material behavior. Between two basic groups of elastic-plastic material models has to be distinguished:

- The load path independent models where the hardening behavior is defined by the theory of Hencky as the total stress strain concept (Elastic-Perfectly Plastic Model, Elastic-Linear Hardening Model, Elastic Exponential Hardening Model, Ramberg Osgood Model).

- The load path dependent models where the hardening behavior is defined by the theory of incremental stress and strain (Mises, Mohr-Coulomb, Drucker-Prager, Critical State Model, Bounding Surface Model).

The class of load path dependent models can be further classified, in the classical plasticity models of von Mises and Tresca where no deviatoric hardening occurs, and if a limiting tensile stress is obtained, plastic strains are developing. In the models of Mohr-Coulomb and Drucker-Prager, deviatoric hardening can be taken into account. The next enhancement of constitutive models was made by the type of Critical State Models where deviatoric and isotropic hardening is concerned. Until now, only montonic loading behavior could be taken into accout (in each of the above mentioned models). Therefore, a further elaboration was made and the class of Bounding Surface Models was developed, which can take into account cyclic loading behavior. But now, first, the class of load path independent models will be described.

Elastic-Perfectly Plastic Model

For an elastic-perfectly plastic material, deformation can increase unboundedly without any additional load after the yield stress σ_0 is reached. The uniaxial stress-strain relation may be

expressed as

$$\varepsilon = \frac{\sigma}{E} \quad \text{for } \sigma < \sigma_0$$

$$\varepsilon = \frac{\sigma_0}{E} + \lambda \quad \text{for } \sigma = \sigma_0 \tag{4.1}$$

where E is Young's modulus and λ a positive scalar. Perfectly Plastic Material behavior may be considered as the limited case of hardening behavior.

Elastic-Linear Hardening Model

Here, as in the perfectly plastic model, the continuous curve can be approximated by two straight lines, replacing the smooth transition curve by a sharp breaking point at the yield stress σ_0. The first straight line branch has a slope of the Young's modulus E. The second straight line branch, representing in an idealized manner the hardening range, has a slope of E_t, where the value of E_t is usually much smaller than E. The stress-strain relation for monotonic loading in tension has the following form:

$$\varepsilon = \frac{\sigma}{E} \quad \text{for } \sigma \leq \sigma_0$$

$$\varepsilon = \frac{\sigma_0}{E} + \frac{1}{E_t}(\sigma - \sigma_0) \quad \text{for } \sigma > \sigma_0 \tag{4.2}$$

As an extension of this model, a piecewise-linear model consisting of several line segments may be constructed.

Elastic-Exponential Hardening Model

Hardening behavior of most materials are nonlinear. Therefore, a simple power expression may be employed as follow:

$$\begin{aligned} \sigma &= E\varepsilon \quad \text{for } \sigma \leq \sigma_0 \\ \sigma &= k\varepsilon^n \quad \text{for } \sigma > \sigma_0 \end{aligned} \tag{4.3}$$

where k and n are material constants which are determined by fitting to an experimentally obtained curve. The two material constants, k and n are not independent: for the stress-strain curve to be continuous at $\sigma = \sigma_0$, the condition $\sigma_0 = k\left(\sigma_0/E\right)^n$ has to be satisfied.

Ramberg-Osgood Model (1943)

In the following, the nonlinear stress-strain curve may be used to represent the elastic-plastic behavior:

$$\varepsilon = \frac{\sigma}{E} + a\left(\frac{\sigma}{b}\right)^n \tag{4.4}$$

in which a, b and n are material constants. In these models, no clear definition of the yield point exists, but the initial slope of the curve has the value of Young's modulus E. Under increasing stresses, the slope is decreasing monotonically [131].

4.1.1 Incremental Stress and Strain relationship

Models based on the total stress strain concept proposed by Hencky [84] are incapable to take into account the dependence of plastic behavior on the loading history. In the theory of Hencky, the plastic strains are functions of the current state of stress and are independent of the history of loading. It assumes further that the principal axes of the plastic strain tensor $\varepsilon_{ij}^{\mathrm{p}}$ are always coincident with those of stresses σ_{ij}. The plastic deviatoric strain tensor e_{ij}^{p} is proportional to the deviatoric stress tensor S_{ij}. No plastic volumetric change occurs. Hardening behavior of the material is described by a positive scalar value, whereas in the case of unloading the scalar value is set to zero. All these assumptions greatly simplifies the problem, however, the plastic strains cannot, in general, be independent of the loading path and deformation theories cannot generally be correct. Whereas the plastic deformation of a soil deposit is frequently an anisotropic process which depends on cyclic loading, on the loading history, on stress reversals and on the plastic volumetric change. For problems like liquefaction which involves unloading and reversed loading, an incremental procedure needs to be employed. In these context, there exists a class of soil models which can simulate liquefaction. First, there is the class of densification models proposed by Zienkiewicz and co-workers [188] where simple elastoplastic behavior of soil by non-associative Mohr-Coulomb model and densification by accumulation of pore pressure were taken into account. The second class of models are the so-called Multi-Surface Kinematic-Hardening Models proposed by Mroz [111] and further elaborated by Morz, Norris and Zienkiewic [112] to Multi-Surface Models. These models are able to reproduce most of the basic features of soils under cyclic loading such as memory of past events and plastic deformation during unloading. Parallel a development of Bounding Surface Models took place which later was elaborated to the concept of generalized plasticity: here, only two surfaces exist, i.e., an outer or consolidation surface and the inner or yield surface. A field of hardening moduli can still be described by prescribing the variation between both surfaces (Dafalias and Popov [49]). In the above mentioned models, the hardening moduli are depending on the direction of loading $\mathbf{u} = {}^{d\sigma}/_{\|d\sigma\|}$, which is taken into account by introducing a direction $\mathbf{n}$ for each mechanism of deformation considered. There are several alternatives to introduce the dependence on the direction of the stress increment among which it is worth mentioning the multilinear laws proposed by Darve and co-workers in Grenoble (Darve and Lanbanieh [51]) or the hypoplastic laws of Dafalias [46] or Kolymbas [96]. Before such enhanced models will be described in more detail, an overview of the basic concept of classical plasticity theory is given.

In the context with the theory of small strains, it will be assumed that the change of strain increments includes an elastic and a plastic part:

$$d\varepsilon_{ij} = d\varepsilon^{\mathrm{e}}_{ij} + d\varepsilon^{\mathrm{p}}_{ij} \tag{4.5}$$

The elastic strain increments are related to the stresses linearly by Hooke's law, whereas the plastic strain increments are generally related to the stresses nonlinearly. Reuss (1930) assumed that the plastic strain increments are at any instant of loading proportional to the instantaneous stress deviations.

In order to determine the actual magnitudes of the plastic strain increments, a yield criterion is required. The incremental theory is founded on Prandtl-Reuss [125, 134] which defines the plastic strain increment $d\varepsilon^{\mathrm{p}}_{ij}$ as

$$d\varepsilon^{\mathrm{p}}_{ij} = d\lambda S_{ij} = \frac{3}{2}\frac{d\varepsilon_{\mathrm{p}}}{\sigma_{\mathrm{e}}} S_{ij} = \frac{3}{2}\frac{\sqrt{2}\, d\gamma_{oct}}{\frac{3}{\sqrt{2}}\tau_{oct}} S_{ij} \tag{4.6}$$

where $d\gamma_{oct}$ is the octahedral plastic shear strain increment, τ_{oct} the octahedral shear stress, and S_{ij} the stress deviator tensor. Instead of the octahedral shear stress τ_{oct}, the equivalent stress σ_{e} and instead of the octahedral plastic shear strain increment $d\gamma_{oct}$ the equivalent plastic strain increment $d\varepsilon_{\mathrm{p}}$ will be used. The original Prandtl-Reuss assumption implies the von Mises yield criterion. For a perfectly plastic material, the Prandtl-Reuss equations may be written as

$$d\varepsilon^{\mathrm{p}}_{ij} = \frac{3}{2}\,\frac{d\varepsilon_P}{\sigma_0} S_{ij} = \frac{3}{2}\frac{\sqrt{2}\, d\gamma_{oct}}{\sigma_0} S_{ij} \tag{4.7}$$

where σ_0 is the yield stress in simple tension. For a material that work hardens, however, σ_{e} may be greater than σ_0, and it is now necessary to find the relation between the equivalent stress σ_{e} and the equivalent plastic strain increment $d\varepsilon_{\mathrm{p}}$. Figure 4.1(a) shows a typical stress-strain relationship of an elastic-plastic material. Until the yield point σ_0, the material behavior is linear-elastic, then nonlinear material behavior starts. Now, the material begins to accumulate permanent strain until the load is removed. The plastic strain ε^{p} remains and the elastic part of the strain vanish. The relation between stress and strain becomes nonlinear. Beyond the yield point, the slope of the stress-strain curve decreases steadily and monotonically with the load and eventually it may become negative. The nonlinear material behavior in the range with the positive slope $\partial\sigma/\partial\varepsilon > 0$, i.e., before peak load, is called hardening, whereas the behavior is called softening when the further deformation requires a decrease in load.

Consider now a loading program in which the stress is increased monotonically from zero to the stress in the tensile plastic region, σ_{T}, and then deformation results in a decrease, as shown in figure 4.1(b). During unloading, linear elastic behavior will persist until some stress σ_{c} is reached, where plastic strain in the opposite direction occurs. The lowering of the compressive yield stress following a plastic preloading in tension is called the Bauschinger effect and is a particular type of anisotropic behavior. The subsequent yield stress in compression, σ_{c}, will generally be different from the initial value $\sigma_{0\mathrm{C}}$. In particular, σ_{c} is smaller than the initial compressive yield stress $\sigma_{0\mathrm{C}}$, i.e., $|\sigma_{0\mathrm{C}}| > |\sigma_{\mathrm{c}}|$. This lowering of the compressive yield stress following a plastic preloading in tension is called the Bauschinger effect. By its very nature,

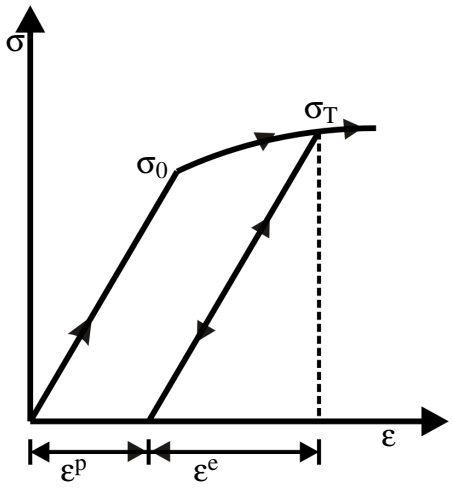

(a) Elastic/Plastic Strain

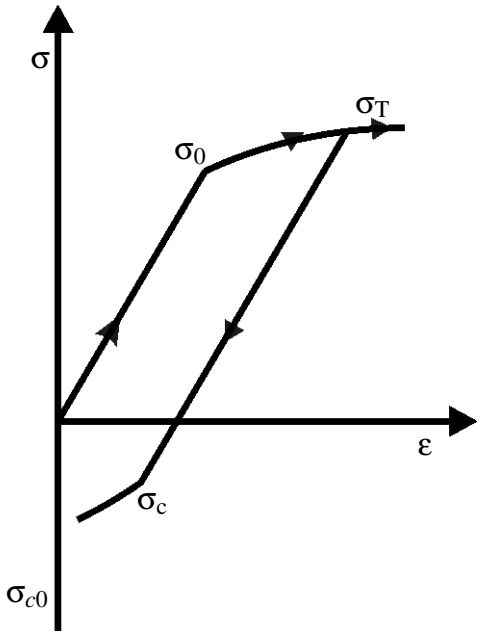

(b) elastic state, plastic state, unloading, reloading

Figure 4.1: Stress-strain behavior under uniaxial montonic loading/unloading and reloading process

plastic deformation is an anisotropic process. The Bauschinger effect is one particular type of directional anisotropy induced by plastic straining, since an initial plastic deformation in one direction reduces the yield stress in the opposite direction during a subsequent reversed loading.

To describe the stress-strain behavior in a mathematical point of view, it has to be distinguished between purely elastic or elastic-plastic behavior. Therefore, a loading criterion is introduced which differentiates the stress-strain behavior into a loading and an unloading process by the sign of the plastic strain.

If it is a hardening material, the evolution process of the elastic range, the yield surface, has to be defined and the history of plastic strain development has to be recorded because the elastic range changes due to the plastic deformation of the material. Furthermore, during plastic deformation, a condition, that the stress state always stays on the boundary of the elastic region, is necessary.

Therefore, in the theory of classical plasticity a loading criterion, a flow rule, a hardening rule, a hardening parameter, and a consistency condition is defined. For perfectly plastic material, the hardening rule is not required and the hardening parameter is zero.

Yield Criterion

In uniaxial stress states, the elastic limit of a material is defined by two yield stress points. In biaxial or general stress states, the elastic limit becomes a curve, in the stress space a surface or a hypersurface. The yield criterion distinguish between the state of elastic or plastic material

behavior. The yield criterion can be expressed by a yield function

$$f\left(\sigma_{ij}\right) = 0 \tag{4.8}$$

which determines the elastic limit and which is in three dimensional space a yield surface. The specific form of this function is material dependent. The size, shape, and position of the yield surface may change during hardening process. If a stress point lies inside the yield surface $f < 0$, only elastic material behavior is expected. On the other hand, for a perfectly plastic material, if the stress state lies on the yield surface $f = 0$ and the straining is still in the loading direction, then only plastic behavior is expected. For a hardening material, the stress state tends to move out of the current yield surface and dragging it with it. In this case, a loading process (see, figure 4.2) can be observed, and both elastic and plastic strains change. Subsequently the configuration of the current yield (or loading) surfaces changes too. If the stress state tends to move into the yield surface, it is an unloading process. Only elastic deformation occurs and the loading surface remains unchanged. Only for ideal elastic-plastic material behavior without hardening the yield surface remains constant during yielding.

Under the presumption of an isotropic material, the orientation of principal stresses is immaterial, and the values of three principal stresses, σ_1, σ_2, σ_3, suffice to describe the state of stress uniquely. A yield criterion, therefore, is expressed by $f(\sigma_1, \sigma_2, \sigma_3) = 0$ or $f(I_1, J_2, J_3) = 0$ where I_1 is the first invariant of the stress tensor σ_{ij} and J_2, J_3 are the second and third invariants of the deviatoric stress tensor S_{ij}, respectively. Additionally, it has to be distinguished between frictionless (metals) and frictional material (soil, rock, concrete). An important experimental observation for frictionless materials, like metals, is that the influence of hydrostatic pressure on yielding is not appreciable. The absence of a hydrostatic pressure effect indicates that the yield function can be reduced to $f(J_2, J_3) = 0$. This is regarded as the most general form of the yield criterion for hydrostatic-pressure-independent isotropic materials.

Hardening Rule

A yield surface changes its current configuration during the loading process so that the stress point always lies on it. The hardening rule describes how the yield surface, i.e., the elastic range of the material evolves. As shown in figure 4.1(b), the elastic region of the material changes when loading occurs.

In the case of hardening, i.e., loading, the initial yield surface can change its size, location, and shape. The subsequent yield surface is, therefore, a function of stress history. Suppose that a material element is submitted to a uniaxial tensile stress σ_T which is greater than σ_0, the yield stress in simple tension. The subsequent yield stress in compression may change, depending on the particular hardening rule employed. Here, an elastic-linear hardening behavior is assumed and the initial yield stresses in tension and compression are taken to be numerically equal to σ_0. At one extreme, the elastic region remains at the same size, so that compressive yielding occurs at point C (see, figure 4.3(a)) where $\sigma = \sigma_T - 2\sigma_0$. This is known as the kinematic hardening rule, since the elastic region moves around in stress space as a rigid body. Therefore, the size, shape, and orientation of the initial yield surface are maintained but the current location of the yielding surface has changed. Path OABCD in figure 4.3(a) illustrates this hardening rule. The

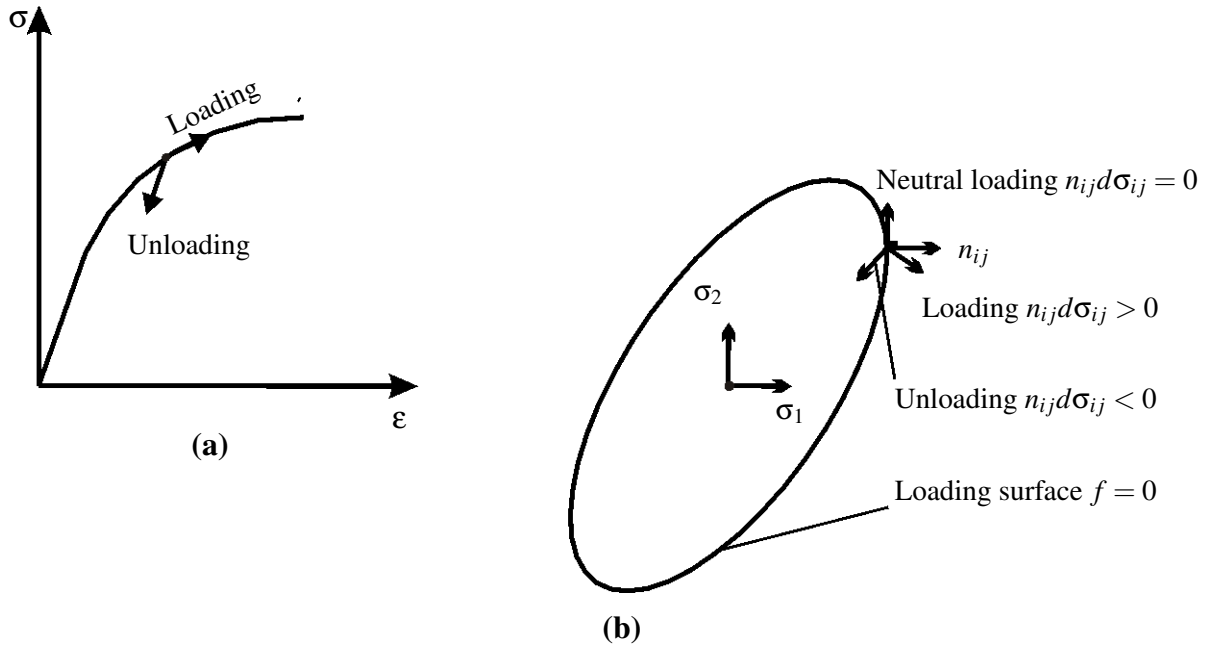

Figure 4.2: Loading criteria for a work-hardening material **(a)** uniaxial case **(b)** multiaxial case

yield surface associated with the kinematic hardening rule (see, figure 4.3(b)) due to Prager may be given mathematically by

$$f\left(\sigma_{ij},\alpha_{ij}\right) = f\left(\sigma_{ij}-\alpha_{ij}\right) - k = 0 \tag{4.9}$$

where k is for ideal-plastic material a constant, α_{ij} is a back stress and gives the coordinates of the center of the loading surface, which is dependent on the plastic loading history. The kinematic hardening rule exhibits the idealized Bauschinger effect and depends on $\bar{\sigma}_{ij} = \sigma_{ij} - \alpha_{ij}$. The distance between the actual state of stress and the moved center of the yield surface is named $\bar{\sigma}_{ij}$. In these case of an kinematic hardening rule, the center of the yield surface is moving. In the case of an isotropic hardening rule, the center of the yield surface remains the same. At the other extreme lies the isotropic hardening rule, as shown by Path 0ABEF in figure 4.3(a). In the case of isotropic hardening, the geometrical shape of the yield surface does not change, but the extension of the shape of the yield surface will change. The yield surface of the isotropic hardening rule is expressed as

$$\begin{aligned} f\left(\sigma_{ij},k\right) = f\left(\sigma_{ij}\right) - k = 0 \\ \text{with } k = k(W_\mathrm{p}) \text{ and } W_\mathrm{p} = \int \sigma_{ij} d\varepsilon^\mathrm{p}_{ij} \\ \text{or with } k = k(\varepsilon^\mathrm{p}_\mathrm{v}) \text{ and } \varepsilon^\mathrm{p}_\mathrm{v} = \int C\sqrt{\left(d\varepsilon^\mathrm{p}_{ij} d\varepsilon^\mathrm{p}_{ij}\right)} \end{aligned} \tag{4.10}$$

where ε_p is the equivalent or effective plastic strain, $d\varepsilon^\mathrm{p}_{ij}$ the plastic strain increment, and C is a constant which depends on the yield function. The plastic work W_p physically represents the energy dissipation associated with plastic deformation. For the von Mises yield function, for

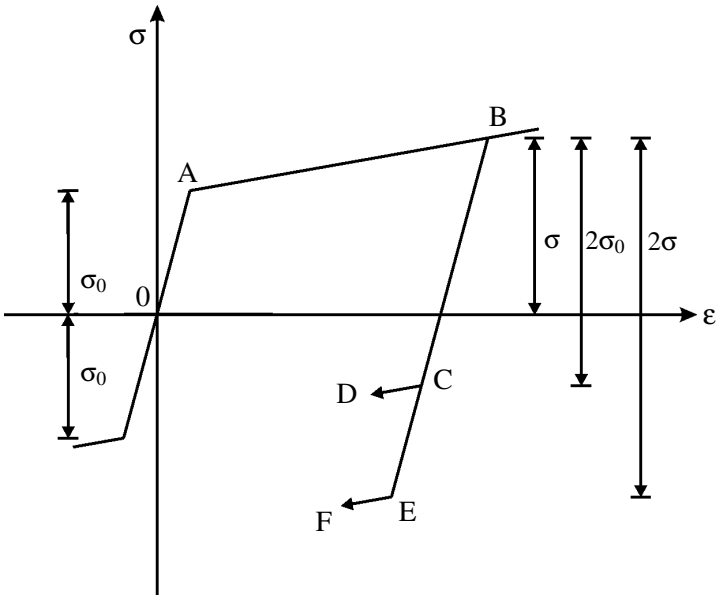

(a) Uniaxial kinematic/isotropic hardening

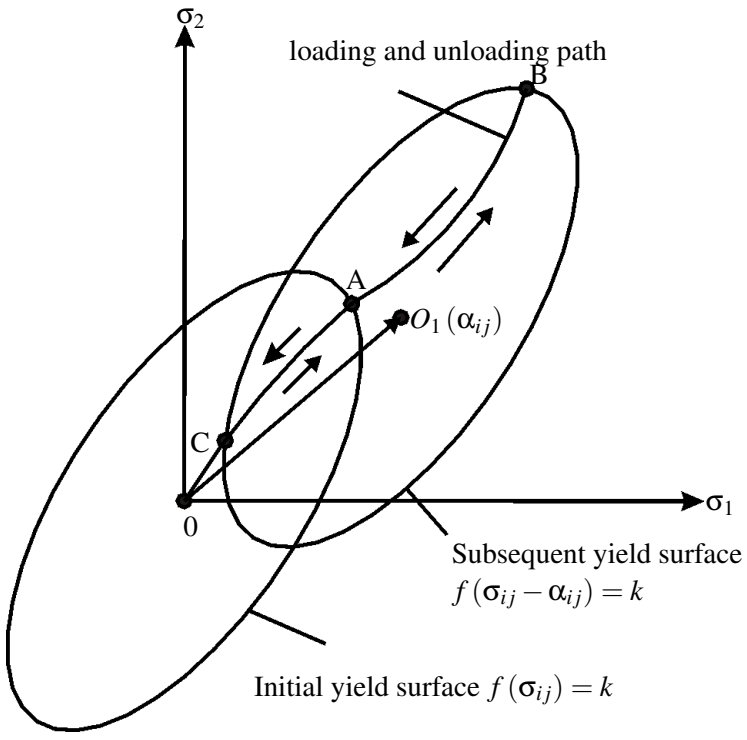

(b) Yield surface for kinematic hardening

Figure 4.3: Hardening in the uniaxial/multiaxial space

instance, the isotropic yield surface $f\left(\sigma_{ij}\right)$ is formed with the aid of the second invariant J_2.

$$f\left(\sigma_{ij},k\right) = \sqrt{J_2} - k = 0 \tag{4.11}$$
$$d\varepsilon_{\mathrm{v}}^{\mathrm{p}} = \int \sqrt{\left(\frac{2}{3} d\varepsilon_{ij}^{\mathrm{p}} d\varepsilon_{ij}^{\mathrm{p}}\right)}$$

where k is a growth/hardening function, which defines the size of the surface. The first hypothesis (work-hardening) assumes that the amount of hardening k depends only on the total plastic work, and is independent of the strain path [85]. Whereas the second hyphothesis (strain-hardening) uses the equivalent plastic strain as the amount of hardening k, and depends on the loading history. Obviously, the isotropic hardening rule contradicts the Bauschinger effect observed in some experiments. Following experimental evidence, plasticity theories postulate that irreversible or plastic strain appears whenever the stress reaches a yield surface $f(\sigma_{ij},k) = 0$. If the growth/hardening function k is a constant, the material cannot sustain a higher stress and failure takes place. This is the reason why the yield surface is sometimes also known as the failure surface. To characterize a yield surface which is subject to a uniform expansion and to a translation, the theory of kinematic and isotropic hardening is combined to the theory of mixed hardening.

A yield surface changes its current configuration during the loading process so that the stress point always lies on it. The hardening rule describes how the yield surface, i.e., the elastic range of the material evolves.

Flow Rule

In the preceding section, the yield criteria and the hardening rule are specified which determines the elastic-plastic limit in general stress space and the development of hardening during yielding, respectively. How the plastic strain increment is characterized in plastic range has to be defined by the flow rule. It is important to distinguish between associated and non-associated flow rule.

Associated flow rule An associated flow rule is mostly appropriate to describe the behavior of frictionless materials, like metals. The associativity of the flow rule is a consequence of Drucker's stability postulate (1952)

$$\left(\sigma_{ij} - \sigma_{ij}^{0}\right) d\varepsilon_{ij}^{\mathrm{p}} \geq 0 \tag{4.12}$$

where σ_{ij} is the actual stress state at the yield surface and σ_{ij}^{0} is the initial stress state at or within the yield surface [60, 61]. It postulates that the work, which is done by the additional set of incremental stresses at the plastic strains, cannot be negative. This postulate can only be fulfilled if the yield surface is convex, and the plastic strain increment vector $d\varepsilon_{ij}^{\mathrm{p}}$ is normal to the tangent to the yield surface. The direction of the plastic strain increment vector and the

magnitude is defined by the flow rule

$$d\varepsilon_{ij}^{\mathrm{p}} = d\lambda \frac{\partial f}{\partial \sigma_{ij}} \tag{4.13}$$

were $d\lambda$ is a non-negative scalar function which varies throughout the plastic loading history. The function $f(\sigma_{ij})$ is defined as a plastic potential. In the case of an associative flow rule, the plastic potential surface and the yield surface are identical.

Non-associated flow rule For frictional materials such as concrete and soil, the associated flow rule is inadequate because the yield surface and the plastic potential depends differently on I_1, the first invariant of the stress tensor. As an extension, the non-associated flow rule has been adopted which assumes a different form of the plastic potential function g in contrast to the yield function f. Introducing the concept of a plastic potential function g, the flow rule

$$d\varepsilon_{ij}^{\mathrm{p}} = d\lambda \frac{\partial g}{\partial \sigma_{ij}} \tag{4.14}$$

is defined by the gradient vector $\partial g/\partial \sigma_{ij}$ and a non-negative scalar $d\lambda$ which varies throughout the plastic loading history. The gradient vector $\partial g/\partial \sigma_{ij}$ defines the direction of the plastic strain increment vector $d\varepsilon_{ij}^{\mathrm{p}}$ at the current stress point. The use of non-associated flow rules in dynamic analyses can lead to plastic energy generation (even though the second law of thermodynamics may be satisfied). If negative amounts of energy can deform an element of material in a strain cycle, the Ill'iushin's postulate is violated by non-associative material models when rate independence is assumed and inertia effects are taken into account. This can be prevented if the reloading modulus is always equal to the unloading modulus. If not, the use of rate-independent, non-associated plasticity may pose mathematical problems but it does not necessarily mean that it has no physical meaning. Non-uniqueness is not impossible in physical situation. Further non-associative flow rules lead to non-symmetric elasto-plastic matrices, so it is more costly from the point of calculation time to solve these matrices.

4.1.2 Elasto-plastic material models for soil

Non-linear material behavior of soil can be described with elasto-plastic material models. Already a small change in the stress deviator leads to a plastic state of the material, but also a change in hydrostatic stresses can also produce permanent deformations. To treat the stress-strain behavior in a realistic way enhanced elasto-plastic material models with multiple yield surfaces, a specified hardening rule and a certain failure surface are required. Here, especially the demands on yield criteria and hardening are described in more detail.

Mohr-Coulomb Yield Criteria

For hydrostatic-pressure-dependent frictional materials like soils the Mohr-Coulomb criterion is the failure criterion most commonly used in practice to represent geologic materials. In con-

trast to the yield criteria of Tresca, the critical value of the shear stress τ is not a constant but a function of the normal stress σ. In the special case of frictionless materials, for which $\phi = 0$, equation (4.15) reduces to the Tresca criterion, and the cohesion becomes equal to the yield stress in pure shear. In this sense the Mohr-Coulomb criteria can be considered as a generalization of the Tresca criterion. The Mohr-Coulomb criterion often used in planar problems, can be expressed if the principal stresses are $\sigma_1 \geq \sigma_2 \geq \sigma_3$ as

$$|\tau| = c - \sigma_n \, tan \, \phi \tag{4.15}$$

where τ is the shear stress, σ_n the normal stress (compression negative) on the failure plane, ϕ the angle of internal friction and c is the cohesion. The material constants cohesion and angle of friction are determined by experiment. In terms of principal stresses the Mohr-Coulomb criterion equation (4.15) may be written as

$$-\frac{\sigma_1 - \sigma_3}{2} cos \, \phi = c - \left(\frac{\sigma_1 + \sigma_3}{2} + \frac{\sigma_1 - \sigma_3}{2} sin \, \phi \right) tan \, \phi \tag{4.16}$$

Alternatively, the Mohr-Coulomb criterion equation (4.16) may be expressed in terms of the stress invariants

$$f(I_1, J_2, \Theta) = \frac{1}{3} I_1 sin\phi + \sqrt{J_2} \left(cos\Theta - \frac{1}{\sqrt{3}} sin\Theta sin\phi \right) - c \, cos \, \phi = 0 \tag{4.17}$$

with the lode angle:

$$\Theta = \frac{1}{3} arcsin \left(-\frac{3\sqrt{3}}{2} \frac{J_3}{J_2^{3/2}} \right) \quad \text{with} \quad -\frac{\pi}{6} \leq \Theta \leq \frac{\pi}{6}$$

$$I_1 = \sigma_1 + \sigma_2 + \sigma_3$$

$$J_2 = \frac{1}{6} \left((\sigma_1 - \sigma_2)^2 + (\sigma_2 - \sigma_3)^2 + (\sigma_3 - \sigma_1)^2 \right)$$

The Mohr-Coulomb criterion is represented in the space of principal stresses as an irregular hexagonal pyramid, which has been depicted in figure 4.4, 4.5(b).

Drucker-Prager Yield Criteria

Another simple yield criterion is defined by Drucker-Prager which was formulated in 1952. This is an extension of the yield criteria of von Mises, which includes the hydrostatic pressure for yielding for frictional materials. In the stress space the Drucker-Prager yield criteria is a right circular cone with its axis equally inclined with respect to each of the coordinate axes and its apex on the hydrostatic axis. Mathematically, this criterion is expressed as

$$f(I_1, J_2) = \alpha I_1 + \sqrt{J_2} - k = 0 \tag{4.18}$$

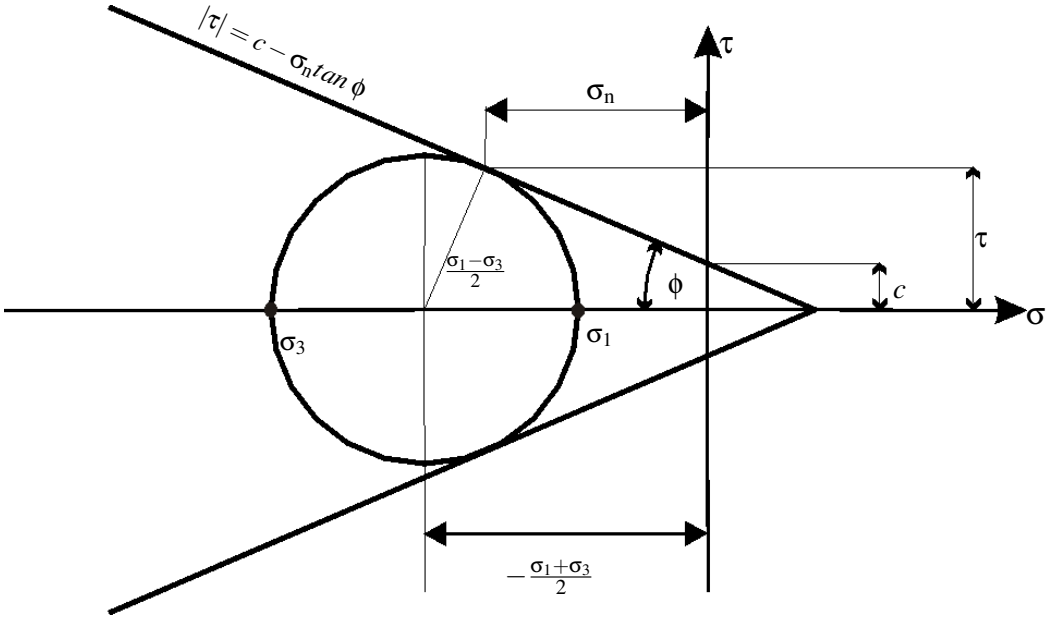

Figure 4.4: Mohr-Coulomb Criteria

where α and k are material constants. When α is equal to zero and $k_{\text{Drucker}-\text{Prager}} = k_{\text{von Mises}}$ the Drucker-Prager criterion reduces to the von Mises criterion. The Mohr-Coulomb hexagonal yield surface is not smooth like the Drucker-Prager yield criterion but it has corners. If the Drucker-Prager criterion is formulated in a way that the outer Drucker-Prager circle coincide along the compressive meridian ρ_c, then the constants α and k of the Drucker-Prager criterion are related to the cohesion c and the angle of internal friction ϕ of the Mohr-Coulomb criterion like in row one in table 4.1. Subsequently, the corresponding Drucker-Prager cone

Table 4.1: Parameter for the yield criteria of Drucker-Prager

	α	k
compressive circle	$\frac{2sin\phi}{\sqrt{3}(3-sin\phi)}$	$\frac{6ccos\phi}{\sqrt{3}(3-sin\phi)}$
tension circle	$\frac{2sin\phi}{\sqrt{3}(3+sin\phi)}$	$\frac{6ccos\phi}{\sqrt{3}(3+sin\phi)}$

circumscribes the hexagonal pyramid of the Mohr-Coulomb criterion. In row two of table 4.1 the material parameters for the Drucker-Prager model are shown in the case that the Drucker-Prager criterion is inscribed in the Mohr-Coulomb hexagon. Therefore, the Drucker-Prager circle coincides with the tensile-meridian of the Mohr-Coulomb criterion. The cross sections of the Π-plane for the Drucker-Prager criterion and the Mohr-Coulomb criterion are shown in figure 4.5(a).

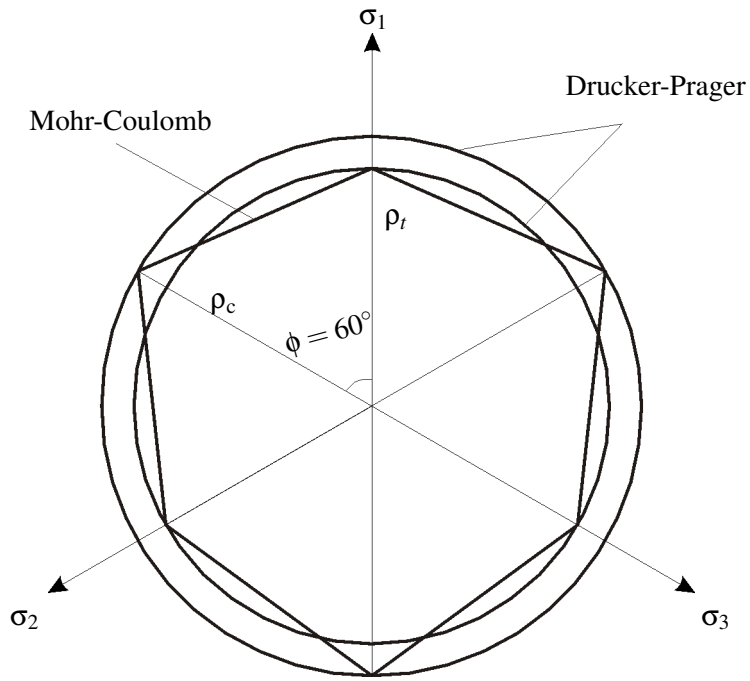

(a) Π-plane/deviatoric-plane

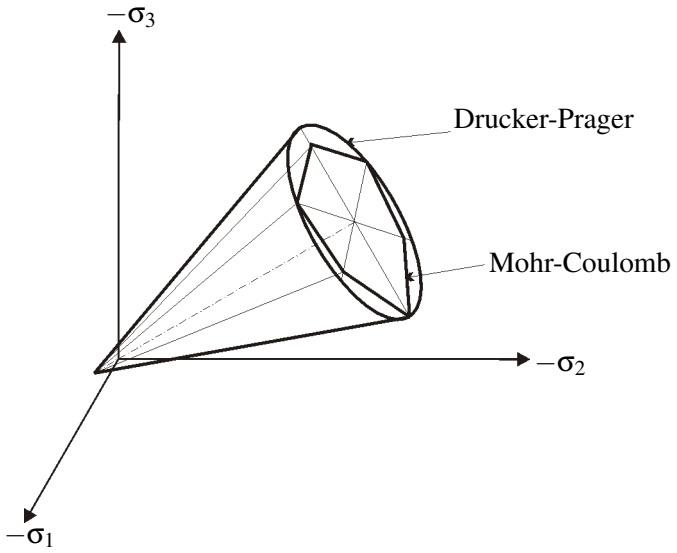

(b) Principal stress space

Figure 4.5: Mohr-Coulomb and Drucker-Prager criteria

4.2 Critical State Model

Modern plasticity models for soils are based on the work of Drucker, Gibson and Henkel [62], who introduced the ideas of volumetric hardening and a closed yield surface. The first critical state models were the series of Cam-clay formulations, developed at the University of Cambridge, by Roscoe and his co-workers. The formulation of the original Cam-clay model as an elasto-plastic constitutive law was presented by Roscoe and Schofield [138] and Schofield and Wroth [151]. The original model assumed that the Roscoe surface was bullet shaped. Afterwards, Roscoe and Burland [137] proposed the modified Cam-clay model with an elliptical shape. The modified Cam-clay model was, like the original Cam-clay model, developed for triaxial loading conditions $\sigma'_2 = \sigma'_3$ and $|\sigma'_1| > |\sigma'_3|$ (compression negative). A basic observation of soil behavior was that the response of the soil depends on mean effective stress and the void ratio. Therefore, the material behavior of clay under slow isotropic perfectly drained compression is shown in figure 4.6. The strength of soil is increasing when it becomes denser (decrease in void ratio). The Modified Cam-clay model proposed by Burland [32] requires the following

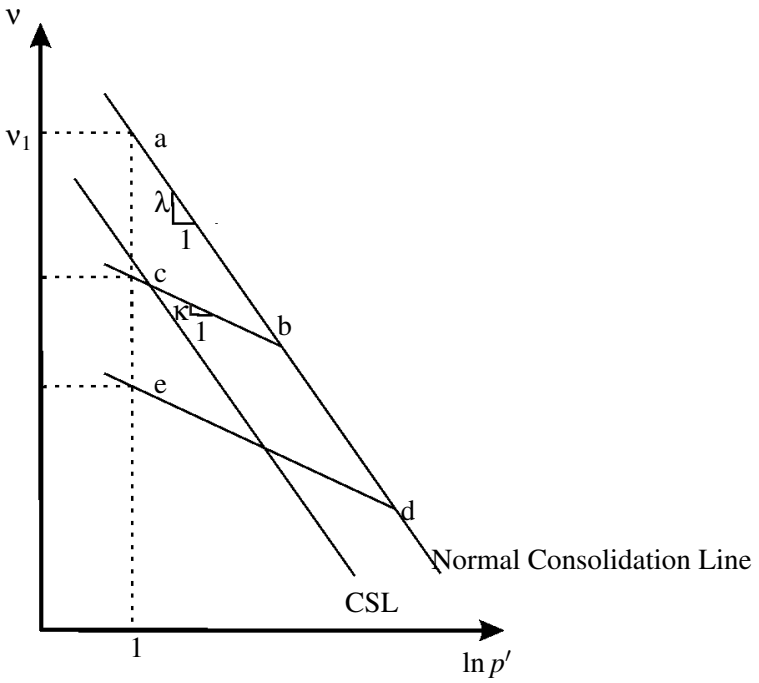

Figure 4.6: Behavior under isotropic compression

material parameters. These parameters are:

λ- The slope of the hydrostatic consolidation line,

ν- the specific volume $\nu = 1 + e$,

κ- the slope of the hydrostatic swelling line in the e-ln p plane,

e- the void ratio, $e = V_v/V_s$ where V_v is the volume of voids and V_s is the volume of solids.

e_1- The void ratio corresponding to a pressure of unity,

e_0- the void ratio at the intersection of the normal consolidation line and the swelling line. e_0 is the hardening parameter of the Cam-clay Model,

p'- the mean effective stress $p' = -I_1 = -\frac{1}{3}\left(\sigma'_1 + 2\sigma'_3\right)$.

p'_0- The initial mean effective stress corresponding to the void ratio e_0, the intersection of the hardening surface (Roscoe surface) with the hydrostatic axis.

The normal consolidation line and the swelling lines are assumed to be straight in *e-ln* p' space and are given by the following equations:

$$\begin{aligned} \nu + \lambda\left(ln\ p'\right) &= \nu_1 \ \text{ consolidation line} \\ \nu + \lambda\left(ln\ p_c\right) &= \Gamma \ \text{ critical state line} \\ \nu + \kappa\left(ln\ p'\right) &= \nu_s \ \text{ swelling line} \end{aligned} \tag{4.19}$$

The material parameters of κ, λ and ν_1 are characteristic values of the specific type of clay, whereas the value of ν_s is different for each swelling line. The volume change along the normal consolidation line is mainly regarded as irreversible or plastic, while the volume change along a swelling line is reversible or elastic. The behavior of a piece of clay under slow isotropic compression is figured out in figure 4.6 where it can be observed:

a-b: That the soil first starts at point a and is consolidating until point b is reached. The actual stress state is moving down the normal consolidation line.

b-c: If the soil is unloaded, the stress state moves up the swelling line until point c is reached.

c-d: Under reloading conditions, the mean effective stress increases, so the mean stress moves down the swelling line, and after point b is reached, it is moving down the normal consolidation line also.

d-e: When the soil is again unloaded, it moves up the swelling line until point e is reached.

The behavior of the soil under increasing triaxial shear stresses is assumed to be elastic until the yield criterion is reached (see, e.g., equation (4.18) for the Drucker-Prager yield criterion). At each swelling line we have elastic material behavior so we can observe another yield surface at each swelling line. The extension of the yield surface depends on the change in the void ratio. If we start with a certain void ratio which goes to unity, the elastic range of the yield surface is small, if the void ratio is reduced, the elastic range of the yield surface increases. Elastic hardening behavior can be observed and is controlled by the parameter p'_0. The value of p'_0 defines on which yield surface in the $(\nu - \ln p')$ space the actual stress state lies and has a particular value for each swelling line. Hardening and softening is isotropic and is controlled by p'_0 which is related to the $d\varepsilon^{\mathrm{p}}_{kk}$ plastic volumetric strain by

$$d\varepsilon^{\mathrm{p}}_{kk} = \frac{dp'_0}{p'_0}\frac{(\lambda - \kappa)}{\nu}. \tag{4.20}$$

In figure 4.7(b), the Modified Cam-clay yield surface is graphed for the triaxial stress state in terms of principal stresses with p' as mean effective stress and the deviatoric stress $q = \sigma'_3 - \sigma'_1$,

$$F\left(\sigma', k\right) = \left(\frac{q}{p'\,M}\right)^2 + \left(1 - \frac{p'_0}{p'}\right) = 0 \tag{4.21}$$

M is the slope of the critical state line, and p'_0 is the value of p' at the intersection of the current swelling line with the consolidation line. The slope of the critical state line obtained from triaxial compression tests is

$$M = M_{\mathrm{c}} = \frac{6sin\phi}{3 - sin\phi} \tag{4.22}$$

where ϕ is the angle of internal friction of the soil. The original Cam-clay model dealt only with isotropic and triaxial compression path, for triaxial extension path the slope of the critical state line in the triaxial plane is

$$M = M_{\mathrm{e}} = \frac{6sin\phi}{3 + sin\phi} \tag{4.23}$$

assuming that the friction angle ϕ is identical for triaxial compression and extension stress paths. The shape of the elliptical hardening (Roscoe) surface is fixed. The apexes of the ellipse on the hydrostatic axis are assumed to pass through the origin and the point p'_0, corresponding to the hardening parameter e_0 (void ratio). The ellipse has a horizontal tangent at the intersection with the critical state line.

The projection of the Roscoe surface in figure 4.7(a) from $\ln p'$-q-e space on to the meridian plane p'-q is plotted in figure 4.7(b). Roscoe explained that the projection of the critical state line appeared to be a straight line in p'-q plane for $e = 0$. The critical state line in figure 4.7(a) in the $\ln p'$-q-e space divides all states into »wet« and »dry« states. If $\nu_\lambda = \nu + \lambda\,(\ln p')$, then there is a region in which $\nu_\lambda < \Gamma$, called the »dry« side of critical state: this is the region in which soils fails with peak strength on a slip surface. The region in which $\nu_\lambda > \Gamma$ is called the »wet« side of critical states and is the region in which soil yields as a ductile plastic continuum. At the critical state line, shear deformation takes place without change of volume. As noted above, behavior along a swelling line is elastic. Therefore, the implication is: if the initial state (p', q, e) of a sample is known, the failure condition (p', q, e) is uniquely determined for a particular triaxial compression stress path. The elastic volumetric strain $\varepsilon^{\mathrm{e}}_{kk}$ under isotropic compression can be determined from equation (4.19)

$$d\varepsilon^{\mathrm{e}}_{kk} = \frac{d\nu}{\nu} = \frac{\kappa}{\nu}\frac{dp'}{p'} \tag{4.24}$$

This gives the elastic bulk modulus, K, as:

$$K = \frac{dp'}{d\varepsilon^{\mathrm{e}}_{kk}} = \frac{\nu p'}{\kappa} \tag{4.25}$$

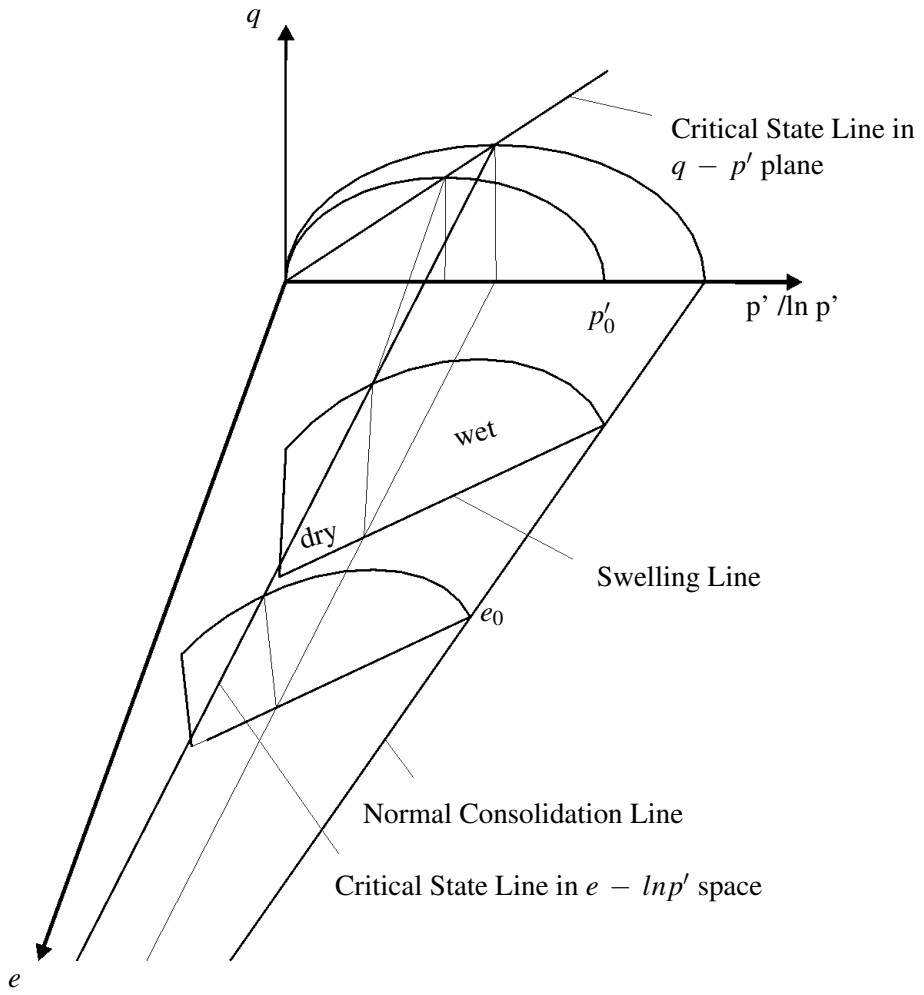

(a) State boundary surface in p’-q-e plane

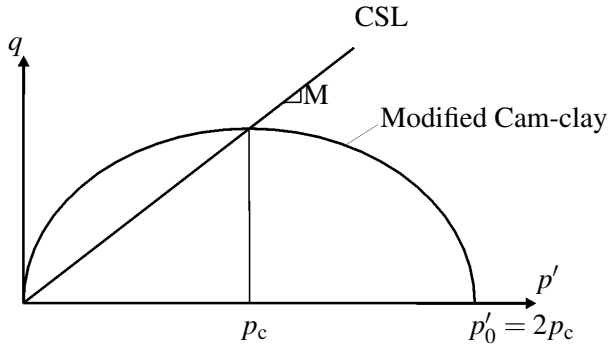

(b) Modified Cam-clay yield surface

Figure 4.7: Cam-clay yield surface

It receives attention that there exists a yield surface for every swelling line. The yield function, given by equation (4.21), defines a surface in e-q-p' space called the Stable State boundary surface (see, figure 4.7(a)).

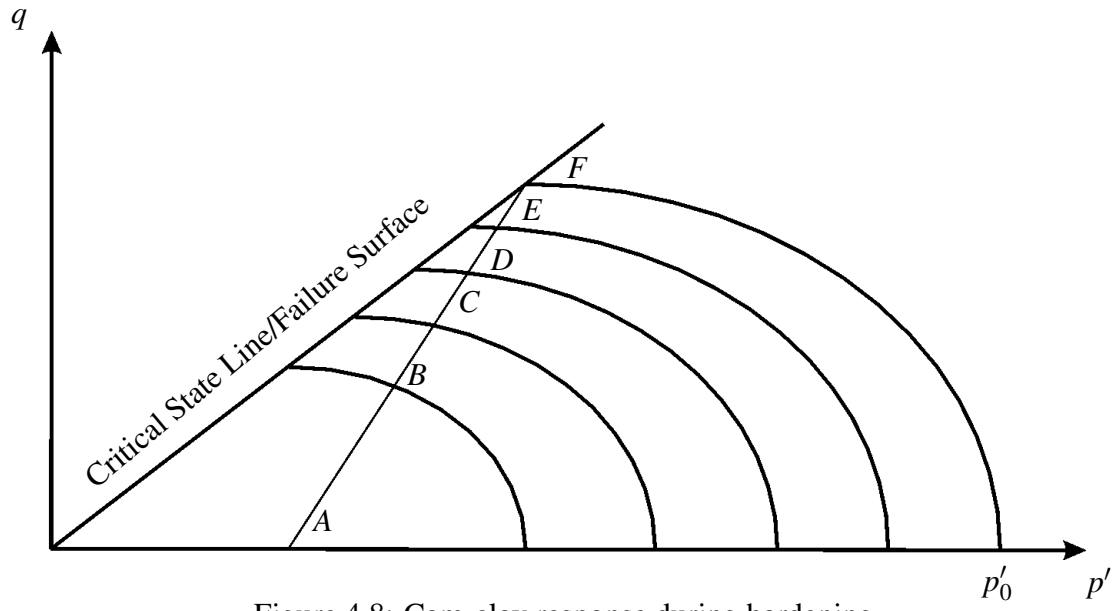

Figure 4.8: Cam-clay response during hardening

In figure 4.8, the stress path of a drained triaxial compression test on a lightly overconsolidated sample is graphed. From point A to point B the material behaves purely elastic (only elastic changes to the void ratio). Further loading produces an elastic response and a subsequent yield surface is reached C, each with the same shape. Eventually, the load path arrives at the critical state line F where failure occurs. The original formulation of Modified Cam-clay was developed for triaxial loading tests (p'-q plane), later an extension to the general stress space $(-I_1, \sqrt{3J_2})$ was defined. The first generalisation [137] is achieved by effectively replacing q by $\sqrt{3J_2}$. In general stress space, this signifies that the yield and plastic potential surfaces (and hence the failure surface) are circles in the deviatoric plane and an elliptic shape in the Meridian plane. However, it is well known that the Drucker-Prager criterion (shape of a circle) does not represent well the failure conditions for soils. The choice of a Mohr-Coulomb failure criterion would be more appropriate. But also the Mohr-Coulomb criterion does not achieve a perfect agreement with observed failure conditions. Therefore, another failure surface has been suggested by Lade [99] which is continuous and has a better agreement with the observed soil failure condition.

4.3 Bounding Surface Model

Many of the plasticity-based constitutive models applied to sands are remarkably similar to the critical state model used for cohesive soils. The Critical State Models was first extended in

the range of application through the Cap Models (hardening laws depending on deviatoric and plastic volumetric strain and a non-associative flow rule). To simulate cyclic loading behavior, the series of Bounding Surface Models was developed.

In the Critical State Model and in the series of Cap Models, material behavior is like in classical plasticity theory inside the yield surface elastic. In the case of Bounding Surface Models exist two surfaces, the loading surface and the bounding surface. The bounding surface is another name for the yield surface of the model and divides the range inside the yield surface in an elastic range and in a plastic range. Plastic behavior is allowed in contrary to classical plasticity theory within the yield surface. On the bounding surface, plastic strain develops according to classical plasticity theory, with directions $\mathbf{n}$ and $\mathbf{n}_g$ given by the normals to the bounding and to plastic potential surfaces, respectively. The plastic modulus is obtained due to the application of the consistency condition describing material hardening or softening properties. When the loading process begins at the bounding surface, the Bounding Surface Model behaves like in classical plasticity theory. In the case of cyclic loading, the Bounding Surface Model is able to introduce plastic deformation by the use of interpolation rules inside the bounding surface [186]. These interpolation rules define the plastic modulus at the loading point by referring it to the image point on the bounding surface where the plastic modulus is well-known. The plastic modulus is recognized as the key phenomenological factor in describing material behavior under stress reversals. Another ability of the model is to simulate pore pressure generation in a fast loading process during a cyclic loading process where compaction of the soil occurs under loading and unloading. The fundamental concept of the Bounding Surface Model developed by Dafalias and Popov [49] is motivated by the general observation how the plastic modulus E_p changes. To describe these idea, a stress state under uniaxial loading is observed. A typical schematic representation of such an experiment is shown in figure 4.9(a) on stress-plastic strain space. Here, every stress-plastic strain curve approaches asymptotically and/or eventually merges with the bounds represented by the straight lines XX',YY'. The material behavior can be described by considering the plastic modulus E^p to be a function of the distance $\delta = A\bar{A}$ of the stress state A from the corresponding bound, and also a function of the value of δ at the initiation of yielding for each loading process, denoted by δ_{in}. In the foregoing context, at the initiation of a new loading process, δ_{in} can be regarded as a parameter measuring how far the material state is from the state represented by the bounds. It is a discrete memory factor which changes only abruptly when loading occurs, preceeded by elastic deformation, and remains constant along the same $\sigma - \varepsilon^p$ curve in any one direction. The diminishing distance δ gives a measure of the increasing proximity to this state. The δ, δ_{in} have dimension of stress only and are always non-negative.

$$E_p = E_0^p + h\left(\frac{\delta}{\delta_{in} - \delta}\right) \tag{4.26}$$

Three different regions can be observed. The first region is an elastic region where E_p has an infinite value. The second region occurs beyond the initial yield stress σ_0; in this region E_p decreases rapidly as a function of the plastic strain ε^p. Then, the third region is reached; E_p takes an almost constant value E_0^p associated with the bounding line XX'. Based on many uniaxial experiments, it may be assumed that in the third region, the $\sigma - \varepsilon^p$ curve lies on, or asymptotically converges to, the bounding line XX' (or YY') which is often assumed to be a

straight line. In multiaxial cases, the projections of the points A, B in figure 4.9(a) become the loading surface and the points $\bar{A}, \bar{B}$ become a second surface enclosing the loading/yield surface, named bounding surface. The kinematic hardening model is a two-surface model consisting of a bounding surface and a loading/yield surface as shown in figure 4.9(b).

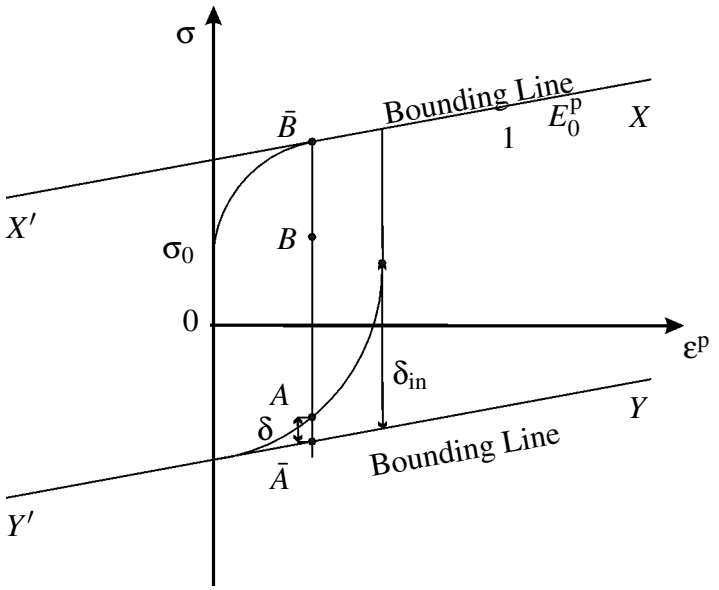

(a) Schematic illustration of δ and δ_{in} [49]

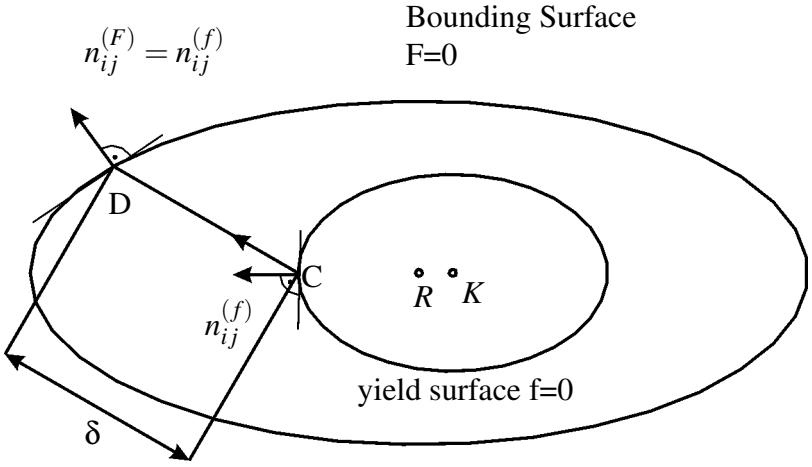

(b) Yield and bounding surface in stress space [38]

Figure 4.9: Kinematic Hardening

4.3.1 Cyclic Plasticity

Inside the loading surface, only elastic behavior is observed. In between bounding surface and loading surface plastic behavior is allowed. The loading surface is general defined as

$$f(\sigma_{ij} - \alpha_{ij}, q_{\mathrm{n}}) = 0 \tag{4.27}$$

where α_{ij} are the center coordinates of the loading surface, represented as point K in figure 4.9(b), and q_{n} are the plastic internal variables (PIV) such as the plastic strain. The bounding surface is defined as the homogeneous function of the form

$$F(\sigma_{ij} - \alpha^*_{ij}, q_{\mathrm{n}}) = 0, \tag{4.28}$$

where α^*_{ij} is the center of point R for the bounding surface.

The two surfaces translate simultaneously in stress space in a coupled way. The loading surface can translate, deform, and contact the bounding surface but not intersect it. The non-intersection is a mathematical convenience to ensure that the plastic loading condition is uniquely defined. The non-intersection condition is necessary when a bilinear constitutive law is derived [130]. The generalized hardening modulus H related to the loading surface is given by

$$H = H(\delta, W_P), \tag{4.29}$$

where δ is the distance between the current stress state σ_{ij}, represented as Point C on the loading surface and the stress state $\bar{\sigma_{ij}}$ at point D, which is obtained by the intersection of the line C-D with the bounding surface as graphed in figure 4.9(b). A multi surface model was developed by Mroz et al. (1978,1979) for clays. A bounding surface F=0 reflects the consolidation history of the soil and the initial yield surface/loading surface f=0 defines the elastic domain within the bounding surface which is the subsequent yield surface. In the model of Mroz, the bounding surface is assumed to expand or to contract isotropically, but the loading surface is allowed to translate, expand, or contract within the domain enclosed by the bounding surface. The translation of the yield surface is governed by the simple rule that the yield surface f will translate towards the bounding surface along C-D in figure 4.9(b). An interpolation rule to define the variation of the hardening moduli between the loading and the bounding surface follows the work of Dafalias and Popov(76) where the hardening modulus is taken as a function of distance between the current stress point C on the yield surface and its conjugate Point D, on the bounding surface [38].

4.3.2 Pastor-Zienkiewicz mark III (1986) Model (PZ3 model)

The PZIII Model is based on the 'bounding surface' variant of the 'generalized plasticity' theory [47, 179, 180]. The Clay Model [178] and the subsequent Sand Model [117] (named Mark-I) are based on the concept in generalized plasticity [179]. The further development was the PZ-MarkIII Model [119] which is incorporated in the program Swandyne. A brief overview of the basic concept of the fundamental concept of the PZIII model will be given in these sections, in the first subsection the clay model, in the second section the Mark-I model with non-associative

constitutive law is described, in the last subsection the particularities of the Mark-III model are given. The constitutive model is written in terms of effective stresses. To characterize material behavior fully, suitable experiments have to be carried out to establish laws for:

- Direction of plastic flow
- Loading-unloading directions
- Plastic moduli

For triaxial tests, two stress parameters p' and q are defined in terms of the stress invariants $p' = -I_1 = -\frac{1}{3}(\sigma'_1 + 2\sigma'_3)$ and $q = \sqrt{3J_2} = \sigma'_3 - \sigma'_1$. The measures of strain are those work associated to p' and q where $\varepsilon_v = -(\varepsilon_1 + 2\varepsilon_3)$ is the volumetric strain and $\varepsilon_q = \frac{2}{3}(\varepsilon_3 - \varepsilon_1)$ is the deviatoric strain. In classical plasticity, the direction $\mathbf{n}$ is specified by a yield surface $F(\sigma', \alpha)$ in which α defines the historical strain hardening parameter and unloading is always assumed to be elastic, (i.e., $H_u = \infty$). When associative behavior is assumed, the direction

$$\mathbf{n} = \frac{\frac{\partial F}{\partial \sigma'}}{\left(\frac{\partial F}{\partial \sigma'}^{\mathrm{T}} \frac{\partial F}{\partial \sigma'}\right)^{\frac{1}{2}}} \tag{4.30}$$

is defined by the unit normal to the yield surface and the necessity to ensure that $dF = 0$ during plastic deformation gives the plastic modulus H_L. Generalized plasticity [179] differentiates between loading and unloading during strain hardening and strain softening.

For a multiaxial problem, the most general description to distinguish between loading and unloading behavior is

$$\begin{aligned} d\sigma' &= \mathbf{D}^{\mathrm{L}} d\varepsilon, \text{ if } \mathbf{n}^{\mathrm{T}} d\sigma' > 0 \\ d\sigma' &= \mathbf{D}^{\mathrm{U}} d\varepsilon, \text{ if } \mathbf{n}^{\mathrm{T}} d\sigma' < 0 \end{aligned} \tag{4.31}$$

in the stress space is used. For stress increments along the plane t, i.e., when $\mathbf{n}^{\mathrm{T}} \mathbf{d}\sigma' = 0$ purely elastic deformation occurs. The elastic volumetric part of the strain increment can be obtained for virgin loading by an isotropic consolidation test of normal specimen by

$$d\varepsilon_v^e = \frac{1}{K} dp' = \frac{\kappa}{1+e} \frac{1}{p'} dp' \tag{4.32}$$

and

$$d\varepsilon_s^e = \frac{1}{G_0 \frac{p'_0}{p'}} dq \tag{4.33}$$

as the elastic deviatoric part of the strain increment.

Elastic and plastic volumetric strain together is written as

$$d\varepsilon_v = \frac{\lambda}{1+e} \frac{dp'}{p'}. \tag{4.34}$$

Therefore, the plastic volumetric part of the strain increment is

$$d\varepsilon_{\mathrm{v}}^{\mathrm{p}} = \frac{\lambda - \kappa}{1+e}\frac{dp'}{p'}. \tag{4.35}$$

Now, in general, if loading occurs for a stress change $d\boldsymbol{\sigma}'$, it is

$$d\boldsymbol{\varepsilon} = d\boldsymbol{\varepsilon}^{\mathrm{e}} + d\boldsymbol{\varepsilon}^{\mathrm{p}} = (\mathbf{D}_{\mathrm{e}})^{-\mathbf{1}} d\boldsymbol{\sigma}' + \left(\mathbf{D}_{\mathrm{p}}^{\mathrm{L}}\right)^{-\mathbf{1}} d\boldsymbol{\sigma}' = (\mathbf{D}_{\mathrm{e}})^{-\mathbf{1}} d\boldsymbol{\sigma}' + \frac{\mathbf{n}_{\mathrm{L}}\mathbf{n}^{\mathrm{T}}}{H_{\mathrm{L}}} d\boldsymbol{\sigma}' \tag{4.36}$$

and for unloading

$$d\boldsymbol{\varepsilon} = d\boldsymbol{\varepsilon}^{\mathrm{e}} + d\boldsymbol{\varepsilon}^{\mathrm{p}} = (\mathbf{D}_{\mathrm{e}})^{-\mathbf{1}} d\boldsymbol{\sigma}' + \left(\mathbf{D}_{\mathrm{p}}^{\mathrm{U}}\right)^{-\mathbf{1}} d\boldsymbol{\sigma}' = (\mathbf{D}_{\mathrm{e}})^{-\mathbf{1}} d\boldsymbol{\sigma}' + \frac{\mathbf{n}_{\mathrm{U}}\mathbf{n}^{\mathrm{T}}}{H_{\mathrm{U}}} d\boldsymbol{\sigma}'. \tag{4.37}$$

The tangent modulus matrix is defined for loading:

$$\left(\mathbf{D}^{\mathrm{L}}\right)^{-\mathbf{1}} = (\mathbf{D}_{\mathrm{e}})^{-\mathbf{1}} + \frac{\mathbf{n}_{\mathrm{L}}\mathbf{n}^{\mathrm{T}}}{H_{\mathrm{L}}} \tag{4.38}$$

and for unloading

$$\left(\mathbf{D}^{\mathrm{U}}\right)^{-\mathbf{1}} = (\mathbf{D}_{\mathrm{e}})^{-\mathbf{1}} + \frac{\mathbf{n}_{\mathrm{U}}\mathbf{n}^{\mathrm{T}}}{H_{\mathrm{L}}} \tag{4.39}$$

In equation (4.38) and (4.39), $\mathbf{n}_{\mathrm{U}}$ and $\mathbf{n}_{\mathrm{L}}$ are arbitrary unit tensors which are the directions of the plastic strain vector. The plastic constitutive relation has the general form

$$\mathbf{D}_{\mathrm{L/U}} = \mathbf{D}^{\mathrm{e}} - \frac{\mathbf{D}^{\mathrm{e}}\mathbf{n}_{\mathrm{L/U}}\mathbf{n}^{\mathrm{T}}\mathbf{D}^{\mathrm{e}}}{H_{\mathrm{L/U}} + \mathbf{n}^{\mathrm{T}}\mathbf{D}^{\mathrm{e}}\mathbf{n}_{\mathrm{L/U}}} \tag{4.40}$$

where $\mathbf{D}_{\mathrm{L/U}}$ is the elasto-plastic matrix (this formula is also applicable if the plastic modulus $H_{\mathrm{L/U}} \to 0$ as in ideal plasticity). The plastic modulus $H_{\mathrm{L/U}}$ has in classical plasticity the following form, when associative behavior is assumed $\mathbf{n}_{\mathrm{L}} = \mathbf{n}$

$$H_{\mathrm{L/U}} = \frac{\frac{\partial F}{\partial \alpha}\left(\frac{\partial \alpha}{\partial \varepsilon_{\mathrm{v}}^{\mathrm{p}}}\right)^{\mathrm{T}}\mathbf{n}}{\left(\left(\frac{\partial F}{\partial \boldsymbol{\sigma}'}\right)^{\mathrm{T}}\left(\frac{\partial F}{\partial \boldsymbol{\sigma}'}\right)\right)^{\frac{1}{2}}}, \tag{4.41}$$

with the direction $\mathbf{n}$ defined by the unit normal to the yield surface

$$\mathbf{n} = \frac{\frac{\partial F}{\partial \boldsymbol{\sigma}'}}{\left(\left(\frac{\partial F}{\partial \boldsymbol{\sigma}'}\right)^{\mathrm{T}}\left(\frac{\partial F}{\partial \boldsymbol{\sigma}'}\right)\right)^{\frac{1}{2}}}. \tag{4.42}$$

The plastic modulus depends on the plastic volumetric strain, which is defined for associative behavior by

$$d\varepsilon_{\mathrm{v}}^{\mathrm{p}} = -\mathbf{n}\mathbf{n}^{\mathrm{T}}\frac{d\boldsymbol{\sigma}'}{H_{\mathrm{L}}} = \frac{1}{H_{\mathrm{L}}}dp'. \tag{4.43}$$

For non-associative behavior, the plastic volumetric strain is defined by

$$d\varepsilon_{\mathrm{v}}^{\mathrm{p}} = -\mathbf{n}_{\mathbf{gL/U}}\mathbf{n}^{\mathrm{T}}\frac{d\boldsymbol{\sigma}'}{H_{\mathrm{L/U}}}. \tag{4.44}$$

Further details on the non-associative model are described in the subsection of the Mark I model.

Clay Model

The Clay Model [178] is founded on a critical state model which has an elliptical shape in the meridian plane and the yield criterion in the deviatoric plane is a rounded Mohr-Coulomb yield criterion (see, figure 4.10(a)). The yield surface of the CSM in classical plasticity is used as the bounding surface of the BSM. A yield surface is identical with the bounding surface when $\delta = 0$. Therefore, the bounding surface $F(\boldsymbol{\sigma}', \alpha) = 0$ has the following formulation:

$$\begin{aligned} F &= n^2\left(p' - \alpha_{\mathrm{c}}\right)^2 + 3\bar{\sigma}'^2 - n^2a^2 = 0 \\ \text{with } n &= \alpha_{\mathrm{c}}\frac{M}{a},\ \alpha_{\mathrm{c}} = \frac{p_{\mathrm{c}}}{R},\ M = \frac{6sin\phi}{3 - sin\phi sin3\theta},\ \bar{\sigma}'^2 = J_2 \\ a &= p_{\mathrm{c}} - \alpha_{\mathrm{c}} = p_{\mathrm{c}}\left(1 - \frac{1}{R}\right),\ R \geq 2,\ p' = -\sigma'_{\mathrm{m}} \end{aligned} \tag{4.45}$$

where p' is the first invariant of stress tensor but opposite in sign to I_1, θ the Lode angle and J_2 the second invariant of stress deviator tensor. The size of the bounding surface depends on α_{c}, therefore, on the preconsolidation pressure $p_{co}^{-\frac{1+e_0}{\lambda-\kappa}\varepsilon_{kk}^{\mathrm{p}}}$ which is determined with the aid of the plastic volumetric strain. In classical plasticity, therefore, in the CSM, it is assumed that ideal isotropic elasticity pertains in the interior of the yield surface with a bulk modulus K which depends on the mean effective stress σ'_{m} as

$$K = -\frac{1+e_0}{\kappa}\sigma'_{\mathrm{m}} \tag{4.46}$$

The shear modulus G can either be a constant value or depend on current stress state. The CSM in classical plasticity is incapable of predicting the behavior under cyclic or transient loads. Therefore, the concept of bounding surface was introduced.

But contrary to classical plasticity where unloading is always elastic, plastic behavior can now occur inside the bounding surface at a typical point P' (see, figure 4.10(b)) with the direction $\mathbf{n}_{\mathrm{L}}$ and the plastic modulus H_{L} which is defined at the »original« point P with the plastic modulus $H_{\mathrm{L}}^{\mathrm{CS}}$ and the direction $\mathbf{n}$. Therefore, the plastic modulus H_{L} is in case of reloading defined by

an interpolation rule [179]

$$H_{\mathrm{L}} = H_{\mathrm{L}}^{\mathrm{CS}} \left(\frac{\delta_0}{\delta_0 - \delta} \right)^{\gamma} \tag{4.47}$$
$$\mathbf{n}_{\mathrm{L}} \text{ at } P' = \mathbf{n} \textit{ at } P,$$

where δ and δ_0 are defined in figure 4.10(b). They depend on the size of the bounding surface and, therefore, on p, the preconsolidation pressure which depends on the plastic volumetric strain

$$H_{\mathrm{L}}^{\mathrm{CS}} = \frac{-\frac{\partial F}{\partial \varepsilon_{\mathrm{v}}^{\mathrm{p}}} \frac{\partial F}{\partial \sigma'_{\mathrm{m}}}}{\left(\frac{\partial F}{\partial \sigma'} \right)^{\mathrm{T}} \left(\frac{\partial F}{\partial \sigma'} \right)}. \tag{4.48}$$

If $\gamma = \infty$, $H_{\mathrm{L}} = \infty$ and $\delta = 0$ at all points of the interior surface, then the bounding surface is a yield surface like in a »standard« critical state model. For finite values of γ, the material behaves in a plastic manner; γ is usually chosen in a range between 5-20 and is determined by experiments. If plastic deformation during unloading should be taken into account, the subsequent formulation

$$H_{\mathrm{U}} = H_{\mathrm{L}}^{\mathrm{CS}} \left(\frac{\delta_0}{\delta} \right)^{\gamma_2} \tag{4.49}$$

can be used to determine the plastic unloading modulus. In the clay model, hardening was reached with purely volumetric strain, in the model which is named Mark I and which is an enhancement of the Clay Model hardening depends on the volumetric and deviatoric plastic strain components [178].

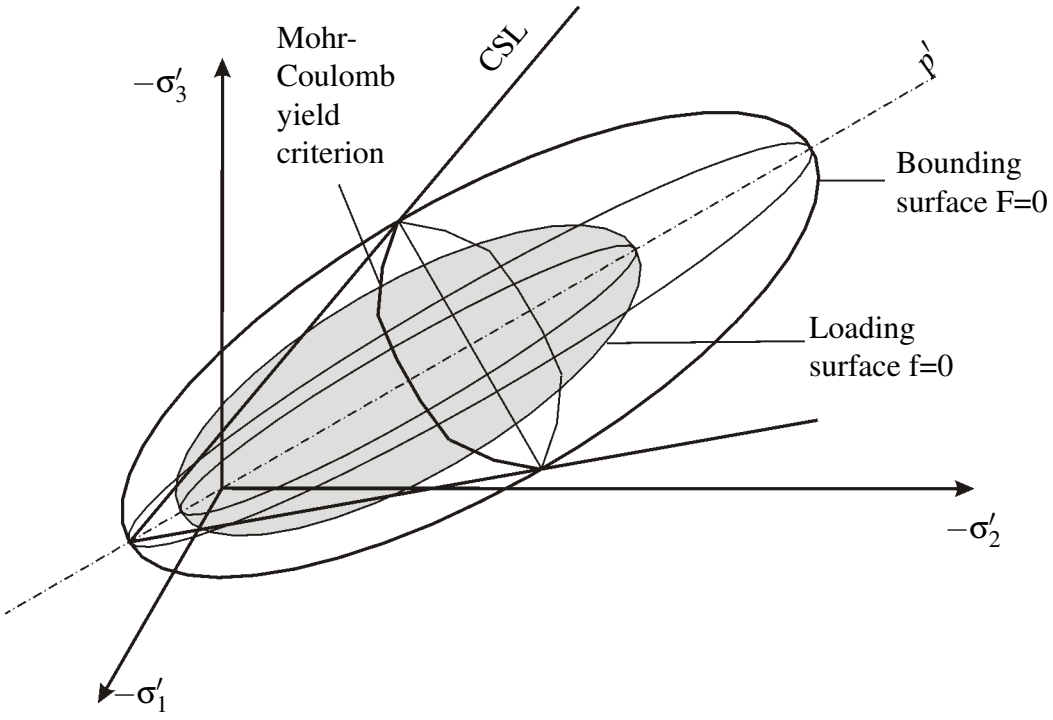

(a) The critical state yield surface for the clay model in the principal stress space [178]

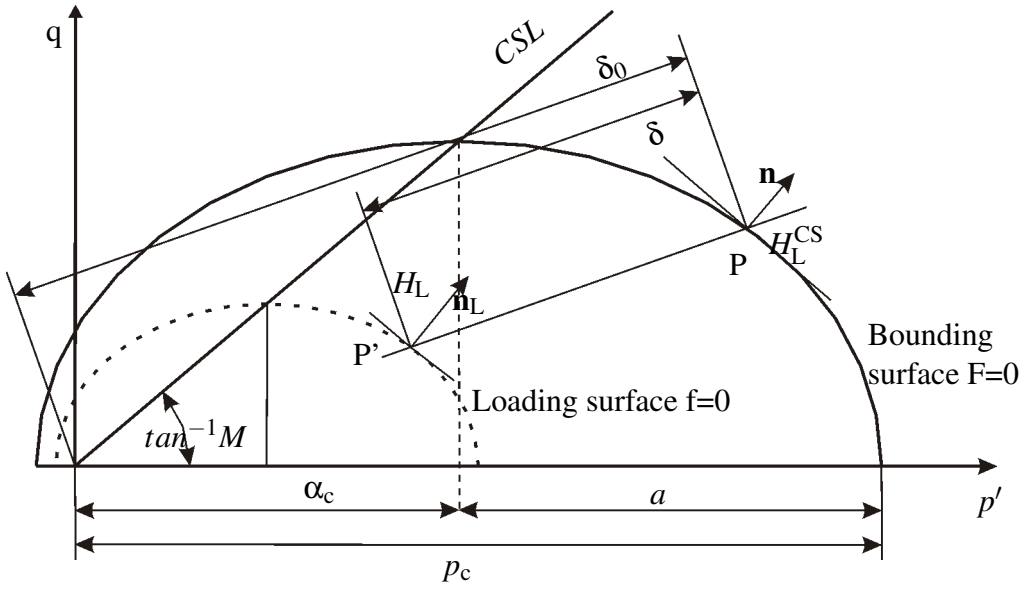

(b) Bounding surface in stress space

Figure 4.10: Bounding surface model for clay [178]

Mark I model

In the following, the extension from the Clay Model to the Mark I model (see, figure 4.11) will be described. In the paper from Pastor [117, 119], the typical behavior of granular material under a monotonic load is listed. These properties are [33]:

i Very loose sand liquefaction under undrained shearing, exhibiting a peak in deviatoric stress after which the strength reduces to zero while the pore pressure increases continuously. Non-associative plasticity is introduced, $\mathbf{n} \neq \mathbf{n}_{GL}$.

ii At the other end of the density range, peaks exist in deviatoric stress during drained shear of very dense sands. Therefore, the deviatoric plastic modulus will be introduced in the Mark III formulation to take into account for

- crossing of the critical state line $\left(\eta = M_{\mathrm{g}}\right)$ without immediately producing failure
- reproduction of softening
- residual condition taking place at CSL.

iii Undrained shearing of medium-loose to dense sands shows the intermediate characteristics. The Critical state line is reached and an upturn in the stress path is produced as soil changes from contractive to dilative behavior [119].

As mentioned before, generalized plasticity [179] differentiates between loading and unloading during strain hardening and strain softening. The sign of the projection of stress increment to a plane t is determined for strain hardening [117]:

$$\begin{aligned} d\sigma'^{\mathrm{T}} * \mathbf{n} &> 0 \text{ loading} \\ d\sigma'^{\mathrm{T}} * \mathbf{n} &< 0 \text{ unloading} \end{aligned} \tag{4.50}$$

and for strain softening:

$$\begin{aligned} d\sigma'^{\mathrm{T}} * \frac{\mathbf{n}}{H_{\mathrm{L}}} &> 0 \text{ loading} \\ d\sigma'^{\mathrm{T}} * \frac{\mathbf{n}}{H_{\mathrm{L}}} &< 0 \text{ unloading.} \end{aligned} \tag{4.51}$$

Therefore, the tangent modulus matrix is defined for loading

$$\left(\mathbf{D}^{\mathrm{L}}\right)^{-\mathbf{1}} = \left(\mathbf{D}_{\mathrm{e}}\right)^{-\mathbf{1}} + \frac{\mathbf{n_{gL}}\mathbf{n}^{\mathrm{T}}}{H_{\mathrm{L}}} \tag{4.52}$$

and for unloading

$$\left(\mathbf{D}^{\mathrm{U}}\right)^{-\mathbf{1}} = \left(\mathbf{D}_{\mathrm{e}}\right)^{-\mathbf{1}} + \frac{\mathbf{n_{gU}}\mathbf{n}^{\mathrm{T}}}{H_{\mathrm{L}}}. \tag{4.53}$$

In equations (4.52) and (4.53), $\mathbf{n_{gU}}$ and $\mathbf{n_{gL}}$ are unit tensors which are defined by experimental tests. The values of $\mathbf{n}$ and of the plastic modulus H_{L} are defined with the aid of interpolation

rules from the bounding surface. The bounding surface is of critical state type as shown in the clay formulation. Values of $\mathbf{n_{gL}}$ and $\mathbf{n_{gU}}$ can be defined directly: if they are different from $\mathbf{n}$, then the flow is non-associative and leads to non-symmetric tangent matrices $\mathbf{D}^{\mathrm{L}}$ and $\mathbf{D}^{\mathrm{U}}$. The direction of the unit normal $\mathbf{n_{gL}}$

$$\begin{aligned} \mathbf{n_{gL}} &= \frac{1}{\sqrt{1+d^2}}[d,s]^{\mathrm{T}} \\ &\text{with } s=1 \quad \text{when } \sigma'_1 < \sigma'_3 \text{ compression} \\ &\text{with } s=-1 \text{ when } \sigma'_1 > \sigma'_3 \text{ extension} \end{aligned} \tag{4.54}$$

is specified by the dilatancy. The dilatancy behavior of drained triaxial tests on loading of sand was investigated by Frossard [79]. The following assumption can be made: Elastic strains are compared to the plastic strains neglectable and the dilatancy is defined as

$$d = \frac{d\varepsilon_{\mathrm{v}}^{\mathrm{p}}}{d\varepsilon_{\mathrm{s}}^{\mathrm{p}}} = \frac{d\varepsilon_{\mathrm{v}}}{d\varepsilon_{\mathrm{s}}}, \tag{4.55}$$

also named ratio of volumetric to deviatoric strain, where the subscript v stands for volumetric strain and the subscript s for deviatoric strain.

Dilatancy is approximated by a linear function of the stress invariant ratio η

$$\begin{aligned} d_{\mathrm{g}} &= \left(1+\alpha_{\mathrm{g}}\right) * \left(M_{\mathrm{g}} - \eta\right) \\ &\text{with } \eta = \frac{q}{p'}, \end{aligned} \tag{4.56}$$

where α_{g} is a constant (the hardening parameter of the potential surface), the slope of the critical state line for 2D problems of the potential surface is $M_{\mathrm{g}} = (6ssin\phi)/(3s - sin\phi)$ (see, figure 4.11), and η is the stress ratio. This dilatancy law was proposed earlier by Nova and Wood [116]. When η is equal to M_{g}, the dilatancy of the soil is zero, no volumetric plastic strain occurs (but deviatoric plastic strain can occur). In this case, the dilatancy line can be named zero dilatancy line which is well known under the name critical state line or characteristic state line or phase transformation line. If $\mathbf{n}_{gL}$ is not already defined by equation (4.54), it can be defined also as normal to the shape of the plastic potential surface which is

$$G = q - M_{\mathrm{g}} p' \left(1 + \frac{1}{\alpha_{\mathrm{g}}}\right)\left(1 - \left(\frac{p'}{p'_{\mathrm{g}}}\right)^{\alpha_{\mathrm{g}}}\right). \tag{4.57}$$

In the equation above, p'_{g} is a size parameter and M_{g} is the slope of the CSL.

The definition for the yield or respectively the bounding surface is given with

$$F\left(\sigma', p_{\mathrm{c}}\right) = q - M_{\mathrm{f}} p' \left(1 + \frac{1}{\alpha_F}\left(1 - \left(\frac{p'}{p_{\mathrm{c}}}\right)^{\alpha_F}\right)\right); \tag{4.58}$$

with this formulation $H_{\mathrm{L}}^{\mathrm{CS}}$ and $\mathbf{n}$ can be defined. In the bounding surface, p_{c} is the isotropic preconsolidation pressure which depends on $\varepsilon_{\mathrm{v}}^{\mathrm{p}}$, i.e., $p_{\mathrm{c}} = p_{\mathrm{c}}\left(\varepsilon_{\mathrm{v}}^{\mathrm{p}}\right)$, while M_{f} and α_F are material

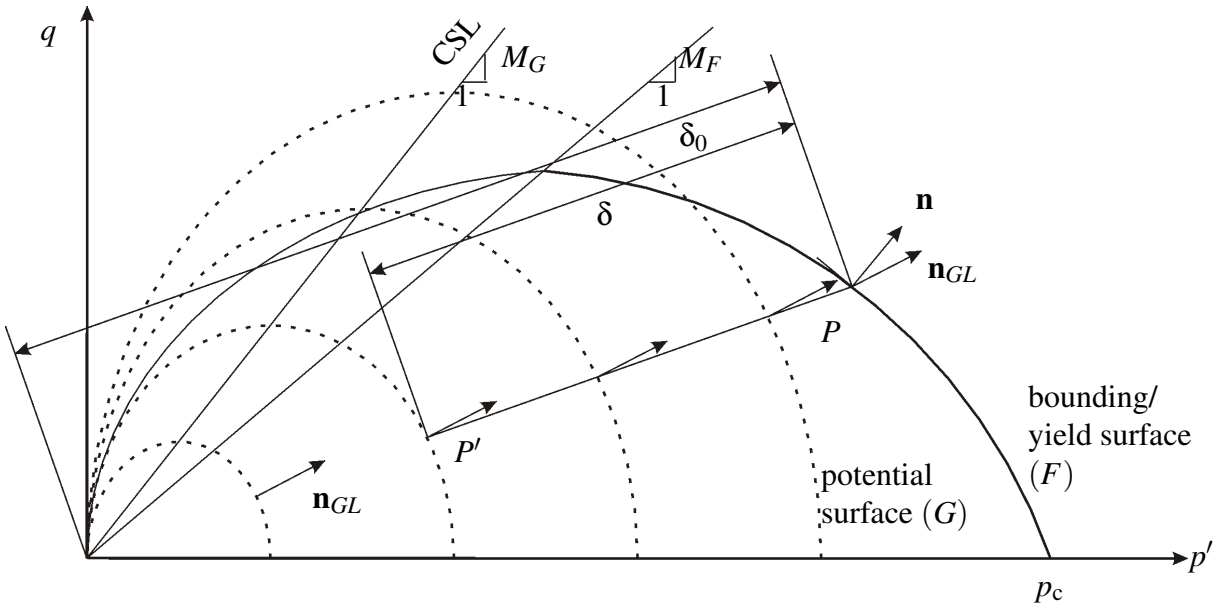

(a) Mark I model for medium/dense sand

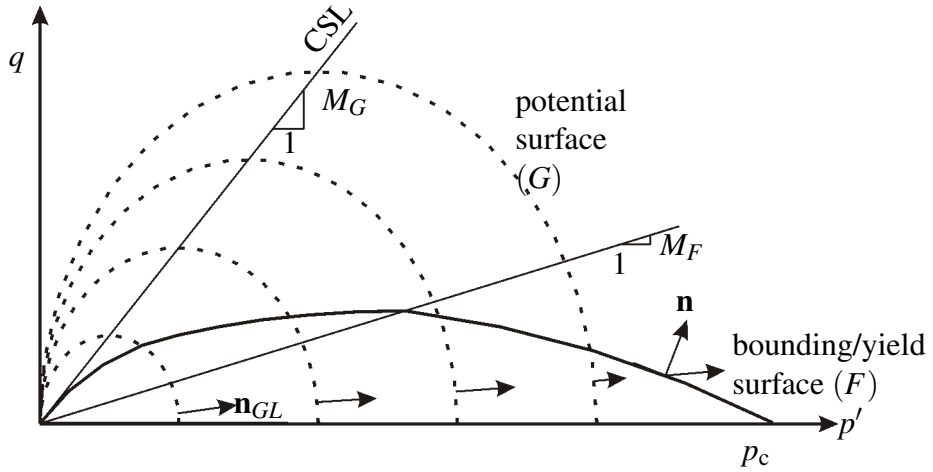

(b) Mark I model for loose sand

Figure 4.11: Yield (boundary) surface and plastic potential surface [117]

constants. The performance of the model depends on the ratio M_F/M_g which can sometimes be taken as D_R, where D_R is the relative density. The size of the bounding surface depends now on the volumetric and the deviatoric strain

$$\alpha = \varepsilon_p^v + f\left(|d\varepsilon_s^p|\right). \tag{4.59}$$

The isotropic preconsolidation pressure p_c represents the volumetric strain hardening behavior of the model. The second hardening parameter is the deviatoric strain which is specified by Wilde [168]

$$\frac{\partial p_c}{\partial\left(\int |d\varepsilon_s^p|\right)} = \beta_0\beta_1\left(\frac{\partial p_c}{\partial \varepsilon_v^p}\right)^{-\beta_0\int |d\varepsilon_s^p|}. \tag{4.60}$$

The volumetric hardening parameter

$$\frac{\partial p_c}{\partial \varepsilon_v^p} = \frac{p_c(1+e)}{\lambda-\kappa} \tag{4.61}$$

is expressed like in the standard CSM (see, equation (4.20)). Parameters λ and κ in the above expression are, respectively, the slopes of virgin loading and reloading branches of isotropic compression curves in sand, and e is the void ratio.

Plastic behavior can, as mentioned before, occur inside the bounding surface at a typical point P' (see, figure 4.11) with the direction $\mathbf{n_{GL}}$ and the plastic modulus H_L, which is defined at the 'original' point P with the plastic modulus H_L^{CS} and the direction $\mathbf{n}$. Here, the unit tensors $\mathbf{n} = \mathbf{n}^{CS}$ and $\mathbf{n}_{GL} = \mathbf{n}_{GL}^{CS}$ are assumed to be the same for points P and P' [180]. In anticipation of cyclic load, loading interpolation of plastic modulus H_L by the form [179]

$$H_L = H_L^{CS}\left(\frac{\delta_0}{\delta_0-\delta}\right)^{\gamma} \tag{4.62}$$

with the plastic modulus

$$H_L^{CS} = -\frac{\frac{\partial F}{\partial p_c}}{\left(\left(\frac{\partial G}{\partial \sigma'}\right)^T\left(\frac{\partial G}{\partial \sigma'}\right)\right)^{\frac{1}{2}}\left(\left(\frac{\partial F}{\partial \sigma'}\right)^T\left(\frac{\partial F}{\partial \sigma'}\right)\right)^{\frac{1}{2}}}\left(\frac{\partial p_c}{\partial \varepsilon_v^p}\frac{\partial G}{\partial p}+\frac{\partial p_c}{\partial \varepsilon_q^p}\frac{\partial G}{\partial q}\right). \tag{4.63}$$

For modeling of unloading, the generation of plastic volumetric strain has to be taken into account

$$
\begin{aligned}
d\varepsilon^{\mathrm{p}} &= \frac{1}{H_{\mathrm{u}}}\mathbf{n}_{\mathrm{gU}}\left(\mathbf{n}d\sigma'\right) \\
\text{with } \mathbf{n}_{\mathrm{gU}} &= \left(n_{\mathrm{gU1}}\, n_{\mathrm{gU2}}\right)^{\mathrm{T}} \\
n_{\mathrm{gU1}} &= -|n_{\mathrm{gL1}}| \\
n_{\mathrm{gU2}} &= -n_{\mathrm{gL2}} \\
\text{where } \mathbf{n}_{\mathrm{gL}} &= \left(n_{\mathrm{gL1}}\, n_{\mathrm{gL2}}\right)^{\mathrm{T}}.
\end{aligned}
\tag{4.64}
$$

The plastic unloading modulus is necessary to model the behavior of liquefaction and cyclic mobility and is defined as

$$
\begin{aligned}
H_{\mathrm{u}} &= H_{\mathrm{uo}}\left(\frac{\eta_{\mathrm{u}}}{M_{\mathrm{g}}}\right)^{-\gamma_{\mathrm{u}}} \text{ for } \left|\frac{\eta_{\mathrm{u}}}{M_{\mathrm{g}}} < 1\right| \\
H_{\mathrm{u}} &= H_{\mathrm{uo}} \text{ for } \left|\frac{\eta_{\mathrm{u}}}{M_{\mathrm{g}}} \geq 1\right| \\
\eta_{\mathrm{u}} &= \left(\frac{q}{p'}\right)_{\mathrm{u}}
\end{aligned}
\tag{4.65}
$$

with η_{u} the unloading stress ratio, selected at the point where unloading occurs. H_{UO} and γ_{U} are specified material constants which needs to be determined. In this formulation, H_{U} is not interpolated like H_{L} from any bounding surface. The law for the plastic unloading modulus takes into account the fact that the plastic volumetric strain increases during unloading more if η_{U} approaches M_{g}. This effect has not to be taken into account for loose sand, because its stress paths are far away form the CSL.

Mark III model

In the Mark III model, the following modifications are considered [118, 186]: The direction of plastic flow $\mathbf{n}_{\mathrm{gL}}$ can be determined in the triaxial space by similar procedures as used in the Mark I model (see, equation (4.54)) $\mathbf{n}_{\mathrm{gL}}^{\mathrm{T}} = \left(n_{\mathrm{gv}}, n_{\mathrm{gs}}\right)$

$$n_{\mathrm{gv}} = \frac{d_{\mathrm{g}}}{\left(1 + d_{\mathrm{g}}^2\right)^{\frac{1}{2}}} \tag{4.66}$$

$$n_{\mathrm{gs}} = \frac{1}{\left(1 + d_{\mathrm{g}}^2\right)^{\frac{1}{2}}} \tag{4.67}$$

For sands, the non-associative flow rule is necessary for modelling unstable behaviour within the hardening region and the direction $\mathbf{n}$ should be different from $\mathbf{n}_{\mathrm{gL}}$ where $\mathbf{n}^{\mathrm{T}} = (n_{\mathrm{v}}, n_{\mathrm{s}})$ with

$$\begin{aligned} n_{\mathrm{v}} &= \frac{d_{\mathrm{f}}}{\left(1 + d_{\mathrm{f}}^2\right)^{\frac{1}{2}}} \\ n_{\mathrm{s}} &= \frac{1}{\left(1 + d_{\mathrm{f}}^2\right)^{\frac{1}{2}}} \\ \text{with} \quad d_{\mathrm{f}} &= (1+\alpha)\left(M_{\mathrm{f}} - \eta\right) \\ \text{and} \quad M_{\mathrm{g}} &= \frac{6 sin\phi}{3 - sin\phi sin3\theta}. \end{aligned} \tag{4.68}$$

The plastic modulus is defined now as

$$H_{\mathrm{L}} = H_0 p' H_{\mathrm{f}} \left(H_{\mathrm{v}} + H_{\mathrm{s}}\right) H_{\mathrm{DM}} \tag{4.69}$$

where

$$\begin{aligned} H_{\mathrm{f}} &= \left(1 - \frac{q}{p'}\frac{1}{\eta_{\mathrm{f}}}\right)^4 \\ n_{\mathrm{f}} &= \left(1 + \frac{1}{\alpha_{\mathrm{f}}}\right) M_{\mathrm{f}} \\ H_0 &= \frac{1+e}{\lambda - \kappa} \\ H_{\mathrm{v}} &= \left(1 - \frac{q}{p'}\frac{1}{M_{\mathrm{g}}}\right) \\ H_{\mathrm{s}} &= \beta_0 \beta_1^{(-\beta_0 \xi)} \text{ with } \xi = \int \left|d\varepsilon_{\mathrm{s}}^{\mathrm{p}}\right| \end{aligned} \tag{4.70}$$

where β_0, β_1 are model parameters, and ξ is the cumulative deviatoric plastic strain. In the equation (4.69), the plastic modulus plays an important rule from transition from hardening to softening regions. If a stress path is considered under a drained triaxial test, during the first part

of the stress path, both H_v and H_s are positive and monotonously decreasing. At the critical state line, $\eta = M_g$, H_v becomes zero, but H_s is still positive. If the process continues, a moment arrives at which H_v and H_s are zero with $\eta_p > M_g$. If the test is run under displacement control, H_s is decreased and the plastic modulus becomes negative. The soil has entered the softening regime, and the deviatoric stress will decrease until it attains a limit value at M_g [120, 186]. To model the soil behavior under reloading, a discrete memory factor is introduced corresponding to the parameter for the Mark I model in equation (4.47). For virgin loading, the discrete memory factor is set to a value of unity. The plastic modulus H_{DM} is a discrete memory factor for reloading which is defined

$$H_{DM} = \left(\frac{\eta_{max}}{\eta} \right)^{\gamma^{DM}}, \tag{4.71}$$

where γ^{DM} is a degradation parameter, and η_{max} is the largest value of the stress ratio. When a higher stress ratio is reached by reloading, less plastic deformation will occur in the reloading process [177, 34].

5 Iterative Coupling of BEM and FEM

To simulate ground liquefaction, the advantages of two different analysis tools, the Finite Element Method (FEM) and the Boundary Element Method (BEM) are required. Each method has their special field of application. The adequate analysis tool for problems which involves non-linearity in domains of finite dimensions is the FEM, while the BEM is very well suited for linear semi-infinite and infinite domains. Another important advantage of the BEM is its accuracy in predicting high gradients. If the problem of interest, i.e., ground liquefaction, includes local non-linearity only in a portion of the infinite domain, then the region should be subdivided into a near-field (using FEM) and a far-field (using BEM). Thanks to this subdivision, the most suited solution technique of each of then can be employed. Therefore, the combination of the FEM with the BEM within a single computational model allows to benefit from the advantages of both methods.

In conventional coupling methods of FEM with BEM, the equations for the FEM and the BEM are assembled into a single, global, equation system. The idea of coupling FEM and BEM was introduced by Zienkiewicz et al. [189]. An overview about conventional coupling procedures is given by Beskos [10, 12, 13].

However, in domain decomposition method, each sub-domain is solved by the BEM or by the FEM. Hence, the assembly and solution of a global coupled equation system is avoided. This is the main advantage of the domain decomposition method. Every equation system of the FEM or of the BEM can be solved by specialized solver, e.g., the system matrix of the FEM has desirable features namely, symmetry, sparsity, and bandedness, on a less positive note is that the system matrix of BEM is non-symmetric. Consequently, an appropriate choice of the solvers saves computational time.

Further, if the FEM is used for a non-linear domain, a Newton-Raphson iteration has to be considered, which includes a renewal of the system matrix at different iterative steps caused to non-linearity, however, the BE systems of equations is not affected by this renewal. In the domain decomposition method separate computing for each sub-domain and a successive renewal of the variables on the interface of both sub-domain are performed to reach final convergence.

One of the most recent methods of coupling the BEM with the FEM are the domain decomposition methods. The basic idea of these approach is close to the statement made by Cruse et al. [44], that a major conclusion drawn from experience with current coupling methods is that it is necessary to preserve the nature of the BEM, rather than to force it into a finite element format. In the method of domain decomposition, the combination of the coefficient matrices of the FEM and the BEM subdomains, as required in conventional coupling methods, is not necessary. Separate computing of each subdomain and successive renewal of the variables on the interface of both subdomains are performed to reach final convergence. Existing domain decomposition methods [88, 103, 76] set the natural boundary conditions on the interface which is between the FEM and the BEM subdomain. Unfortunately, these methods are not applicable when only Neumann boundary conditions are preserved on the whole external boundary of the

FEM subdomain. This would lead to singularity of the matrices and to non-unique solution. More general than standard domain decomposition are interface relaxation methods which are presented by Rice [135].

In the interface relaxation method for linear and non-linear elastic material behavior, the displacement values calculated by a FE run would be used as prescribed boundary conditions for the BE run. The local non-linear region, which is liquefying, would be modeled entirely with finite elements and the tractions at the interface to the BE region would be calculated at every nodal point. A corrective term, the relaxation parameter is employed at the iteration procedure in every time step on the calculated Dirichlet boundary conditions until convergence is achieved. The BE mesh restricted to the region around the liquefying area can be used with the FE values of the tractions as boundary conditions. The positions of the nodal points of the BE mesh must be identical to those of the corresponding nodal points; otherwise, some form of extrapolation is necessary.

Coupling the FE and the BE method iteratively is advantageous (see, Eleithy et al. [70, 71, 72]) because it avoids to couple the banded matrices of the FE system with the not banded and fully populated BE matrices. This means that the optimized solvers can still be employed for the FEM matrices. If in the conventional coupling method within the FE subdomain occurs some nonlinearity, which is the case in ground liquefaction, a big coupled system of equations would have to be solved in each step of iteration process for nonlinearity, i.e., a few times within each time step. This effect can be avoided by using interface relaxation methods because, there, every subdomain is modeled with the appropriate analysis tool. An algorithm for coupling nonlinearity FEM with BEM was presented by Elleithy [75, 165]

Interface Relaxation algorithm for poroelasticity For simulation of ground liquefaction, a interface relaxation algorithm for poroelasticity is required. Therefore, the Dirichlet-Neumann domain decomposition with initial Dirichlet data assumed on the FEM/BEM interface presented in [71, 165] for coupling linearity and nonlinearity is being enhanced for coupling of poroelastic FEM with BEM subdomains in this thesis.

To facilitate the development of the iterative algorithm, first consider the boundary value problem for a linearly poroelastic body Ω subjected to external loadings. The body is decomposed arbitrarily into two subdomains Ω_1 and Ω_2. Each subdomain can be treated using either the FEM or the BEM, i.e., the equation (2.12a) and (3.27) are used, respectively. It is required that the locations of the nodal points of both subdomains match along the interface. The proposed algorithm is based on the sequential Dirichlet-Neumann method with single relaxation, which has been investigated by [70, 71].
FEM: Employing the u_i^s-p-formulation of the Finite Element Method (equation (2.12a)), the equation of dynamic equilibrium can be written as

$$\begin{bmatrix} \mathbf{M}^{\mathrm{F}} & \mathbf{0} \\ \mathbf{0} & \mathbf{0} \end{bmatrix} \begin{bmatrix} \ddot{\bar{\mathbf{u}}}^{\mathrm{F}} \\ \mathbf{0} \end{bmatrix} + \begin{bmatrix} \mathbf{0} & \mathbf{0} \\ \mathbf{Q}^{\mathrm{F}\mathrm{T}} & \mathbf{S}^{\mathrm{F}} \end{bmatrix} \begin{bmatrix} \dot{\bar{\mathbf{u}}}^{\mathrm{F}} \\ \dot{\bar{\mathbf{p}}}^{\mathrm{F}} \end{bmatrix} + \begin{bmatrix} \mathbf{K}^{\mathrm{F}} & -\mathbf{Q}^{\mathrm{F}} \\ \mathbf{0} & \mathbf{H}^{\mathrm{F}} \end{bmatrix} \begin{bmatrix} \bar{\mathbf{u}}^{\mathrm{F}} \\ \bar{\mathbf{p}}^{\mathrm{F}} \end{bmatrix} = \begin{bmatrix} \mathbf{f}^{\mathrm{t,F}} \\ \mathbf{f}^{\mathrm{q,F}} \end{bmatrix} \tag{5.1}$$

where the upper right index F marks the FEM subdomain, with $\mathbf{M}^{\mathrm{F}}$ mass matrix, $\mathbf{Q}^{\mathrm{F}}$ coupling matrix, $\mathbf{S}^{\mathrm{F}}$ compressibility matrix, $\mathbf{K}^{\mathrm{F}}$ stiffness matrix, $\mathbf{H}^{\mathrm{F}}$ permeability matrix, $\mathbf{f}^{\mathrm{t,F}}$ external force at the boundary and $\mathbf{f}^{\mathrm{q,F}}$ flux at the boundary, $\bar{\mathbf{u}}^{\mathrm{F}}$ is the vector of nodal displacements,

$\dot{\bar{\mathbf{u}}}^{\mathrm{F}}$ is the vector of nodal velocities, $\ddot{\bar{\mathbf{u}}}^{\mathrm{F}}$ is the vector of nodal accelerations, $\bar{\mathbf{p}}^{\mathrm{F}}$ is the vector of pore pressure and $\dot{\bar{\mathbf{p}}}^{\mathrm{F}}$ is the vector of pore pressure rate. BEM equation (3.27) may be written in matrix notation

$$\begin{bmatrix} \mathbf{T}^{\mathrm{s}} & \mathbf{Q}^{\mathrm{s}} \\ \mathbf{T}^{\mathrm{f}} & \mathbf{Q}^{\mathrm{f}} \end{bmatrix} \begin{bmatrix} \mathbf{u}^{\mathrm{B}} \\ \mathbf{p}^{\mathrm{B}} \end{bmatrix} = \begin{bmatrix} \mathbf{U}^{\mathrm{s}} & \mathbf{P}^{\mathrm{s}} \\ \mathbf{U}^{\mathrm{f}} & \mathbf{P}^{\mathrm{f}} \end{bmatrix} \begin{bmatrix} \mathbf{t}^{\mathrm{B}} \\ \mathbf{q}^{\mathrm{B}} \end{bmatrix} \tag{5.2}$$

where the upper right index B marks the BEM subdomain, see (3.27) with U, T, P, Q, fundamental solutions for displacement, traction, pore pressure and flux and $\bar{\mathbf{u}}^{\mathrm{B}}$ vector of nodal displacements, $\bar{\mathbf{p}}^{\mathrm{B}}$ vector of pore pressure, $\bar{\mathbf{t}}^{\mathrm{B}}$ vector of nodal tractions and $\bar{\mathbf{q}}^{\mathrm{B}}$ vector of nodal flux. The coupling of the subdomain is ensured by imposing the appropriate equilibrium and compatibility conditions at the interface boundaries. In the proposed method, these conditions are formulated as equilibrium of forces and flux at the interface node, and compatibility of displacements and pore pressure.

The following notation is going to be used in the following iterative coupling procedure, $\mathbf{f}^{\mathrm{t,F}}_{i(n)}$ where the lower left index i marks the time step and the lower right index n marks the iterative step. The upper left index t, q, u or p marks the traction, flux, displacement or pore pressure and the upper right index F or B the FEM or the BEM subdomain. The algorithm shown in figure 5.1 summarizes the iterative coupling procedure being used. At the interface of the BEM and FEM subdomain the equation of equilibrium for the tractions

$$\mathbf{f}^{\mathrm{t,F}}_{i(n)} + \mathbf{M}\mathbf{t}^{\mathrm{B}}_{\mathbf{i}} = \mathbf{0} \tag{5.3}$$

and for the flux

$$\mathbf{f}^{\mathrm{q,F}}_{i(n)} + \mathbf{M}\mathbf{q}^{\mathrm{B}}_{\mathbf{i}} = \mathbf{0} \tag{5.4}$$

must be fulfilled, where M is a converting matrix, which depends on the interpolation functions used to represent tractions and flux on the interface.

The compatibility equation for the displacements at the interface nodes

$$\mathbf{u}^{\mathrm{F}}_{i(n)} = \mathbf{u}^{\mathrm{B}}_{i(n)} \tag{5.5}$$

and for the pore pressure at the interface nodes

$$\mathbf{p}^{\mathrm{F}}_{i(n)} = \mathbf{p}^{\mathrm{B}}_{i(n)} \tag{5.6}$$

has also to be satisfied.

Iterative coupling algorithm The proposed algorithm is based on the sequential Schwarz Dirichlet Neumann method with single relaxation which has been developed by Elleithy and Tanaka for linear-elastic analysis [71] and with a second relaxation parameter for the Neumann Dirichlet method by von Estorff [165]. In the present work, however, the coupling of the fluid of the FEM subdomain with the BEM subdomain is introduced additionally. Therefore, a third and a fourth relaxation parameter is required. The different relaxation parameters are set as

Time-step loop

Repeat until convergence achieved.

Set initial values $\mathbf{u}^{\mathrm{F}}_{i(n)}$ and $\mathbf{p}^{\mathrm{F}}_{i(n)}$ at the interface at the Ω_1 subdomain

Solve the FE problem. Obtain the nodal forces and the integrated flux at the interface: $\mathbf{f}^{\mathrm{t,F}}_{i(n)}$, $\mathbf{f}^{\mathrm{q,F}}_{i(n)}$.

Use the equilibrium condition for the tractions $\mathbf{f}^{\mathrm{t,F}}_{i(n)} + \mathbf{M}\mathbf{t}^{\mathrm{B}}_{i} = \mathbf{0}$ and for the flux $\mathbf{f}^{\mathrm{q,F}}_{i(n)} + \mathbf{M}\mathbf{q}^{\mathrm{B}}_{i} = \mathbf{0}$

Adoption of a relaxation parameter γ and δ in order to ensure and/or speed up convergence for the tractions: $\mathbf{t}^{\mathrm{B}}_{i(n+1)} = (1-\gamma)\,\mathbf{t}^{\mathrm{B}}_{i(n)} - \gamma\mathbf{t}^{\mathrm{F}}_{i(n)}$ and for the flux: $\mathbf{q}^{\mathrm{B}}_{i(n+1)} = (1-\delta)\,\mathbf{q}^{\mathrm{B}}_{i(n)} - \delta\mathbf{q}^{\mathrm{F}}_{i(n)}$.

Apply $\mathbf{t}^{\mathrm{B}}_{i(n)}$ and $\mathbf{q}^{\mathrm{B}}_{i(n)}$ and solve the BE problem. Obtain the displacement and the pore pressure at the interface: $\mathbf{u}^{\mathrm{B}}_{i(n)}$ and $\mathbf{p}^{\mathrm{B}}_{i(n)}$

Check for convergence

yes

Exit loop

no

Adoption of a relaxation parameter α and β in order to ensure and/or speed up convergence for the displacements: $\mathbf{u}^{\mathrm{F}}_{i(n+1)} = (1-\alpha)\,\mathbf{u}^{\mathrm{F}}_{i(n)} + \alpha\mathbf{u}^{\mathrm{B}}_{i(n)}$ and for the pore pressure: $\mathbf{p}^{\mathrm{F}}_{i(n+1)} = (1-\beta)\,\mathbf{p}^{\mathrm{F}}_{i(n)} + \beta\mathbf{p}^{\mathrm{B}}_{i(n)}$.

Start again

Actualization (and impression) of results related to the FEM.

End of calculation

Figure 5.1: Algorithm for the iterative coupling of BEM/FEM

constant values for all iterations. The optimal value may be obtained by experimenting with different values, as relaxation parameters for the displacement and the flux a value of 0.6 is a good choice. Thus, a sequential Dirchlet-Neumann method for poroelastic material has been obtained. Moreover, the method has also been applied to the coupling of non-linear poro FEM subdomain with poroelastic BEM subdomain.

Convergence criteria When an iterative solution procedure is used, appropriate identification of convergence is essential. In the present study, two different convergence criteria are employed, which will be outlined in the following. The first of the convergence criteria is based on a displacement increment measure and is given by

$$\frac{||\mathbf{u}^{\mathrm{B}}_{i(n+1)} - \mathbf{u}^{\mathrm{B}}_{i(n)}||}{||\mathbf{u}^{\mathrm{B}}_{i(n+1)}||} < \varepsilon_{\mathrm{u}} \tag{5.7}$$

and the second criterion is based on the pore pressure increment measure:

$$\frac{||\mathbf{p}^{\mathrm{B}}_{i(n+1)} - \mathbf{p}^{\mathrm{B}}_{i(n)}||}{||\mathbf{p}^{\mathrm{B}}_{i(n+1)}||} < \varepsilon_{\mathrm{p}}. \tag{5.8}$$

Convergence is assumed to be achieved if criterion (5.7) and criterion (5.8) are satified. In all the examples presented hereafter, as convergence tolerance $\varepsilon_{\mathrm{u}} = 1.0 \cdot 10^{-4}$ and $\varepsilon_{\mathrm{p}} = 0.5$ were chosen. The convergence characteristics of the sequential Dirchlet-Neumann FEM-BEM iterative coupling method was studied extensively by Elleithy and co-workers [67, 70]. The initial guess of interface displacements does not influence the existence of convergence [67, 70]. Convergence depends on the mesh density of the subdomains, the specified types of boundary conditions, and the geometrical as well as material properties. Most importantly, it depends on the selection of the relaxation parameter. It seems natural that these findings can be transferred to the algorithm for poroelastic media, proposed in this thesis. Moreover, the choice of the analysis methods for the subdomains, as well as the choice of the respective time step durations, may also influence the convergence behavior.

Finally, it should be mentioned that the employment of the relaxation substep for the tractions seems to be of no significant advantage in the linear elastic calculations, whereas the relaxation substep for the flux is significant and the relaxation parameter for the pore pressure seems to improve the convergence characteristics for the poroelastic case of the algorithm.

5.1 Numerical studies

In order to validate the proposed poroelastic iterative coupling algorithm, the following problems are investigated.

- First, the iterative FEM-BEM coupling routine is used for the linear-elastic case and validated with the results from a pure FEM calculation and a pure BEM calculation of a 2-d column. Here, the iterative coupling algorithm is validated for the *linear-elastic* case in a 2-d example.
- Second, the iterative FEM-BEM coupling routine is used for a one-dimensional (1-d) poroelastic column and validated with the results from a pure poroelastic FEM calculation and a pure BEM calculation. In this example, the proposed iterative coupling algorithm is validated for the *poroelastic* case in *1-d*.
- Third, the iterative FEM-BEM coupling routine is used for a two-dimensional (2-d) poroelastic halfspace and validated with the results from a pure poroelastic 2-d FEM and/or 2-d BEM calculation. The validation for a *2-d poroelastic* case of the proposed iterative coupling algorithm is shown here.
- Fourth, the influence of the *spatial discretization* and the influence of different *time step size* for the poroelastic case in the investigated halfspace is studied. The purpose of this investigation is to check the effect of the time step size and of the loading rate.
- Fifth, the iterative FEM-BEM coupling routine is tested for a 2-d poroplastic (FEM)-poroelastic (BEM) halfspace and compared with another test run where the same poroplastic FEM area is surrounded by a poroelastic FEM strip and the poroelastic (BEM) halfspace. Here, the iterative coupling algorithm is verified for *poroplastic* material behavior.
- Sixth, for different input sets of material data, the behavior of the poroplastic FEM area in the coupled 2-d halfpsace is examined.
- Seventh, a concrete dyke which is lying on the poroplastic FEM subdomain is supplied to the input of an earthquake load.

5.1.1 Linear-elastic 2-d column

To demonstrate the validity of the iterative coupling algorithm, a linear elastic, homogeneous isotropic two-dimensional column shown in figure 5.2 is analyzed and compared with the results from a pure FEM calculation and a pure BEM calculation of a 2-d column. The problem geometry and the material data of the 2-d column is shown in figure 5.2. The displacement of the column of 10 m (height) times 5 m (width) is fixed in x- and y- direction on one end and excited at the FEM side by tractions according to a sinusoidal function with a period of 20 s. The remaining surfaces are traction free. The BEM model consists for the uncoupled case of 30 nodes and 30 linear elements, whereas the uncoupled case of the FEM model is discretized

with 66 nodes and 50 quadrilateral linear elements. The discretized boundary of the BEM model for the coupled case has 20 nodes and 20 linear elements and the FEM mesh consists of 36 nodes and 25 quadrilateral linear elements. In every model, the mesh length is 1 m .

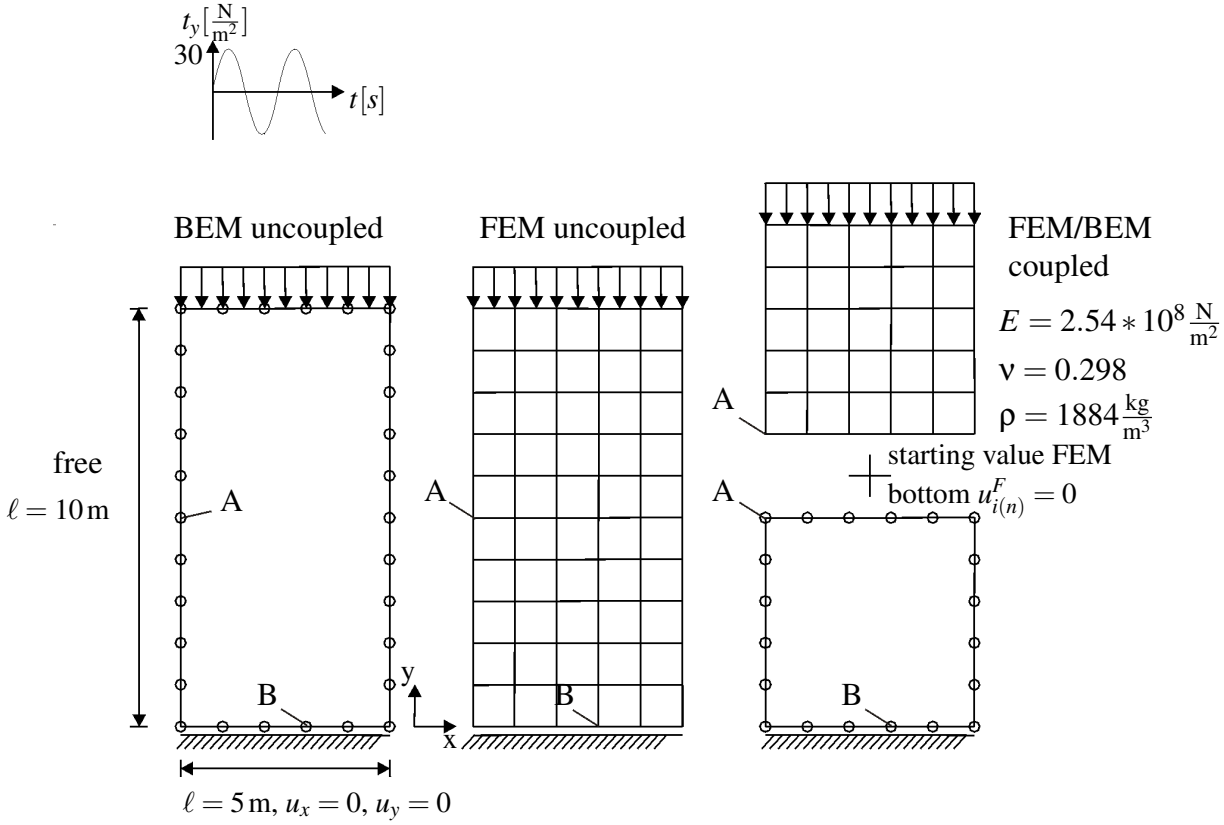

Figure 5.2: 2-d column elastic: Geometry, boundary conditions, discretization of uncoupled BEM, uncoupled FEM, coupled FEM-BEM

For all three meshes, the displacements and the tractions at the corner of the interface point A and at the edge close to the bearing point B is plotted versus time in figure 5.3. The results for the displacement as well as for the traction are in excellent agreement with the solution of the uncoupled FEM mesh and the uncoupled BEM mesh.

5.1.2 Poroelastic 1-d column

In a second step, the iterative FEM-BEM coupling routine is used for a one dimensional poroelastic column and validated with the results from a pure poroelastic FEM calculation and a pure poroelastic BEM calculation. A 1-d column of length 10 m, as sketched in figure 5.4, is considered. For the uncoupled case, the BEM model is discretized with 30 nodes and 30 linear elements. The uncoupled FEM model has 66 nodes and 50 quadrilateral linear elements. For the coupled case, the BEM model consists of 20 nodes and 20 linear elements and the FEM model consists of 36 nodes and 25 quadrilateral linear elements. The mesh length is 1 m .

(a)

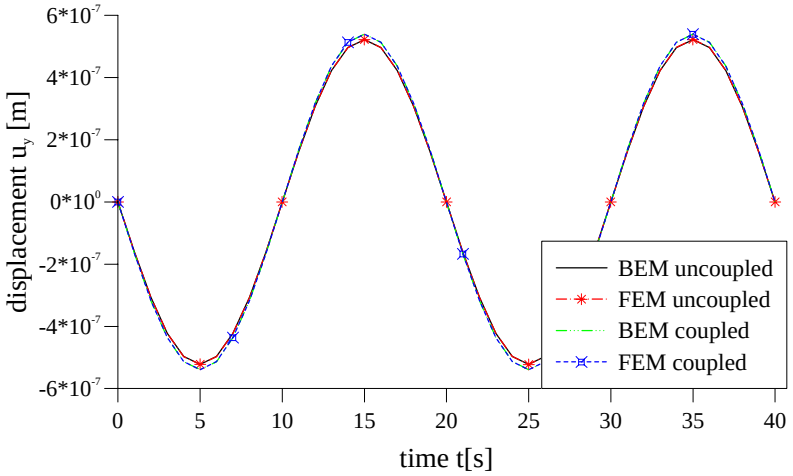

(a) u_y at point A

(b)

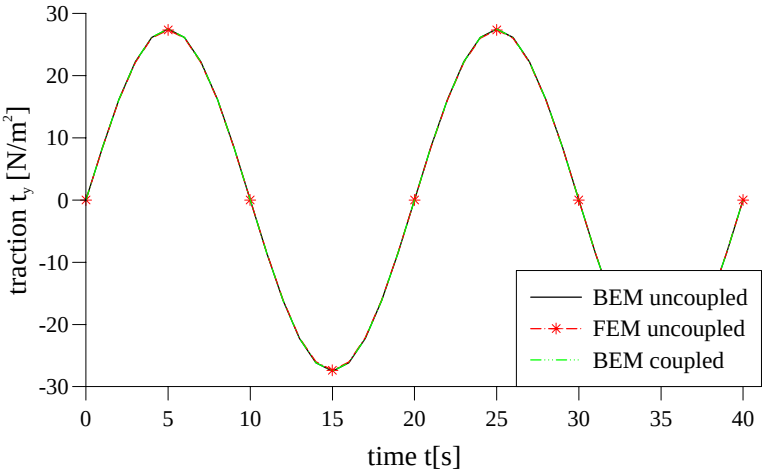

(b) t_y at point B

Figure 5.3: Displacement u_y and traction t_y of the elastic 2-d column (discretization, see, figure 5.2)

It is assumed that the Dirichlet boundary conditions are fixed at the bottom. At the top, Neumann boundary conditions are imposed. The side walls have a constraint displacement in x-direction and are impermeable. Hence, the displacements normal to the surface are zero and the column is otherwise free to slide only parallel to the wall. Due to these restrictions, the 2-d continuum is reduced to a 1-d continuum with the only degree of freedom in y-direction.

Two different load cases with different material data (see, table 5.1 and the discretization, see, figure 5.4) are investigated. Under CASE I, a nearly incompressible material [95] (coarse sand) was chosen. This material was excited on the FEM side at the top by first a linear increasing, later constant influx q of $-1 \cdot 10^{-5}\,\mathrm{m/s}$. A time step width of 1 s was applied. For CASE II, a more compressible soil was subjected to a stress load which first increased linearly and had later a constant value of $-30\,\mathrm{N/m^2}$.

Table 5.1: Material data of CASE I, CASE II, CASE III soil

	$E[\frac{\mathrm{N}}{\mathrm{m}^2}]$	ν	$\rho\,[\frac{\mathrm{kg}}{\mathrm{m}^3}]$	$\rho_\mathrm{f}\,[\frac{\mathrm{kg}}{\mathrm{m}^3}]$	ϕ	$K_\mathrm{s}\,[\frac{\mathrm{N}}{\mathrm{m}^2}]$	$K_\mathrm{f}\,[\frac{\mathrm{N}}{\mathrm{m}^2}]$	α	$\kappa_\mathrm{f}\,[\frac{\mathrm{m}}{\mathrm{s}}]$
I	$2.544 \cdot 10^8$	0.29	1884	1000	0.48	$1.1 \cdot 10^{10}$	$3.3 \cdot 10^9$	0.98	$3.48 \cdot 10^{-5}$
II	$2.544 \cdot 10^8$	0.29	1884	1000	0.48	$4.4 \cdot 10^8$	$3.3 \cdot 10^9$	0.52	$3.48 \cdot 10^{-5}$
III	$2.544 \cdot 10^8$	0.29	1884	1000	0.48	$4.4 \cdot 10^8$	$3.3 \cdot 10^8$	0.52	$3.48 \cdot 10^{-5}$

In figure 5.5(a), the results for the coupled FEM/BEM column, material data and load of CASE I, are compared for the flux with the uncoupled FEM mesh at the interface of the column at point B, and, supplementary, the flux is compared at point C, on the bottom of the column. Next, the pore pressure is compared at point A, at the top of the column, and at point B, at the interface of the column, with the results of the uncoupled FEM mesh (see, figure 5.5(b)). The results for the flux and for the pore pressure are in good agreement with the solutions of the uncoupled FEM mesh and the uncoupled BEM mesh.

The results for CASE II for flux and pore pressure with higher compressible material and under a constant stress load is depicted versus time in figure 5.6. The coupled poroelastic output for the flux and the pore pressure matches very well the output of the uncoupled poroelastic calculation.

5.1.3 Poroelastic 2-d halfspace

The displacement and the pore pressure in a poroelastic FEM-BEM coupled halfspace (mesh I and mesh II) will be investigated and compared with the results from a pure poroelastic 2D BEM calculation and a pure FEM calculation of a 30 m x 30 m area. The pure FEM mesh comprises 900 quadrilateral elements on 961 nodes (discretization, see, figure 5.12). The bottom of the FEM mesh is fixed and impermeable, i.e., with flux assumed to be zero. The sides are impermeable and the displacements normal to the sides are constraint. The top of the FEM

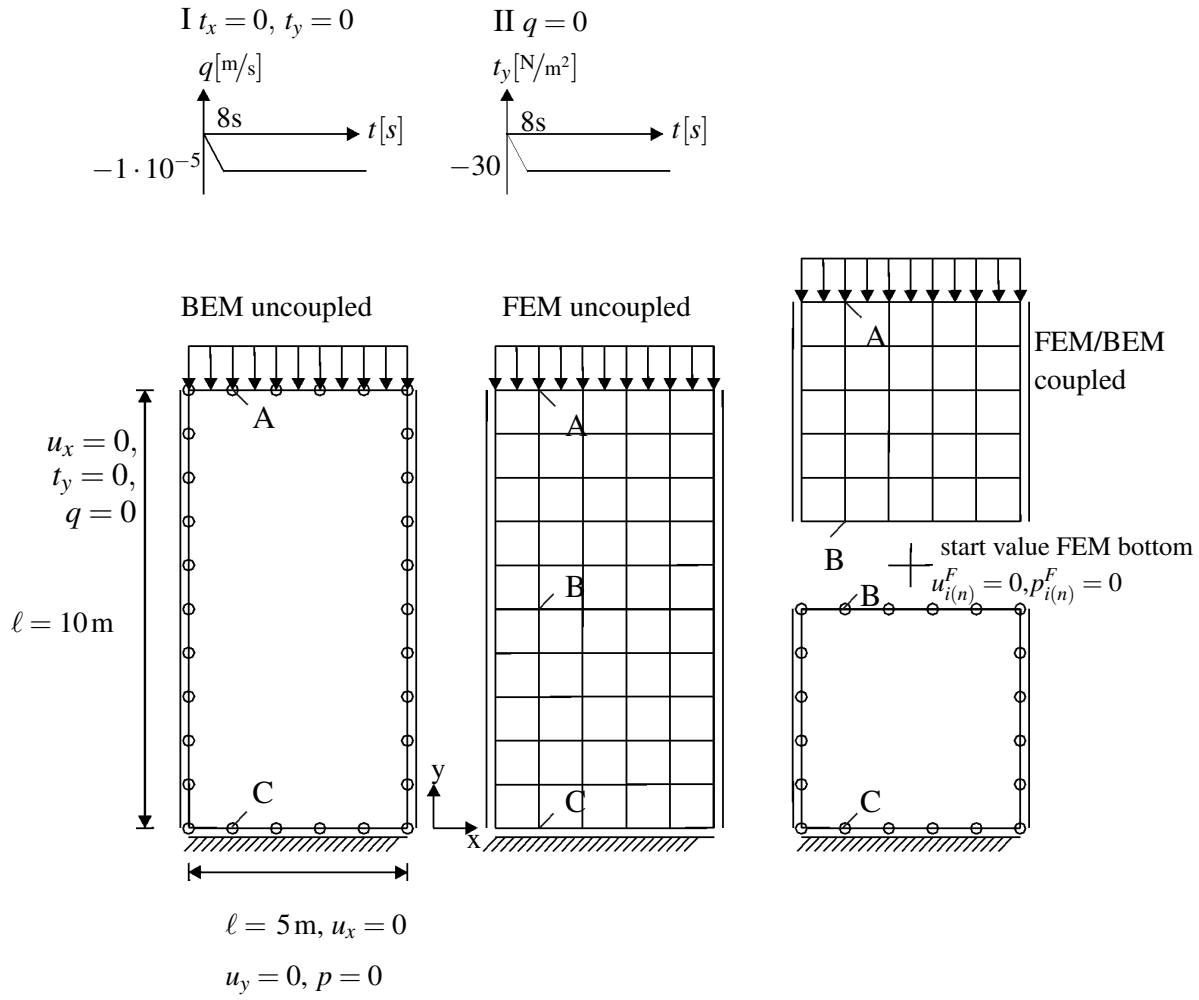

Figure 5.4: 2-d column poroelastic: Geometry, boundary conditions, discretization of uncoupled BEM, uncoupled FEM, coupled FEM-BEM

(a)

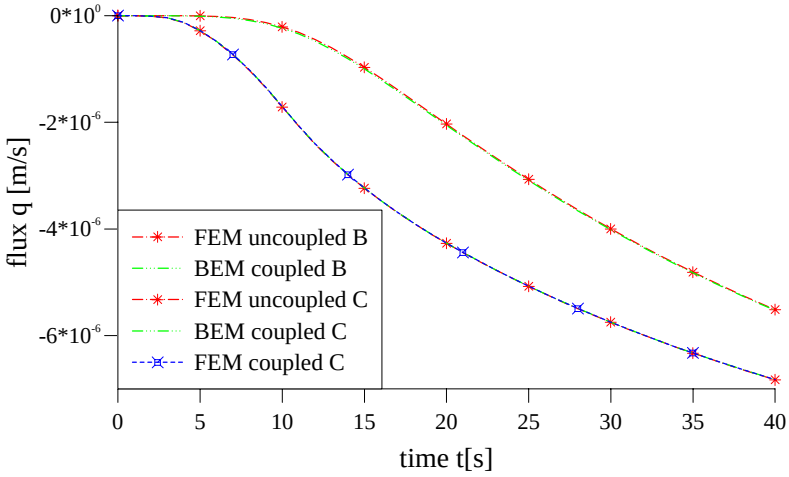

(a) q at point B and C

(b)

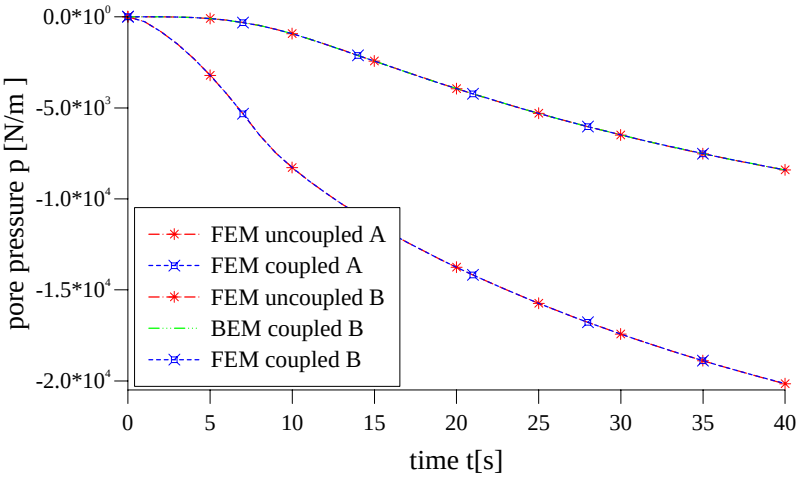

(b) p at point A and B

Figure 5.5: CASE I: Flux q and pore pressure p of the poroelastic 2-d column (discretization, see, figure 5.4)

(a)

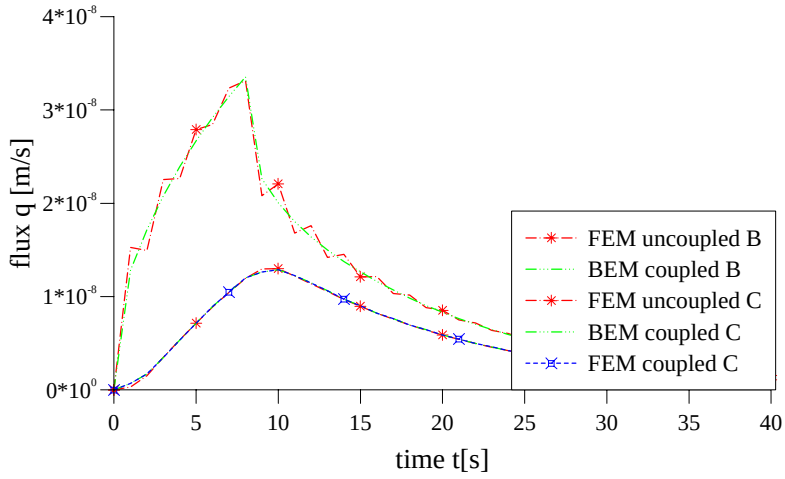

(a) *flux* at point B and C

(b)

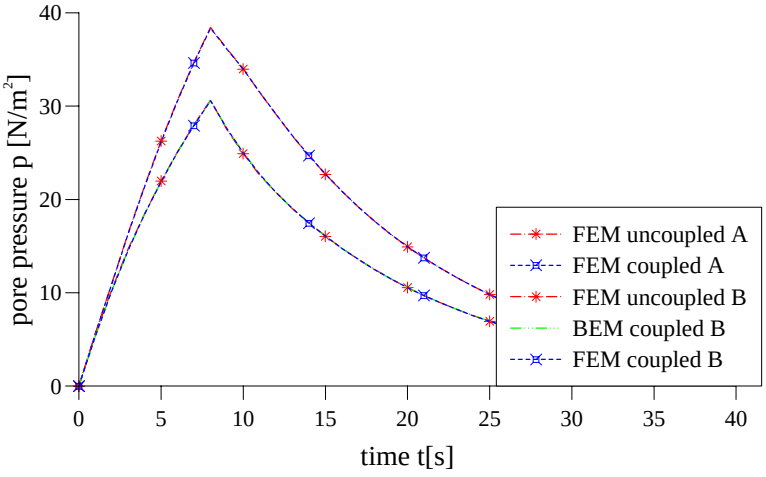

p at point A and B

Figure 5.6: CASE II: Flux q and pore pressure p of the poroelastic 2-d column (discretization, see, figure 5.4)

domain is permeable and traction free. For comparison, a pure BEM mesh is discretized with 40 linear elements on 47 nodes. The surface of the BEM halfspace is free and permeable. The problem geometry and the associated boundary condition of the BEM halfspace are shown in figure 5.8. These two discretizations, the pure FEM and the pure BEM mesh are compared with the coupled FEM/BEM halfspace. The coupled halfspace (here: mesh I) possesses in the FEM area 8 quadrilateral elements on 30 nodes. The BEM halfspace, which belongs to this first coupling example presented in figure 5.9(Ia), consists of 38 linear elements on 45 nodes. The surface of the coupled halfspace is traction free and permeable. Mesh II, which is displayed in figure 5.9(IIa), is discretized for the FEM subdomain with 32 quadrilateral elements on 45 nodes, the element edge length is 1m, while the appropiate BEM subdomain consists of 42 linear elements on 49 nodes and the surface is permeable and traction free. In every case (pure BEM/pure FEM – mesh I/mesh II), the top of the halfspace is excited vertically by a first linear increasing later constant pressure load of -3000 $\mathrm{N/m^2}$. As material data, the values in table 5.1 for case III with a lower compression modulus of the fluid $3.3 \cdot 10^8\,\mathrm{N/m^2}$ are used. In figure 5.7(a), the vertical displacement u_y at point A versus time is depicted for the pure BEM subdomain and for the two coupled FEM/BEM halfspaces. For the uncoupled FEM area and for mesh I and mesh II the pore pressure is plotted versus time in a depth of two meters (see, figure 5.7(b)). Both results agree very well with the results of the pure BEM and pure FEM domain. As mentioned in the literature, if only Neumann boundary conditions are specified on the entire external boundary of the FEM sub-domain, the Dirichlet Neumann algorithm will not converge. A BEM poroelastic halfspace was coupled with only one FEM element and this coupled poroelastic example leads to non-convergence. Non-convergence could be observed too if a FEM region of 3 elements in x-direction and 30 elements in y-direction is coupled with the BEM halfspace. The reason could be the ratio of coupled FEM nodes to uncoupled FEM nodes in the FEM subdomain, or the small number of nodes where the Neumann condition is imposed. Next, the same problem, which was investigated before with a constant pressure load, will be now subjected to a soliton wave with an input of $F(t) = -300 \cdot [sin(t - \frac{\pi}{2}) + 1]$ for $t < 2\pi$; $F(t) = 0$ for $t > 2\pi$. The chosen time step width is 0.314 s. The material data of a coarse sand (CASE I), which was taken for this example, can be found in table 5.1. The description of the discretization of the coupled halfspace for mesh I and mesh II and of the pure FEM mesh can be found in the example above (see, page 84). The coupled FEM-BEM halfspace (mesh I and mesh II) is sketched in figure 5.9 for load case i. In figure 5.12i, the pure FEM mesh with an area of 30 m times 30 m is displayed and in figure 5.8, the pure BEM halfspace. Reflection can be observed in the uncoupled FEM area of 30 m times 30 m.

First, the pore pressure in a depth of 2 m and a distance of approximately 3 m from the excitation point is presented in figure 5.10(a) for point B. In the uncoupled FEM area of 8 m times 4 m, the pore pressure is higher as in the coupled halfspace because of the wave reflection at the boundaries. The coupled FEM/BEM mesh for mesh I and mesh II matches very well the solution of the uncoupled FEM area of 30 m times 30 m. A zoom-in on the first peak is taken: there, it can be seen that Mesh II of the coupled half space is a little bit closer to the true solution for the pore pressure of the 30 m times 30 m area which may depend on the discretized area which is bigger as in Mesh I and, therefore, the FEM/BEM interface is a little bit farther away from the examined point. In figure 5.10(b), the displacement at point D of the coupled halfspace is depicted versus time. The coupled true solution of the coupled halfspace is lower than the uncoupled solution of the uncoupled FEM area of 8m times 4m and a little bit lower than the

(a)

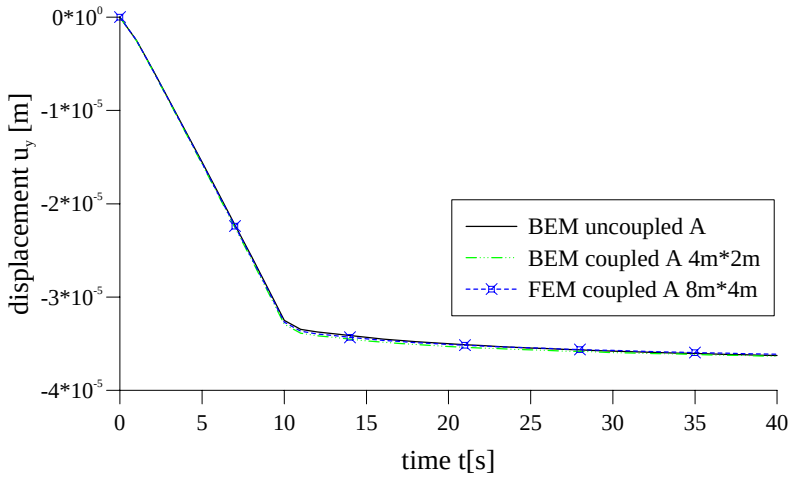

u at point A

(b)

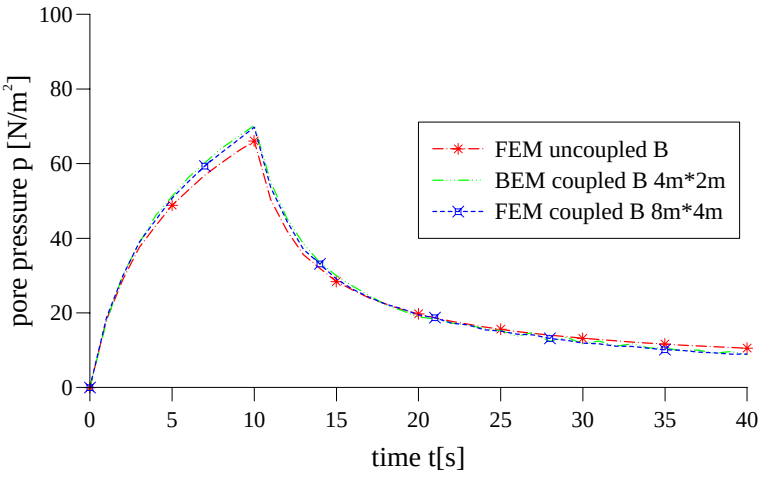

p at point B

Figure 5.7: Displacement *u* and pore pressure *p* of the poroelastic 2-d halfspace uncoupled and coupled (discretization see figure 5.8/5.9).

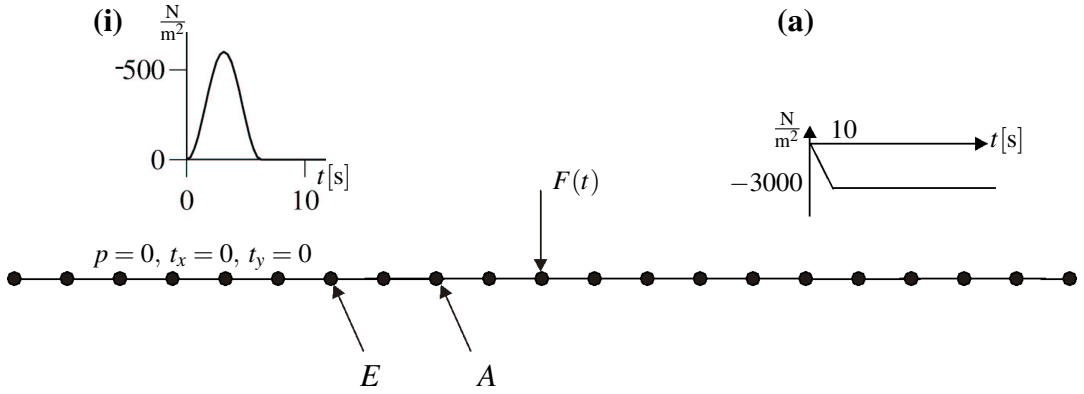

Figure 5.8: 2-d halfspace poroelastic: Geometry, boundary conditions, discretization of uncoupled BEM

solution of the uncoupled FEM area of 30 m times 30 m because, here, the boundary conditions lead for the displacement solution still to some reflection of the wave. The displacements in figure 5.10(c) at point E are for both investigated cases of the coupled FEM/BEM halfspace identical with those of the pure BEM solution.

5.2 Influence of the spatial and time discretization

First, the influence of the spatial discretization is studied using three meshes with different mesh width in the FEM subdomain. The pore pressure of all three different meshes will be compared with a pure FEM calculation of an area of 30 m x 30 m (see, figure 5.12b) which is described above. In the following, the pure FEM area will be compared with three different coupled spatial

Table 5.2: Investigated time steps at the spatial discretization of three meshes

element edge length	time step						
1 m	1 s	0.5 s	0.25 s	0.125 s	0.1 s	0.0625 s	0.02 s
0.5 m							
0.25 m							

discretizations. The three chosen discretizations are shown in figure 5.11, a FEM mesh with 32 quadrilateral elements on 45 nodes with an element edge length of 1 m (mesh 1), a finer mesh with 64 quadrilateral elements on 153 nodes with an element edge length of 0.5 m (mesh 2) and a very fine mesh with 128 quadrilateral elements on 561 nodes with an element edge length of 0.25 m for the FEM subdomain. For all meshes, linear shape functions on quadrilaterals are used in the FEM domain and isoparametric linear shape function in the BEM domain [128]. The coupled BEM subdomain consists for mesh 1 on 42 elements with 49 nodes, for mesh 2 on 58 elements on 65 nodes and for mesh 3 on 90 linear elements on 97 nodes. In all three cases,

(I)

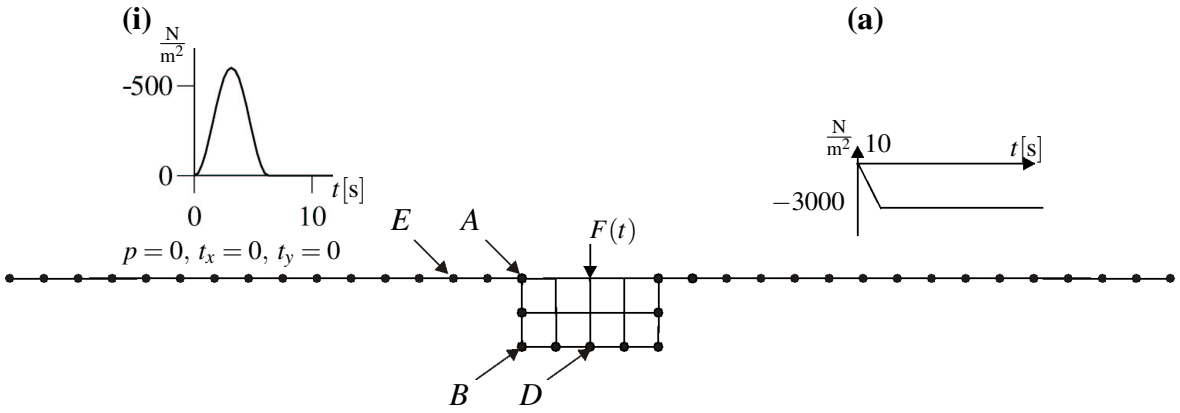

(II)

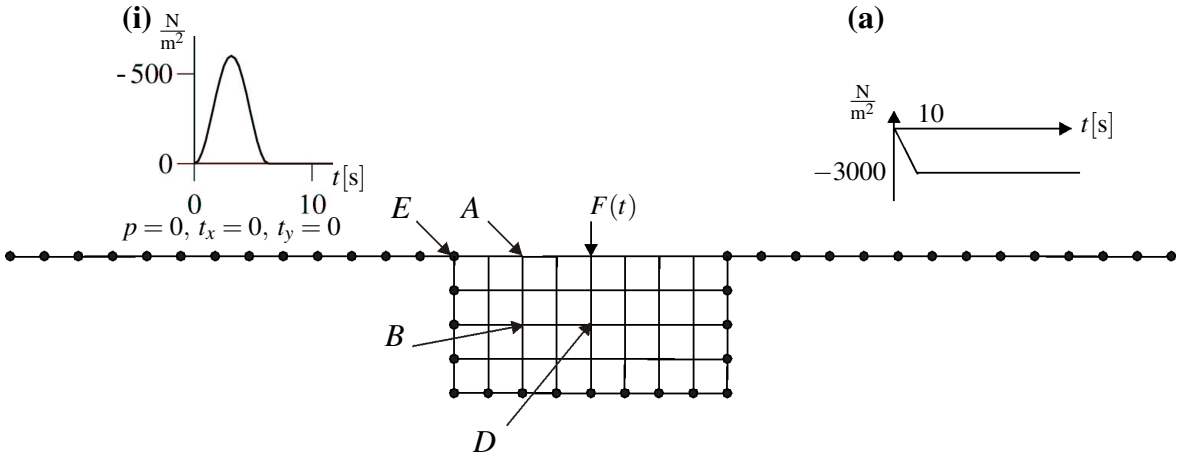

Figure 5.9: 2-d halfspace poroelastic: Geometry, boundary conditions, discretization of coupled FEM/BEM halfspace, i.e., different example: **(I)** mesh I: FEM area $4\,\mathrm{m} \cdot 2\,\mathrm{m}$, **(II)** mesh II: FEM area $8\,\mathrm{m} \cdot 4\,\mathrm{m}$.

(a)

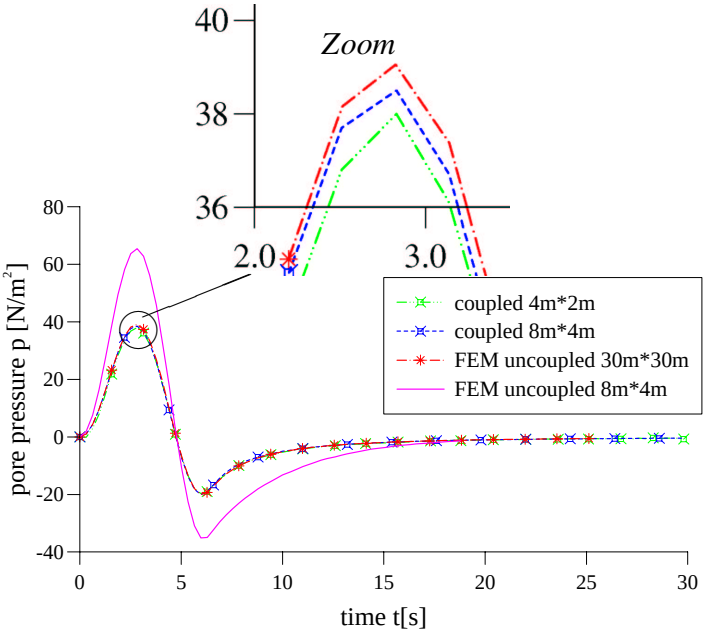

(b)

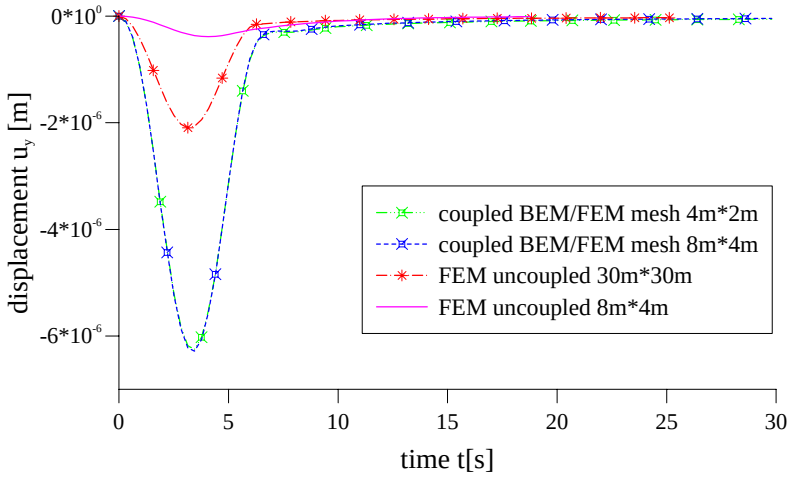

(c)

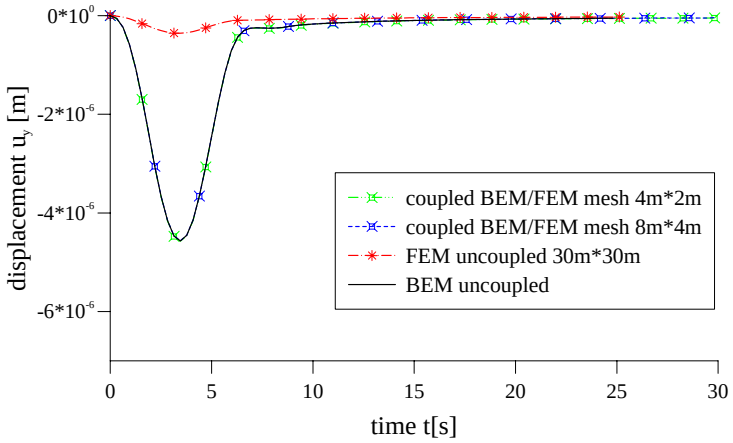

Figure 5.10: Input of a soliton signal into the poroelastic 2-d halfspace i.e., output of **(a)** pore pressure p at point B, **(b)** displacement u_y at point D, **(c)** displacement u_y at point E (discretization, see, figure 5.9 load case i).

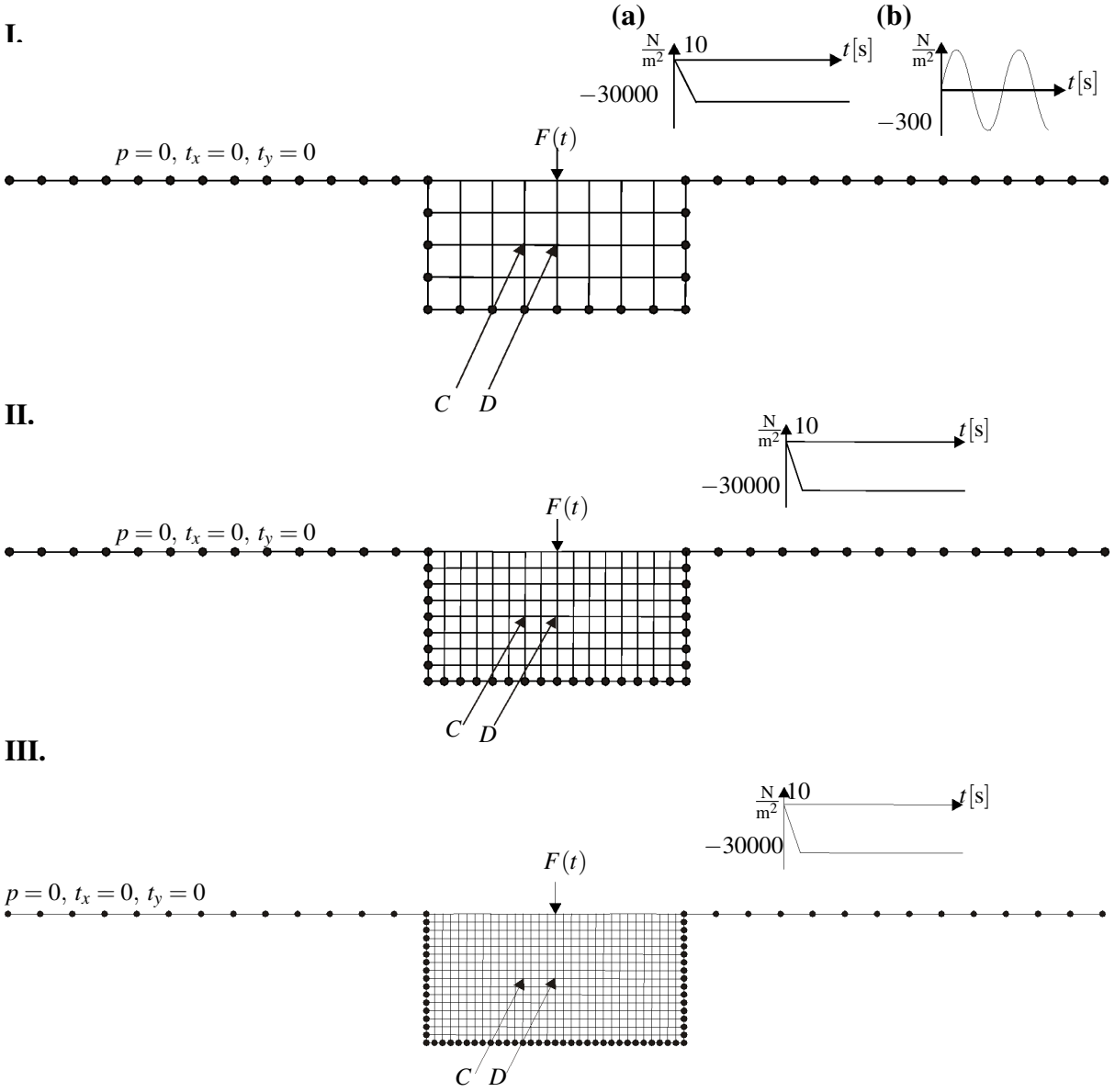

Figure 5.11: 2-d halfspace poroelastic: Geometry, boundary conditions, discretization of coupled FEM/BEM halfspace, i.e., different mesh width **I.** 1m mesh 1 **II.** 0.5m mesh 2 **III.** 0.25m mesh 3

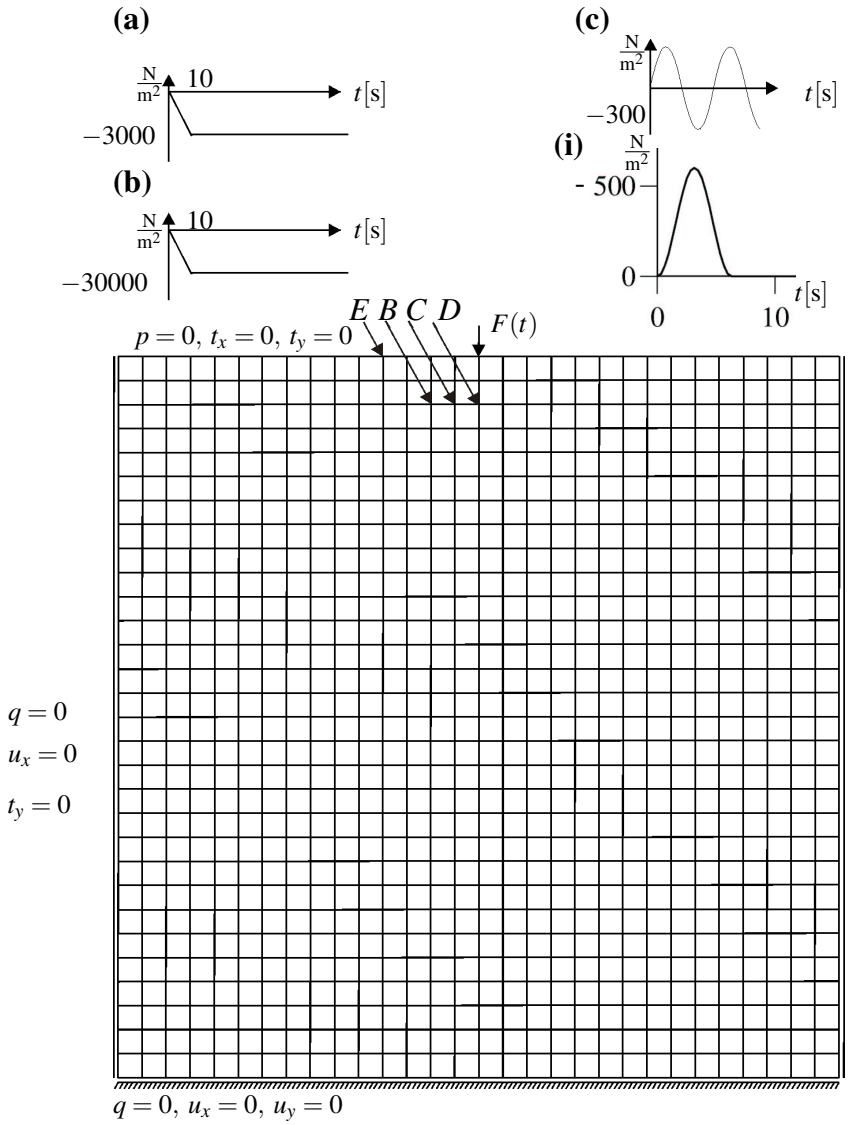

Figure 5.12: 2-d halfspace poroelastic: Geometry, boundary conditions, discretization of uncoupeled FEM area 30 m x 30 m

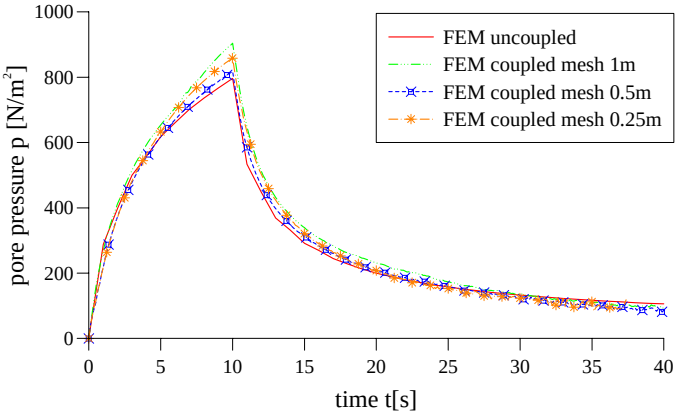

Figure 5.13: Pore pressure p of the poroelastic 2-d halfspace (used time step 0.125 s) at point C. Influence of mesh size i.e., different mesh width (discretization, see, figure 5.11 and 5.12(b))

the top of the halfspace is excited vertically by a first linearly increasing, later constant pressure load of -30000 $\mathrm{N/m^2}$. The remaining surface of the halfspace is traction free and permeable. The used time step is 0.125 s. As material data, case III in table 5.1 is used. For all three meshes, the pore pressure in the center of the FEM sub-domain in a depth of 2m (point C) is plotted versus time in figure 5.13. The results for the pore pressure are in good agreement with the result of the pure FEM domain (discretization, see, figure 5.12 with load case b). Mesh 2 reproduces the jumps for the pore pressure solution best. However, for computational time consuming reasons, for the pore pressure mesh 1 is sufficient. For different time step sizes ($\Delta t = 1s$, $\Delta t = 0.5s$, $\Delta t = 0.25s$), the pore pressure in the center of the FEM sub-domain (point D) is depicted versus time in figure 5.14 for mesh 1 (discretization, see, figure 5.11 part I). For mesh 1, nearly no dependence on the time step size is observed. All three meshes were investigated for different time steps which are mentioned in table 5.2. Clearly, all meshes have an optimal time step size. For mesh 1, a time step of 1s is sufficient, whereas for mesh 2 the time step should be 0.125 s and for mesh 3 at 0.0625 s. If the time step size is chosen too big, the assumption of neglecting the relative fluid acceleration in the u-p formulation plays a role, and at the first time steps, the pore pressure will overshoot. A reduction of the time step helps to reduce this effect but it cannot completely eliminated.

5.2.1 Spatial discretization and time discretization under different frequency input

In the previous study, the top of the halfspace was excited vertically by a first linearly increasing, later constant pressure load. Here, the effects of different frequencies of the input load will be studied and compared with the solution of the pure FEM area of 30 m x 30 m (discretization,

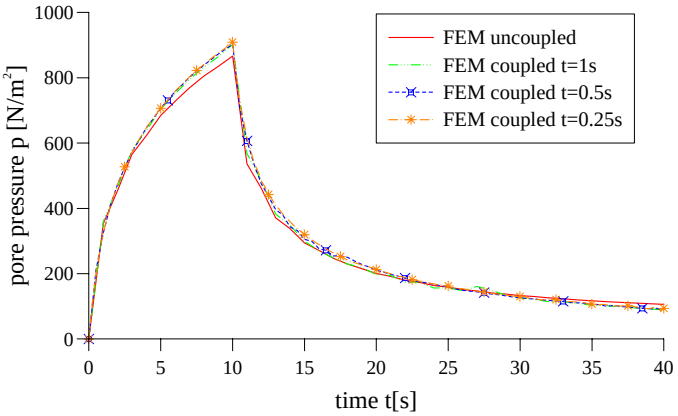

Figure 5.14: Pore pressure p of the poroelastic 2-d halfspace at point **D**: Influence of time step size, i.e., 1s, 0.5s, 0.25s (discretization, see, figure 5.11(a), 5.12(b))

see, figure 5.12(c)). The pure FEM area (30 m x 30 m) is further described in section 5.1.3. The discretization of the coupled FEM subdomain consists of 32 quadrilateral elements on 45 nodes with an element edge length of 1m. This subdomain is coupled with the BEM subdomain. It is discretized with 42 linear isoparametric elements as shown in figure 5.11 part I (mesh 1) with load case b. The data of the material, which were used, may be found in table 5.1, case III. The used time step is 0.005 s. In the middle of the discretized part, a sinusoidal load $F(t) = -300 \cdot sin(2\pi t/period)$ is applied. The rest of the surface is traction free and permeable. The coupled halfspace were investigated for a period of 0.02 s, 0.04 s, 0.08 s, 0.32 s and 0.5 s of the sinus load input. Therefore, the pore pressure at the center of the loaded area in 2m depth is displayed versus time for different periods in figure 5.15(a, b, c) and in figure 5.16(d, e). In figure 5.15(a, b), the sine curve is not modeled correctly: this depends on the error due to the spatial discretization of the FE mesh. When a smaller mesh width (more elements) will be chosen, this effect can be eliminated. For a period of 0.02 s ($f = 50$ Hz), the coupled FEM/BEM subdomain is overshooting the result of the FEM subdomain. Whereas for the case of 0.04s ($f = 25$ Hz) and 0.08 s ($f = 12.5$ Hz), a certain damping can be observed in the coupled FEM/BEM area. To avoid this, a smaller time step could be chosen. Generally, it can be said that the results for the pore pressure are in good agreement with the result of the pure FEM domain.

(a)

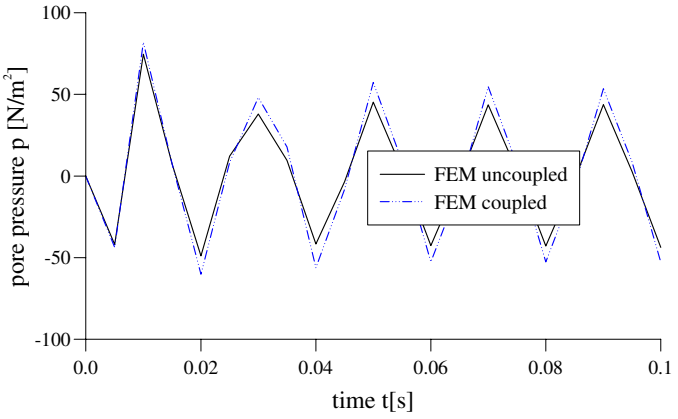

(b)

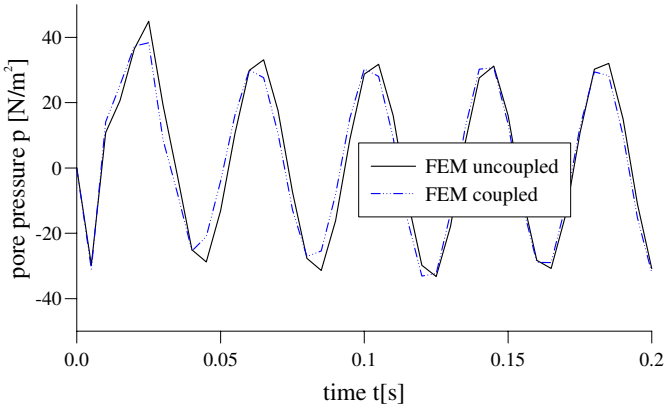

(c)

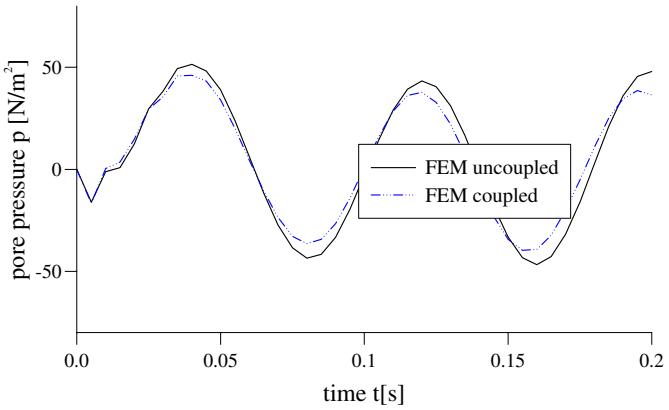

Figure 5.15: Pore pressure p of the poroelastic 2-d halfspace at point D Influence of a different input period i.e., 0.02 s, 0.04 s, 0.08 s (discretization, see, figure 5.11 part I load case (b))

(d)

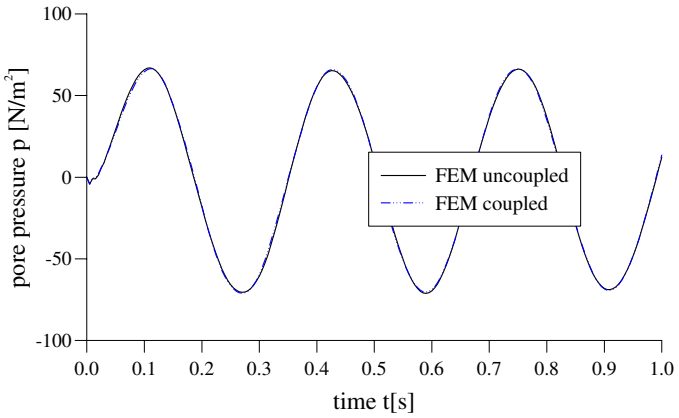

(e)

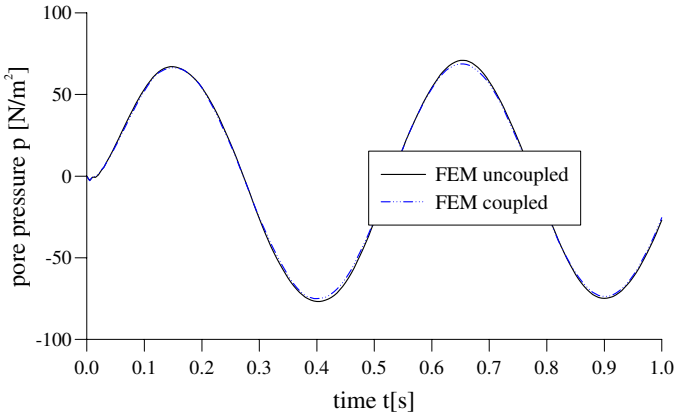

Figure 5.16: Pore pressure p of the poroelastic 2-d halfspace at point D Influence of a different input period i.e., 0.32 s, 0.5 s (discretization, see, figure 5.11 part I load case (b))

Next, the BEM halfspace is coupled with a fictious bottom and the behavior under different periodic loads of the coupled FEM/BEM example is investigated. The center of the bottom of the BEM halfspace is excited by a sinusoidal load of $F(t) = -30000 \cdot sin(2\pi\, t/period)$. The rest of the bottom is traction free and impermeable, whereas the surface of the 2d-halfspace is permeable and traction free. A different loading period is studied using three meshes with different mesh widths in the FEM subdomain. The three discretizations are displayed in figure 5.17. Quadrilateral elements are used in the FEM subdomain. Mesh 1 is discretized in the FEM subdomain with 32 elements on 45 nodes, mesh 2 as finer mesh consists of 64 elements on 153 nodes and the very fine mesh has 128 elements on 561 nodes. The coupled BEM subdomain consists for mesh 1 of 58 linear elements with 68 nodes, for mesh 2 of 74 linear elements with 84 nodes and for mesh 3 of 106 linear elements on 116 nodes. The selected material data can be found in table 5.1 case III. A time step 0.0625 s is used. A loading period of 3 s, 5 s and 10 s is studied. The pore pressure is depicted versus time at point C in figure 5.18(a, b, c) for a period of 3 s, 5 s and 10 s, respectively. The results of the three different spatial discretizations are matching each other very well. This behavior was expected due to the results in section 5.2.

5.3 Coupled poroplastic-poroelastic 2d-halfspace

An adequate Young's modulus has to be chosen for coupling the poroplastic FEM subspace with the poroelastic BEM subspace for the poroelastic area. For the poroplastic area, an inital E_0 Young's modulus is known. With the aid of the mean effective stress p at the corresponding depth of the interface and the initial pore pressure p_0, the Young's modulus for the BEM procedure

$$E_{\mathrm{BEM}} = E_0 \frac{p}{p_0} \tag{5.9}$$

is calculated. In the FEM program SWANDYNE, a linearly increasing Young's modulus for the poroplastic area (PZ3-model) (which depends on the depth of the soil) is taken into account.

Further, to receive the initial stress state for poroplastic material behavior, the inertia terms have to be concerned. The initial vertical effective stress state can be obtained by

$$\sigma'_{1\,\mathrm{initial}} = g \left(\frac{\rho_s + e\rho_{\mathrm{f}}}{1+e} - \rho_{\mathrm{f}} \right) d \tag{5.10}$$

where d is the distance between the surface of the halfspace and the investigated location. The horizontal initial effective stress state can be obtained by multiplying the initial vertical effective stress state with Poisson's ratio $\sigma'_{2\,\mathrm{initial}} = (\nu/1-\nu)\,\sigma'_{1\,\mathrm{initial}}$. The effective principal stress state is consequently the summation of the effective stresses and the effective initial stress state. Now, a first example for the liquefying soil is calculated. The poroplastic region of the FEM subdomain uses the PZ3 model, which is explained in detail in section 4.3.2. The FEM subdomain is discretized with 32 quadrilateral elements on 90 nodes, as sketched in figure 5.19. The corresponding BEM subdomain consists of 58 linear elements on 68 nodes. The bottom of the BEM subdomain is traction free and impermeable, whereas the top of the surface of the coupled BEM/FEM region is permeable and traction free. In this example, a time step of

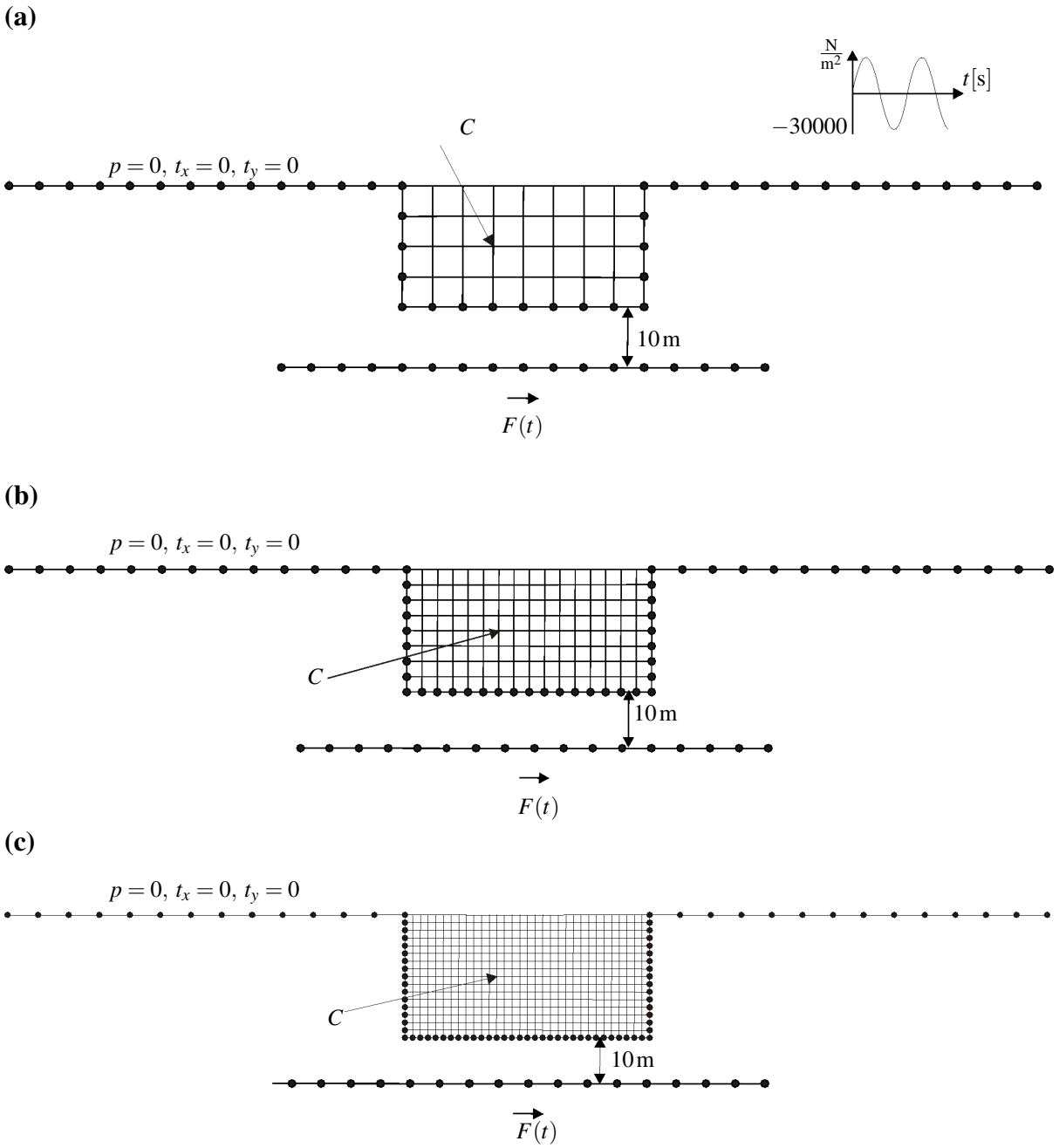

Figure 5.17: 2-d halfspace poroelastic: Geometry, boundary conditions, discretization of coupled FEM/BEM halfspace, i.e., different frequency input by different mesh width **(a)** 1m mesh 1 **(b)** 0.5 m mesh 2 **(c)** 0.25 m mesh 3

(a)

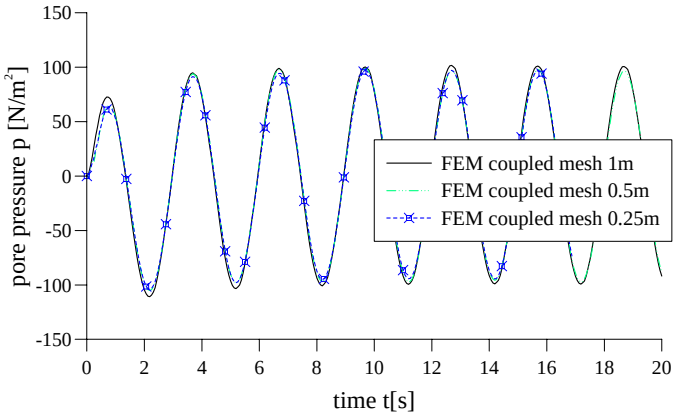

(b)

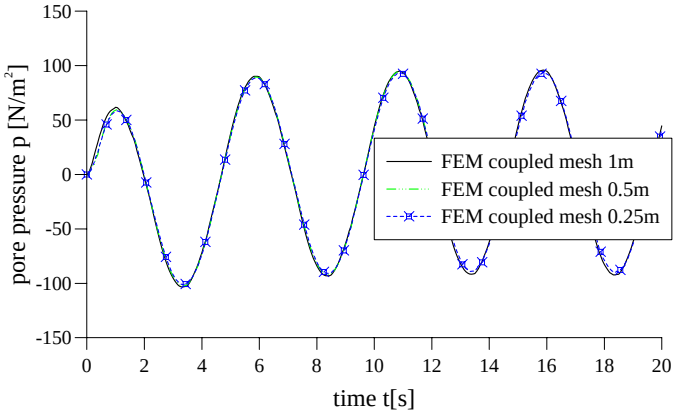

(c)

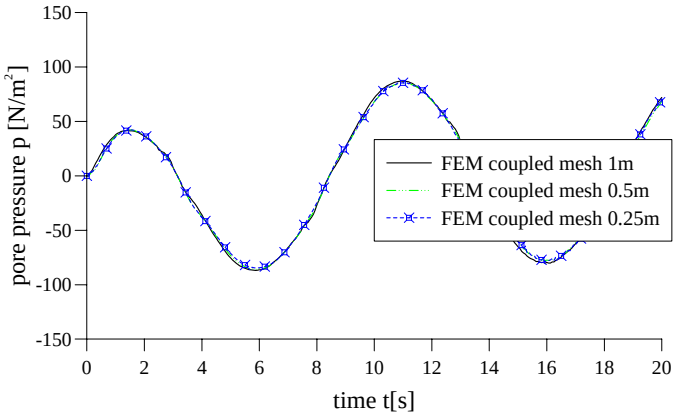

Figure 5.18: Pore pressure p of the poroelastic 2-d halfspace at point **(a)** at point C Influence of different mesh width and different input period i.e., 3 s, 5 s, 10 s (discretization, see, figure 5.17)

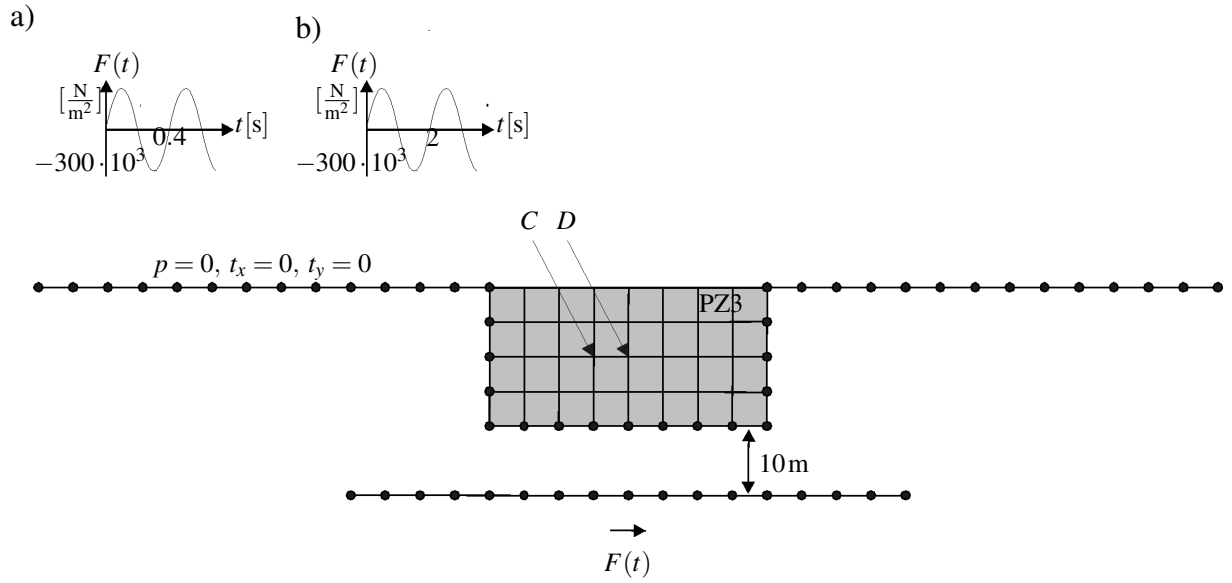

Figure 5.19: 2-d halfspace poroplastic-poroelastic: Geometry, boundary conditions, discretization of coupled FEM/BEM halfspace 8 m x 4 m

0.02 s is used. The data for the material model is summarized in table 5.3. As input, a sinus load $F(t) = -300000 \cdot sin(2\pi t/period)$ was applied at the bottom of the discretized BEM subdomain. The chosen period for the sinus load is 0.4 s. In figure 5.20, the pore pressure of the liquefying soil is depicted versus time for points C and D (in a depth of 2 m) of the poroplastic FEM subdomain. The soil is liquefying, the pore pressure reach an asymptotic line at a value of 22000 N/m^2 which has nearly the same magnitude as the initial vertical effective stress of 21768 N/m^2. Different to the example before, here, a FEM subdomain with two different constitutive relations is investigated. The purpose of this example, which is sketched in figure 5.21, is to show that the solution of this problem for the poroplastic case is identical with the solution of the problem which was investigated before, where the poroelastic area, which is now belonging to the FEM area, belongs to the BEM subdomain. In the poroplastic area of 4 m times 2 m, the PZ3 model is used (see, figure 5.21). This area is surrounded by a poroelastic stripe of 2 m in the FEM subdomain. The material data for the PZ3 area can be found in table 5.3b and for the poroelastic FEM stripe and the surrounding BEM halfspace in table 5.3a. The total FEM subdomain consists of 72 quadrilateral elements on 182 nodes. The surface of the coupled FEM/BEM domain is traction free and permeable. The complementary poroelastic BEM subdomain is made up of 74 elements on 84 nodes. At the bottom of the BEM subdomain Neumann boundary conditions are imposed. Like in the example described above, a sinus input load $F(t) = -300000 \cdot sin(2\pi t/period)$ is applied at the center of the bottom of the BEM subdomain with a period of 0.4 s and a time step size of 0.02 s. The pore pressure at the points C and D for the liquefying soil is displayed versus time in figure 5.22. When this result is compared with the result before (see, figure 5.20), it can be seen that they have, as expected, nearly the same magnitude.

Next, the behavior of the PZ3 model under a set of different material parameters will be analyzed. The problem geometry and the associated boundary conditions are sketched in figure 5.19(b). Number and kind of elements, boundary conditions are described in the first exam-

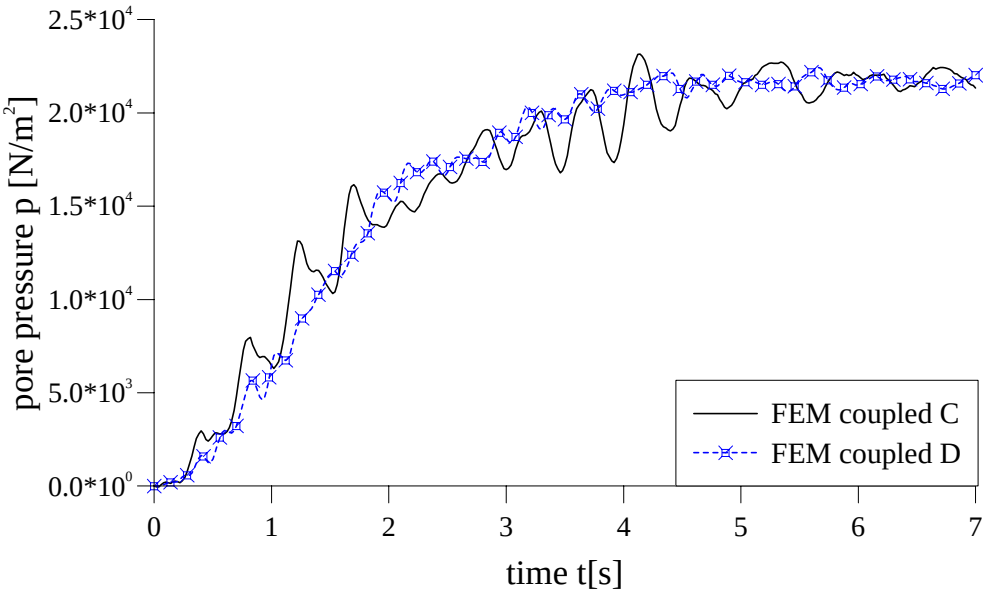

Figure 5.20: Pore pressure p of the poroplastic 2-d halfspace at point C and D (discretization, see, figure 5.19)

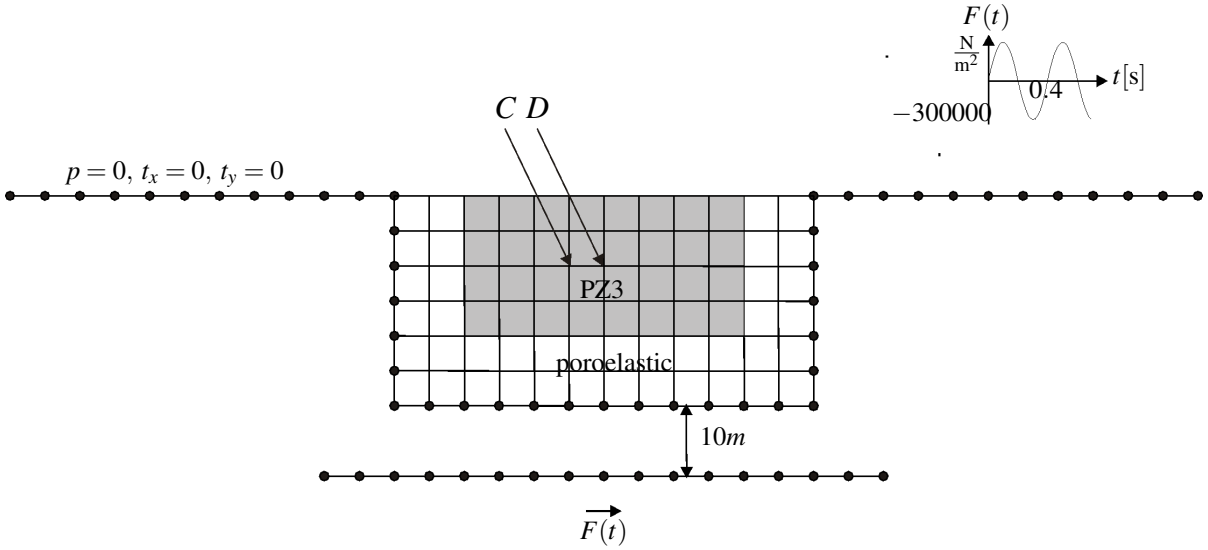

Figure 5.21: 2-d halfspace poroplastic: Geometry, boundary conditions, discretization of coupled FEM/BEM halfspace $12\,\mathrm{m} \cdot 6\,\mathrm{m}$

Table 5.3: Material data of the coupled PZ3-FEM area with the BEM sudomain

(a) *poroelastic* material data

	$E[\frac{\mathrm{N}}{\mathrm{m}^2}]$	ν	$\rho\,[\frac{\mathrm{kg}}{\mathrm{m}^3}]$	$\rho_\mathrm{f}\,[\frac{\mathrm{kg}}{\mathrm{m}^3}]$	ϕ	$K_\mathrm{s}\,[\frac{\mathrm{N}}{\mathrm{m}^2}]$	$K_\mathrm{f}\,[\frac{\mathrm{N}}{\mathrm{m}^2}]$	α	$\kappa_\mathrm{f}\,[\frac{\mathrm{m}}{\mathrm{s}}]$
poroelastic	$2.97\cdot10^8$	0.285	2095	980	0.36	$1.0\cdot10^{20}$	$1.092\cdot10^9$	1	$2.1\cdot10^{-3}$

(b) *poroplastic* material data

	$E_0[\frac{\mathrm{N}}{\mathrm{m}^2}]$	M_f	$p_0\,[\frac{\mathrm{N}}{\mathrm{m}^2}]$	H_L	$H_\mathrm{U}\,[\frac{\mathrm{N}}{\mathrm{m}^2}]$	$G_0\,[\frac{\mathrm{N}}{\mathrm{m}^2}]$	$K_0\,[\frac{\mathrm{N}}{\mathrm{m}^2}]$	α_f=α_g	γ_Hu= γ_DM
poroplastic	$450\cdot10^4$	22.9°	$4\cdot10^4$	350	$600\cdot10^4$	$175\cdot10^4$	$350\cdot10^4$	0.45	2

ple above at the beginning of this section at page 99. The non-linear FEM subdomain, where the PZ3-model is used, is coupled with a infinite BEM halfspace. In a depth of 10 m, the BEM halfspace is coupled with an arbitrary internal boundary. This arbitrary internal boundary is excited by a sinus wave with an input of $F(t) = -300000 \cdot sin(2\pi\, t/_{period})$. The chosen time step size for the test was $\Delta t = 0.02$ s and the period of the sinus input load was chosen as 2 seconds. The material data of the three investigated parameters, are given for the poroplastic region in table 5.4a. Where for every testing parameter two sets of different material parameters are given. The material data for the poroelastic region is given in table 5.3a.

First, the influence of different initial shear moduli is examined as depicted for the pore pressure at point C in figure 5.23(a). Second, the material behavior under a small variation of the bulk moduli is drawn in figure 5.23(b) for point C. Increasing compressibility leads to higher pore pressure. Third, the behavior of the PZ3 model under different slopes of the Critical State Line (CSL) is displayed in figure 5.24(a). Like before, the pore pressure p at point C is plotted versus time. A higher slope of the CSL increases the range of plasticity before failure for the solid structure, subsequently the pore pressure is smaller. The results presented in figure 5.24(b) are calculated with a different Young's modulus for the poroelastic area.

The set of parameters for these examples can be found in table 5.4. In figure 5.24(b), the pore pressure is smaller when Young's modulus is chosen higher, i.e., the stiffness of the material is increasing. In figure 5.25, the pore pressure is depicted versus time for different loading plastic moduli and different unloading plastic moduli. If the plastic modulus is a little bit higher, the pore pressure is rising a little bit more; for the plastic unloading modulus, the behavior is inverse. Here, not like before, another value for the bulk modulus was chosen. The material data is given in table 5.3a and table 5.4a .

Table 5.4: Material data for testing different material parameters

(a) Different input parameter for the *poroplastic* area

	$E_0[\frac{\mathrm{N}}{\mathrm{m}^2}]$	M_f	$p_0\,[\frac{\mathrm{N}}{\mathrm{m}^2}]$	H_L	$H_\mathrm{U}\,[\frac{\mathrm{N}}{\mathrm{m}^2}]$	$G_0\,[\frac{\mathrm{N}}{\mathrm{m}^2}]$	$K_0\,[\frac{\mathrm{N}}{\mathrm{m}^2}]$	α_f=α_g	γ_Hu=γ_DM
G_0 1						$140\cdot10^4$			
G_0 2	$450\cdot10^4$	22.9°	$4\cdot10^4$	350	$600\cdot10^4$	$210\cdot10^4$	$350\cdot10^4$	0.45	2
K 1							$280\cdot10^4$		
K 2	$450\cdot10^4$	22.9°	$4\cdot10^4$	350	$600\cdot10^4$	$175\cdot10^4$	$420\cdot10^4$	0.45	2
M_f 1		18.3°							
M_f 2	$450\cdot10^4$	27.5°	$4\cdot10^4$	350	$600\cdot10^4$	$175\cdot10^4$	$350\cdot10^4$	0.45	2
H_L 1				315					
H_L 2	$450\cdot10^4$	22.91°	$4\cdot10^4$	385	$600\cdot10^4$	$175\cdot10^4$	$300\cdot10^4$	0.45	2
H_U 1					$540\cdot10^4$				
H_U 2	$450\cdot10^4$	22.91°	$4\cdot10^4$	350	$660\cdot10^4$	$175\cdot10^4$	$300\cdot10^4$	0.45	2

(b) Different input parameter for the *poroelastic* area

	$E[\frac{\mathrm{N}}{\mathrm{m}^2}]$	ν	$\rho\,[\frac{\mathrm{kg}}{\mathrm{m}^3}]$	$\rho_\mathrm{f}\,[\frac{\mathrm{kg}}{\mathrm{m}^3}]$	ϕ	$K_\mathrm{s}\,[\frac{\mathrm{N}}{\mathrm{m}^2}]$	$K_\mathrm{f}\,[\frac{\mathrm{N}}{\mathrm{m}^2}]$	α	$\kappa_\mathrm{f}\,[\frac{\mathrm{m}}{\mathrm{s}}]$
poroelastic E 1	$2.83\cdot10^8$	0.285	2095	970	0.36	$1.0\cdot10^{20}$	$1.092\cdot10^9$	1	$2.1\cdot10^{-3}$
poroelastic E 2	$3.56\cdot10^8$	0.285	2095	970	0.36	$1.0\cdot10^{20}$	$1.092\cdot10^9$	1	$2.1\cdot10^{-3}$

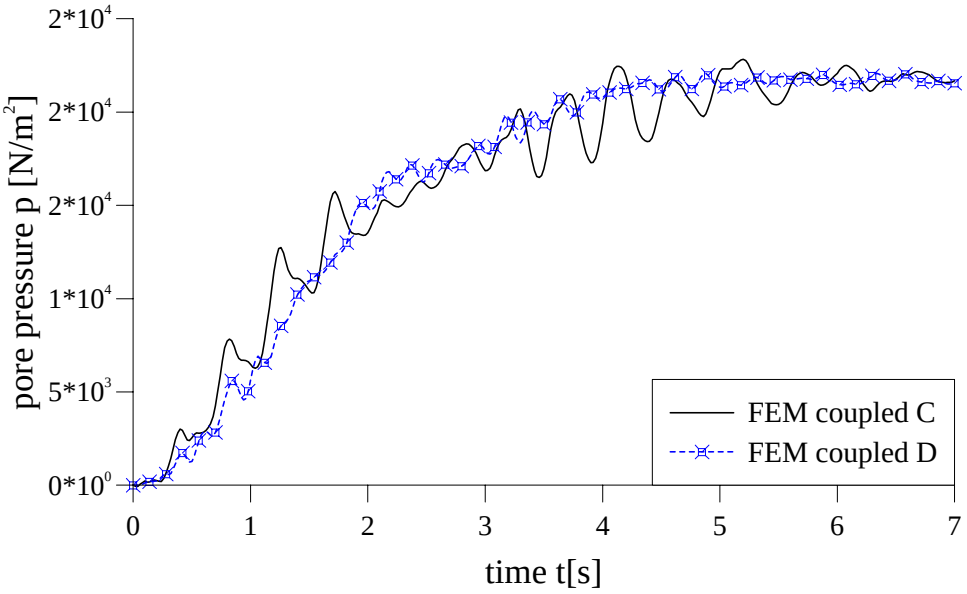

Figure 5.22: Pore pressure p of the poroplastic 2-d halfspace with 2 different material at point C and D (discretization, see, figure 5.21)

(a)

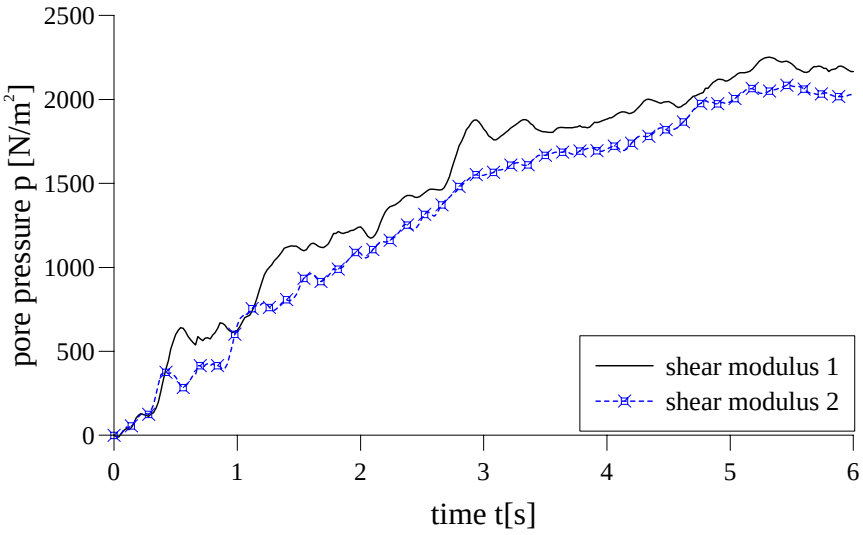

(b)

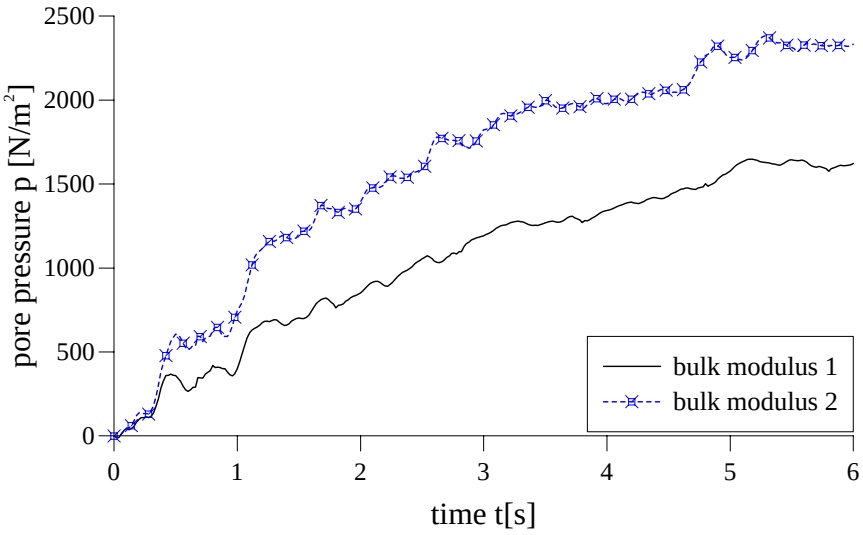

Figure 5.23: Pore pressure p of the poroelastic 2-d halfspace at point C Investigation of different material parameter i.e., **(a)** G_0 shear moduli , **(b)** K bulk moduli (discretization, see, figure 5.19 load case b)

(a)

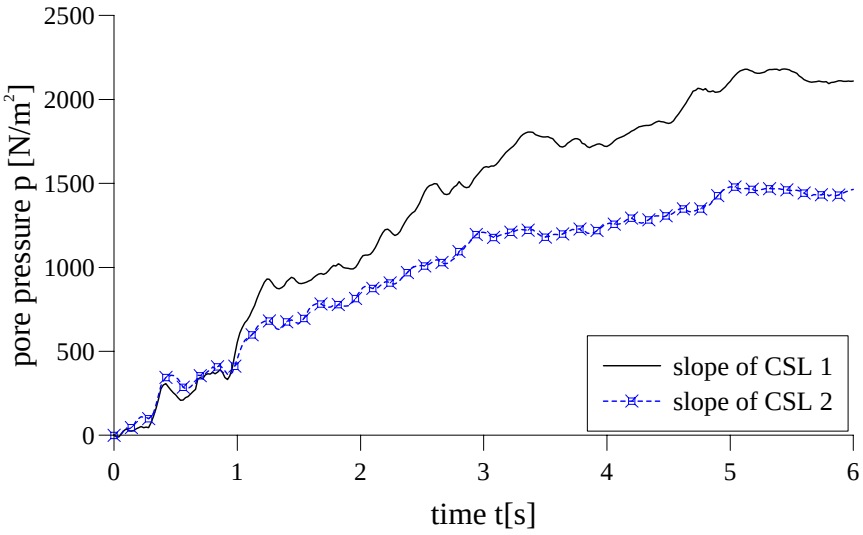

(b)

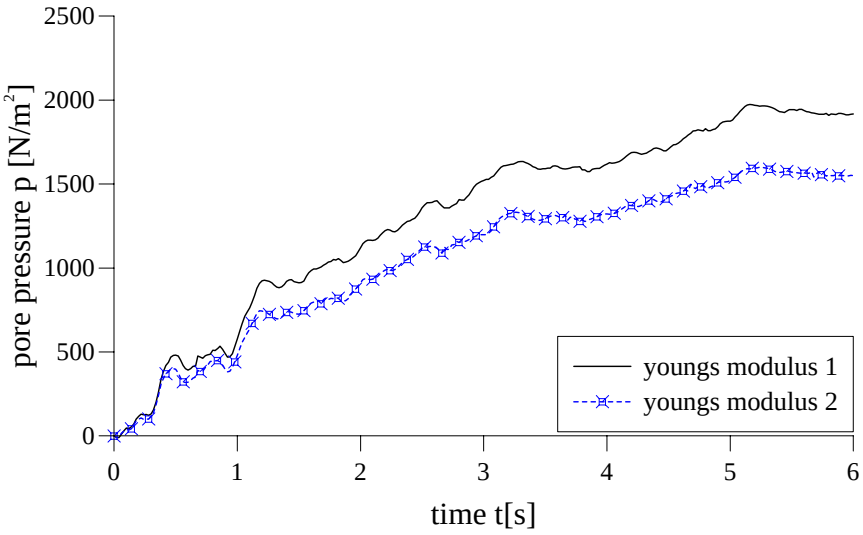

Figure 5.24: Pore pressure p of the poroelastic 2-d halfspace at point C Investigation of different material parameter i.e., **(a)** M_f slope of CSL, **(b)** E youngs moduli (discretization, see, figure 5.19 load case b)

(a)

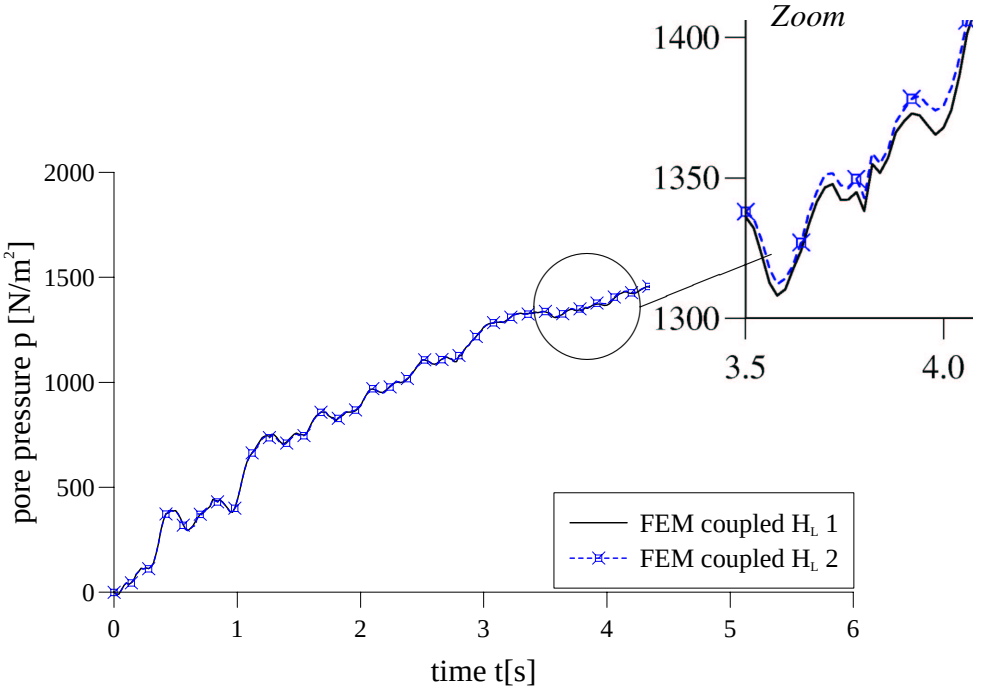

(b)

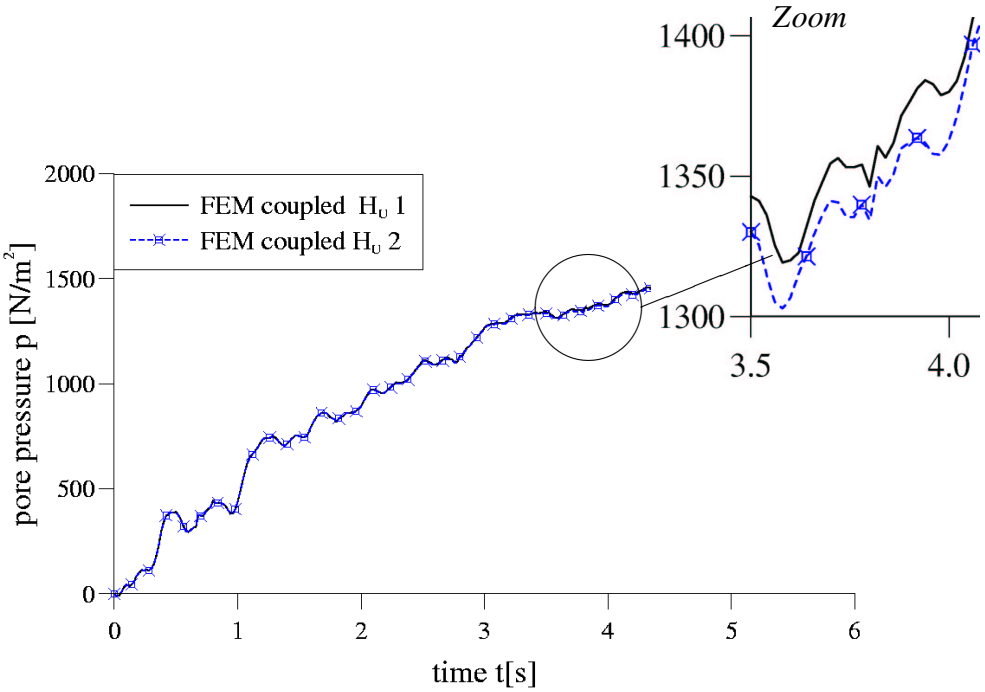

Figure 5.25: Pore pressure p of the poroelastic 2-d halfspace at point C Investigation of different material parameter i.e., **(a)** H_L loading plastic modulus, **(b)** H_U unloading plastic modulus (discretization, see, figure 5.19 load case b)

5.3.1 Seismic excitation of the coupled 2d-halfspace

In the studies above, an arbitrary internal boundary was excited by a sinusoidal stress load. Here, a concrete dyke, lying on the poroplastic soil area which is surrounded by the poroelastic halfspace, is excited by an earthquake load. The initial stress state is determined as in the section before. The input for earthquake analysis is based on measured recorded data of actual earthquakes and is generally presented as the values of the displacement u and/or of the acceleration $\ddot{u}$. In figure 5.26 a triangular structure is resting on a soil foundation of unlimited extent, the arbitrary internal boundary is excited by the input motion.

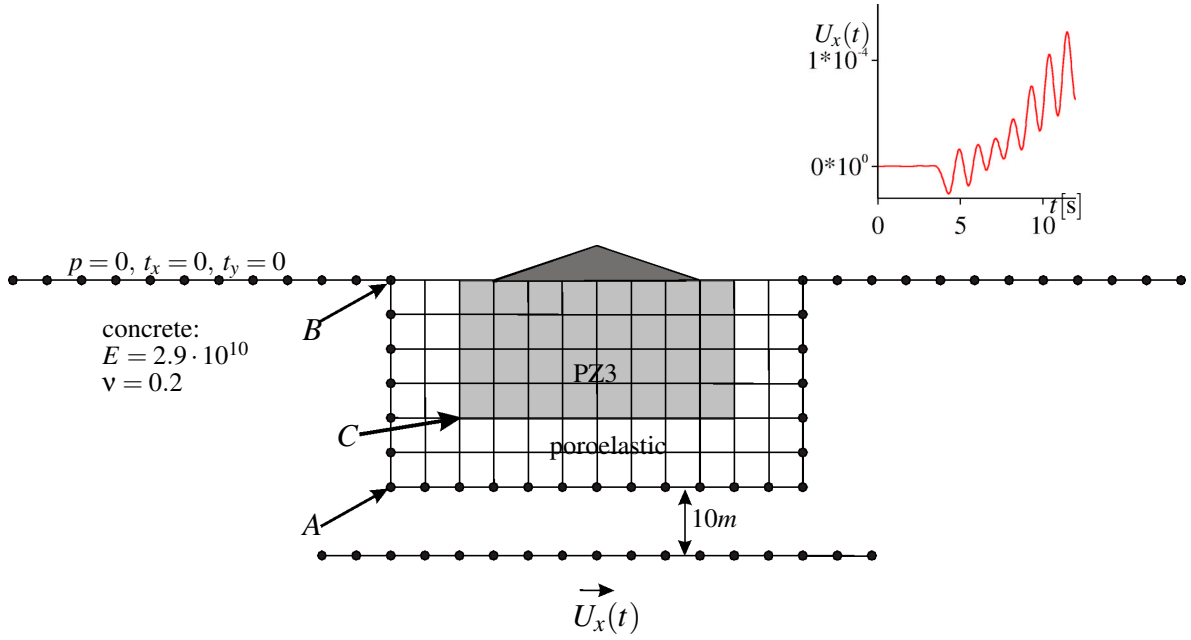

Figure 5.26: 2-d halfspace poroplastic: Geometry, boundary conditions, discretization of coupled FEM/BEM halfspace 12 m · 6 m with concrete dyke

In this example, three different constitutive relations hold for the FEM subdomain: The dyke, which is sketched in the color of dark grey, consists of linear elastic elements (two triangle and four quadrilateral). The dyke itself is lying on a poroplastic area of 4 m times 2 m. In the poroplastic area the PZ3 model is used. The material data for the concrete is given in figure 5.26, for the PZ3 area in table 5.3b, and for the poroelastic FEM stripe and the surrounding BEM halfspace in table 5.3a.

The total FEM subdomain consists of 76 quadrilateral and two triangle elements on 187 nodes. The surface of the coupled FEM/BEM domain is traction free and permeable. The complementary poroelastic BEM subdomain is made up of 74 elements on 84 nodes. At the arbitrary internal boundary of the BEM subdomain, Neuman boundary conditions are imposed. In the center of the arbitrary internal boundary an earthquake load $U_x(t)$ is applying. As time step size 0.02 s was chosen.

In figure 5.27, the displacement figure of the dyke and of the near-field soil is rendered. In

figure 5.28, the pore pressure at point A and C and the displacements at point A and B are displayed versus time. The output of the displacement curve is quite similar to the displacement of the earthquake input.

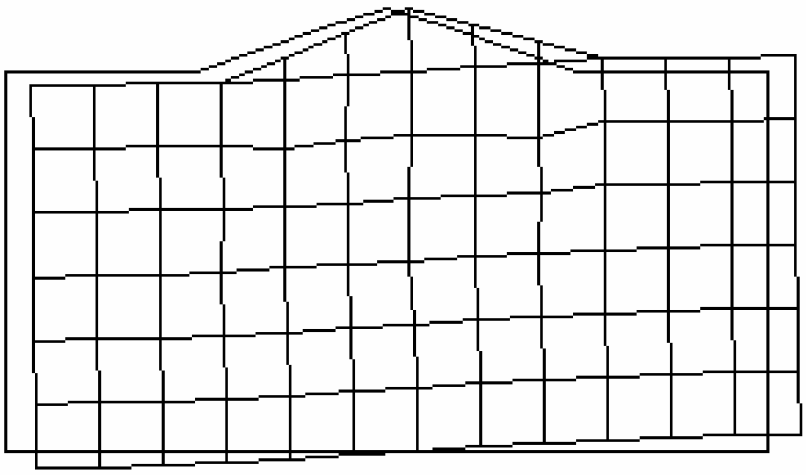

Figure 5.27: Displacement of the dyke and the 'near-field' soil after 14.38 s (magnification factor 10000) (discretization, see, figure 5.26

(a)

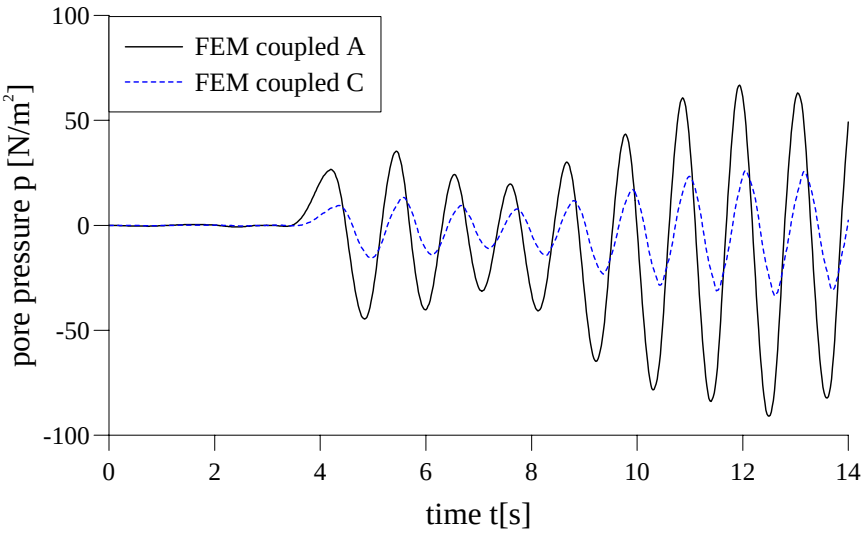

(b)

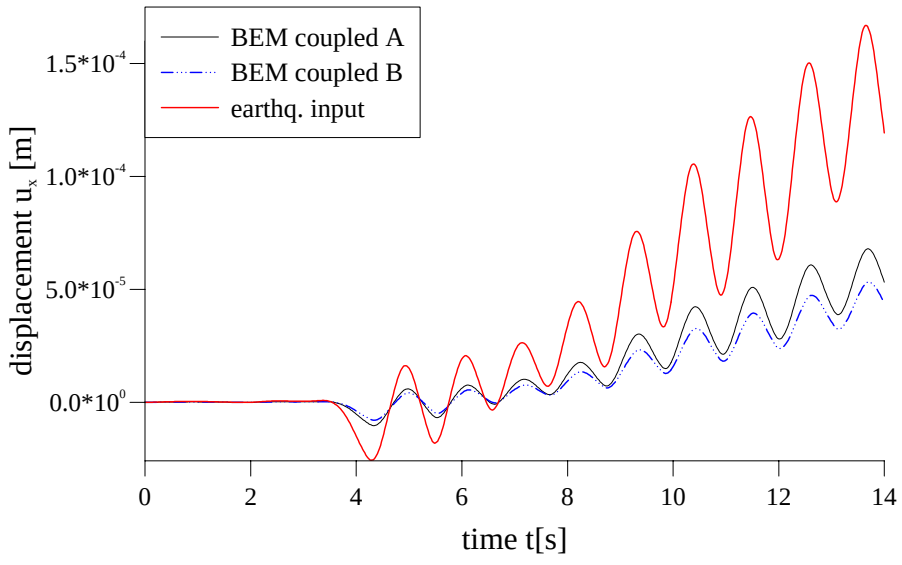

Figure 5.28: Dyke at point C i.e., **(a)** pore pressure p **(b)** displacement u_x, (discretization, see, figure 5.26)

Conclusions

Significant damage of foundations and tilted buildings are results from ground liquefaction. This phenomenon appears when during an earthquake motion the interstitial pore pressure increases. This implies a reduction of the interparticle forces in the solid phase of the soil and its strength. The main characteristics of the numerical procedure for the simulation of ground liquefaction are:

- The description by the behavior of a two phase material, fluid filled saturated pores and solid skeleton, in the form of Biot's theory of porous media.
- The enhancement of the constitutive model with respect to nonlinear soil behavior and
- the application of the earthquake motion.

These demands have to be considered. Therefore, the infinite-domain is subdivided into a near-field (FEM), including local-nonlinarity, and a far-field (BEM), to enable energy dissipation through radiation. Consequently, for treating wave propagation problems in a non-linear poroelastic model, a coupled BE-FE procedure is the best choice. Since iterative coupling algorithms exists so far only for elasticity problems, an enhanced version is necessary.

In this work, an iterative coupling algorithm for FEM and BEM subdomains for time-dependent poroelastic media has been developed. The proposed algorithm is based on the sequential Dirichlet-Neumann method with double relaxation. Furthermore, this algorithm was applied to the coupling of linear and non-linear poroelastic problems, e.g., ground liquefaction. The major advantage of the iterative coupling procedure, deduced here, is, compared to conventional, direct coupling procedure, that a global coupled coefficient matrix of FE and BE subdomains can be avoided. The iterative coupling algorithm enables the use of appropriate equation solver which are optimized with respect to the employed subdomain analysis method. By means of the proposed iterative coupling scheme for porous media, the FEM program SWANDYNE, developed by the Computational Engineering group of the department of Civil Engineering, University of Birmingham was coupled with the BEM code of the Institute of Applied Mechanics of Civil Engineering, University of Braunschweig. For the coupling of the FEM with the BEM the same basic assumptions of the physical conditions are required. The used FEM is based on the u-p formulation of Biot's theory of porous media with neglected derivative of the seepage velocity, termed simplified poroelasticity.

Simplified poroelasticity In order to receive an identical formulation for the BEM, a fundamental solution for simplified poroelasticity was developed in both 2-d and 3-d, and implemented in the program. For different examples, this formulation has been compared with the time domain formulation of the general poroelastic model [145]. The program has been validated on examples where analytical solutions are available. A 1-d column was investigated analytically and compared with the approximated results of the simplified poroelastic solution, and a half space under a vertical load was considered for studying the difference between the

complete u-p formulation and the formulation with omitting the derivative of the seepage velocity. For the investigated materials, the solution from the simplified poroelasticity matches the solution of the general poroelastic model very well. Hence, the influence of the derivative of the seepage velocity can be neglected. This corresponds to the findings of Zienkiewicz et al. [187]. The range of applicability of the simplified theory of poroelasticity was investigated by Zienkiewicz et al. [187]. There, it is pointed out that the simplified theory can be used for the low frequencies range, e.g., earthquakes, without loss of accuracy. Only for explicit transients, where shocks and very high frequency are involved, the general poroelastic model has to be used [186].

Iterative coupling An essential requirement of the numerical model is the approximation of the infinite half-space. The infinite half space is discretized as a two-phase medium with an absorbing boundary which avoids the reflection of any outgoing wave. This is achieved by coupling the FEM with a time domain linear BE formulation using the sequential Dirichlet-Neumann algorithm which is deduced in the present work for poroelastic media. An interface relaxation algorithm for coupling the FEM domain with the BEM domain existed so far only for application in linear elastostatics developed by Lin [103] and also by Feng and Owen [76]. The later was enhanced in the present work for application in poroelasticity. This algorithm has been applied and verified not only for linear poroelastic problems, but also for coupling of linear and non-linear poroelastic problems, like liquefaction. It could be confirmed by the investigated examples that a good choice of the first relaxation parameter for the displacements considerably influences the convergence behavior. For applications to linear elastostatics, this was studied by Elleithy et al. [67, 70]. For the coupling of the fluid a third and a fourth relaxation parameter were introduced in the proposed algorithm. Further, it was found out that the established fourth relaxation parameter for the flux is of great importance for the convergence behavior of the iterative coupling algorithm, whereas the relaxation substep of the tractions is insignificant. The relaxation parameter for the pore pressure improves the convergence characteristics for the poroelastic case. The validity of the enhanced sequential Dirichlet-Neumann algorithm for poroelastic media was proven by solving different examples. For application in poroelasticity, the algorithm was checked for a poroelastic column and for a semi-infinite domain. The tested coupled examples were compared with those obtained using the FEM and the BEM separately. By this comparison for the poroelasticity case, excellent results were obtained which matched nearly exactly to the expected ones. The stability and accuracy of the proposed algorithm was shown with respect to influence of spatial discretization and time step size. Further, the validity for non-linear material behavior, like liquefaction, could be determined. Numerical studies have been conducted to study the suitability of the proposed coupling algorithm for different material parameters in the non-linear FEM subdomain, for reaching the limit state of liquefaction and for seismic input.
A limitation of the model is the requirement that the locations of the nodal points of both subdomains match along the interface. This could be achieved by the development and implementation of mortar domain decomposition methods which are available for elliptic partial differential equations [169] and which have to be developed for hyperbolic partial differential equations. The accuracy of the here proposed numerical model could be enhanced, if in the BEM formulation the gravitation acceleration would be taken into account, i.e., an initial stress

state could be obtained directly for the whole domain. Further, a parallel implementation of the proposed algorithm should speed the physical time required for the computation [88].

The purpose of this work – to establish a complete numerical model for the simulation of seismically induced liquefaction – by developing an iterative coupling algorithm for wave propagation in a non-linear poroelastic model and deducing a simplified poroelastic formulation for the BEM is achieved. Hence, with the developed numerical model, different geotechnical actions, e.g., densification, lowering of the ground water table, replacing the soil, can be simulated and their benefit to reduce the vulnerability of the exposed objects due to liquefaction can be assessed.

A Explicit Expressions for the Fundamental Solutions

A.1 Fundamental solutions

The explicit expressions of the poroelastodynamic fundamental solutions for the simplified poroelastic model are given in the following for a 2-d and 3-d continuum.

A.1.1 Solutions in 3-d

The elements of the matrix **G** (3.14) are the displacements caused by a Dirac force in the solid

$$\hat{U}^{\mathrm{s}}_{ij} = \frac{1}{4\pi r\rho s^2}\left[R_1\frac{\lambda_4^2-\lambda_2^2}{\lambda_1^2-\lambda_2^2}e^{-\lambda_1 r} - R_2\frac{\lambda_4^2-\lambda_1^2}{\lambda_1^2-\lambda_2^2}e^{-\lambda_2 r} + \left(\delta_{ij}\lambda_3^2 - R_3\right)e^{-\lambda_3 r}\right] \tag{A.1a}$$

with $R_k = \frac{3r_{,i}r_{,j}-\delta_{ij}}{r^2} + \lambda_k\frac{3r_{,i}r_{,j}-\delta_{ij}}{r} + \lambda_k^2 r_{,i}r_{,j}$ and $\lambda_4^2 = \frac{s^2\rho}{K+\frac{4}{3}G}$. The pressure caused by the same load is

$$\hat{P}^{\mathrm{s}}_j = \frac{\alpha r_{,i}}{4\pi r\kappa\left(K+\frac{4}{3}G\right)\left(\lambda_1^2-\lambda_2^2\right)}\left[\left(\lambda_1+\frac{1}{r}\right)e^{-\lambda_1 r} - \left(\lambda_2+\frac{1}{r}\right)e^{-\lambda_2 r}\right]. \tag{A.1b}$$

For a Dirac source in the fluid the respective displacement solution is

$$\hat{U}^{\mathrm{f}}_i = \left(1-\frac{s\rho_{\mathrm{f}}\kappa}{\alpha}\right)s\hat{P}^{\mathrm{s}}_i \tag{A.1c}$$

and the pressure

$$\hat{P}^{\mathrm{f}} = \frac{1}{4\pi r\kappa\left(\lambda_1^2-\lambda_2^2\right)}\left[\left(\lambda_1^2-\lambda_4^2\right)e^{-\lambda_1 r} - \left(\lambda_2^2-\lambda_4^2\right)e^{-\lambda_2 r}\right]. \tag{A.1d}$$

In the above given solutions the roots $\lambda_i,\ i=1,2,3$ from (3.9) are used.

In the derivation of the poroelastodynamic boundary integral equation (3.20) several abbreviations (3.21) corresponding to an 'adjoint' traction or flux are introduced. First, the 'adjoint' traction solution is presented. However, due to the extensive expression only parts are given

$$\hat{T}^{\mathrm{s}}_{ij} = \left[\left(\left(K-\frac{2}{3}G\right)\hat{U}^{\mathrm{s}}_{kj,k} + \alpha s\hat{P}^{\mathrm{s}}_j\right)\delta_{i\ell} + G\left(\hat{U}^{\mathrm{s}}_{ij,\ell} + \hat{U}^{\mathrm{s}}_{\ell j,i}\right)\right]n_\ell \tag{A.2a}$$

$$\hat{U}^{\mathrm{s}}_{kj,k}\delta_{i\ell}n_\ell = \frac{r_{,j}n_i}{4\pi r s^2\rho\left(\lambda_1^2-\lambda_2^2\right)}\left[e^{-\lambda_1 r}\left(\frac{1}{r}+\lambda_1\right)\lambda_1^2\left(\lambda_2^2-\lambda_4^2\right) - e^{-\lambda_2 r}\left(\frac{1}{r}+\lambda_2\right)\lambda_2^2\left(\lambda_1^2-\lambda_4^2\right)\right]$$

$$\begin{aligned}\left(\hat{U}^{\mathrm{s}}_{ij,\ell}+\hat{U}^{\mathrm{s}}_{\ell j,i}\right)n_\ell = \frac{1}{4\pi r s^2\rho}\Bigg[&\frac{R_5 6}{r^3}\left(\frac{\lambda_4^2-\lambda_2^2}{\lambda_1^2-\lambda_2^2}e^{-\lambda_1 r}-\frac{\lambda_4^2-\lambda_1^2}{\lambda_1^2-\lambda_2^2}e^{-\lambda_2 r}-e^{-\lambda_3 r}\right)\\ &+\frac{R_5 6}{r^2}\left(\frac{\lambda_4^2-\lambda_2^2}{\lambda_1^2-\lambda_2^2}\lambda_1 e^{-\lambda_1 r}-\frac{\lambda_4^2-\lambda_1^2}{\lambda_1^2-\lambda_2^2}\lambda_2 e^{-\lambda_2 r}-\lambda_3 e^{-\lambda_3 r}\right)\\ &+\frac{R_6 2}{r}\left(\frac{\lambda_4^2-\lambda_2^2}{\lambda_1^2-\lambda_2^2}\lambda_1^2 e^{-\lambda_1 r}-\frac{\lambda_4^2-\lambda_1^2}{\lambda_1^2-\lambda_2^2}\lambda_2^2 e^{-\lambda_2 r}-\lambda_3^2 e^{-\lambda_3 r}\right)\\ &-2r_{,n}r_{,i}r_{,j}\left(\frac{\lambda_4^2-\lambda_2^2}{\lambda_1^2-\lambda_2^2}\lambda_1^3 e^{-\lambda_1 r}-\frac{\lambda_4^2-\lambda_1^2}{\lambda_1^2-\lambda_2^2}\lambda_2^3 e^{-\lambda_2 r}-\lambda_3^3 e^{-\lambda_3 r}\right)\\ &-\lambda_3^2\left(\delta_{ij}r_{,n}+r_{,i}n_j\right)\left(\lambda_3+\frac{1}{r}\right)e^{-\lambda_3 r}\Bigg]\end{aligned}$$

with $R_5 = r_{,j}n_i + r_{,i}n_j + r_{,n}\left(\delta_{ij}-5r_{,i}r_{,j}\right)$ and $R_6 = r_{,j}n_i + r_{,i}n_j + r_{,n}\left(\delta_{ij}-6r_{,i}r_{,j}\right)$. The other explicit expressions are

$$\hat{Q}^{\mathrm{s}}_j = \frac{\alpha n_i}{4\pi r\left(K+\frac{4}{3}G\right)\left(\lambda_1^2-\lambda_2^2\right)}\left[R_2 e^{-\lambda_2 r}-R_1 e^{-\lambda_1 r}\right] \tag{A.2b}$$

$$\begin{aligned}\hat{T}^{\mathrm{f}}_i = \frac{1}{4\pi r\kappa\left(\lambda_1^2-\lambda_2^2\right)}\Bigg[&\frac{n_j s\left(\alpha-s\rho_{\mathrm{f}}\kappa\right)2G}{K+\frac{4}{3}G}\left(R_2 e^{-\lambda_2 r}-R_1 e^{-\lambda_1 r}\right)\\ &+n_i e^{-\lambda_2 r}\left(\frac{s\left(\alpha-s\rho_{\mathrm{f}}\kappa\right)\left(K-\frac{2}{3}G\right)}{K+\frac{4}{3}G}\lambda_2^2-\alpha s\left(\lambda_2^2-\lambda_4^2\right)\right)\\ &-n_i e^{-\lambda_1 r}\left(\frac{s\left(\alpha-s\rho_{\mathrm{f}}\kappa\right)\left(K-\frac{2}{3}G\right)}{K+\frac{4}{3}G}\lambda_1^2-\alpha s\left(\lambda_1^2-\lambda_4^2\right)\right)\Bigg]\end{aligned} \tag{A.2c}$$

$$\begin{aligned}\hat{Q}^{\mathrm{f}} = \frac{r_{,n}}{4\pi r\left(\lambda_1^2-\lambda_2^2\right)}\Bigg[&\left(\lambda_2+\frac{1}{r}\right)\left(\lambda_2^2-\lambda_4^2\right)e^{-\lambda_2 r}\\ &-\left(\lambda_1+\frac{1}{r}\right)\left(\lambda_1^2-\lambda_4^2\right)e^{-\lambda_1 r}\Bigg].\end{aligned} \tag{A.2d}$$

A.1.2 Solutions in 2-d

In 2-d, the expressions for displacements induced by a unit point force in the solid are

$$\hat{U}^{\mathrm{s}}_{ij} = \frac{1}{2\pi s^2\rho}\left(\frac{\lambda_4^2-\lambda_2^2}{\lambda_1^2-\lambda_2^2}R_1-\frac{\lambda_4^2-\lambda_1^2}{\lambda_1^2-\lambda_2^2}R_2+\left(\delta_{ij}\lambda_3^2 K_0(\lambda_3 r)-R_3\right)\right), \tag{A.3a}$$

the pressure for the same load is

$$\hat{P}_j^{\mathrm{s}} = \frac{\alpha r_{,i}}{2\pi\kappa(K+\frac{4}{3}G)}\left(\frac{\lambda_1 K_1(\lambda_1 r)}{(\lambda_1^2-\lambda_2^2)}+\frac{\lambda_2 K_1(\lambda_2 r)}{(\lambda_2^2-\lambda_1^2)}\right). \tag{A.3b}$$

The displacement fundamental solution for a fluid point source is

$$\hat{U}_i^{\mathrm{f}} = \left(1-\frac{s\rho_{\mathrm{f}}\kappa}{\alpha}\right) s\hat{P}_j^{\mathrm{s}}, \tag{A.3c}$$

and the pressure solution

$$\hat{P}^{\mathrm{f}} = \frac{1}{2\pi\kappa(\lambda_1^2-\lambda_2^2)}\left(K_0(\lambda_1 r)(\lambda_1^2-\lambda_4^2)-K_0(\lambda_2 r)(\lambda_2^2-\lambda_4^2)\right), \tag{A.3d}$$

with $R_k = (2r_{,i}r_{,j}-\delta_{ij})\frac{\lambda_k}{r}K_1(\lambda_k r)+r_{,i}r_{,j}\lambda_k^2 K_0(\lambda_k r)$ and $\lambda_4^2 = \frac{(s^2\rho)}{K+\frac{4}{3}G}$. K_0 and K_1 denote the modified Bessel Functions of the second kind.

In 2-d, the expressions for 'adjoint' traction and flux are

$$\hat{T}_{ij}^{\mathrm{s}} = \left[\left(\left(K-\frac{2}{3}G\right)\hat{U}_{kj,k}^{\mathrm{s}}+\alpha s\hat{P}_j^{\mathrm{s}}\right)\delta_{i\ell}+G\left(\hat{U}_{ij,\ell}^{\mathrm{s}}+\hat{U}_{\ell j,i}^{\mathrm{s}}\right)\right]n_\ell \tag{A.4a}$$

$$\hat{U}_{kj,k}^{\mathrm{s}}\delta_{i\ell}n_\ell = \frac{r_{,j}n_i}{2\pi s^2\rho\left(\lambda_1^2-\lambda_2^2\right)}\left[\lambda_1^3 K_1\left(\lambda_1 r\right)\left(\lambda_2^2-\lambda_4^2\right)-\lambda_2^3 K_1\left(\lambda_2 r\right)\left(\lambda_1^2-\lambda_4^2\right)\right]$$

$$\begin{aligned}\left(\hat{U}_{ij,\ell}^{\mathrm{s}}+\hat{U}_{\ell j,i}^{\mathrm{s}}\right)n_\ell =& \frac{1}{\pi}\left[\frac{\lambda_4^2-\lambda_2^2}{\lambda_3^2\left(\lambda_1^2-\lambda_2^2\right)}\left(R_7\frac{\lambda_1}{r}\left(\lambda_1 K_0\left(\lambda_1 r\right)+\frac{2K_1\left(\lambda_1 r\right)}{r}\right)-r_{,i}r_{,j}r_{,n}\lambda_1^3 K_1\left(\lambda_1 r\right)\right)\right.\\ &-\frac{\lambda_4^2-\lambda_1^2}{\lambda_3^2\left(\lambda_1^2-\lambda_2^2\right)}\left(R_7\frac{\lambda_2}{r}\left(\lambda_2 K_0\left(\lambda_2 r\right)+\frac{2K_1\left(\lambda_2 r\right)}{r}\right)-r_{,i}r_{,j}r_{,n}\lambda_2^3 K_1\left(\lambda_2 r\right)\right)\\ &\left.-\frac{R_7}{\lambda_3 r}\left(\lambda_3 K_0\left(\lambda_3 r\right)+\frac{2K_1\left(\lambda_3 r\right)}{r}\right)-\frac{r_{,n}\left(\delta_{ij}-2r_{,i}r_{,j}\right)+r_{,i}n_{,j}}{2}\lambda_3 K_1\left(\lambda_3 r\right)\right]\end{aligned}$$

with $R_7 = \left[r_{,n}\left(\delta_{ij}-4r_{,i}r_{,j}\right)+r_{,j}n_{,i}+r_{,i}n_{,}\right]\frac{1}{r}\lambda_1\left[\lambda_1 K_0\left(\lambda_1 r\right)+\frac{2K_1(\lambda_1 r)}{r}\right]-r_{,i}r_{,j}r_{,n}\lambda_1^3 K_1\left(\lambda_1 r\right)$.

The other explicit expressions are:

$$\begin{aligned}\hat{Q}_j^{\mathrm{s}} = \frac{1}{2\pi s^2\rho}&\left[\frac{r_{,j}r_{,n}}{\lambda_1^2-\lambda_2^2}\left(\alpha\lambda_4^2\lambda_2^2 K_0\left(\lambda_2 r\right)-\alpha\lambda_4^2\lambda_1^2 K_0\left(\lambda_1 r\right)\right)\right.\\ &\left.+\frac{2r_{,n}r_{,j}-n_j}{r\left(\lambda_1^2-\lambda_2^2\right)}\left(\alpha\lambda_4^2\lambda_2^2 K_1\left(\lambda_2 r\right)-\alpha\lambda_4^2\lambda_1^2 K_1\left(\lambda_1 r\right)\right)\right]\end{aligned} \tag{A.4b}$$

$$\begin{aligned}\hat{T}_i^{\mathrm{f}} =& \frac{1}{2\pi\kappa\left(\lambda_1^2-\lambda_2^2\right)\left(K+\frac{4}{3}G\right)}\Bigg[2r_{,i}r_{,n}s\left(\alpha-s\rho_{\mathrm{f}}\kappa\right)G \\ & \left(\left(\lambda_2^2K_0\left(\lambda_2 r\right)+\frac{\lambda_2}{r}K_1\left(\lambda_2 r\right)\right)-\left(\lambda_1^2K_0\left(\lambda_1 r\right)+\frac{\lambda_1}{r}K_1\left(\lambda_1 r\right)\right)\right) \\ & -2\left(n_i-r_{,i}r_{,n}s\left(\alpha-s\rho_{\mathrm{f}}\kappa\right)G\right)\left(\frac{\lambda_2}{r}K_1\left(\lambda_2 r\right)-\frac{\lambda_1}{r}K_1\left(\lambda_1 r\right)\right) \\ & +n_i\left[\left(K-\frac{2}{3}G\right)s\left(\alpha-s\rho_{\mathrm{f}}\kappa\right)\lambda_2^2-\alpha s\left(K+\frac{4}{3}G\right)\left(\lambda_2^2-\lambda_4^2\right)\right]K_0\left(\lambda_2 r\right) \\ & -n_i\left[\left(K-\frac{2}{3}G\right)s\left(\alpha-s\rho_{\mathrm{f}}\kappa\right)\lambda_1^2-\alpha s\left(K+\frac{4}{3}G\right)\left(\lambda_1^2-\lambda_4^2\right)\right]K_0\left(\lambda_1 r\right)\Bigg]\end{aligned} \tag{A.4c}$$

$$\hat{Q}^{\mathrm{f}} = \frac{r_{,n}}{2\pi\left(\lambda_1^2-\lambda_2^2\right)}\left[\left(\lambda_2^2-\lambda_4^2\right)\lambda_2K_1\left(\lambda_2 r\right)-\left(\lambda_1^2-\lambda_4^2\right)\lambda_1K_1\left(\lambda_1 r\right)\right] \tag{A.4d}$$

with $R_k = (2r_{,i}r_{,j}-\delta_{ij})\frac{\lambda_k}{r}K_1(\lambda_k r)+r_{,i}r_{,j}\lambda_k^2K_0(\lambda_k r)$.

B Mathematical Preliminaries

In the following, a few necessary mathematical definitions are recalled. For a rigorous presentation of these definitions, the reader is referred to the mathematical literature.

B.1 Matrix of Cofactors

The *matrix of cofactors* of an $n \times n$ square matrix $\mathbf{A}$ is defined as

$$\mathbf{A}^{co} = \begin{bmatrix} a_{11}^{co} & \dots & a_{1n}^{co} \\ \vdots & \ddots & \vdots \\ a_{n1}^{co} & \dots & a_{nn}^{co} \end{bmatrix}^{\mathrm{T}} , \tag{B.1}$$

where a_{ij}^{co} is the *cofactor* of element a_{ij} of the matrix $\mathbf{A}$. The cofactor is the determinant of the matrix with row i and column j deleted, prefixed with a sign depending on the element position, i.e.,

$$a_{ij}^{co} = (-1)^{i+j} \begin{vmatrix} a_{11} & \dots & a_{1\,j-1} & a_{1\,j+1} & \dots & a_{1n} \\ \vdots & \ddots & \vdots & \vdots & \ddots & \vdots \\ a_{i-1\,1} & \dots & a_{i-1\,j-1} & a_{i-1\,j+1} & \dots & a_{i-1\,n} \\ a_{i+1\,1} & \dots & a_{i+1\,j-1} & a_{i+1\,j+1} & \dots & a_{i+1\,n} \\ \vdots & \ddots & \vdots & \vdots & \ddots & \vdots \\ a_{n1} & \dots & a_{n\,j-1} & a_{n\,j+1} & \dots & a_{nn} \end{vmatrix} . \tag{B.2}$$

Details may be found, e.g., in [121]. One of the most important properties of the cofactor matrix is its relation to the inverse matrix

$$\mathbf{A}^{-1} = \frac{1}{\det(\mathbf{A})} \mathbf{A}^{\mathrm{co}} . \tag{B.3}$$

B.2 Distributions or Generalized Functions

In many engineering fields, physical phenomena can not be described by functions, e.g., a point force at $x = a$ is everywhere zero except at the point $x = a$. Such a phenomenon is mostly treated with the Dirac "function". However, this is not a function but a distribution or generalized function. Also, sometimes it is necessary to differentiate a piecewise defined function, which is only possible in the theory of distributions. This theory was introduced by Schwartz [152]. Here, the definitions in a non mathematical way are given very briefly. Details or more mathematical rigorous treatment can be found, e.g., in [80] or [136]. The following definitions are taken from [136].

First, a more general definition of functions, the *linear functional*

$$\langle f, \varphi \rangle = \int_{-\infty}^{\infty} f(x)\, \varphi(x)\, \mathrm{d}x \tag{B.4}$$

has to be introduced with the *test function* $\varphi(x)$. Contrary to the classical function which associates a number $y = f(x)$ with every point x (the value of f at x), in the definition (B.4) the value of the functional $\langle f, \varphi \rangle$ is also a number, but represents a "weighted average" of the function f weighted by the test function φ. Such an indirect description of a function is common in engineering. A measuring instrument, such as a voltmeter, does not measure the instantaneous value $f(t_0)$ of the voltage at time t_0, but rather a weighted average over a short time period of time $2T : 1/2T \int_{t_0-T}^{t_0+T} f(t)\, \varphi(t)\, \mathrm{d}t$, where φ is a characteristics of the measuring instrument.

For our purpose here, the treatment of integral- and differential equations, it will be convenient to restrict the term test function to those functions φ that are continuous, have continuous derivatives of all orders, and vanish outside of a certain finite interval, i.e.,

DEFINITION B.2.1 A *test function* φ belongs to the space of C^∞ functions and has a compact support. The *support* of a function $f(x)$ is the closure of the set of points on which $f(x) \neq 0$.

To find a function in C^∞, i.e., vanishing outside of a certain finite interval and with continuous derivatives of all orders, is easy, but for a test function the derivatives of all orders must also be continuous at the boundaries, i.e., they must also vanish. The following function fulfills all conditions and, therefore, can be test a function

$$\varphi(x) = \begin{cases} e^{\frac{1}{x^2-1}} & |x| < 1 \\ 0 & |x| \geq 1\,. \end{cases} \tag{B.5}$$

The compact support in equation (B.5) is $[-1, 1]$ and all derivatives vanish at $|x| = 1$ [159].

For the following a definition of convergence of a test function is necessary:

DEFINITION B.2.2 A sequence $\varphi_n(x)$ of test functions *converges to zero* ($\varphi_n \to 0$) if:

(a) for each k, the sequence of kth derivatives $\varphi_1^{(k)}, \varphi_2^{(k)}, \ldots$ converges uniformly to zero;

(b) the φ_n have uniformly bounded supports, i.e., there is an interval $[a, b]$, independent of n, such that every $\varphi_n(x)$ vanishes outside of $[a, b]$.

Similarly, it is valid that $\varphi_n \to \varphi$ if the sequence $(\varphi - \varphi_n) \to 0$.

With the definition of the linear functional, now, the derivative of function f can be defined even if f is not continuous at every point. The derivative of a linear functional and later also of a distribution is given

$$\langle f', \varphi \rangle = \int_{-\infty}^{\infty} f'(x)\, \varphi(x)\, \mathrm{d}x = -\int_{-\infty}^{\infty} f(x)\, \varphi'(x)\, \mathrm{d}x = -\langle f, \varphi' \rangle\,. \tag{B.6}$$

For a continuously differentiable function f equation (B.6) results from integration by parts. The boundary terms in the partial integration vanish due to the compact support of the test function φ. A very important and often used not continuous function is the *Heaviside* or *Unit step* function

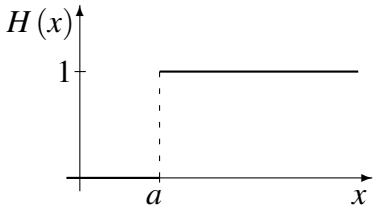

$$H(x-a) = \begin{cases} 0 & x < a \\ 1 & x > a \,. \end{cases} \tag{B.7}$$

With definition (B.6) a derivative for all x is possible

$$\begin{aligned} \langle H'(x-a), \varphi \rangle &= -\langle H(x-a), \varphi' \rangle = -\int_{-\infty}^{\infty} H(x-a)\,\varphi'(x)\,\mathrm{d}x = -\int_{a}^{\infty} \varphi'(x)\,\mathrm{d}x \\ &= \varphi(a) \ , \end{aligned} \tag{B.8}$$

using the property $H(x<a) = 0$ and in the last step that a test function vanishes as $x \to \infty$ (compact support). However, the result is not a function in the usual sense, it is a *distribution* or *generalized function*. The distribution in (B.8) is known as the *Dirac* distribution $\delta(x)$ with the known *filter* property

$$\int_{-\infty}^{\infty} \delta(x-a)\,\varphi(x)\,\mathrm{d}x = \varphi(a) \ . \tag{B.9}$$

As a consequence of equation (B.8), it is found

$$H'(x-a) = \delta(x-a) \quad \text{and} \quad H(x-a) = \int_{-\infty}^{x-a} \delta(t)\,\mathrm{d}t = \begin{cases} 0 & x < a \\ 1 & x > a \,. \end{cases} \tag{B.10}$$

With (B.9) a distribution was introduced without a definition which will follow now:

DEFINITION B.2.3 A *distribution* T is a mapping from the set of all test functions into the real or complex numbers, such that the following conditions hold:

(a) (Linearity) $\langle T, a\varphi(x) + b\psi(x) \rangle = a \cdot \langle T, \varphi(x) \rangle + b \cdot \langle T, \psi(x) \rangle$ for all test functions φ, ψ and all constants a, b.

(b) (Continuity) If $\varphi_n(x) \to 0$ in the sense defined in definition B.2.2, then $\langle T, \varphi_n(x) \rangle \to 0$

DEFINITION B.2.4 Let $f(x)$ be a piecewise continuous function on the real axis. Then we define the distribution T_f corresponding to f by

$$\langle T_f, \varphi(x) \rangle = \int_{-\infty}^{\infty} f(x)\,\varphi(x)\,\mathrm{d}x \,. \tag{B.11}$$

With the last definition the connection between the "normal" functions and the distributions are given. Distributions which are definable in terms of locally integrable functions according to equation (B.11) are called *regular* distributions. All other distributions are called *singular* distributions.

Finally, the properties of the distributions must be presented.

DEFINITION B.2.5 Let S and T be arbitrary distributions. Then we define new distributions $S+T, aT\,(a=\text{constant}), T', T\,(ax)\,(a\neq 0 \text{ is constant}), T\,(x-a), g\,(x)\,T\,(x)$ (where $g\,(x)$ is a C^{∞} function) by:

$$\langle S+T,\varphi\rangle = \langle S,\varphi\rangle + \langle T,\varphi\rangle \tag{B.12a}$$

$$\langle aT,\varphi\rangle = a\langle T,\varphi\rangle \tag{B.12b}$$

$$\langle T',\varphi\rangle = -\langle T,\varphi'\rangle \tag{B.12c}$$

$$\langle T\,(ax),\varphi\rangle = |a|^{-1}\langle T,\varphi\left(\frac{x}{a}\right)\rangle \tag{B.12d}$$

$$\langle T\,(x-a),\varphi\rangle = \langle T,\varphi\,(x+a)\rangle \tag{B.12e}$$

$$\langle g\,(x)\,T\,(x),\varphi\rangle = \langle T,g\,(x)\,\varphi\,(x)\rangle \tag{B.12f}$$

These, together with convolution (see, e.g., [136]), are the primary operations on distributions. This may seem a rather restrictive list, e.g., there is no definition for the product $S\cdot T$ of two distributions. Unfortunately, the price to be paid for introducing generalized functions (distributions) is that many operations on ordinary functions make no sense in this wider context.

The derivative of a functional was introduced with (B.6) which can be directly applied to distribution as equation (B.12c) shows. For a repeated derivation the rule (B.12c) can be generalized

$$\langle D^k T,\varphi\,(x)\rangle = (-1)^k\,\langle T,\varphi^{(k)}\,(x)\rangle \tag{B.13}$$

with the differential operator D^k denoting the k-th derivative. Thus, equation (B.13) yields the remarkable conclusion that every distribution can be differentiated as often as desired. A distribution can of course be generated by functions which are not differentiable in the ordinary sense, but the theory of distribution provides a way to differentiate such functions in the distributional sense resulting in a distribution, e.g., the Heaviside function.

A final remark must be added. All of the above mentioned can be applied also to n-dimensional distributions.

B.3 Convolution Quadrature Method

The 'Convolution Quadrature Method' developed by Lubich numerically approximates a convolution integral for $n=0,1,\ldots,N$

$$y\,(t)=\int_0^t f\,(t-\tau)\,g\,(\tau)\,\mathrm{d}\tau \quad\rightarrow\quad y\,(n\Delta t)=\sum_{k=0}^{n}\omega_{n-k}\,(\Delta t)\,g\,(k\Delta t)\,, \tag{B.14}$$

by a quadrature rule whose weights are determined by the Laplace transformed function $\hat{f}$ and a linear multistep method. This method was originally published in [105] and [106]. Application to the boundary element method may be found in [147]. Here, a brief overview of the method is given.

In formula B.14, the time t is divided in N equal steps Δt. The weights $\omega_n(\Delta t)$ are the coefficients of the power series

$$\hat{f}\left(\frac{\gamma(z)}{\Delta t}\right) = \sum_{n=0}^{\infty} \omega_n(\Delta t)\, z^n \tag{B.15}$$

with the complex variable z. The coefficients of a power series are usually calculated with Cauchy's integral formula. After a polar coordinate transformation, this integral is approximated by a trapezoidal rule with L equal steps $\frac{2\pi}{L}$. This leads to

$$\omega_n(\Delta t) = \frac{1}{2\pi i} \int\limits_{|z|=\mathscr{R}} \hat{f}\left(\frac{\gamma(z)}{\Delta t}\right) z^{-n-1}\, \mathrm{d}z \approx \frac{\mathscr{R}^{-n}}{L} \sum_{\ell=0}^{L-1} \hat{f}\left(\frac{\gamma\left(\mathscr{R} e^{i\ell\frac{2\pi}{L}}\right)}{\Delta t}\right) e^{-in\ell\frac{2\pi}{L}}, \tag{B.16}$$

where $\mathscr{R}$ is the radius of a circle in the domain of analyticity of $\hat{f}(z)$.

The function $\gamma(z)$ is the quotient of the characteristic polynomials of the underlying multistep method, e.g., for a BDF 2, $\gamma(z) = \frac{3}{2} - 2z + \frac{1}{2}z^2$. The used linear multistep method must be $A(\alpha)$-stable and stable at infinity [106]. Experience shows that the BDF 2 is the best choice [143]. Therefore, it is used in all calculations in this thesis.

If one assumes that the values of $\hat{f}(z)$ in B.16 are computed with an error bounded by ε, then the choice $L = N$ and $\mathscr{R}^N = \sqrt{\varepsilon}$ yields an error in ω_n of size $\mathscr{O}\left(\sqrt{\varepsilon}\right)$ [105]. Several tests conducted in [146] lead to the conclusion that the parameter $\varepsilon = 10^{-10}$ is the best choice for the kind of functions dealt with here. The assumption $L = N$ leads to a order of complexity $\mathscr{O}\left(N^2\right)$ for calculating the N coefficients $\omega_n(\Delta t)$. Due to the exponential function at the end of formula B.16 this can be reduced to $\mathscr{O}(N \log N)$ using the technique of the Fast Fourier Transformation (FFT).

Notation Index

$\mathbf{A}$	matrix or matrix differential operator
$\mathbf{A}^*$	adjoint operator matrix
$\mathbf{A}^{\mathrm{co}}$	matrix of cofactors
$\mathbf{B}^{\mathrm{F}}$	displacement-strain transformation matrix
$\mathbf{a}$	vector
$a(t)$	source in the pore fluid
α	Biot's effective stress coefficient
α, β, γ, δ	relaxation parameter
c_{ij}	integral free term
$\gamma = 0.577216$	Euler constant
δ_{ij}	Kronecker symbol
$\delta(t)$	Dirac distribution
E	Young's modulus
ε_{ij}	component of the strain tensor
ε_{p}	equivalent plastic strain
$\varepsilon_{ij}^{\mathrm{P}}$	plastic strain
$d\varepsilon_{ij}^{\mathrm{P}}$	plastic strain increment
$\varepsilon_{kk}^{\mathrm{e}}$	elastic volumetric strain
$\varepsilon_{kk}^{\mathrm{P}}$	plastic volumetric strain
$d\varepsilon_{\mathrm{s}}^{\mathrm{e}}$	elastic deviatoric part of the strain increment
$d\varepsilon_{\mathrm{v}}^{\mathrm{p}}$	plastic volumetric part of the strain increment
f	yield function
$\partial f/\partial\sigma_{ij}$	gradient vector of the yield function
F_i	component of bulk body force
$\mathbf{G}$	fundamental solutions matrix
g	plastic potential function
$\partial g/\partial\sigma_{ij}$	gradient vector of the plastic potential
G	shear modulus
$\mathbf{G}^{\mathrm{F}}$	dynamic seepage force matrix
$d\gamma_{oct}$	octahedral plastic shear strain increment
$H(t)$	Heaviside- or unit step function
$\mathbf{H}^{\mathrm{F}}$	permeability matrix
$\mathbf{I}$	identity matrix
I_1	first invariant of the stress tensor σ_{ij}
$\mathbf{J}$	jacobian matrix
J_2, J_3	second and third invariant of the deviatoric stress tensor S_{ij}
$\mathbf{K}^{\mathrm{F}}$	linear elastic stiffness matrix

$\mathbf{K_T}^{\mathrm{F}}$	tangential stiffness matrix
K	compression modulus
K_{s}	compression modulus of the solid grains
K_{f}	compression modulus of the fluid
$K_i(z)$	i-th order modified Bessel function of second kind
κ	permeability
L	amount of integration steps for determining ω_n
$\mathbf{M}$	converting matrix
$d\lambda$	a non-negative scalar
λ_k	root of the operator matrix determinant Eq. (3.9)
$\mathbf{M}^{\mathrm{F}}$	mass matrix
N	total amount of time steps
$N_e^{\mathrm{f}}(\mathbf{x})$	spatial shape function
N_i^{u} N^{p}	shape function
$\mathbf{n}$, n_i	normal vector, it's component
ν	Poisson's ratio
ν_p	specific volume
$P_j^{\mathrm{s}}, P^{\mathrm{f}}$	pore pressure fundamental solutions
p	pore pressure
ϕ	porosity
$\mathbf{Q}^{\mathrm{F}}$	coupling matrix
$Q_j^{\mathrm{s}}, Q^{\mathrm{f}}$	flux fundamental solutions
q	specific flux
ρ	bulk density
ρ_{f}	fluid density
ρ_{s}	solid density
ρ_{a}	apparent mass density
$r = \lvert\mathbf{x}-\mathbf{y}\rvert$	distance of the points $\mathbf{x}$ and $\mathbf{y}$
$\mathbf{r} = \mathbf{x}-\mathbf{y}$	distance vector
R	poroelastic material parameter (1.4)
$\mathscr{R}$	radius of a circle in the domain of analyticity of $\hat{f}\left(\frac{\gamma(z)}{\Delta t}\right)$
$\mathbf{S}^{\mathrm{F}}$	compressibility matrix
S_{ij}	stress deviator tensor
$s \in \mathbb{C}$	complex Laplace variable
σ_0	yield stress in simple tension
σ_e	equivalent stress $\equiv$ τ_{oct} octahedral shear stress
σ_{ij}	component of the total stress tensor
$\sigma_{ij}^{\mathrm{s}}, \sigma^{\mathrm{f}}$	solid resp. fluid partial stress
$T_{ij}^{\mathrm{s}}, T_i^{\mathrm{f}}$	fundamental solutions of the traction
t_i	traction vector component
t, τ	time

τ_{oct}	the octahedral shear stress
Δt	time step size
$U_{ij}^{\mathrm{s}}, U_i^{\mathrm{f}}$	fundamental solutions of the displacement
$u_i^{\mathrm{s}}, u_i^{\mathrm{f}}$	displacement vector component
$u_i^\star$ $v_i^\star$	set of arbitrary weighting functions
V	volume
ω_n	integration weight
Ω, Γ	domain with boundary
ζ	variation of fluid volume per unit reference volume
$()^{\mathrm{s}}, ()^{\mathrm{f}}$	solid, fluid
$\|\cdot\|$	norm of $\cdot$
$\frac{\partial}{\partial()}$	partial derivative
∂_i or $()_{,i}$	partial derivative with respect to x_i
$\nabla = [\partial_i]^{\mathrm{T}}$, $\nabla^2 = \partial_i \partial_i$	Nabla operator
$\dot{()}$	time derivative
$f(t) * g(t)$	convolution of the functions $f(t)$ and $g(t)$
$f(x) = \mathscr{O}(g(x))$	Landau symbol: $\lim_{x \to x_0} \left\| \frac{f(x)}{g(x)} \right\| < C$
$\mathscr{L}\{f(t)\}, \hat{f}(s)$	Laplace transform of f
$\mathscr{L}^{-1}\{\hat{f}(s)\}$	inverse Laplace transform of f
$\Re(s), \Im(s)$	real and imaginary part of complex number s

Bibliography

[1] Antes, H.: A Boundary Element Procedure for Transient Wave Propagations in Two-dimensional Isotropic Elastic Media. *Finite Elements in Analysis and Design*, **1**, 313–322, 1985.

[2] Antes, H.; Latz, K.: Soil–Structure–Fluid Interaction. In *Boundary Element Techniques in Geomechanics*. (Manolis, G.D.; Davies, T.G., Eds.), Elsevier, London, Chapter 12, 408–442, 1993.

[3] Antes, H.; von Estorff, O.: Dynamic Soil-Structure Interaction by BEM in the Time and Frequency Domain. *In Proc. 8th Europ. Conference on Earthquake Engineering 2*, 5.5/30-40 Lab. Nac. Eng. Civil, Lisbon, 1986.

[4] Antes, H.; von Estorff, O.: Transient Behavior of Strip Foundations Resting on Different Soil Profiles by Time Domain B.E.M.. In *Proc. Conf. Soil Dynamics Earthquake Engng.* (Cakmak, A.S., Ed.), Princeton, 291–305, 1987.

[5] Antes, H.; von Estorff, O.: Dynamic Response Analysis of Rigid Foundations and of Elastic Structures by Boundary Element Procedures. *Soil Dynamics and Earthquake Engineering*, **8**, 68–74, 1989.

[6] Babuska, I.: Error Bounds for finite element methods. *Numerische Mathematik*, **16**, 322–333, 1971.

[7] Babuska, I.: The Finite Element Method with Lagrange Multipliers. *Numerische Mathematik*, **20**, 179–192, 1973.

[8] Banerjee, P.K.; Butterfield, R.: Boundary Element Methods in Geomechanics. In *Finite Elements in Geomechanics*. (Gudehus, G., Ed.), J. Wiley and Sons, London, 529–570, 1977.

[9] Beer, G.; Meek, J.L.: The coupling of boundary and finite element methods for infinite domain problems in elasticity. In *Boundary element methods*. (Brebbia, C.A., Ed.), Springer Verlag, Berlin, 575–591, 1981.

[10] Beskos, D.E.: Boundary Element Methods in Dynamic Analysis. *Applied Mechanics Review*, **40**(1), 1–23, 1987.

[11] Beskos, D.E.: Introduction to Boundary Element Methods. In *Boundary Element Methods in Mechanics*. (Beskos, D.E., Ed.), Mechanics and Mathematical Methods, North-Holland, Amsterdam, New York, 1–21, 1987.

[12] Beskos, D.E.: Boundary Element Methods in Dynamic Analysis: Part II (1986-1996). *Applied Mechanics Review*, **50**(3), 149–197, 1997.

[13] Beskos, D.E.: Dynamic Analysis of Structures and Structural Systems. In *Boundary Element Advances in Solid Mechanics*. (Beskos, D.E.; Maier, G., Eds.), Vol. 440, *CISM*, Springer-Verlag, Wien, Chapter 1, 1–54, 2003.

[14] Bettess, P.: *Infinite Elements*. Penshaw Press, 1992.

[15] Biot, M.A.: Consolidation settlement under a rectangular load distribution. *Journal of Applied Physics*, **12**, 426–430, 1941.

[16] Biot, M.A.: General Theory of Three-Dimensional Consolidation. *Journal of Applied Physics*, **12**, 155–164, 1941.

[17] Biot, M.A.: Theory of Elasticity and Consolidation for a Porous Anisotropic Solid. *Journal of Applied Physics*, **26**, 182–185, 1955.

[18] Biot, M.A.: Theory of Deformation of a Porous Viscoelastic Anisotropic Solid. *Journal of Applied Physics*, **27**(5), 459–467, 1956.

[19] Biot, M.A.: Theory of Propagation of Elastic Waves in a Fluid-Saturated Porous Solid. I. Low-Frequency Range, II. Higher Frequency Range. *Journal of the Acoustical Society of America*, **28**(2), 168–191, 1956.

[20] Biot, M.A.: Theory of Propagation of Elastic Waves in a Fluid-Saturated Porous Solid.I. Low-Frequency Range. *Journal of the Acoustical Society of America*, **28**(2), 168–178, 1956.

[21] Biot, M.A.: Theory of Propagation of Elastic Waves in a Fluid-Saturated Porous Solid.II. Higher Frequency Range. *Journal of the Acoustical Society of America*, **28**(2), 179–191, 1956.

[22] Bonnet, G.: Basic Singular Solutions for a Poroelastic Medium in the Dynamic Range. *Journal of the Acoustical Society of America*, **82**(5), 1758–1762, 1987.

[23] Bonnet, G.; Auriault, J.-L.: Dynamics of Saturated and Deformable Porous Media: Homogenization Theory and Determination of the Solid-Liquid Coupling Coefficients. In *Physics of Finely Divided Matter*. (Boccara, N.; Daoud, M., Eds.), Springer Verlag, Berlin, 306–316, 1985.

[24] Bowen, R.M.: Theory of Mixtures. In *Continuum Physics*. (Eringen, A.C., Ed.), Vol. III, Acadenic Press, New York, 1–127, 1976.

[25] Bowen, R.M.: Incompressible Porous Media Models by use of the Theory of Mixtures. *International Journal of Engineering Science*, **18**, 1129–1148, 1980.

[26] Bowen, R.M.: Compressible Porous Media Models by use of the Theory of Mixtures. *International Journal of Engineering Science*, **20**(6), 697–735, 1982.

[27] Brebbia, C.A.: *The Boundary Element Method for Engineers*. Pentech Press, London, 1978.

[28] Brebbia, C.A.; Domínguez, J.: Boundary Element Methods for Potential Problems. *Applied Mathematical Modeling*, **1**, 372–378, 1977.

[29] Brebbia, C.A.; Georgiou, P.: Combination of boundary and finite elements in elastostatics. *Applied Mathematical Modeling*, **3**, 212 – 220, 1979.

[30] Brebbia, C.A.; Telles, J.C.F.; Wrobel, L.C.: *Boundary Element Techniques*. Springer-Verlag, Berlin, New York, 1984.

[31] Brezzi, F.: On the existence, uniqueness and approximation of saddle point problems arising from Lagrange multipliers. *R.A.I.R.D.*, 1974.

[32] Burland, J.B.: *Deformation of Soft Clays, Ph.D.Thesis*. Cambridge University, Cambridge, 1967.

[33] Castro, G.: *Liquefaction of sands*. PhD thesis, Harvard University, Harvard Soil Mechanics, 1969. Series No. 81.

[34] Chan, A.H.C.: *A unified Finite Element Solution to Static and Dynamic Geomechanics problems*. PhD thesis, University College of Swansea, Wales, 1988.

[35] Chen, J.: Time Domain Fundamental Solution to Biot's Complete Equations of Dynamic Poroelasticity. Part I: Two-Dimensional Solution. *International Journal of Solids and Structures*, **31**(10), 1447–1490, 1994.

[36] Chen, J.: Time Domain Fundamental Solution to Biot's Complete Equations of Dynamic Poroelasticity. Part II: Three-Dimensional Solution. *International Journal of Solids and Structures*, **31**(2), 169–202, 1994.

[37] Chen, J.; Dargush, G.F.: Boundary Element Method for Dynamic Poroelastic and Thermoelastic Analysis. *International Journal of Solids and Structures*, **32**(15), 2257–2278, 1995.

[38] Chen, W.F.: *Constitutive Equations for Engineering Materials Volume2:Plasticity and Modeling*. Elsevier Science, Amsterdam, 1994.

[39] Cheng, A. H.-D.; Badmus, T.; Beskos, D.E.: Integral Equations for Dynamic Poroelasticity in Frequency Domain with BEM Solution. *Journal of Engineering Mechanics ASCE*, **117**(5), 1136–1157, 1991.

[40] Commission, California Seismic Safety: Earthquake Risk Mangement: Tools for Decision Makers. *SSC Report 99-04*, 1999.

[41] Crespellani, T.; Madiai, C.; Vannucchi, G.: Liquefaction Hazard during Earthquakes at Nocera Scalo, Italy Part I: Assessment of Liquefaction Potential using simplified Procedures. *Rivista Italiana di Geotecnica*, **4**, 26 – 47, 2002.

[42] Crespellani, T.; Madiai, C.; Vannucchi, G.: Liquefaction Hazard during Earthquakes at Nocera Scalo, Italy Part II: Total and Effective Stress Analyses for Liquefaction Potential Assessment. *Rivista Italiana di Geotecnica*, **4**, 48 – 67, 2002.

[43] Cruse, T.A.: A Direct Formulation and Numerical Solution of the General Transient Elastodynamic Problem, II. *Journal of Mathematical Analysis and Applications*, **22**, 341–355, 1968.

[44] Cruse, T.A.; Osias, J.R.: Issues in merging the finite element and boundary integral equation methods. *Math. Comput. Modelling*, **15**, 103 – 118, 1991.

[45] Cruse, T.A.; Rizzo, F.J.: A Direct Formulation and Numerical Solution of the General Transient Elastodynamic Problem, I. *Journal of Mathematical Analysis and Applications*, **22**, 244–259, 1968.

[46] Dafalias, Y.F.: Bounding surface plasticity. I: Mathematical foundation and hypoplasticity. *Journal of Engineering Mechanics ASCE*, **112**, 966 – 987, 1986.

[47] Dafalias, Y.F.; Hermann, L.R.: Bounding Surface Formulation of Soil Plasticity. In *Soil Mechanics – Transient and Cyclic Loads*. (Pande, G.N.; Zienkiewicz, O.C., Eds.), Wiley, 253–282, 1982.

[48] Dafalias, Y.F.; Popov, E.P.: A model of non-linearly hardening materials for complex loadings. *Acta Mechanica*, **21**, 173–192, 1975.

[49] Dafalias, Y.F.; Popov, E.P.: Plastic Internal Variables Formalism of Cyclic Plasticity. *Journal of Applied Mechanics*, 1976.

[50] D'Arcy, H.: *Les fonteines publiques de le villa de Dijon*. Delmont, Paris, 1856.

[51] Darve, F.; Labanieh, S.: Incremental constitutive law for sands and clays: simulation of monotonic and cyclic tests. *International Journal for Numerical and Analytical Methods in Geomechanics*, 1982.

[52] Dasgupta, G.: A finite element formulation for unbounded homogeneous continua. *Journal of Applied Mechanics, ASME*, **49**, 136 – 140, 1982.

[53] de Boer, R.: *Theory of Porous Media*. Springer-Verlag, Berlin, 2000.

[54] de Boer, R.; Ehlers, W.: Theorie der Mehrkomponentenkontinua mit Anwendungen auf bodenmechanische Probleme, Teil I. Forschungsbericht aus dem Fachbereich Bauwesen 40, Universität - GH Essen, 1986.

[55] de Boer, R.; Ehlers, W.: A Historical Review of the Formulation of Porous Media Theories. *Acta Mechanica*, **74**, 1–8, 1988.

[56] de Boer, R.; Ehlers, W.: The Development of the Concept of Effective Stresses. *Acta Mechanica*, **83**, 77–92, 1990.

[57] Diebels, S.: Mikropolare Zweiphasenmodelle: Formulierung auf der Basis der Theorie Poröser Medien. Bericht Nr. II-4, Universität Stuttgart, Institut für Mechanik, Lehrstuhl II, 2000.

[58] Domínguez, J.: Boundary Element Approach for Dynamic Poroelastic Problems. *International Journal for Numerical Methods in Engineering*, **35**(2), 307–324, 1992.

[59] Domínguez, J.: *Boundary Elements in Dynamics*. Computational Mechanics Publication, Southampton, 1993.

[60] Drucker, D.C.: Some Implications of Work Hardening and Ideal Plasticity. *Quarterly of Applied Mathematics*, 1950.

[61] Drucker, D.C.: A More Fundamental Approach to Plastic Stress-Strain Relations. In *1st US Congress of Applied Mechanics*. (ASME, Ed.), New York, 487 – 491, 1952.

[62] Drucker, D.C.: Soil Mechanics and Work hardening Theories of Plasticity. *Journal of American Society of Civil Engineers*, **122**, 338 – 346, 1957.

[63] Ehlers, W.: Poröse Medien – ein kontinuumsmechanisches Modell auf der Basis der Mischungstheorie. Forschungsbericht aus dem Fachbereich Bauwesen 47, Universität - GH Essen, 1989.

[64] Ehlers, W.: Compressible, Incompressible and Hybrid Two-phase Models in Porous Media Theories. *ASME: AMD-Vol.*, **158**, 25–38, 1993.

[65] Ehlers, W.: Constitutive Equations for Granular Materials in Geomechanical Context. In *Continuum Mechanics in Environmental Sciences and Geophysics*. (Hutter, K., Ed.), CISM Courses and Lecture Notes, No. 337, Springer-Verlag, Wien, 313–402, 1993.

[66] Ehlers, W.; Kubik, J.: On Finite Dynamic Equations for Fluid-Saturated Porous Media. *Acta Mechanica*, **105**, 101–117, 1994.

[67] El-Gebeily, M.; Elleithy, W.M.; Al-Gahtani, H.J.: Convergence of the domain decomposition finite element-boundary element coupling methods. *Computational Methods Applied Mechanics Engineering*, **191**(43), 4851 – 4868, 2002.

[68] Elleithy, W.M.; Al-Gahtani, H.J.: An Overlapping Domain Decomposition Approach for Coupling the Finite and Boundary Element Methods. *Engineering Analysis with Boundary Elements*, **24**(5), 391 – 398, 2000.

[69] Elleithy, W.M.; Al-Gahtani, H.J.; El-Gebeily, M.: Convergence of the Iterative coupling of BEM and FEM. In *21st World Conference on the Boundary Element Method*. (21, BEM, Ed.), Oxford University, UK, 281 – 290, 1999.

[70] Elleithy, W.M.; Al-Gahtani, H.J.; El-Gebeily, M.: Iterative Coupling of BE and FE Methods in Elastostatics. *Engineering Analysis with Boundary Elements*, **25**(8), 685 – 695, 2001.

[71] Elleithy, W.M.; Tanaka, M.: Domain Decomposition Coupling of FEM and BEM. *Japan Society for Computational and Engineering and Science*, **20010050**, 2001.

[72] Elleithy, W.M.; Tanaka, M.: A Domain Decomposition Finite Element/Boundary Element Algorithm. *Boundary Elements Communications: An International Journal*, **13**(2), 27 – 34, 2002.

[73] Elleithy, W.M.; Tanaka, M.: Interface relaxation algorithms for coupling the FEM and BEM. In *24th World Conference on the Boundary Element Method*. (24, BEM, Ed.), Sintra, Portugal, 721 – 730, 2002.

[74] Elleithy, W.M.; Tanaka, M.: Interface relaxation algorithms for BEM-BEM coupling and FEM-BEM coupling. *Computer Methods in Applied Mechanics and Engineering*, **192**, 2977 – 2992, 2003.

[75] Elleithy, W.M.; Tanaka, M.; Guzik, A.: Interface relaxation FEM-BEM coupling method for elasto-plastic analysis. *Engineering Analysis with Boundary Elements*, **28**, 849 – 857, 2004.

[76] Feng, Y.T.; Owen, D.R.J.: Iterative Solution of Coupled FE/BE Discretization for Plate-Foundation Interaction Problems. *International Journal for Numerical Methods in Engineering*, **39**, 1889 – 1901, 1996.

[77] Fillunger, P.: Der Auftrieb von Talsperren, Teil I-III. *Österr. Wochenschrift für den öffentlichen Baudienst*, 532–570, 1913.

[78] Fredholm, I.: Sur une Classe d'Equations Fonctionelles. *Acta Mathematica, Sweden*, **27**, 365–390, 1903.

[79] Frossard, E.: Une équation d'écoulement simple pour les materiaux granulaires. *Géotechnique*, **33**(1), 21 – 29, 1983.

[80] Gel'fand, I. M.; Shilov, G. E.: *Generalized Functions*, Vol. I. Academic Press, New York and London, 1964.

[81] Gerstle, W.H.; Prasad, N.; Xie, M.: Solution Method for Coupled Elastostatics BEM and FEM Domains. *Seventh International Conference on Boundary Element Technology*, Computational Mechanics Publications, Southampton, 213 – 226, 1992.

[82] Ghaboussi, J.; Wilson, E.L.: Variational formulation of dynamics of fluid-saturated porous elastic solids. *Journal of the Engineering Mechanics Division, ASCE*, **98**(4), 947–963, 1972.

[83] Ghaboussi, J.; Wilson, E.L.: Flow of compressible fluid in porous elastic media. *International Journal for Numerical Methods in Engineering*, **5**, 419–442, 1973.

[84] Hencky, H.Z.: Zur Theorie Plastischer Deformationen und der hierdurch im Material hervorgerufenen Nachspannungen. *Zeitschrift für Angewandte Mathematik und Mechanik*, 1924.

[85] Hill, R.: *The Mathematical Theory of Plasticity*. Oxford Univ. Press, London, 1950.

[86] Hörmander, L.: *Linear Partial Differential Operators*. Springer-Verlag, 1963.

[87] Kamiya, N.; Iwase, H.: BEM and FEM Combination Parallel Analysis Using Conjugate Gradient and Condensation. *Engineering Analysis with Boundary Elements*, **20**, 319 – 326, 1997.

[88] Kamiya, N.; Iwase, H.; Kita, E.: Parallel implementation of boundary element method with domain decomposition. *Engineering Analysis with Boundary Elements*, **18**, 209 – 216, 1996.

[89] Karabalis, D.L.; Beskos, D.E.: Dynamic Response of 3-D Rigid Surface Foundations by Time Domain Boundary Element Method. *Earthquake Engineering and Structural Dynamics*, **12**, 73–93, 1984.

[90] Karabalis, D.L.; Beskos, D.E.: Dynamic response of 3-D flexible foundations by time domain BEM and FEM. *Soil Dynamics and Earthquake Engineering*, **4**, 91–101, 1985.

[91] Karabalis, D.L.; Beskos, D.E.: Dynamic Response of 3-D Rigid Sembedded Foundations by the Boundary Element Method. *Computer Methods in Applied Mechanics and Engineering*, **56**, 91–120, 1986.

[92] Katona, M.G.; Zienkiewicz, O.C.: A unified set of single step algorithms Part 3: The Beta-m method, a generalization of the Newmark scheme. *International Journal for Numerical Methods in Engineering*, **21**, 1345–1359, 1985.

[93] Kelly, D.W.; Mustoe, G.; Zienkiewicz, O.C.: Coupling boundary element methods with other numerical methods. In *Developments in boundary element methods - I*. (Banerjee, P.K.; Butterfield, R., Eds.), Applied Science, London, 251 – 285, 1979.

[94] Kim, J.K.; Koh, H.M.; Kwon, K.J.; Yi, J.S.: A three-dimensional transmitting boundary formulated in Cartesian co-ordinate system for the dynamics of non-axisymmetric foundations. *Earthquake Engineering and Structural Dynamics*, **29**, 1527–1546, 2000.

[95] Kim, Y.K.; Kingsbury, H.B.: Dynamic Characterization of Poroelastic Materials. *Experimental Mechanics*, **19**, 252–258, 1979.

[96] Kolymbas, D.: An outline of hypoplasticity. *Archive of Applied Mechanics*, **61**, 143 – 151, 1991.

[97] Krieg, R.D.: A practical two surface plasticity theory. *Journal of Applied Mechanics, ASME*, **42**, 641 – 646, 1975.

[98] Kupradze, V.D.: *Potential Methods in the Theory of Elasticity*. Israel Program for Scientific Translations, Jerusalem, 1965.

[99] Lade, P.V.; Duncan, J.M.: Elasto-Plastic Stress-Strain Theory for Cohesionless Soil. *Journal of Geotechnical Engineering Division, ASCE*, **101**, 1037 – 1053, 1975.

[100] Leung, K.H.: *Earthquake response of saturated soils and liquefaction*. PhD thesis, University College of Swansea, 1984.

[101] Lewis, R.W.; Schrefler, B.A.: *The Finite Element Method in the Static and Dynamic Deformation and Consolidation of Porous Media*. John Wiley and Sons, Chichester, 1998.

[102] Li, H.B.; Han, G.M.; Man, H.A.; Torzicky, P.: A new method for the coupling of finite element and boundary element discretized subdomain of elastic bodies. *Computer Methods in Applied Mechanics and Engineering*, **54**, 161 – 185, 1986.

[103] Lin; Chin-Ching; Lawton, E.C.; Caliendo, J.A.; Anderson, L.R.: An Iterative Finite Element Boundary Element Algorithm. *Computers & Structures*, **39**(5), 899 – 909, 1996.

[104] Lions, P.L.: On the Schwarz alternating method III: a variant for nonoverlapping subdomains. In *Proceedings of the Third International Symposium on Domain decomposition methods for partial differential equations, Houston, TX, 1989, SIAM*. (Chan, T.F.; Glowinski, R.; Périaux, J.; Widlund, O.B.; Widlund, O.B., Eds.), Philadelphia, USA, 202 – 223, 1990.

[105] Lubich, C.: Convolution Quadrature and Discretized Operational Calculus. I. *Numerische Mathematik*, **52**, 129–145, 1988.

[106] Lubich, C.: Convolution Quadrature and Discretized Operational Calculus. II. *Numerische Mathematik*, **52**, 413–425, 1988.

[107] Lysmer, J.; Kuhlemeyer, R.L.: Finite dynamic model for infinite media. *Journal of Engineering Mechanics ASCE*, **95**(EM4), 859–877, 1969.

[108] Mansur, W. J.: *A Time-Stepping Technique to Solve Wave Propagation Problems Using the Boundary Element Method*. Phd thesis, University of Southampton, 1983.

[109] Mansur, W.J.; Brebbia, C.A.: Transient Elastodynamics Using a Time-Stepping Technique. In *Boundary Elements*. (Brebbia, C.A.; Futagami, T.; Tanaka, M.; Tanaka, M., Eds.), Springer-Verlag, Berlin, 677–698, 1983.

[110] Margulies, M.: Combination of the boundary element and finite element methods vol. 1. In *Progress in boundary element methods*. (Brebbia, C.A., Ed.), Pentech Press, London, 1981.

[111] Mroz, Z.: On the description of anisotropic work-hardening. *Journal of the Mechanics and Physics of Solids*, **15**, 163 – 175, 1967.

[112] Mroz, Z.; Norris, V.A.; Zienkiewicz, O.C.: An Anisotropic Hardening Model for Soils and its Application to Cyclic Loading. *International Journal for Numerical and Analytical Methods in Geomechanics*, **2**, 203 – 221, 1978.

[113] Mroz, Z.; Norris, V.A.; Zienkiewicz, O.C.: An Anisotropic Critical State Model for Soils subjected to cyclic loading. *Geophysics*, **31**, 451 – 469, 1981.

[114] Newmark, N.M.: A method of computation for structural dynamics. *Proceedings of the American Society of Civil Engineers*, 67–94, 1959.

[115] Nour, A.; Alam, M.J.: Use of generalized Smith boundary for loads having non-vanishing time average. *Computers and Geotechnics*, **29**, 235–255, 2002.

[116] Nova, R.; Wood, D.M.: A Constitutive Model for Sand in Triaxial Compression. *International Journal for Numerical and Analytical Methods in Geomechanics*, **3**, 225 – 278, 1979.

[117] Pastor, M.; Zienkiewicz, O. C.; Leung, K. H.: Simpe Model for Transient Soil Loading in Earthquake Anaysis. II. Non-Associative Models for Sands. *International Journal for Numerical and Analytical Methods in Geomechanics*, **9**, 477 – 498, 1985.

[118] Pastor, M.; Zienkiewicz, O.C.: A Generalized Plasticity, Hierachical Model for Sand under Monotonic and Cyclic Loading. In *Proceedings 2nd International Conference Numerical Models in Geomechanics:*. (Pande, G.N.; Impe, W.F. Van, Eds.), M. Jackson and Son Pub., Ghent Belgium, 131 – 150, 1986.

[119] Pastor, M.; Zienkiewicz, O.C.; Chan, A.H.C: Generalized Plasticity and the Modelling of Soil Behaviour. *International Journal for Numerical and Analytical Methods in Geomechanics*, **14**, 151 – 190, 1990.

[120] Pastor, M.; Zienkiewicz, O.C.; Guang-Dou, Xu; Peraire, J.: Modelling of Sand Behaviour: Cyclic Loading, Ansiotropy and Localization. In *Modern Approaches to Plasticity*. (Kolymbas, D., Ed.), Elsevier, Amsterdam, 469 – 492, 1993.

[121] Pease, M.C.: *Methods of Matrix Algebra*, Vol. 16, *Mathematics in Science and Engineering*. Academic Press, 1965.

[122] Perera, R.; Ruiz, A.; Alarcon, E.: FEM-BEM Coupling Procedure through the Stelkov-Poincare Operator. *Boundary Element XV*, Computational Mechanics Publications, Southampton, 621 – 632, 1993.

[123] Plate, E.: Towards development of a Human Security Index. In *Flood Events: Are We Prepared?* (Workshop, OSIRIS, Ed.), Berlin, 2003.

[124] Plona, T.J.: Observation of a Second Bulk Compressional Wave in Porous Medium at Ultrasonic Frequencies. *Applied Physics Letters*, **36**(4), 259–261, 1980.

[125] Prandtl, L.: Spannungsverteilung in plastischen Körpern. In *Proceedings of the 1st International Congress of Applied Mechanics*. (Waltmann, J., Ed.). Technische Boekhandel en Druckerij, 43 – 54, 1925.

[126] Prevost, J.H.: Nonlinear transient phenomena in saturated porous media. *Computer Methods in Applied Mechanics and Engineering*, **20**, 3–18, 1982.

[127] Prevost, J.H.: Wave Propagation in Fluid-Saturated Porous Media: An Efficient Finite Element Procedure. *Soil Dynamics and Earthquake Engineering*, **4**(4), 183–202, 1985.

[128] Pryl, D.: *Influences of Poroelasticity on Wave Propagation: A Time Stepping Boundary Element Formulation*, Vol. 58, *Braunschweiger Schriften zur Mechanik*. Mechanik Zentrum der Technischen Universität Braunschweig, 2005.

[129] Pryl, D.; Schanz, M.: Mixed Shape Functions for a Poroelastic Boundary Element Formulation. In *Advances in Boundary Element Techniques V*. (Leitão, V.M.A.; Aliabadi, M.H., Eds.), EC Ltd., UK, 63–68, 2004.

[130] Puzrin, A.M.; Houlsby, G.T.: On the non-intersection dilemma in muliple surface plasticity. *Geophysics*, **51**(4), 369 – 372, 2001.

[131] Ramberg, W.; Osgood, W. R.: Description of Stress-Strain Curves by Three Parameters. *NACA Technical Note*, **902**, 1943.

[132] Rashed, Y.F.: Boundary Element Primer 5: Fundamental Solutions – II Matrix Operators. *Boundary Element Communications: An International Journal*, **13**(2), 35–45, 2002.

[133] Rückversicherungs-Gesellschaft, Münchener: Claims management following natural catastrophes Experience, analyses, action plans. *Knowledge Series*, **Order number 302-04646**, 1985.

[134] Reuss, E.: Berücksichtigung der elastischen Formänderungen in der Plastizitätstheorie. *Zeitschrift für Angewandte Mathematik und Mechanik*, **10**, 266 – 274, 1930.

[135] Rice, J.R.; Tsompanopoulou, P.; Vavalis, E.A.: Interface Relaxation Methods for Elliptic Differential Equations. *Applied Numerical Mathematics*, **32**, 219 – 245, 1999.

[136] Richards, J.I.; Youn, H.K.: *Theory of Distributions: A Non-technical Introduction*. Cambridge University Press, 1990.

[137] Roscoe, K.H.; Burland, J.B.: On the generalized stress-strain behaviour of 'wet' clay. In *Engineering Plasticity*. (Heymann, J.; Leckie, F.A., Eds.), Cambridge Univ. Press, 535–609, 1968.

[138] Roscoe, K.H.; Schofield, A.N.: Mechanical behaviour of an idealised 'wet' clay. *Proceedings of the Second European Conference on Soil Mechanics and Foundation Engineering*, 1, Wiesbaden, 47–54, 1963, ECSMFE.

[139] Ruge, P.; Trinks, C.; Witte, S.: Time-domain analysis of unbounded media using mixed-variable formulations. *Earthquake Engineering and Structural Dynamics*, **30**, 899–925, 2001.

[140] Safjan, A.J.: Iterative radiation boundary conditions for the finite element solutions of the scalar wave equation. *Computer Methods in Applied Mechanics and Engineering*, **190**, 6373–6398, 2001.

[141] Safjan, A.J.; Newman, M.: On two-dimensional infinite elements utilizing basis functions with compact support. *Computer Methods in Applied Mechanics and Engineering*, **190**, 6399–6424, 2001.

[142] Sandhu, R.S.; Wilson, E.L.: Finite-element analysis of seepage in elastic media. *Journal of the Engineering Mechanics Division, ASCE*, **95**(3), 641–652, 1969.

[143] Schanz, M.: A Boundary Element Formulation in Time Domain for Viscoelastic Solids. *Communications in Numerical Methods in Engineering*, **15**, 799–809, 1999.

[144] Schanz, M.: Application of 3-d Boundary Element Formulation to Wave Propagation in Poroelastic Solids. *Engineering Analysis with Boundary Elements*, **25**(4-5), 363–376, 2001.

[145] Schanz, M.: *Wave Propagation in Viscoelastic and Poroelastic Continua: A Boundary Element Approach*. Lecture Notes in Applied Mechanics. Springer-Verlag, Berlin, Heidelberg, New York, 2001.

[146] Schanz, M.; Antes, H.: Application of 'Operational Quadrature Methods' in Time Domain Boundary Element Methods. *Meccanica*, **32**(3), 179–186, 1997.

[147] Schanz, M.; Antes, H.: A New Visco- and Elastodynamic Time Domain Boundary Element Formulation. *Computational Mechanics*, **20**(5), 452–459, 1997.

[148] Schanz, M.; Cheng, A.H.-D.: Transient Wave Propagation in a One-Dimensional Poroelastic Column. *Acta Mechanica*, **145**, 1–18, 2000.

[149] Schanz, M.; Diebels, S.: A Comparative Study of Biot's Theory and the Linear Theory of Porous Media for Wave Propagation Problems. *Acta Mechanica*, **161**(3-4), 213–235, 2003.

[150] Schanz, M.; Pryl, D.: Dynamic Fundamental Solutions for Compressible and Incompressible Modeled Poroelastic Continua. *International Journal of Solids and Structures*, **41**(15), 4047–4073, 2004.

[151] Schofield, A.N.; Wroth, C.P.: *Critical state soil mechanics*. McGraw Hill, London, 1968.

[152] Schwartz, L.: *Théorie des distributions*. Herman, Paris, 1966.

[153] Shaw, R.P.; Falby, W.: F.e.b.i.e - combination of the finite element and boundary integral methods. *Journal of Computers and Fluids*, **6**(3), 153 – 160, 1978.

[154] Simo, J.C.; Taylor, R.L.: Consistent tangent operators for rate independent elastoplasticity. *Computer Methods in Applied Mechanics and Engineering*, **48**, 101–118, 1985.

[155] Simon, B.R.; Wu, J.S.; Zienkiewicz, O.C.: Evaluation of higher order mixed and hermitean finite element procedures for dynamic analysis of saturated porous media. *International Journal for Numerical and Analytical Methods in Geomechanics*, 1986.

[156] Simon, B.R.; Wu, J.S.; Zienkiewicz, O.C.: Evaluation of u-w and u-π finite element methods for the dynamic response of saturated porous media using one-dimension. *International Journal for Numerical and Analytical Methods in Geomechanics*, 1986.

[157] Soares, Jr.D.; von Estorff, O.; Mansur, W.J.: Iterative coupling of BEM and FEM for nonlinear dynamic analysis. *Computational Mechanics*, **34**(1), 67 – 73, 2004.

[158] Sommerfeld, A.: *Partial Differential Equations in Physics*. Academic Press, New York, 1949.

[159] Stakgold, I.: *Green's Functions and Boundary Value Problems*. Pure and Applied Mathematics. John Wiley & Sons, 2nd edition, 1998.

[160] Terzaghi, K.: *Theoretical soil mechanics*. John Wiley and Sons, New York, 1943.

[161] Truesdell, C.; Toupin, R.A.: The Classical Field Theories. In *Handbuch der Physik*. (Flügge, S., Ed.), Vol. III/1, Springer-Verlag, Berlin, 226–793, 1960.

[162] Vardoulakis, I.; Beskos, D.E.: Dynamic Behavior of Nearly Saturated Porous Media. *Mechanics of Composite Materials*, **5**, 87–108, 1986.

[163] von Estorff, O.: Dynamic response of elastic blocks by time domain BEM and FEM. *Computers & Structures*, **38**(3), 289 – 300, 1991.

[164] von Estorff, O.; Antes, H.: On FEM-BEM coupling for fluid structure interaction analysis in the time domain. *International Journal for Numerical Methods in Engineering*, **31**, 1151 – 1168, 1991.

[165] von Estorff, O.; Hagen, C.: Iterative coupling of FEM and BEM in 3D transient elastodynamics. *Engineering Analysis with Boundary Elements*, **29**, 775 – 787, 2005.

[166] von Estorff, O.; Prabucki, M.J.: Dynamic response in the time domain by coupled boundary and finite elements. *Computational Mechanics*, **6**, 35 – 46, 1990.

[167] Wiebe, Th.; Antes, H.: A Time Domain Integral Formulation of Dynamic Poroelasticity. *Acta Mechanica*, **90**, 125–137, 1991.

[168] Wilde, P.: Two Invariants-dependent Models of Granular Media. *Archives of Mechanics*, **29**(6), 799 – 809, 1977.

[169] Wohlmuth, B.I.: *Discretization Methods and Iterative Solvers Based on Domain Decomposition*. Lecture Notes in Applied Mechanics. Springer-Verlag, Berlin, Heidelberg, New York, 2001.

[170] Wolf, J.P.: *Finite-Element Modeling of Unbounded Media*. John Wiley & Sons, 1996.

[171] Wolf, J.P.: Response of unbounded soil in scaled boundary finite-element method. *Earthquake Engineering and Structural Dynamics*, **31**, 15–32, 2002.

[172] Wolf, J.P.; Song, Ch.: Dynamic-stiffness matrix of unbounded soil by finite-element multi-cell cloning. *Earthquake Engineering and Structural Dynamics*, **23**, 235–255, 1994.

[173] Zienkiewicz, 0.C.; Bicanic, N.; Shen, F.Q.: Single step averaging generalized Smith transmitting boundary in computational dynamics. In *Proc. Int. Conf. on Numerical Methods in Engineering: Theory and Applications Vol. II, paper T49/1, Swansea*. (Pande, G. N.; Moddleton, J., Eds.), Martinus Nijhoff Publishers, Dordrecht, 6 – 10, 1987.

[174] Zienkiewicz, O.C.: Coupled problems and their numerical solution. In *Numerical Methods in Coupled Systems*. (Lewis, R.W.; Bettess, P.; Hinton, E.; Hinton, E., Eds.), Wiley, 35–38, 1984.

[175] Zienkiewicz, O.C.: The coupled problems of soil-pore fluid-external fluid interaction: Basis fo a general geomechanics code. *ICONMIG*, 5, 1731–1740, 1985.

[176] Zienkiewicz, O.C.; Bettess, P.: Soils and other Saturated Media under Transient, Dynamic Conditions; General Formulation and the Validity of various simplifiying assumptions. In *Soil Mechanics – Transient and Cyclic Loads*. (Pande, G.N.; Zienkiewicz, O.C., Eds.), Wiley, 1–16, 1982.

[177] Zienkiewicz, O.C; Chan, H.C.; Pastor, M.; Paul, D.K.; Shiomi, T.: Static and Dynamic Behaviour of Soils: A Rational Approach to Quantitative Solutions. I. Fully Saturated Problems. *Proceedings of the Royal Society of London*, **429**(A), 285–309, 1990.

[178] Zienkiewicz, O.C.; Leung, K.H.; Pastor, M.: Simple Model for Transient Soil Loading in Earthquake Analysis. I. Basic Model and its Application. *International Journal for Numerical and Analytical Methods in Geomechanics*, **9**, 453 – 476, 1985.

[179] Zienkiewicz, O.C.; Mroz, Z.: Generalized plasticity formulation and applications to geomechanics. In *Mechanics of Engineering Materials*. (Desai, C.S.; Gallagher, R.H., Eds.), Wiley, Chapter 33, 655–679, 1984.

[180] Zienkiewicz, O.C.; Mroz, Z.: Uniform formulation of constitutive laws for clays and sands. In *Mechanics of Engineering Materials*. (Desai, C.S.; Gallagher, R.H., Eds.), Wiley, Chapter 22, 415–449, 1984.

[181] Zienkiewicz, O.C.; Newton, R.E.: Coupled vibrations of a structure submerged in a compressible fluid. In *Proceedings International Symposium of Finite Element Techniques*. (Sorensen, M., Ed.), University of Stuttgart, Stuttgart, 359 – 379, 1969.

[182] Zienkiewicz, O.C; Qu, S.; Taylor, R.L.; Nakazawa, S.: The Patch Test for Mixed Formulation. *International Journal for Numerical Methods in Engineering*, **23**, 1873–1883, 1986.

[183] Zienkiewicz, O.C.; Shiomi, T.: Dynamic Behaviour of Saturated Porous Media; The Generalized Biot Formulation and its Numerical Solution. *International Journal for Numerical and Analytical Methods in Geomechanics*, **8**, 71–96, 1984.

[184] Zienkiewicz, O.C.; Taylor, R.L.: *The Finite Element Method - Volume I: Basic Formulation and Linear Problems*. McGraw-Hill Book Company, London, 1989.

[185] Zienkiewicz, O.C; Taylor, R.L.; Simo, J.C.; Chan, A.H.C.: The Patch Test - A conditon for assessing F.E.M. Convergence. *International Journal for Numerical Methods in Engineering*, **22**, 39–62, 1986.

[186] Zienkiewiecz, O.C.; Chan, A.H.C.; Pastor, M.; Schrefler, B.A.; Shiomi, T.: *Computational geomechanics with special reference to earthquake engineering*. Wiley, Chichester, 1999.

[187] Zienkiewiecz, O.C.; Chang, C.; Bettess, P.: Drained undrained consolidating and dynamic behavior assumptions in soils. *Géotechnique*, **30**(4), 385 – 395, 1980.

[188] Zienkiewiecz, O.C.; Chang, C.T.; Hinton, E.: Non-linear seismic response and liquefaction. *International Journal for Numerical and Analytical Methods in Geomechanics*, **2**, 381 – 404, 1978.

[189] Zienkiewiecz, O.C.; Kelly, D.W.; Bettess, P.: The Coupling of the Finite Element Method and Boundary Solution procedures. *International Journal for Numerical Methods in Engineering*, **11**, 355 – 375, 1977.

[190] Zienkiewiecz, O.C.; Taylor, R.L.: Coupled Problems - A simple time-stepping procedure. *Communications in Applied Numerical Methods*, **1**, 233–239, 1985.

[191] Zienkiewiecz, O.C.; Wood, W.L.; Hine, N.W.: A unified set of single step algorithms Part 1: General formulation and applications. *International Journal for Numerical Methods in Engineering*, **20**, 1529–1552, 1984.

[192] Zienkiewiecz, O.C.; Wood, W.L.; Taylor, R.L.: An alternative single-step algorithm for dynamic problems. *Earthquake Engineering and Structural Dynamics*, **8**, 31–40, 1980.

Braunschweiger Schriften zur Mechanik – BSM

Bisher erschienene Berichte in dieser Reihe

1–1990 Plonski, Thomas:
Dynamische Analyse von schnelldrehenden Kreiszylinderschalen

2–1991 Wegener, Konrad:
Zur Berechnung grosser plastischer Deformationen mit einem Stoffgesetz vom Überspannungstyp

3–1992 Gröhlich, Hubert:
Finite-Element-Formulierung für vereinheitlichte inelastische Werkstoffmodelle ohne explizite Fliessflächenformulierung

4–1992 Hesselbarth, Hanfried:
Simulation von Versetzungsstrukturbildung, Rekristallisation und Kriechschädigung mit dem Prinzip der zellulären Automaten

5–1992 Schlums, Hartmut:
Ein stochastisches Werkstoffmodell zur Beschreibung von Kriechen und zyklischem Verhalten metallischer Werkstoffe

6–1992 Kublik, Frithjof:
Vergleich zweier Werkstoffmodelle bei ein- und mehrachsigen Versuchsführungen im Hochtemperaturbereich

7–1992 Bechtloff, Jürgen:
Interpolationsverfahren höheren Grades für Robotersteuerungen

8–1993 Müller, Michael:
Dreidimensionale elastodynamische Analyse von Tanks mit fluidbenetzten Einbauten

9–1993 Senker, Peter:
Stabilitätsanalyse elastischer Rotorsysteme

10–1993 Cheng, Weimin:
Schallabstrahlung einer schwingenden Reisner/Mindlin Platte

11–1993 Wiebe, Thomas:
Wellenausbreitung in poroelastischen Medien: Untersuchung mit Randintegralgleichungen

12–1993 Hahne, Matthias:
Beschreibung der plastischen Längsdehnung bei Torsion mit einem makroskopischen Stoffgesetz

13–1993 Heisig, Gerald:
Zum statischen und dynamischen Verhalten von Tiefbohrsträngen in räumlich gekrümmten Bohrlöchern

14–1994 de Araújo, Francisco Célio:
Zeitbereichslösung linearer dreidimensionaler Probleme der Elastodynamik mit einer gekoppelten BE/FE-Methode

15–1994 Kristen, Martin:
Untersuchungen zur elektrischen Ansteuerung von Formgedächtnis-Antrieben in der Handhabungstechnik

16–1994 Latz, Kersten:
Dynamische Interaktion von Flüssigkeitsbehältern und Baugrund

17–1994 Jäger, Monika:
Entwicklung eines effizienten Randelementverfahrens für bewegte Schallquellen

18–1994 August, Martin:
Schwingungen und Stabilität eines elastischen Rades, das auf einer nachgiebigen Schiene rollt

19–1995 Erbe, Matthias:
Zur Simulation von Risswachstum in dreidimensionalen, elastisch-plastischen Strukturen mit der Methode der Finiten Elemente

20–1995 Gerdes, Ralf:
Ein stochastisches Werkstoffmodell für das inelastische Materialverhalten metallischer Werkstoffe im Hoch- und Tieftemperaturbereich

21–1995 Tröndle, Georg:
Effiziente Schallberechnung mit einem adaptiven Mehrgitterverfahren für die 3-D Randelementmethode

22–1996 Degenhardt, Richard:
Nichtlineare dynamische Bauwerksprobleme und Interaktion mit dem Baugrund

23–1996 Feise, Hermann Josef:
Modellierung des mechanischen Verhaltens von Schüttgütern

24–1996 Haubrok, Dietmar:
Reibungsfreie Kontaktprobleme der 2-D Elastostatik und -dynamik als Optimierungsaufgabe mit REM-Matrizen

25–1996 Lehmann, Lutz:
Numerische Simulation der Spannungs- und Geschwindigkeitsfelder in Silos mit Einbauten

26–1996 Klein, Ralf:
Dynamische Interaktion von dünnwandigen Tragwerken und Boden mit Abschirmschlitzen

27–1996 Kopp, Thilo:
Simulation grosser inelastischer Deformationen bei Torsionsversuchen

28–1997 Harder, Jörn:
Simulation lokaler Fliessvorgänge in Polykristallen

29–1997 Lewerenz, Malte Christian:
Zur numerischen Behandlung von Werkstoffmodellen für zeitabhängig plastisches Materialverhalten

30–1997 Meywerk, Martin:
Stabilität und Verschleiss bei auf Schienen laufenden Eisenbahnradsätzen

31–1997 Plagge, Frank:
Nichtlineares, inelastisches Verhalten von Spiralseilen

32–1997 Neubert, Michael:
Richtungsregelung beim Tiefbohren

33–1998 Sangi, Daryoush:
Die Versetzungsstrukturbildung in Metallen

34–1998 Thielecke, Frank:
Parameteridentifizierung von Simulationsmodellen für das viskoplastische Verhalten von Metallen - Theorie, Numerik, Anwendung

35–1998 Vietgen, Jürgen:
Numerische Simulation duktilen Risswachstums unter Berücksichtigung von Schädigung

36–1998 Läer, Bernard:
Einfluss transienter Anregungen auf die Zylinderkopf-Akustik

37–1998 Scheld, Christian:
Auswirkungen dynamischer Interaktionen auf das Schwingungsverhalten von Tanks

38–1999 Baaran, Jens:
Schallfeldanalyse bei sich bewegenden schallerzeugenden Körpern

39–1999 Daros, Carlos:
Wave propagation in unbounded piezoelectric media of transversely isotropic symmetry

40–2000 Nils, Wagner:
Untersuchung der Boden-Fahrzeug-Interaktion mit gekoppelten Rand- und Finite-Element-Methoden

41–2001 Langer, Sabine:
Schalltransmission durch Isolierverglasung

42–2001 Schacht, T.:
Orientierungsabhängige Rissbildung in duktilen Metallen

43–2002 Ackerman, Lutz:
Simulation der Schalltransmission durch Wände

44–2002 Barthold, Franz-Joseph:
Zur Kontinuummechanik inverser Geometrieprobleme

45–2002 Böhrnsen, Jens-Uwe:
Dynamisches Verhalten von Schüttgütern beim Entleeren aus Silos

46–2002 Zorn, C.:
Plastisch instabile Verformung aufgrund dynamischer Reckalterung und korrelierten Versetzungsgleitens

47–2002 Küsel, M.:
Wellige Verschleissmuster auf Laufflächen von Eisenbahnrädern

48–2002 Bross, S.:
Versetzungsdynamik und Reckalterung als Ursache instabilen Materialverhaltens beim Portevin-Le Chatelier-Effekt

49–2002 Vesper, Matthias:
Modellierung von Korn und Korngrenze in polykristallinen Gefügen

50–2003 Steindorf, Jan:
Partitionierte Verfahren für Probleme der Fluid-Struktur Wechselwirkung

51–2003 Meyer, Marcus:
Reduktionsmethoden zur Simulation des aeroelastischen Verhaltens von Windkraftanlagen

52–2003 Wittich, Hauke:
Inhomogene Gleitung bei nahgeordneten CuAl-Legierungen

53–2003 Hupfer, Knut:
Einfluss der Mikrostruktur auf die Festigkeitseigenschaften von Metallschäumen

54–2004 Schmelzer, Martin:
Identifikation der Parameter von Zeitbereichsmodellen linear-viskoelastischer Werkstoffe

55–2004 Ostendorf, Michael:
Geschwindigkeitsmessungen in Silos mit der Particle Image Velocimetry

56–2004 Engelhardt, Marek:
Numerische Verfahren zur Identifizierung von Fehlstellen aus Randdaten

57–2005 Keese, Andreas:
Numerical Solution of Systems with Stochastic Uncertainties - A General Purpose Framework for Stochastic Finite Elements

58–2005 Pryl, Dobromil:
Influences of Poroelasticity on Wave Propagation: A Time Stepping Boundary Element Formulation

59–2005 Fries, Thomas-Peter:
A Stabilized and Coupled Meshfree/Meshbased Method for Fluid-Structure Interaction Problem

60–2005 Kayser-Herold, Oliver:
Least-Squares Methods for the Solution of Fluid-Structure Interaction Problems

61–2006 Hampel, Sebastian:
Numerische Simulation der Schallausbreitung unter Berücksichtigung meteorologischer Einflüsse